



Terms and Conditions of Use of Digitised Theses from Trinity College Library Dublin

Copyright statement

All material supplied by Trinity College Library is protected by copyright (under the Copyright and Related Rights Act, 2000 as amended) and other relevant Intellectual Property Rights. By accessing and using a Digitised Thesis from Trinity College Library you acknowledge that all Intellectual Property Rights in any Works supplied are the sole and exclusive property of the copyright and/or other IPR holder. Specific copyright holders may not be explicitly identified. Use of materials from other sources within a thesis should not be construed as a claim over them.

A non-exclusive, non-transferable licence is hereby granted to those using or reproducing, in whole or in part, the material for valid purposes, providing the copyright owners are acknowledged using the normal conventions. Where specific permission to use material is required, this is identified and such permission must be sought from the copyright holder or agency cited.

Liability statement

By using a Digitised Thesis, I accept that Trinity College Dublin bears no legal responsibility for the accuracy, legality or comprehensiveness of materials contained within the thesis, and that Trinity College Dublin accepts no liability for indirect, consequential, or incidental, damages or losses arising from use of the thesis for whatever reason. Information located in a thesis may be subject to specific use constraints, details of which may not be explicitly described. It is the responsibility of potential and actual users to be aware of such constraints and to abide by them. By making use of material from a digitised thesis, you accept these copyright and disclaimer provisions. Where it is brought to the attention of Trinity College Library that there may be a breach of copyright or other restraint, it is the policy to withdraw or take down access to a thesis while the issue is being resolved.

Access Agreement

By using a Digitised Thesis from Trinity College Library you are bound by the following Terms & Conditions. Please read them carefully.

I have read and I understand the following statement: All material supplied via a Digitised Thesis from Trinity College Library is protected by copyright and other intellectual property rights, and duplication or sale of all or part of any of a thesis is not permitted, except that material may be duplicated by you for your research use or for educational purposes in electronic or print form providing the copyright owners are acknowledged using the normal conventions. You must obtain permission for any other use. Electronic or print copies may not be offered, whether for sale or otherwise to anyone. This copy has been supplied on the understanding that it is copyright material and that no quotation from the thesis may be published without proper acknowledgement.

HEAT TRANSFER CHARACTERISTICS OF SWIRLING IMPINGING JETS

KARL J. BROWN

Department of Mechanical & Manufacturing Engineering

Parsons Building

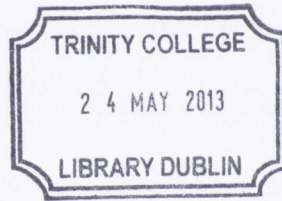
Trinity College

Dublin 2

Ireland

April 2013

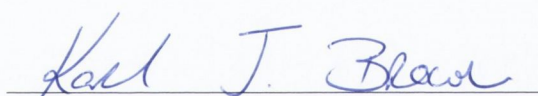
A confirmation thesis submitted to the University of Dublin in
partial fulfillment of the requirements for the degree of Ph.D.



Thesis 9899

Declaration

I declare that I am the author of this thesis and that all work described herein is my own, unless otherwise referenced. Furthermore, this work has not been submitted, in whole or part, to any other university or college for any degree or qualification. I authorize the library of Trinity College, Dublin to lend or copy this thesis.

A handwritten signature in blue ink that reads "Karl J. Brown". The signature is written in a cursive style and is positioned above a horizontal line.

Karl J. Brown, April 2013

To Molly and Alfred

Abstract

The application of impinging jets for cooling purposes is an ongoing search for greater levels of heat dissipation in a world where manufacturing processes are getting more advanced and electrical systems are becoming smaller and more confined for aesthetic reasons, such that they are in constant need of increased thermal management. Over the years, a number of methods have been investigated to enhance the heat transfer in systems by varying different aspects of the method being used.

The following study evaluates the heat transfer from a horizontal heated surface due to a contoured nozzle conventional impinging jet and the enhancement that is gained by introducing swirl generators into the nozzle structure which produce a series of swirling impinging jets. This study sets out to describe the background of both the flow structure and the levels of heat transfer commonly associated with a conventional impinging jet. Past studies conducted into the formation and influence of swirling impinging jets are also presented as a precursor to the findings of this study.

Two experimental set-ups are used to evaluate the heat transfer characteristics of each of the impinging jet configurations at a range of nozzle to surface heights from $0.5D$ to $10D$ and Reynolds numbers from 8,000 to 20,000. Through the method of infrared thermography, a two-dimensional map of the heat transfer is created and this allows the uniformity of the distribution to be realised. Using a hot-film sensor in the second measurement method, a more defined heat transfer distribution is produced primarily due to the higher spatial resolution of the sensor compared to the thermal imaging camera. This sensor also allows the fluctuations of the heat transfer from the surface due to the impinging jets to be evaluated.

Through experimental testing with the different techniques, it is noted that each of the swirling impinging jets causes a local enhancement up to 20% in the heat transfer within the stagnation region for low nozzle heights and high Reynolds numbers in the range of parameters examined. From the fluctuating heat transfer measurements, the conventional impinging jet is found to have significant increasing levels of fluctuations as the distance from the stagnation point is increased at low H/D . At higher nozzle to surface spacings, the near zero fluctuations in the stagnation region increase with respect to the development of the impinging jet. With the same method, the swirling impinging jets display high levels of fluctuations in the region around $r/D=0$ for low H/D , and as the height of the nozzle is increased, the heat transfer fluctuation levels resemble those of a conventional impinging jet.

In order to determine the mechanisms that govern the heat transfer distributions produced, flow visualisation of each of the impinging jet configurations is conducted. The flow fields of each of the impinging jets permit local aspects to be identified and referred to specifics in the different local and fluctuating heat transfer distributions, including the characterisation of vortical structures in the wall jet generating additional peaks in the local heat transfer of the conventional impinging jet for low H/D . Flow visualisation of the swirling impinging jets illustrates the change in flow structure compared to the conventional impinging jet and highlights recirculation towards the center of the jet at specific nozzle heights, which can further reduce the local heat transfer.

Acknowledgements

This incredible opportunity granted to me could not have occurred without the inspiration and guidance of my supervisor, Prof. Darina Murray. The level of gratitude owed to her is immeasurable. I am also very appreciative of Dr. Tony Robinson, Dr. Tadhg O'Donovan and Dr. Tim Persoons for their additional assistance along the way and who were incredibly helpful when needed. Mr. Gerry Byrne deserves a lot of credit also due to his practical knowledge and experience which keeps all systems and studies running like clockwork. I would like to thank the gentlemen in the workshop for creating the parts necessary for my apparatus to take shape and for permitting my frequent visits. All of the staff I have gotten to know over the past few years also have my appreciation for making this an incredibly friendly place to work for myself and everyone else.

Without my friends and colleagues who have provided optimism, encouragement and many tea breaks, the future would not look as bright. Specifically to Seamus, Alan, Brian, Tom, Rayhaan, Gerard, Oisin, David and Stephen; your help made the last few years go past far too quickly.

To my family, you have always pushed me to aim higher. The success of each chapter of my life has been down to your encouragement and support for which I am eternally grateful. Hopefully the next chapter will be able to top this one.

Finally, I would like to acknowledge the Irish Research Council and Trinity College Dublin for funding this study.

Contents

List of Figures	ix
List of Tables	xxi
Nomenclature	xxiii
1 Introduction	1
1.1 Research Objectives	2
2 Background	5
2.1 Convective Cooling Processes	5
2.2 Jet Impingement Fundamentals	6
2.2.1 Structure and Flow Characteristics	7
2.2.1.1 Free Jet	7
2.2.1.2 Impinging Jet	8
2.2.2 Heat Transfer Characteristics	11
2.3 Convective Heat Transfer Measurements and Thermal Boundary Conditions	15
2.4 Impinging Jet Heat Transfer	18
2.4.1 Conventional Impinging Jets	18
2.4.2 Obliquely Impinging Jets	30
2.4.3 Impinging Jets with Bluff Bodies	31
2.4.4 Synthetic Jets	33
2.4.5 Swirling Impinging Jets	35

CONTENTS

2.5	Flow Visualisation and Measurement Techniques	51
2.6	Concluding Remarks	57
3	Test Facility and Instrumentation	59
3.1	Impinging Jet Geometry	59
3.1.1	Swirl Generators	62
3.2	Case 1: Infrared Thermography	66
3.2.1	Impingement Surface	66
3.2.2	Thermal Imaging Camera	67
3.2.3	Time-Averaged Heat Transfer Experimental Procedure	68
3.3	Case 2: Hot-Film Sensor Analysis	70
3.3.1	Impingement Surface	70
3.3.2	Constant Temperature Anemometry	72
3.3.3	Time-Averaged Heat Transfer Experimental Procedure	73
3.4	Flow Visualisation & Particle Image Velocimetry	74
3.5	Concluding Remarks	76
4	Experimental Analysis	77
4.1	Case 1: Infrared Thermography	78
4.2	Case 2: Hot-Film Sensor Analysis	90
4.2.1	Fluctuating Heat Transfer Analysis	96
4.3	Uncertainty Analysis	98
4.3.1	Uncertainty for Case 1	100
4.3.2	Uncertainty for Case 2	101
5	Heat Transfer Results & Discussion	103
5.1	Case 1: Infrared Thermography	104
5.1.1	Conventional Impinging Jet - Heat Transfer	104
5.1.2	Swirling Impinging Jets - Heat Transfer	108
5.1.3	Case 1 : Comparison of Conventional and Swirling Impinging Jets	114

5.2	Case 2: Hot-Film Sensor Analysis	120
5.2.1	Conventional Impinging Jet - Heat Transfer	120
5.2.2	Comparison of CIJ Heat Transfer: Case 1 vs. Case 2	123
5.2.3	Swirling Impinging Jets - Heat Transfer	125
5.2.4	Comparison of SIJ Heat Transfer: Case 1 vs. Case 2	129
5.2.5	Case 2 : Comparison of Conventional and Swirling Impinging Jets	132
5.3	Fluctuating Heat Transfer	136
5.3.1	Conventional Impinging Jet - Fluctuating Heat Transfer	136
5.3.2	Conventional Impinging Jet - Local and Fluctuating Heat Transfer	139
5.3.3	Swirling Impinging Jets - Fluctuating Heat Transfer	142
5.3.4	Swirling Impinging Jets - Local and Fluctuating Heat Transfer .	146
5.4	Concluding Remarks	148
6	Flow Visualisation & Particle Image Velocimetry Measurements	151
6.1	Conventional Impinging Jet	151
6.2	Swirling Impinging Jet	160
6.2.1	Large generator with swirl core L_c	160
6.2.2	Large generator without swirl core L_{no}	163
6.2.3	Small generator with swirl core S_c	168
6.2.4	Small generator without swirl core S_{no}	171
6.3	Concluding Remarks	176
7	Conclusion	179
7.1	Conclusions	179
7.2	Further Work	183
	Bibliography	187
	Appendix	199

List of Figures

2.1	Schematic distribution of velocity and turbulence in an axisymmetric jet, Gardon and Akfirat.	7
2.2	Flow visualization of an axisymmetric air jet by Örlü and Alfredsson	8
2.3	Flow regimes associated with impingement of a circular submerged jet	10
2.4	Local Nusselt number distributions versus radial distance from the stagnation point of a straight pipe impinging jet for nozzle to surface heights of (a) greater than $5D$, and (b) less than $5D$, Incropera and DeWitt	12
2.5	Nusselt number distribution illustrating inner peaks and secondary peaks, Gardon and Akfirat	13
2.6	Local Nusselt number for a conventional impinging jet at a Reynolds number of $Re=23,000$ and height of $H/D=2$ for different thermal boundary conditions, Sagot <i>et al.</i>	16
2.7	Illustration of typical heat flux sensor	16
2.8	Local (a) and fluctuating (b) Nusselt number for $0.5 < H/D < 2$ and Reynolds number of 10,000, O'Donovan and Murray	19
2.9	Local heat transfer results from a conventional impinging jet with a Reynolds number of 20,000 with $H/D=0.5, 2$ and 4 using two different measurement devices as reported by O'Donovan <i>et al.</i>	20
2.10	Multi-channel impinging jet as used by Emin Arzutug <i>et al.</i>	21
2.11	Nusselt number distribution for three different shaped nozzles at $H/D=0.5$ for $Re=5,000$ and 10,000 as reported by Gulati <i>et al.</i>	22
2.12	Stagnation point Nusselt number for high velocity flows at $1 < H/D < 12$ as reported by Limaye <i>et al.</i>	22

LIST OF FIGURES

2.13	Example of contoured nozzle geometry as used by O'Donovan <i>et al.</i> . . .	23
2.14	Nusselt number distribution for $H/D=1.125$ and $Re=12,300$ as reported by Liu and Sullivan	24
2.15	Impinging jet with orifice nozzle, as used by Lee and Lee	25
2.16	Vena contracta	25
2.17	Illustration of difference between fluid flow for a confined jet and an unconfined jet, for example an orifice plate and a straight pipe impinging jet respectively, Behnia <i>et al.</i>	26
2.18	Change of Richardson number as a function of Gr^* and Re for $H/D=2$, Koseoglu and Baskaya	27
2.19	Geometry of orifice nozzle and reported heat transfer results by Collucci and Viskanta	28
2.20	Schematic of obliquely impinging jet, O'Donovan and Murray	30
2.21	Demonstration of displacement of maximum heat transfer and stagnation point as reported by Vipat <i>et al.</i>	31
2.22	Triangular tabs added to exit of round impinging jet nozzle, Gao <i>et al.</i>	31
2.23	Fluid flow from a straight nozzle around (a) a stationary/oscillating cylinder and (b) an oscillating airfoil, Bhattacharya and Ahmed	32
2.24	Illustration of fluid (a) suction and (b) ejection processes due to a syn- thetic jet with an orifice nozzle, Krishnan and Mohseni	34
2.25	Axial and radial velocity gradients of a swirling impinging jet, Shiri <i>et al.</i>	35
2.26	Breakdown of flow structure of jet as swirl number, S , increases with (a) $S=0$, (b) $S=0.06$, (c) $S=0.29$, (d) $S=0.65$, (e) $S=0.94$ and (f) $S>0.94$, Toh <i>et al.</i>	37
2.27	Swirling jet generator as used by Ward and Mahmood	38
2.28	Example of guide vane style swirl generator in a straight pipe nozzle, Bakirci and Bilen	39
2.29	Swirling jet geometry (a) and flow visualisation of swirling jets with swirl numbers of (b) $S=0$, (c) $S=0.41$ and (d) $S=1.0$, Alekseenko <i>et al.</i>	40
2.30	Impinging jet arrangement as used by Senda <i>et al.</i>	41
2.31	Swirl generators as used by Lee <i>et al.</i>	42

2.32	Flow inserts for a MCIJ and three SIJs of different angles as used by Bakirci and Bilen	43
2.33	Surface temperature visualisation using liquid-crystal techniques and contours of constant Nusselt number by Bakirci and Bilen	44
2.34	Impinging jet arrangement for a CIJ, MCIJ and different SIJs, with swirl angles of 15°, 30° and 45° as used by Huang and El-Genk	45
2.35	Swirling impinging jet set-up as used by Nozaki <i>et al.</i>	46
2.36	Position of swirl generating guide vanes as used by Kinsella <i>et al.</i>	46
2.37	Thermal image showing surface temperature distribution on impingement surface under influence of swirling impinging jet by Kinsella <i>et al.</i>	47
2.38	Experimental set-up displaying deflecting element in accordance with Yilmaz <i>et al.</i>	48
2.39	Development of swirling jet flow as it emerges from the jet nozzle as reported by Billant <i>et al.</i>	49
2.40	Downstream view of swirling jet as reported by Maciel <i>et al.</i>	50
2.41	Illustration of jet development at $H/D=1.2$ and $Re=5,000$ by Popiel and Trass	51
2.42	Influence of confinement on impinging jet flow at $H/D=1$ and $Re=4,800$ by Baydar and Ozmen	52
2.43	Variation in flow dynamics between (a) a convention impinging jet and (b) a swirling impinging jet as reported by Huang and El-Genk	53
2.44	Azimuthal and axial velocity distributions for a jet flow with increasing swirl number as reported by Billant <i>et al.</i>	54
2.45	Typical set-up for particle image velocimetry, Raffel <i>et al.</i>	55
2.46	Mie scattering for 1 μm particle of oil as described by Raffel <i>et al.</i>	56
2.47	Flow field velocity for $H/D = 2, 3$ and 4 as reported by Felli <i>et al.</i>	57
3.1	Impinging jet nozzle geometry; elevation view and plan view	60
3.2	Top section (a) and central section (b) of jet assembly	61
3.3	Cross-section of full jet assembly	61

LIST OF FIGURES

3.4 Swirl generators (a) Large, with swirl core - “ L_c ”, (b) Large, no swirl core - “ L_{no} ”, (c) Small, with swirl core - “ S_c ” and (d) Small, no swirl core - “ S_{no} ” 62

3.5 Position of outer vanes 63

3.6 Image of each of the four swirl generators to further illustrate the size and aspect differences 64

3.7 Cross-section of full jet assembly including swirl generator “ L_c ” 65

3.8 Cross-section of full jet assembly including swirl generator “ L_{no} ” 65

3.9 Lambda GEN6-200 power supply 66

3.10 Impingement surface for Case 1 67

3.11 FLIR Systems A-40 thermal imaging camera (a) and system arrangement for Case 1 while foil undergoes cooling (b) 68

3.12 Thermal image of foil during jet impingement under (a) an adiabatic and (b) a heated scenario 69

3.13 System arrangement for Case 2 study 70

3.14 Senflex hot-film sensor SF0303 71

3.15 Nickel film in Senflex hot-film sensor SF0303 71

3.16 Constant temperature anemometer Wheatstone bridge including hot-film sensor probe 73

3.17 Experimental instrumentation used to conduct flow visualisation and particle image velocimetry measurements 75

4.1 Illustration of heat transfer to and from stainless steel foil with one side coated in matt black paint 78

4.2 Heat flux due to natural convection from the lower side of the foil under the influence of a conventional impinging jet with $Re=12,000$ and $H/D=1$ 82

4.3 Heat flux due to radiation from (a) lower and (b) upper side of the foil under the influence of a conventional impinging jet with $Re=12,000$ and $H/D=1$ 84

4.4	Heat flux due to lateral conduction in (a) the foil and (b) the paint under the influence of a conventional impinging jet with $Re=12,000$ and $H/D=1$	86
4.5	Heat flux levels of heat loss mechanisms for a conventional impinging jet at a nozzle to surface height of $H/D=1$ and Reynolds number of 12,000	88
4.6	Heat flux levels of heat loss mechanisms as a percentage of the heat flux generated within the foil for a conventional impinging jet at a nozzle to surface height of $H/D=1$ and Reynolds number of 12,000	88
4.7	Resultant (a) heat flux and (b) heat transfer coefficient due to conventional impinging jet with $Re=12,000$ and $H/D=1$	89
4.8	Resultant Nusselt number due to conventional impinging jet with $Re=12,000$ and $H/D=1$	89
4.9	Illustration of stagnation point in 320×240 array and directions in which results are extracted	90
4.10	Calibration of hot-film sensor resistance versus temperature	91
4.11	Effective area against geometric area of hot-film sensor with respect to the temperature difference between the impingement surface and the impinging jet	94
4.12	Comparison of the uncertainties associated with the calculation of the natural convection heat flux, radiation heat flux, impinging jet heat flux, heat transfer coefficient and Nusselt number for a conventional impinging jet at $H/D=1$ and Reynolds number of 12,000 for $0 < r/D < 10100$	
4.13	Variation of effective area uncertainty as temperature difference between the heated surface and the impinging jet increases	102
5.1	Nusselt number distribution for the conventional impinging jet at $H/D = 1$ for all Reynolds numbers using infrared thermography in Case 1 . .	105
5.2	Nusselt number distribution for the conventional impinging jet at $H/D = 10$ for all Reynolds numbers using infrared thermography in Case 1 .	106

LIST OF FIGURES

5.3 Stagnation point Nusselt number for the conventional impinging jet at each H/D and Reynolds number using infrared thermography in Case 1 106

5.4 Mean Nusselt number for the conventional impinging jet averaged over a distance of $0 < r/D < 5.0$ at each H/D and Reynolds number using infrared thermography in Case 1 107

5.5 Instantaneous temperature distributions for swirling impinging jets employing generators (a) “ L_c ” (Large with swirl core), (b) “ L_{no} ” (Large without swirl core), (c) “ S_c ” (Small with swirl core) and (d) “ S_{no} ” (Small without swirl core) at $H/D = 2$ and a Reynolds number of 14,000 109

5.6 Nusselt number distribution for swirling impinging jets employing generators (a) “ L_c ” (Large with swirl core), (b) “ L_{no} ” (Large without swirl core), (c) “ S_c ” (Small with swirl core) and (d) “ S_{no} ” (Small without swirl core) at $H/D = 1$ for all Reynolds numbers 111

5.7 Nusselt number distribution for swirling impinging jets employing generators (a) “ L_c ” (Large with swirl core), (b) “ L_{no} ” (Large without swirl core), (c) “ S_c ” (Small with swirl core) and (d) “ S_{no} ” (Small without swirl core) at $H/D = 8$ for all Reynolds numbers 112

5.8 Nusselt number at $r/D=0$ for swirling impinging jets employing generators (a) “ L_c ” (Large with swirl core), (b) “ L_{no} ” (Large without swirl core), (c) “ S_c ” (Small with swirl core) and (d) “ S_{no} ” (Small without swirl core) at each H/D and Reynolds number 113

5.9 Mean Nusselt number for swirling impinging jets employing generators (a) “ L_c ” (Large with swirl core), (b) “ L_{no} ” (Large without swirl core), (c) “ S_c ” (Small with swirl core) and (d) “ S_{no} ” (Small without swirl core) averaged over a distance of $0 < r/D < 5.0$ at each H/D and Reynolds number 114

5.10 Nusselt number distribution for each of the conventional and swirling impinging jets examined with a Reynolds number of 14,000 at H/D of (a) 0.5, (b) 4 and (c) 10 116

5.11 Stagnation point Nusselt number, Nu_{stag} for each of the conventional and swirling impinging jets examined at each H/D with a Reynolds number of (a) 8,000, (b) 14,000 and (c) 20,000 117

5.12 Mean Nusselt number, Nu_{mean} , for each of the conventional and swirling impinging jets examined at each H/D with a Reynolds number of (a) 8,000, (b) 14,000 and (c) 20,000 119

5.13 Local Nusselt number distribution for a conventional impinging jet at $H/D = 1$ for all Reynolds numbers using a hot-film sensor in Case 2 . . . 120

5.14 Local Nusselt number distribution for a conventional impinging jet at $H/D = 4$ for all Reynolds numbers using a hot-film sensor in Case 2 . . . 121

5.15 Local Nusselt number distribution for a conventional impinging jet at $H/D = 10$ for all Reynolds numbers using a hot-film sensor in Case 2 . . . 122

5.16 Comparison of Nusselt number distributions from Case 1 using infrared thermography and Case 2 using hot-film sensor analysis for a conventional impinging jet at a Reynolds number of 14,000 and H/D of (a) 1, (b) 4 and (c) 10 124

5.17 Nusselt number distribution from Case 1 using FLIR A-40 and SC-6000 thermal imaging cameras and Case 2 using hot-film sensor analysis for Reynolds number of $Re=10,000$ and $H/D=1$ 125

5.18 Nusselt number distribution for swirling impinging jets employing generators (a) “ L_c ” (Large with swirl core), (b) “ L_{no} ” (Large without swirl core), (c) “ S_c ” (Small with swirl core) and (d) “ S_{no} ” (Small without swirl core) at $H/D = 1$ for all Reynolds numbers 127

5.19 Nusselt number distribution for swirling impinging jets employing generators (a) “ L_c ” (Large with swirl core), (b) “ L_{no} ” (Large without swirl core), (c) “ S_c ” (Small with swirl core) and (d) “ S_{no} ” (Small without swirl core) at $H/D = 10$ for all Reynolds numbers 129

LIST OF FIGURES

5.20 Comparison of Nusselt number distributions from Case 1 using infrared thermography and Case 2 using hot-film sensor analysis for each swirling impinging jet [(a) “ L_c ” (Large with swirl core), (b) “ L_{no} ” (Large without swirl core), (c) “ S_c ” (Small with swirl core) and (d) “ S_{no} ” (Small without swirl core)] at a Reynolds number of 12,000 and H/D of 2 . . . 131

5.21 Nusselt number distribution for each of the conventional and swirling impinging jets examined with a Reynolds number of 14,000 at H/D of (a) 0.5, (b) 4 and (c) 10 133

5.22 Percentage enhancement of maximum Nusselt number for each swirling impinging jet compared to conventional impinging jet at a Reynolds number of 14,000 and $H/D=0.5$ for both experimental measurement methods 134

5.23 Nusselt number distribution for each of the conventional and swirling impinging jets examined with a Reynolds number of 20,000 at $H/D=0.5$ 135

5.24 Fluctuating Nusselt number for a conventional impinging jet at all Reynolds numbers and H/D of (a) 1, (b) 4 and (c) 10 138

5.25 Local and fluctuating Nusselt number for a conventional impinging jet at a Reynolds number of 14,000 and H/D of (a) 1, (b) 4 and (c) 10 . . 140

5.26 Local and fluctuating Nusselt number for a conventional impinging jet at a Reynolds number of 14,000 and $H/D=1$ 141

5.27 Fluctuating Nusselt number for each swirling impinging jet [(a) “ L_c ” (Large with swirl core), (b) “ L_{no} ” (Large without swirl core), (c) “ S_c ” (Small with swirl core) and (d) “ S_{no} ” (Small without swirl core)] at all Reynolds numbers and $H/D=0.5$ 144

5.28 Fluctuating Nusselt number for each swirling impinging jet [(a) “ L_c ” (Large with swirl core), (b) “ L_{no} ” (Large without swirl core), (c) “ S_c ” (Small with swirl core) and (d) “ S_{no} ” (Small without swirl core)] at all Reynolds numbers and $H/D=6$ 145

5.29 Local and fluctuating Nusselt number for each swirling impinging jet [(a) “ L_c ”, (b) “ L_{no} ”, (c) “ S_c ”, (d) “ S_{no} ”] at a Reynolds number of 14,000 and $H/D=0.5$ 146

5.30	Local and fluctuating Nusselt number for each swirling impinging jet [(a) " L_c ", (b) " L_{no} ", (c) " S_c ", (d) " S_{no} "] at a Reynolds number of 14,000 and $H/D=10$	147
6.1	Instantaneous flow visualisation of a conventional impinging jet at a Reynolds number of 14,000 and nozzle to surface heights of $H/D =$ (a) 0.5, (b) 1 and (c) 2	152
6.2	Instantaneous flow visualisation of a conventional impinging jet at a Reynolds number of 14,000 and nozzle to surface heights of $H/D =$ (a) 6 and (b) 10	154
6.3	Instantaneous flow structure of a conventional impinging jet superimposed against the corresponding local and fluctuating Nusselt number at $Re=14,000$ and $H/D=1$	156
6.4	Time-averaged velocity vector distribution using particle image velocimetry of flow field from conventional impinging jet with a Reynolds number of 14,000 and $H/D=1$	156
6.5	Illustration of reduction of internal flow velocity for conventional impinging jet with Reynolds number of 14,000 at $H/D=10$	157
6.6	Plan view of conventional impinging jet recorded 2mm above impingement surface with Reynolds number of 14,000 at $H/D=5$: (a) Instantaneous raw image showing concentration of the seeding particles, (b) time-averaged velocity vectors demonstrating direction of motion of the jet	159
6.7	Instantaneous flow visualisation of swirling impinging jet with generator " L_c " (Large with swirl core) at a Reynolds number of 14,000 and nozzle to surface heights of $H/D =$ (a) 2, (b) 10	161
6.8	Plan view of swirling impinging jet with generator L_c recorded 2mm above impingement surface with Reynolds number of 14,000 at $H/D=5$: (a) Instantaneous raw image showing concentration of the seeding particles, (b) time-averaged velocity vectors demonstrating direction of motion of the jet	162

LIST OF FIGURES

6.9 Instantaneous flow structure of a swirling impinging jet with generator “ L_c ” superimposed against the corresponding local and fluctuating Nusselt number at $Re=14,000$ and $H/D=1$ 163

6.10 Instantaneous flow visualisation of swirling impinging jet with generator “ L_{no} ” (Large without swirl core) at a Reynolds number of 14,000 and nozzle to surface heights of $H/D =$ (a) 2, (b) 10 164

6.11 Plan view of swirling impinging jet with generator “ L_{no} ” recorded 2mm above impingement surface with Reynolds number of 14,000 at $H/D=5$: (a) Instantaneous raw image showing concentration of the seeding particles, (b) time-averaged velocity vectors demonstrating direction of motion of the jet 166

6.12 Illustration of recirculation intermittency of flow in swirling impinging jet with generator “ L_{no} ” (Large without swirl core) with Reynolds number of 14,000 and $H/D=1$ 166

6.13 Instantaneous flow visualisation of swirling impinging jet with generator “ L_{no} ” (Large without swirl core) at a Reynolds number of 14,000 and nozzle to surface heights of $H/D = 2$ 167

6.14 Instantaneous flow structure of a swirling impinging jet with generator “ L_{no} ” superimposed against the corresponding local and fluctuating Nusselt number at $Re=14,000$ and $H/D=1$ 167

6.15 Instantaneous flow visualisation of swirling impinging jet with generator “ S_c ” (Small with swirl core) at a Reynolds number of 14,000 and nozzle to surface heights of $H/D =$ (a) 2, (b) 10 169

6.16 Plan view of swirling impinging jet with generator “ S_c ” recorded 2mm above impingement surface with Reynolds number of 14,000 at $H/D=5$: (a) Instantaneous raw image showing concentration of the seeding particles, (b) time-averaged velocity vectors demonstrating direction of motion of the jet 170

6.17 Instantaneous flow structure of a swirling impinging jet with generator “ S_c ” superimposed against the corresponding local and fluctuating Nusselt number at $Re=14,000$ and $H/D=1$ 171

6.18 Instantaneous flow visualisation of swirling impinging jet with generator “ S_{no} ” (Small without swirl core) at a Reynolds number of 14,000 and nozzle to surface heights of $H/D =$ (a) 2, (b) 10 172

6.19 Plan view of swirling impinging jet with generator “ S_{no} ” recorded 2mm above impingement surface with Reynolds number of 14,000 at $H/D=5$: (a) Instantaneous raw image showing concentration of the seeding particles, (b) time-averaged velocity vectors demonstrating direction of motion of the jet 173

6.20 Illustration of recirculation of flow in swirling impinging jet with generator S_{no} with Reynolds number of 14,000 at $H/D=2$ 174

6.21 Instantaneous flow structure of a swirling impinging jet with generator “ S_{no} ” superimposed against the corresponding local and fluctuating Nusselt number at $Re=14,000$ and $H/D=1$ 175

List of Tables

3.1	Characteristic dimensions of swirl generators	64
4.1	Case 1: Uncertainty levels for 95% confidence	101
4.2	Case 2: Uncertainty levels for 95% confidence	102

Nomenclature

\dot{Q}	Volumetric flow rate	[m ³ /s]
A	Area	[m ²]
G_X	Axial flux of axial momentum	[kg/s ²]
G_Φ	Axial flux of angular momentum	[kgm/s ²]
Gr	Grashof number	[-]
I	Current	[A]
M	Mach number	[-]
Nu	Nusselt number	[-]
Pr	Prandtl number	[-]
Q	Rate of heat energy	[W]
Ra	Rayleigh number	[-]
Re	Reynolds number	[-]
Ri	Richardson number	[-]
R	Resistance	[Ω]
S	Swirl number	[-]
T	Temperature	[°C or K]
V	Potential difference	[V]
d, D	Diameter	[m]
g	Acceleration due to gravity	[m/s ²]
h	Heat transfer coefficient	[W/m ² K]
i, j, k	Numerical domain definition	[-]
k	Thermal conductivity	[W/mK]
l, L	Length	[m]

NOMENCLATURE

q''	Heat flux	[W/m ²]
r	Radius	[m]
t	Thickness	[m]
u, U	Axial velocity	[m/s]
v, V	Radial velocity	[m/s]
w, W	Azimuthal velocity	[m/s]
x, y, z	Domain definition	[m]
z, H	Height	[m]

Greek Symbols

α	Thermal coefficient of resistance	[1/°C or 1/K]
β	Volumetric thermal expansion coefficient	[1/K]
ϵ	Emissivity	[-]
μ	Dynamic Viscosity	[kg/ms]
ρ	Density	[kg/m ³]
σ	Stefan-Boltzmann constant	[W/m ² K ⁴]
θ	Angle	[°]
ν	Kinematic viscosity	[m ² /s]

Superscripts

* Fluctuating component

Subscripts

∞	Ambient
c	Swirl generator including swirl core
eff	Effective
$foil$	Foil
f	Fluid
jet	Jet
max	Maximum
$mean$	Mean
no	Swirl generator excluding swirl core

o Stagnation point

Surr Surroundings

S Surface

Acronyms

CIJ Conventional Impinging Jet

MCIJ Multi-channel Impinging Jet

SIJ Swirling Impinging Jet

UWF Uniform Wall Flux

UWT Uniform Wall Temperature

“You can know the name of a bird in all the languages of the world, but when you’re finished, you’ll know absolutely nothing whatever about the bird. So let’s look at the bird and see what it’s doing - that’s what counts.” - Richard Feynman

Chapter 1

Introduction

This research is aimed at experimentally investigating the effect on the convective heat transfer from a heated surface subject to an impinging air jet when a swirl component is induced in the jet flow. Impinging jets have been established over many years as a well defined approach to dissipating heat from high temperature surfaces such as those found commonly in electrical circuitry, manufacturing processes or in the post-processing stages of manufactured materials.

In the past, a range of ideas on how to enhance the heat transfer using impinging jets have been brought forward, illustrating that the area of jet impingement is quite diverse. This includes altering the basic geometry of the jet nozzle and changing the chamfering of the orifice of the jet nozzle. Other methods which have been looked at to improve the heat dissipation from a surface using impinging jets involve inducing a change in the flow of the fluid before and after the nozzle exit. Examples of this include synthetic jets, swirling jets, mist jets and jet arrays.

This investigation looks at the diverse aspects of impinging jets which have been seen in past studies and particularly focuses on the heat transfer enhancement which can be achieved with swirling impinging jets compared to that of a non-swirling impinging jet. The mechanisms behind the changes in heat transfer due to the induced swirling flow are characterised using flow visualisation techniques and fast response heat flux sensors to simultaneously view the flow field and the impact on the heated impingement surface.

1.1 Research Objectives

The proposed research is aimed at understanding the convective heat transfer mechanisms of swirling impinging jets and assessing whether an induced swirling flow in an impinging jet, with air as the working fluid, can enhance the heat transfer from a heated surface compared to an ordinary impinging jet under the same experimental testing conditions. Such conditions include variations in air flow rate and elevation of the jet nozzle above the heated impingement surface. This study explores the use of four separate swirl generators with different attributes. When the heat transfer due to each of these generators is compared, an ideal geometry can be determined.

Infrared thermography is initially used to evaluate the local heat transfer and to give a whole field measurement for the test surface. As the study progressed it was necessary to use a second apparatus in conjunction with a flow visualisation system to determine the flow regimes of the impinging jets at various heights and Reynolds numbers. The second apparatus is employed to explore the fluctuations in the heat transfer over the test surface using a hot-film sensor. It also provides time-averaged local heat transfer data to reinforce the findings of the previous case. Thus, a separate method of calculating the corresponding heat transfer is used.

Due to a difference in thermal boundary conditions and measurement techniques between the two systems, the results produced will illustrate how the measured heat transfer distributions may vary by employing different methods. While the resultant heat transfer is not solely dependant on the method used, these findings will demonstrate that, when comparing results with past studies, the measurement method should be taken into consideration.

To finalise this study, flow visualisation alongside particle image velocimetry measurements, PIV, is performed to show the development of each of the impinging jet flow fields. These techniques will allow specific aspects in the heat transfer, including the appearance of maxima and minima in the local and fluctuating measurements, due to each of the jet flows to be explained. Views of both the elevation and plan of the jet will be acquired to illustrate the rotational aspect of the swirling impinging jets and

the change in the flow structures between the different impinging jet configurations at various nozzle to surface heights.

Chapter 2

Background

This chapter discusses the importance of convective cooling processes in both common everyday devices and industrial operations, with a particular focus on jet impingement cooling. The study of impinging jets has been continuing for many years and different forms of jets have been developed to increase their effectiveness through altering the fluid flow characteristics. While this study reports primarily on the use of impinging jets for cooling applications, jets employed for heating purposes are not uncommon. In order to discover the governing factors behind the flow field and development of an impinging jet, different techniques to visualise the flow have been developed and are also examined in this chapter since knowledge of the flow structure for impinging jets is critical to the understanding of the convective heat transfer mechanisms.

2.1 Convective Cooling Processes

The necessity for more efficient cooling techniques is becoming more and more important as technology increases in complexity while at the same time decreasing in size. The realisation of the increase in components on integrated circuitry was noted in 1965 by Gordon Moore [1]. Commonly known as Moore's law, the observation was made that the number of transistors on integrated circuits doubles approximately every two years, increasing the potential heat generated per unit area. Manufacturing processes are also being performed on a nano-scale which can produce high levels of

heat. In high temperature electronic components, such as those found in computers, a heat sink is commonly used to remove heat from the source to the environment; these have a limit as to how much heat they can possibly remove, so to increase this level of heat dissipation a fan is also attached. In manufacturing processes, such as drilling and milling, a mixture of water and oil is frequently used as both a lubricant and a way of cooling the procedure. By developing an impinging jet suitable for the set-ups mentioned, along with others used in different applications, energy savings have the potential to increase along with the operational costs being decreased.

2.2 Jet Impingement Fundamentals

Jet flows have been explored for many years now in an attempt to understand their formation in a free surface environment and in an environment where an impingement surface is present. The interaction between the fluid of the jet and the surrounding fluid environment has a significant effect on the development of the jet. Depending on the environment, a jet may be defined as a free surface jet or a submerged jet. A free surface jet is known as one which is surrounded by a fluid of lower density, e.g. a jet with water as the working fluid surrounded by air. A submerged jet on the other hand is one with a fluid density lower or equal to the surrounding fluid. Other factors which influence the jet formation are the basic category of nozzle (pipe, orifice, converging etc.) which determines the exit conditions of the flow, the cross-sectional shape of the nozzle, the Reynolds number of the jet flow and the specific type of jet being used, e.g. conventional, swirl, synthetic etc.; these factors are discussed by Dewan *et al.* [2]. The following discussion concerns primarily submerged impinging jets, with the working fluid and the surrounding fluid being the same.

2.2.1 Structure and Flow Characteristics

2.2.1.1 Free Jet

The structure of the flow emerging from a conventional jet nozzle has been studied by many researchers in the past and is a well defined aspect in the area of fluid dynamics. From Gardon and Akfirat [3], figure 2.1 represents the flow structure of an axisymmetric jet without being impaired by obstructions (free jet). As the fluid leaves the jet nozzle, the velocity is at a uniform maximum across the full width of the jet. When the fluid moves further away from the nozzle exit however, this region of uniform velocity is reduced. This central region, known as the potential core, is the area in which the velocity of the jet remains at the same velocity as that at the jet exit. The reduction of this region as the distance from the nozzle exit increases is a consequence of the flow mixing with the ambient fluid surrounding the jet in the region known as the shear layer, seen in figure 2.1. The boundary between the potential core and the ambient fluid is seen as the area of highest turbulence. Past the end of the potential core, commonly a distance equivalent to $6D$ from the nozzle exit, the maximum turbulence level lies on the central axis of the jet.

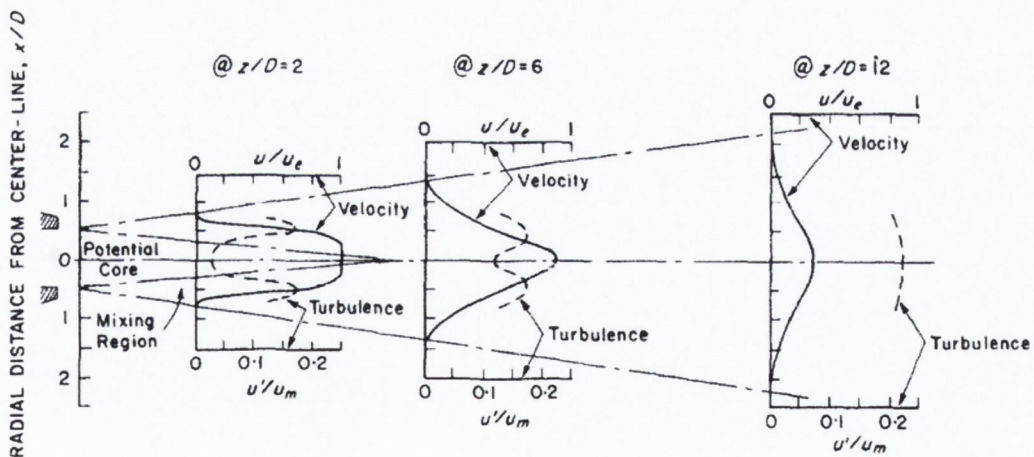


Figure 2.1: Schematic distribution of velocity and turbulence in an axisymmetric jet, Gardon and Akfirat [3]

2.2. JET IMPINGEMENT FUNDAMENTALS

The development of a conventional impinging jet contains two main aspects which are interconnected: the reduction of the width of the potential core and the occurrence of the Kelvin-Helmholtz instability between the jet flow and the surrounding fluid [5]. The Kelvin-Helmholtz instability is caused by a shear interaction between the high velocity jet flow and the stagnant ambient fluid surrounding it. As the jet initially emerges from the jet nozzle small vortical disturbances at the boundary of the two fluids are created. These vortical structures grow in

size as the jet flow develops away from the nozzle exit, reducing the width of the potential core, until they interfere with the jet completely and the potential core ends, as displayed in figure 2.2 from the study by Örlü and Alfredsson [4]. The vortices then collapse and form a fully turbulent flow. This explains the distributions seen in figure 2.1. The high level of turbulence in the ‘mixing region’ is a result of this instability generated between the jet flow and surrounding fluid. The location of this turbulence travels towards the axis of the jet and increases in magnitude due to the increasing size of the vortical structures, until a fully turbulent flow is formed.

2.2.1.2 Impinging Jet

When a surface is placed in the path of the jet, in the jet impingement configuration, the structure of the fluid flow changes to take account of the obstruction. Conventional jets impinging upon a horizontal surface inherently have four flow zones. The following points describe these four zones which are illustrated in figure 2.3.

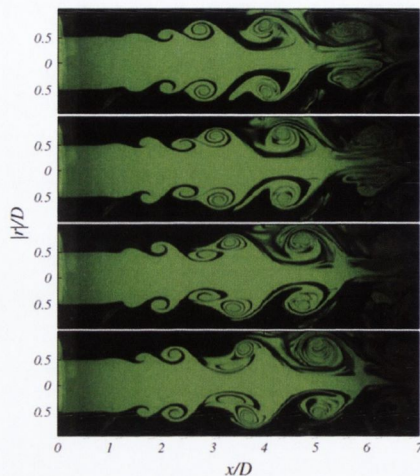


Figure 2.2: Flow visualization of an axisymmetric air jet by Örlü and Alfredsson [4]

1: Initial Mixing Region

The jet flow emerging from the nozzle begins to interact with the ambient fluid surrounding it. As the jet of fluid begins to mix with the ambient fluid there remains an area around its central axis where the velocity of the jet is unaffected by the entrainment of the surrounding air and remains at a magnitude matching that of the original jet exit velocity. This potential core starts out at the size of the jet nozzle and then decreases as it moves away from the nozzle exit in a conical fashion, as indicated in figure 2.3. The potential core varies in length depending on the geometry of the nozzle and the Reynolds number of the jet flow but is found to be equivalent to approximately 6 nozzle diameters in length for Reynolds numbers greater than 4,000 for a conventional round impinging jet [6]. For a rectangular slot nozzle, Beaubert and Viazzo [7] reported that the potential core varies for Reynolds numbers between 3,000 and 7,500 but for Reynolds numbers greater than 7,500 is consistent with a length of $4D$. Flow confinement, which is discussed in further detail later, was shown to lengthen the potential core up to 20% as a result of lower levels of turbulence, Ashforth-Frost and Jambunathan [8].

2: Established Free Jet Region

The free jet region is the term commonly given to the area of the jet's development which follows on from the initial mixing zone, figure 2.3. At this stage the potential core has ended and the flow acts as would a submerged jet without an impingement surface. However, if an impingement surface were positioned within the length of the potential core of the jet, this region would not be present.

2.2. JET IMPINGEMENT FUNDAMENTALS

3: Impingement/Stagnation Region

In this area, the flow is affected by the approaching impingement surface. The surface creates an obstruction, causing the flow to alter from a downwards axial direction to a radial direction outwards from the central point of impingement, the geometric stagnation point.

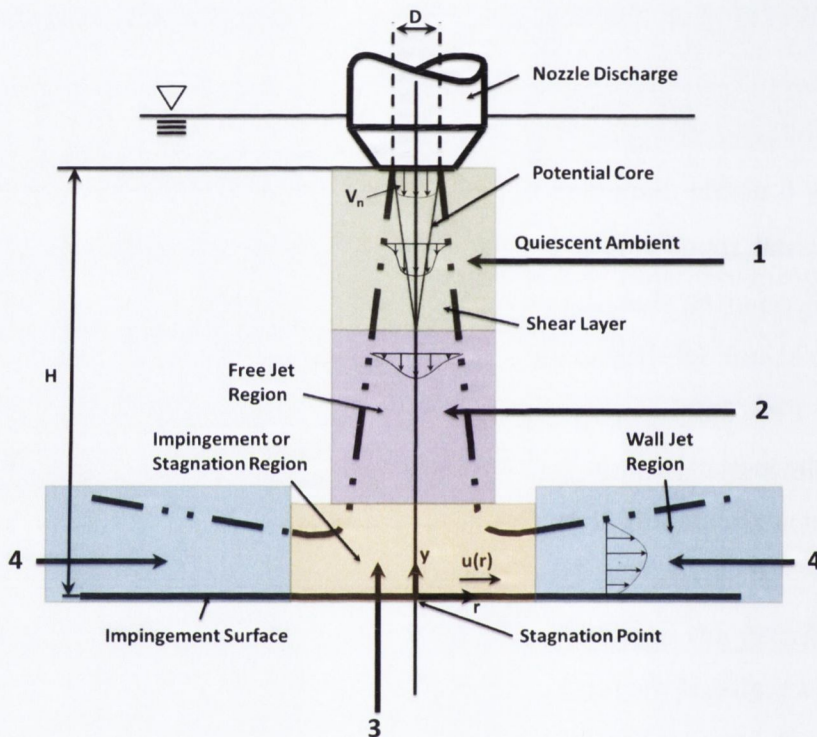


Figure 2.3: Flow regimes associated with impingement of a circular submerged jet

4: Wall Jet Region

As the flow moves from the stagnation point radially outwards, it is bounded by the impingement surface and the ambient fluid. As seen in figure 2.3, the velocity profile of the wall jet contained between these two boundaries has a maximum lying approximately equidistant between the two boundaries while the velocity is zero at each boundary.

2.2.2 Heat Transfer Characteristics

The convective heat transfer between a surface and a fluid flow can be characterised in different ways, the most common of which is via the non-dimensional Nusselt number. The Nusselt number, Nu , which relates convective to conductive heat transfer in the fluid adjacent to the surface, can be evaluated using equation 2.1, where h is the heat transfer coefficient [W/m^2K], x is a characteristic length of the system [m] and k_f is the thermal conductivity of the fluid [W/mK].

$$Nu_x = \frac{hx}{k_f} \quad [-] \quad (2.1)$$

To evaluate the effect of an impinging jet in heat transfer studies a flat surface is generally used; the surface used can also be mounted to any angle depending on what type of study is being conducted.

Impinging jets are commonly employed to control the temperature of specific surfaces or devices and to reduce their chances of overheating. They have been utilised more and more due to their high heat transfer rates and their ability to be adapted to different scales and space requirements. They also have the capability to focus on specific hot spots if required. The highest level of heat transfer is generally found to reside around the stagnation point. This characteristic has been discussed by Incropera and DeWitt [9] and an illustration of such results is shown in figure 2.4.

The spacing at which an impinging jet is placed from the impingement surface is regularly non-dimensionalised using the diameter of the jet's nozzle and is designated as H/D , or z/D , where H , or z , is the distance between the exit of the jet nozzle and the impingement surface and D is the nozzle diameter. The radial distance away from the stagnation point is also represented using the same notation with r , the radial distance, being used in place of H . In the case of slot jet nozzles, with square/rectangular nozzle exit geometries, the equivalent length parameter used to non-dimensionalise each of the characteristics is commonly the width, B , of the slot nozzle. Using this non-dimensional technique, experimental results may be compared across separate studies.

Figure 2.4 is presented in two sections with (a) showing the typical Nusselt number, Nu , distribution when the jet is positioned at least $5D$ from the impingement

2.2. JET IMPINGEMENT FUNDAMENTALS

surface and (b) when it is positioned within $5D$ of the surface. For the case of the conventional impinging jet being positioned at a distance greater than $5D$ from the target surface, the maximum heat transfer is located at the stagnation point, $r/D=0$, and then decreases as the radial distance from the stagnation point increases, following a bell curve distribution. This distribution changes when the spacing between the jet and the surface is reduced to below $5D$, as shown in figure 2.4b. While the maximum Nusselt number remains at the stagnation point, the subsequent decrease is not continuous. Instead a secondary peak appears a distance from the stagnation point; after this secondary peak, the Nusselt number decreases, in a manner similar to that evident in figure 2.4a.

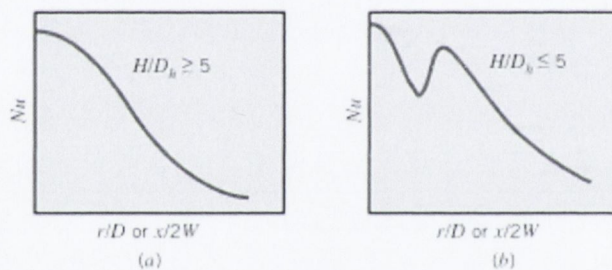


Figure 2.4: Local Nusselt number distributions versus radial distance from the stagnation point of a straight pipe impinging jet for nozzle to surface heights of (a) greater than $5D$, and (b) less than $5D$, Incropera and DeWitt [9]

The appearance of the secondary peak seen in figure 2.4b has been reported many times in the past and is commonly argued to be the result of the transition from a laminar to turbulent flow within the wall jet (section 2.2.1); this secondary peak is usually located at a radial distance of between $1.5D$ - $2.5D$ from the stagnation point, $r/D=0$, [3, 10–12].

Although the local heat transfer distribution shown in figure 2.4 is well established, different heat transfer patterns have been reported in which a local minimum of the Nusselt number was found to be located at the stagnation point instead of a local maximum, as seen in figure 2.5. The local minimum was noted by Gardon and Akfirat [3] along with ‘inner peaks’ which surrounded it at approximately $0.5D$ from the stagnation point. It was reported that this minimum occurs at heights up to $3D$ and

the conclusion was made that the peaks are associated with a minimum thickness of the boundary layer, which is created in the radial flow outwards from the stagnation point. Pamadi and Belov [12] challenged this idea and through numerical modelling put forward the hypothesis that the inner peaks are in fact a result of “mixing-induced non-uniform turbulence in the developing jet”. This theory is supported by the profiles presented in figure 2.1, which show the turbulence levels along with the velocity of the jet at different distances away from the nozzle exit. The turbulence levels were found by Gardon and Akfirat [3] to be at a maximum at the boundary of the potential core. This point of maximum turbulence resides at a distance equivalent to $0.5D$ from the jet’s central axis as the fluid exits the nozzle but travels inwards towards the axis as the distance from the nozzle exit increases. This results in the maximum heat transfer due to the jet being located at approximately $r/D=0.5$ for low H/D and at the stagnation point for high H/D . The nozzle height relating to the point when the inner peaks disappear and the maximum heat transfer lies at the stagnation point corresponds to the length of the potential core of the jet, at which point the mixing in the shear layer has fully penetrated the jet structure [13].

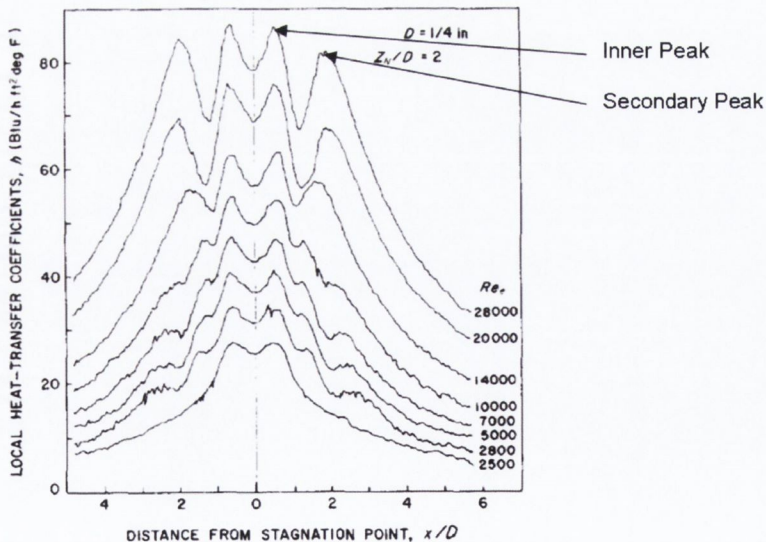


Figure 2.5: Nusselt number distribution illustrating inner peaks and secondary peaks, Gardon and Akfirat [3]

In a review carried out by Jambunathan *et al.* [13], it was proposed that the differences in reported findings were related to the variations in the shapes of the nozzles used. Thus, the velocity profiles of the fluid flow exiting the jet nozzles were affected by the geometry of the nozzle used, as were the turbulence levels. This review reported the common characteristics in the fluid flow from jets which had been described by Schundler and Gnielinski [14] in a study that identified that the maximum turbulence and maximum stagnation point heat transfer occur at a jet to surface distance equivalent to $7.5D$. This distance relates to the end of the potential core of the jet, as previously mentioned. An investigation by Gardon and Cobonpue [15] was also examined in the review by Jambunathan *et al.* [13]. This report by Gardon and Cobonpue [15] points out that the maximum heat transfer coefficient as a result of the impinging jet is located at approximately $0.5D$ from the stagnation point, for nozzle to surface distances of up to $H/D=6$, higher than what was reported by Gardon and Akfirat [3]. This investigation by Gardon and Cobonpue [15] also produced a tertiary peak at a distance of $2.5D$ from the stagnation point alongside the secondary peak preciously described. This additional peak can be seen in figure 2.5 for $2,800 < Re < 10,000$ at $r/D \approx 2.5$. The explanation for this additional peak in heat transfer was suggested to be a result of toroidal vortices, which formed in the shear region around the jet, disrupting the boundary layer as they come into contact with the impingement surface. The tertiary peak was also noted by O'Donovan *et al.* [16], who considered it to be an artefact of the measurement technique used.

This section has described the main features of the flow field and associated local heat transfer distributions for jet impingement. Since the flow structure and the resulting heat transfer for an impinging jet has been studied extensively, further work has gone into altering the jet flow characteristics in order to increase the heat transfer capabilities. This can be achieved by changing the nozzle geometry of the jet or the way in which the flow is ejected from the nozzle. Some examples of heat transfer characteristics with modified jets are considered in section 2.4.

2.3 Convective Heat Transfer Measurements and Thermal Boundary Conditions

Impingement surfaces can be heated through different methods, but generally the surfaces approximate one of two different thermal boundary conditions: uniform wall temperature or uniform wall flux.

A uniform wall temperature (UWT) thermal boundary condition is commonly formed using conductive heating, e.g. an electrical heater mounted underneath a plate with a high conductivity where the plate is the impingement surface. In contrast, a uniform wall flux (UWF) thermal boundary condition is produced usually through ohmic heating, e.g. applying a potential difference across a thin metallic foil. To illustrate the difference in heat transfer that the two heating methods produce, figure 2.6 represents the local Nusselt number for a conventional impinging jet at a Reynolds number of $Re=23,000$ and height of $H/D=2$ for both thermal boundary conditions as reported by Sagot *et al.* [17] from a numerical study. It can be determined from this that the stagnation point Nusselt number is independent of the thermal boundary condition and that the first local maximum is located closer to the stagnation point for UWT than UWF conditions while the second local maximum occurs at the same position. Although the second maximum is more prominent for the UWT case, the results for this thermal boundary condition are significantly lower elsewhere, compared with the UWF case, and the difference between the two cases increases for $r/D > 3$.

In experimental studies, the heat transfer levels due to an impinging jet on a surface with a uniform wall temperature boundary condition can be determined by many methods but the most popular are point measurement techniques, such as the use of thermocouples or heat flux sensors.

2.3. CONVECTIVE HEAT TRANSFER MEASUREMENTS AND THERMAL BOUNDARY CONDITIONS

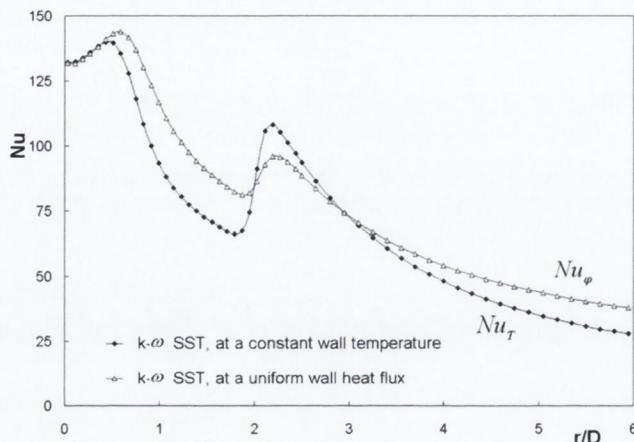


Figure 2.6: Local Nusselt number for a conventional impinging jet at a Reynolds number of $Re=23,000$ and height of $H/D=2$ for different thermal boundary conditions, Sagot et al. [17]

While thermocouples generate a voltage which is proportional to the temperature at the junction of the device by way of the Seebeck effect, heat flux sensors commonly contain a series of thermocouples, known as a thermopile, which generate a voltage that is proportional to the heat flux of the surface it is attached to.

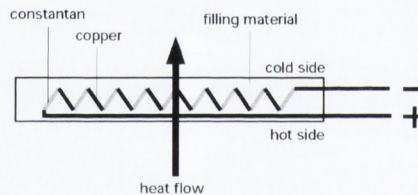


Figure 2.7: Illustration of typical heat flux sensor [18]

An additional sensor which is used to evaluate the heat flux is a hot-film sensor, used in studies such as O'Donovan *et al.* [16] and Scholten and Murray [19]. The voltage necessary for this device to remain at a defined temperature above the temperature of the surface it is attached to can be associated with a known heat transfer rate using a known correlation. The operation of this device is described in detail in section 3.3.

While the majority of experimental studies of impinging jets are performed using a uniform wall temperature thermal boundary condition, a uniform wall flux thermal boundary condition has also been considered in investigations by Baughn and Shimizu [20], Gulati *et al.* [21], Guerra *et al.* [22] and Limaye *et al.* [23] to name a few. As mentioned, this thermal boundary condition is commonly formed by applying a potential difference across a thin metallic foil. The heat dissipation from the

surface of the foil is then evaluated using, for example, an infrared thermal imaging device, temperature sensitive liquid crystals or thermocouples to detect the surface temperature while undergoing cooling from an impinging jet.

When this technique of impingement surface heating is used, it is commonly assumed that the metallic foil is thermally thin, such that the temperature on the top of the surface is the same as the temperature on the bottom. This depends on the thickness and conductivity of the material being used. With this assumption, while the impinging jet impacts upon one side of the foil, the equivalent thermal gradients may be estimated from the other. The use of thermal imaging or temperature sensitive liquid crystals would allow the full area of affected by the impinging jet to be recorded. These measurement methods are less common for uniform wall temperature boundary condition experiments since only one side of the impingement surface is free to view and the impinging jet would obstruct the view of the camera being used to visualise the surface.

Temperature sensitive, or thermochromic, liquid crystals are commonly use to visualise the temperature difference on heated surfaces undergoing cooling or to locate hot spots on circuit boards. By determining which colour produced represents which temperature, the thermal gradient of a surface can be evaluated. With high speed imaging, transient temperature differences can be tracked over a specified area.

Thermal imaging, or infrared thermography, operates on the technique of detecting the radiation emitted from a source in the region of the electromagnetic spectrum, approximately $0.1\mu m$ - $100\mu m$ [24]. Using a specialised lens which allows the infrared wavelength range to penetrate, the level of radiation can be determined and calibrated to display the temperature of the object being viewed. While this method is used to generally differentiate between hot and cold objects, in cases such as security surveillance and building maintenance, the thermal emissivity of multiple objects can differ. For accurate temperature readings, the emissivity of the target object must be known. Like the thermochromic liquid crystals, infrared thermography allows the temperature of an area of interest to be determined, giving an advantage over point measuring devices on surfaces with temperature gradients which may miss important aspects if not positioned in the correct location.

2.4 Impinging Jet Heat Transfer

As mentioned previously, impinging jets have been used in the past with a range of techniques to change the flow regime of the jet in an attempt to increase the heat transfer of the system. The geometry of the nozzle from which an impinging jet is formed is quite important to the jet flow structure, as different nozzles can alter the exit boundary layer of the jet [25]. This section describes the typical conventional impinging jet and some of the enhancement methods explored.

2.4.1 Conventional Impinging Jets

A conventional impinging jet (CIJ) can also be described as an impinging jet which has not been modified specifically to enhance or alter surface heat transfer; the working fluid leaves the exit of the nozzle and impinges perpendicularly upon the target surface. Conventional impinging jets are widely used as a result of the understanding of their structure that has emerged from years of research and specifically, in the field of heat transfer, due to the high heat transfer rates which can be achieved. Conventional jets may be formed using a range of nozzle geometries, the most popular being a straight pipe design along with contoured nozzles and nozzles formed by an orifice in a plate.

Straight Pipe Nozzles

Straight pipe nozzles are most commonly used for impinging jet design due to the low level of flow confinement they provide. Other nozzle geometries, orifice nozzles in particular, frequently encompass a support structure which can interfere with the fluid flow after leaving the nozzle. The straight pipe nozzle shape is useful due to the well defined nature of internal flow development in a pipe and can produce fully developed fluid flow at the nozzle exit.

Much work has been done on convective heat transfer for straight pipe impinging jets by O'Donovan [26] and O'Donovan and Murray [27,28]. While primarily looking at the heat transfer distributions due to impinging jets, these investigations also focused upon local heat transfer fluctuations using hot-film sensor techniques and on velocity fluctuations in the impingement region. Through velocity measurements close to the

impingement surface it was observed that axial fluctuations influenced the heat transfer more than fluctuations in a radial direction. The fluctuation levels caused by the jet depend upon the development stage of the vortices created in the shear layer of the jet. When the jet is placed in close proximity to the impingement surface, the vortices are in an early stage of development and are strong in magnitude. These young vortices promote separation in the boundary layer of the surface causing high fluctuations. For higher nozzle to surface spacings the vortices are weaker as they come into contact with the surface, so their contribution to the heat dissipated is reduced.

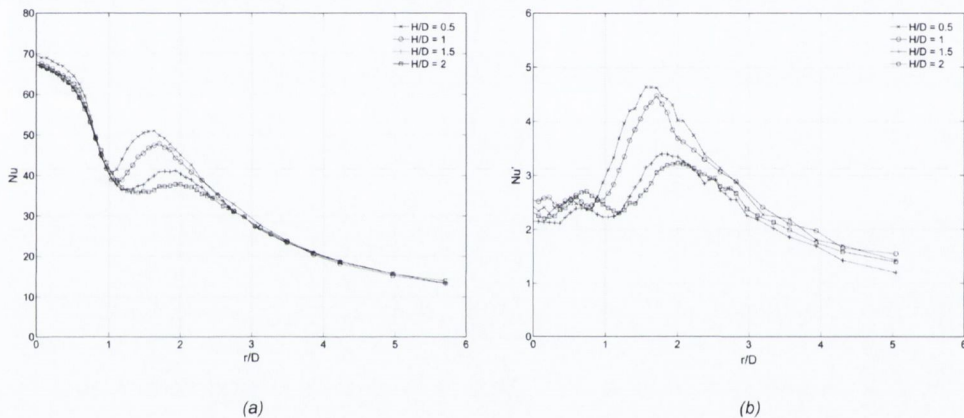


Figure 2.8: Local (a) and fluctuating (b) Nusselt number for $0.5 < H/D < 2$ and Reynolds number of 10,000, O'Donovan and Murray [28]

Figure 2.8 illustrates the influence of the nozzle to surface distance, for values of $H/D \leq 2$, on the local and fluctuating heat transfer while the Reynolds number is held constant. Figure 2.8a demonstrates how the stagnation point is consistent across the range of H/D but the secondary peak decreases in magnitude and its radial location moves away from the stagnation point as the height is increased.

The fluctuating Nusselt number, Nu' , mirrors this change with a consistent magnitude at the stagnation point and a maximum point which decreases in magnitude and moves away from the stagnation point with increasing height. The maximum points in figure 2.8b between $0.5 < r/D < 2$ corresponds with the secondary peaks in figure 2.8a indicating that these maxima represent the change in the transition from a laminar boundary layer to a turbulent boundary layer in the wall jet, as previously mentioned.

2.4. IMPINGING JET HEAT TRANSFER

It is noted that the stagnation point heat transfer displayed in figure 2.8a demonstrates a local maximum at these low levels of H/D which is different from the characteristics shown previously in figures 2.5 and 2.6. This difference in stagnation point may be associated with the measurement method used in the study. To reinforce this, the heat transfer distributions evaluated by O'Donovan *et al.* [16] using an RdF MicroFoil heat flux sensor and a Tao Systems hot-film sensor illustrated in figure 2.9 demonstrate how the measurement technique used may result in a change in the local heat transfer trend, especially around the stagnation zone.

To change the flow emerging from a straight pipe nozzle, methods such as introducing a cross flow or dividing the flow before it exits the nozzle, amongst others, have been explored to determine their influences on the associated heat transfer. Goldstein and Behbahani [29] used a straight pipe nozzle to investigate the influence of a cross flow on the impinging jet flow and subsequently on the heat transfer on the impingement surface. While the straight pipe nozzle was placed at a height of $H/D=6$, an orifice type nozzle (discussed later) was also examined for a height of $H/D=12$. Both jets were utilised for a range of Reynolds numbers. For the straight pipe nozzle, their results showed an increase in the Nusselt number for a defined range of cross flow rates. Also noted was a decrease in the maximum Nusselt number at the stagnation point as the cross flow was increased for the orifice nozzle at a height equivalent to $12D$.

Emin Arzutug *et al.* [30] also made use of the simple geometry of the straight pipe nozzle to explore the change in mass transfer for a multi-channel impinging jet (MCIJ)

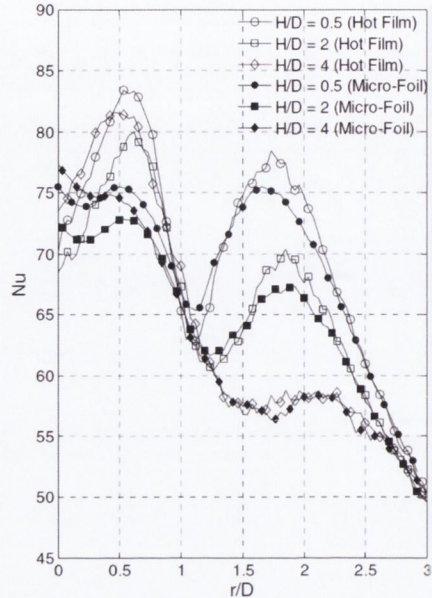


Figure 2.9: Local heat transfer results from a conventional impinging jet with a Reynolds number of 20,000 with $H/D=0.5$, 2 and 4 using two different measurement devices as reported by O'Donovan *et al.* [16]

as compared with a conventional impinging jet. A special insert was developed and positioned inside the pipe in order to divide the flow into four streams, creating the multi-channel jet, as shown in figure 2.10. While the conventional jet produced similar results to those discussed previously, the multi-channel jet caused a change in the mass transfer coefficient such that the multi-channel jet had a higher level of mass transfer than the conventional jet for low H/D ($H/D=2$) whereas for high H/D , ($H/D=8$) the mass transfer was lower than for the conventional jet.

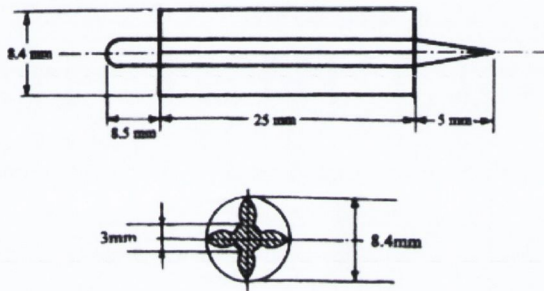


Figure 2.10: Multi-channel impinging jet as used by Emin Arzutug et al. [30]

Gulati *et al.* [21] inspected the changes in heat transfer using differently shaped nozzles for Reynolds numbers ranging from 5,000 to 15,000 and heights of $0.5 < H/D < 12$. It was concluded that the performance of the circular, square and rectangular jets were similar with respect to increasing heat transfer rates with increasing Reynolds number. The square and circular nozzles produced very comparable results whereas the rectangular nozzle produced higher levels of heat transfer for low H/D , as shown in figure 2.11.

Using infrared thermography in studies like this allows a full two-dimensional view of the impingement surface which, in turn, helps to identify areas of high and low heat transfer that may be missed when using temperature or heat flux point measuring instruments such as thermocouples or heat-flux sensors. This is especially useful in cases with non-axisymmetric nozzle shapes, for instance the rectangular nozzle used by Gulati *et al.* [21]. Limaye *et al.* [23] used the same set-up as Gulati *et al.* [21], but in this study looked at much higher Reynolds numbers, equivalent to Mach numbers ranging from 0.2 to 1, for a number of heights. Despite the higher Reynolds numbers used, similar results were discovered to those conducted for the lower jet velocities.

2.4. IMPINGING JET HEAT TRANSFER

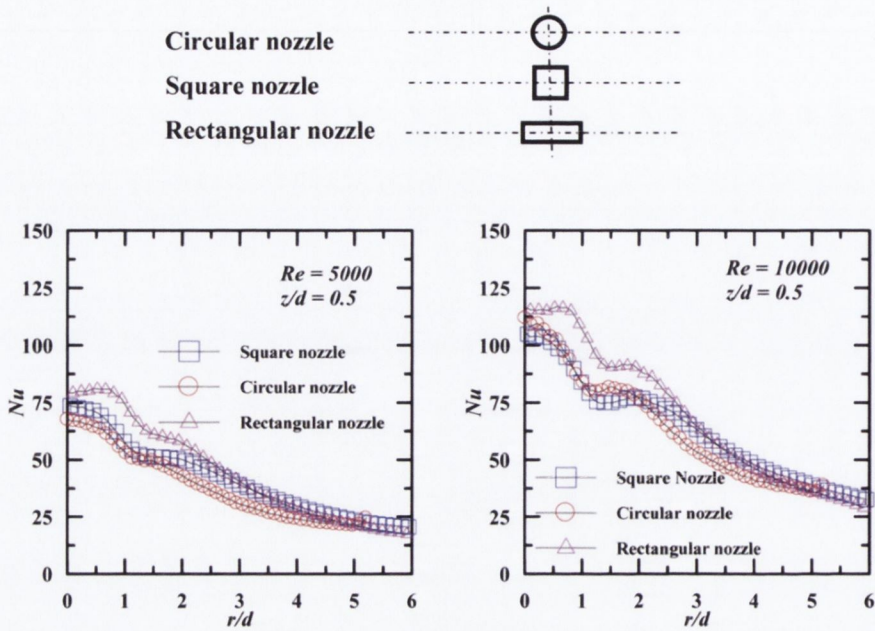


Figure 2.11: Nusselt number distribution for three different shaped nozzles at $H/D=0.5$ for $Re=5,000$ and $10,000$ as reported by Gulati et al. [21]

The local heat transfer reached a maximum in the stagnation zone, the appearance of secondary peaks between $2 < r/D < 2.5$ was noted for low H/D and the maximum heat transfer at the stagnation point occurred for $6 < H/D < 8$, as presented in figure 2.12.

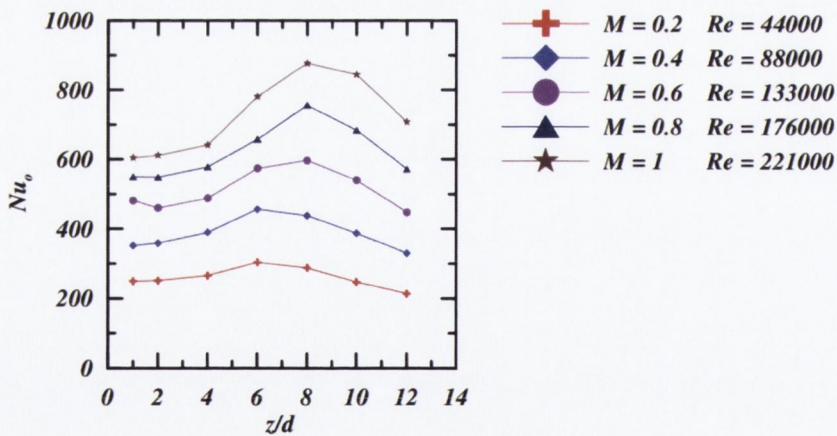


Figure 2.12: Stagnation point Nusselt number for high velocity flows at $1 < H/D < 12$ as reported by Limaye et al. [23]

Contoured Nozzles

Contoured nozzles are defined by their geometry. While the fluid may come from a straight pipe or plenum chamber to begin with, the internal diameter reduces non-linearly at the nozzle exit. This nozzle geometry has been used many times to determine the heat dissipating characteristics of impinging jets by such researchers as O'Donovan *et al.* [16], Liu and Sullivan [31] and Goldstein *et al.* [32].

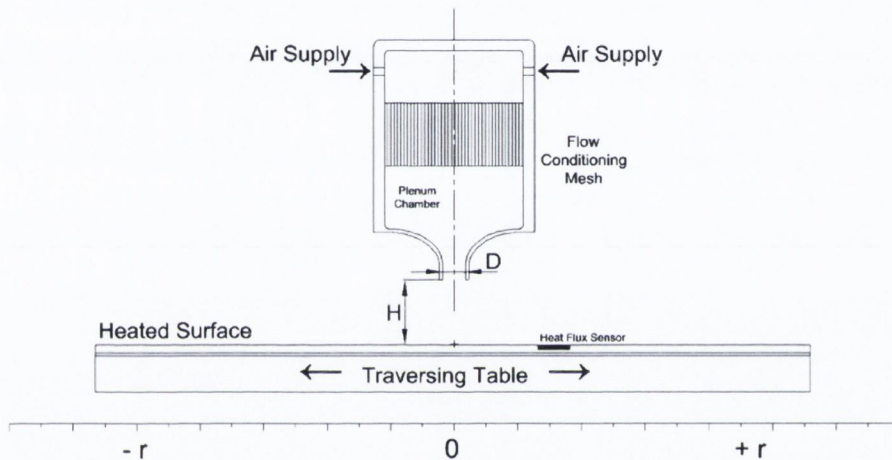


Figure 2.13: Example of contoured nozzle geometry as used by O'Donovan *et al.* [16]

O'Donovan *et al.* [16] used this style of nozzle in conjunction with a conductively heated surface with flush mounted sensors, while Liu and Sullivan [31] and Goldstein *et al.* [32] used electrically heated metallic foils. Though the nozzle has a different geometry to that of a straight pipe, the results obtained from past heat transfer studies show a strong level of consistency depending on the nature of the fluid flow and the height of the nozzle from the impingement surface. The appearance of a tertiary peak, discussed previously, can also be seen to be a common result at low H/D and for Reynolds numbers of around 10,000; this is seen in the work of O'Donovan *et al.* [16] and Liu and Sullivan [31]. Figure 2.14 shows the Nusselt number distribution produced by Liu and Sullivan [31] at a height of $H/D=1.125$ and Reynolds number of 12,300. While the primary and secondary peaks are well pronounced at $r/D \approx 0.75$ and 1.5 , a slight tertiary peak at $r/D \approx 2.5$, circled, also appears.

The, almost non-existent, third peak corresponds with Gardon and Akfirat's [3]

2.4. IMPINGING JET HEAT TRANSFER

results shown previously in figure 2.5. The final noticeable third peak in figure 2.5 is at a Reynolds number of 10,000 while at 14,000 the tertiary peaks have disappeared. This tertiary peak was also noted in the experimental results of O'Donovan *et al.* [16] but only for a Reynolds number of 10,000 at $H/D=1$.

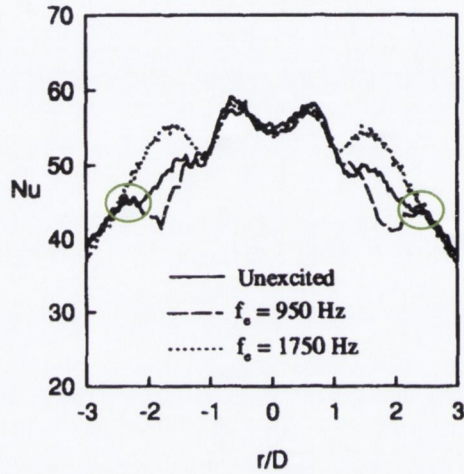


Figure 2.14: Nusselt number distribution for $H/D=1.125$ and $Re=12,300$ as reported by Liu and Sullivan [31]

Orifice Nozzles

An orifice nozzle is the final of the three main nozzle geometries used. An illustration of one such nozzle is shown in figure 2.15. With the previous two nozzle geometries the fluid flow reaches the nozzle exit with either a gradual reduction in the inner diameter of the jet or none at all. Whereas with an orifice style nozzle, the inner diameter of the nozzle is suddenly reduced. This sudden contraction in jet diameter has an effect on the way the working fluid emerges from the nozzle. The abrupt change in the nozzle diameter causes the flow to contract to a width less than that of the actual nozzle diameter. This width is commonly known as the vena contracta, see figure 2.16. Orifice nozzles are also known to cause a flow confinement effect on the fluid flow, as illustrated in figure 2.17.

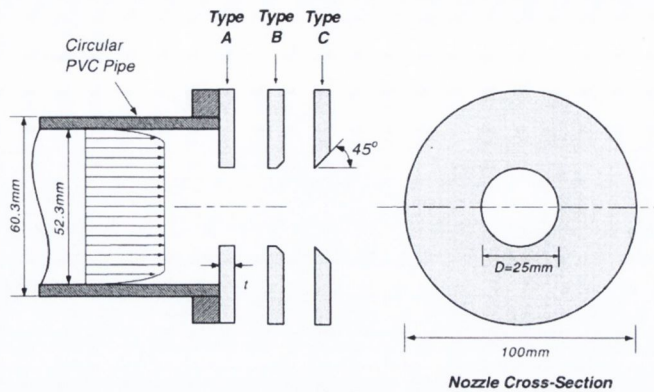


Figure 2.15: Impinging jet with orifice nozzle, as used by Lee and Lee [33]

Depending on nozzle-to-surface distance, this confinement issue can have an adverse effect on the level of heat transfer due to the recirculation of warm fluid towards the stagnation region in cases with a heated impingement surface. Using numerical methods, Behnia *et al.* [34] investigated the influence which confinement could impart on the heat transfer. It was reported that confinement does not have

a considerable impact on the heat dissipated unless the nozzle is positioned within a distance of $0.25D$ from the surface. Fenot *et al.* [35] discovered that the influence of confinement is weak at the conditions explored and had more of an effect on the effectiveness of the impinging jet, a parameter which is a ratio between the temperatures of the jet, the ambient air and the adiabatic surface.

Lee and Lee [33] explored how the shape of the orifice edge may alter the flow regime and consequently the heat transfer from an impingement surface. The three edges employed are shown in figure 2.15. In general the sharp-edged nozzle, ‘Type C’, performed the best out of the three tested when comparing distributions of the Nusselt number versus radial distance from the stagnation point. It was also noticed that, from the same distributions, when judging the orifice results against past results

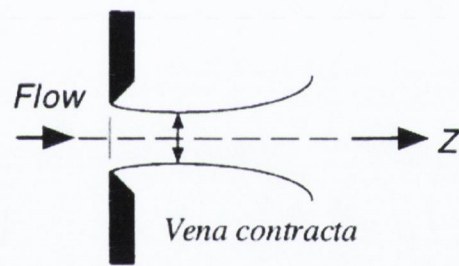


Figure 2.16: Vena contracta [33]

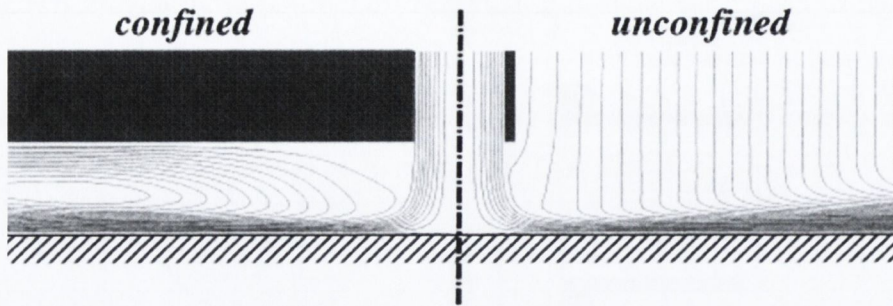


Figure 2.17: Illustration of difference between fluid flow for a confined jet, for example an orifice plate impinging jet, and an unconfined jet, for example a straight pipe impinging jet, Behnia et al. [34]

from straight pipe nozzles and contoured nozzles, that the orifice nozzles performed 25-55% better than a straight pipe set-up and 50-75% better than a contoured nozzle. This was attributed to the alteration of the initial flow structure at the nozzle exit. However, in an article by Lupton *et al.* [36], the flow confinement resulting from impinging jets with orifice nozzles was discovered to have the effect of reducing the convective heat transfer from a heated surface compared to a jet which was unconfined for a range of Reynolds numbers and nozzle to surface heights. A consistent reduction in the heat transfer was noted for a confined jet when compared to an unconfined jet at Reynolds numbers of 7,000 and 12,000 and nozzle to surface distances in the range of $1 < H/D < 6$. This reduction, which was more significant than reported by other researchers, was attributed to the small jet diameter (1mm) used in this study. The reduction in the heat transfer was a consequence of a strong recirculation effect inevitably reducing the local temperature difference.

Just as straight pipe nozzles are not restricted to having a circular cross-section, nor are orifice nozzles. Square and rectangular nozzles are common examples that have also been examined along with geometries such as an elliptical shape studied by Koseoglu and Baskaya [37]. By comparing their experimental results to a circular orifice nozzle a level of enhancement was found for low H/D , despite an element of recirculation due to confinement. Following on from this, Koseoglu and Baskaya [38] opted for a circular nozzle in a mixed convection jet impingement study, using numerical and experimental methods. The buoyancy due to natural convection was shown to have

the possibility of both opposing and assisting the heat transfer at different locations. It was determined from this work that for low Reynolds number, in the range of less than 1,000, natural convection has an impact on the results. The influence of natural convection was illustrated through the representation of the Richardson number, Ri , defined in chapter 4.

Figure 2.18 is one such representation of the results gathered. The modified Grashof number, Gr^* , is used to signify the level of heating of the impingement surface, i.e. the higher the value of Gr^* , the higher the temperature of the surface is. Figure 2.18 shows that at Reynolds numbers higher than 3,000, the influence of buoyancy due to natural convection is negligible.

As previously mentioned, orifice nozzles are not specific to one geometric shape. Amongst the many geometries considered are those that have been investigated by Collucci and Viskanta [39]. The geometry explored consisted of a hyperbolic diverging nozzle, shown in figure 2.19, and compared with heat transfer results acquired using a common orifice nozzle similar to ‘Type A’ in figure 2.15. The experiments performed showed that the primary and secondary peaks, commonly seen near the stagnation area, were more pronounced when the separation distance between the nozzle and the surface decreased, which was also noted by Fitzgerald and Garimella [40]; in some cases the secondary peak was greater than the primary peak. The location of the secondary peak was also found to be related to the size of the curvature of the orifice outlet, indicated by R_{max} in figure 2.19. Two diverging nozzle designs were tested against a common orifice and both were found to produce higher levels of heat transfer.

Orifice nozzles have also been utilized in situations involving jet arrays. Generally orifice jets are organized in a square or in-line arrangement, such as in the study by

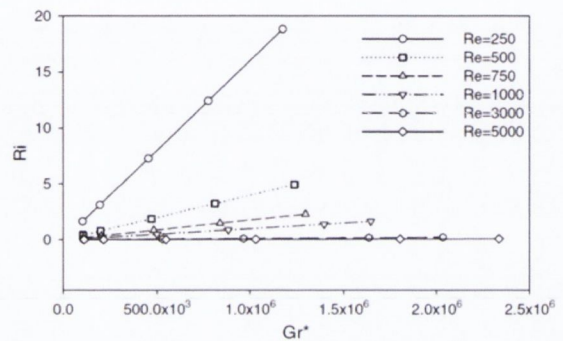


Figure 2.18: Change of Richardson number as a function of Gr^* and Re for $H/D=2$, Koseoglu and Baskaya [38]

2.4. IMPINGING JET HEAT TRANSFER

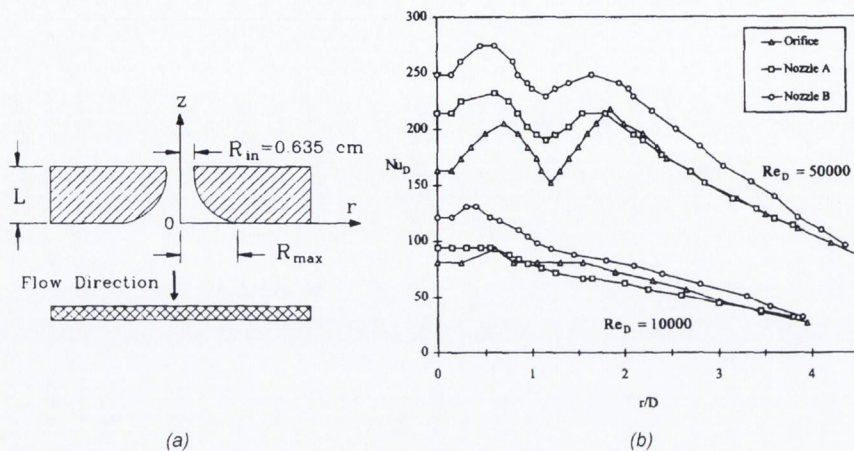


Figure 2.19: Geometry of orifice nozzle and reported heat transfer results by Collucci and Viskanta [39]

Garimella and Schroeder [41], but they are not restricted to this geometry. In a study by Geers *et al.* [42], a square and a hexagonal set-up were examined along with two nozzle geometries. The first geometry is of a sharp edged orifice, again similar to ‘Type A’ in figure 2.15. The second however was a contoured orifice which was used to reduce the vena contracta effect of the sharp edged nozzle. The difference in the orifice geometries results in the sharp edged orifices having higher heat transfer in the impingement region than the contoured orifice, due to higher velocities caused by the vena contracta effect. The aspect ratio between the thickness of the orifice plate and the diameter of the nozzle also leads to an effect on the heat transfer as discovered by Garimella and Nenaydykh [43]; it was reported that the thinner the orifice plate was compared to the nozzle diameter, the higher the achievable heat transfer would be. However this result was only effective for low H/D .

In general, orifice nozzles have been shown to perform more effectively than the straight pipe and contoured nozzles under comparatively similar conditions. It has been concluded that this increase in performance in heat transfer dissipation is primarily due to the increase in velocity of the fluid flow due to the vena contracta effect of the nozzle geometry. Despite the confinement influence which tends to decrease the local heat transfer, under certain circumstances it can be used to assist in the heat dissipation from a target surface.

Conventional Impinging Jet Correlations

The study of impinging jet cooling has led to correlations describing the magnitude of the heat transfer at the stagnation point for different ranges of Reynolds numbers, nozzle to surface distances and nozzle geometries. For correlations governing the stagnation point Nusselt number, the thermal boundary condition of the heated surface can be disregarded since this does not affect the stagnation area [17]. A correlation analytically derived by Shadlesky [44] and confirmed by Liu and Sullivan [31] established that the stagnation point Nusselt number, for a contoured nozzle up to a nozzle to surface spacing of $H/D < 2$ and a Reynolds number range of $12,000 < Re < 15,000$, can be described by:

$$Nu_o = 0.5856Re^{0.5}Pr^{0.4} \begin{cases} H/D < 2 \\ 12,000 < Re < 15,000 \end{cases} \quad (2.2)$$

Lytle and Webb [11] produced a correlation which only takes into account the nozzle to surface spacing and the Reynolds number of the flow. This equation was generated with a straight pipe nozzle and is valid for $H/D < 1$ and $3,700 < Re < 30,000$:

$$Nu_o = 0.726Re^{0.53} (z/D)^{-0.191} \begin{cases} H/D < 1 \\ 3,700 < Re < 30,000 \end{cases} \quad (2.3)$$

While the methods used to generate these correlations are different, equations 2.2 and 2.3 have a similar trend in that the exponential power of the Reynolds number is approximately 0.5. Indeed the dependence of the Nusselt number on this power has also been noted in other studies.

Other correlations have been determined from past studies with regard to the local and mean Nusselt number for specific impinging jet configurations, thermal boundary conditions and measurement techniques but are not included here.

2.4.2 Obliquely Impinging Jets

An impinging jet which is adjusted to strike a surface at an angle other than 90° is commonly referred to as an obliquely impinging jet. In an investigation into obliquely impinging jets, O'Donovan and Murray [45] found the appearance of both strong and weak vortical structures due to the angle of impingement of the jet, resulting in higher levels of heat transfer fluctuations in the uphill direction and low levels in the downhill direction. In the uphill direction the vortices from the jet are strong since they have comparatively less time to disperse energy to the surrounding environment compared to those in the downhill direction, which are at a weaker level by the time they impinge upon the surface.

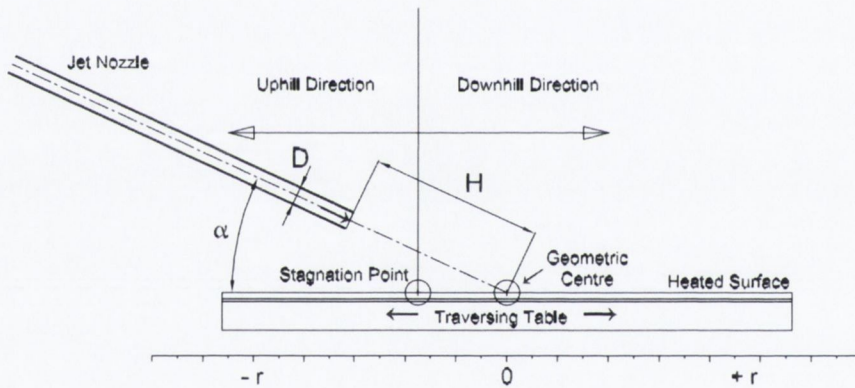


Figure 2.20: Schematic of obliquely impinging jet, O'Donovan and Murray [45]

A similar investigation was conducted by Vipat *et al.* [46] and came to comparable conclusions to that of O'Donovan and Murray [45]. The maximum heat transfer is seen in figure 2.21 to be displaced from the geometric stagnation point in the uphill direction of the impingement surface as does the equivalent pressure distribution upon the impingement surface.

The results from these studies provide information regarding the positioning of an impinging jet when employed for cooling purposes. In applications such as the cooling of a manufacturing process, if the impinging jet being used was not at 90° to the target surface an uneven level of cooling would occur which might affect the material properties in different areas.

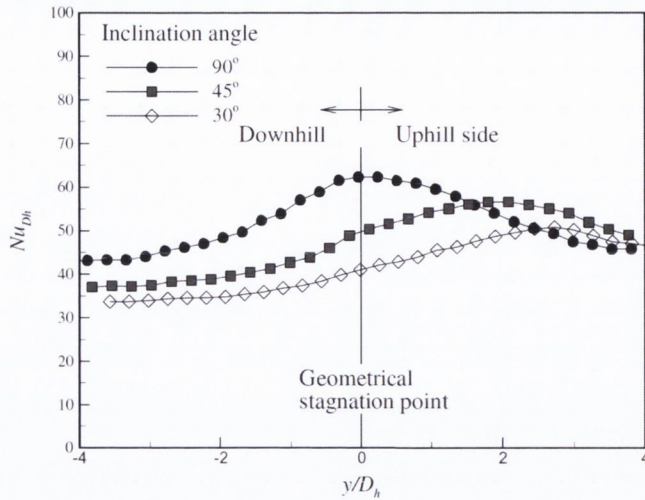


Figure 2.21: Demonstration of displacement of maximum heat transfer and stagnation point as reported by Vipat et al. [46]

2.4.3 Impinging Jets with Bluff Bodies

In some studies, additional edges are added to the jet nozzle, an example of which is displayed in figure 2.22, or bluff bodies such as spheres, cylinders or air-foils are placed in the path of the fluid flowing from a nozzle, as shown in figure 2.23.

The aim of this is to generate turbulent mixing of the fluid before it impinges on a heated surface, thereby attempting to enhance heat transfer. Gao *et al.* [47] used the straight pipe nozzle geometry for their study with the addition of triangular tabs at the exit of the nozzle. The triangular tabs forced the fluid to change its flow structure and in doing so the speed of the fluid between the individual tabs increased, as did the turbulence level after the tabs. The tabs caused an enhancement of the heat transfer, mainly in the stagnation region and also affected the nozzle-to-plate distance

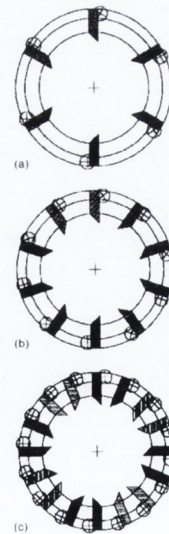


Figure 2.22: Triangular tabs added to exit of round impinging jet nozzle, Gao et al. [46]

2.4. IMPINGING JET HEAT TRANSFER

that the maximum heat transfer occurred at. The turbulence mixing induced by the tabs reduced the optimal height from $6-8D$, as would be the case for a conventional impinging jet, to $4-6D$.

Through the use of thermal imaging techniques, Bhattacharya and Ahmed [48] investigated how a bluff body, such as a cylinder or air-foil, might affect the flow emerging from an impinging jet nozzle and whether the resultant alteration in the flow would enhance or diminish the heat transfer. It was determined that when a cylinder is placed in the path of the jet flow, figure 2.23a, wake vortex shedding from around the bluff body would increase the level of mixing in the region where normally the potential core of the jet would be. A similar result was obtained when an air-foil was placed in the path of the jet flow, however the vortices would primarily occur on one side of the air-foil due to its asymmetric geometry, figure 2.23b.

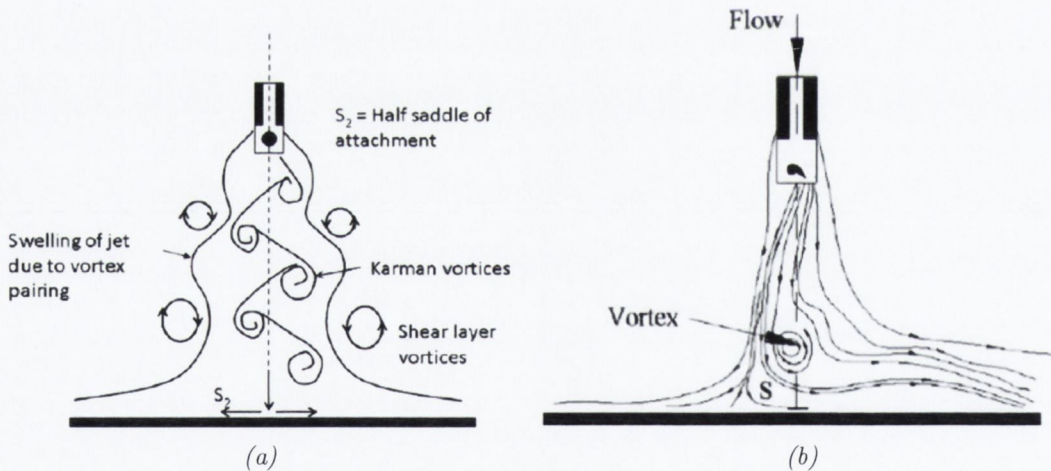


Figure 2.23: Fluid flow from a straight nozzle around (a) a stationary/oscillating cylinder and (b) an oscillating airfoil, Bhattacharya and Ahmed [48]

The air-foil configuration was discovered to produce the highest heat transfer rates of those tested, including an impinging jet with no obstruction. This was attributed to the minimal amount of recirculation along the axis of the jet which occurred when using the cylinder along with the large vortical structure, seen in figure 2.23b, which was produced with the air-foil acting as the bluff body.

Annular jets can also be considered within this category of impinging jets since the central section can be viewed as obstructing the flow. Celik and Eren [49] studied

how the thickness of the internal section of an annular jet can result in different heat transfer rates. Three annular jets, each with different configurations, were compared to a conventional impinging jet of the same external diameter to determine enhancement in heat transfer. For each of the jets tested, the conventional impinging jet gave the lowest heat transfer while the geometry with an annulus of $0.55D$, where D is the outer diameter of the jet, had the highest. Following these results it was concluded that if a localised cooling effect is desired, a small annulus is needed, while a large annulus should be used for a more uniform cooling effect over a wide region.

2.4.4 Synthetic Jets

Synthetic jets are devices that have been developed which do not require a continuous supply of fluid from pumps or compressors, thereby reducing the cost and increasing the convenience of the process. This is accomplished through the use of an oscillating diaphragm, most commonly found in an electromagnetic actuator or an acoustic speaker. The actuator is generally positioned above a jet nozzle but is not restricted to this arrangement. As shown in figure 2.24, the system undergoes two stages to produce the impinging jet flow. During the first stage, the diaphragm of the actuator moves away from the jet nozzle and introduces the working fluid into the jet enclosure. In the second stage, the diaphragm moves towards the jet nozzle, expelling the fluid which was drawn in during the first stage towards the target. The cycle then repeats at a frequency defined by the operator. The displacement of the diaphragm may also be controlled, leading to a specific volume of fluid emerging from the jet exit.

The wall region of a synthetic impinging jet was examined by Krishnan and Mohseni [50] using the technique of hot-wire anemometry. The flow regime of the synthetic jet in the wall region showed similarities to a continuous jet. However, since the synthetic jet is primarily dominated by vortices due to the actuator driving the flow, the rate at which the jet decayed and spread was found to be considerably different. As with the other forms of impinging jets, synthetic jets can be used with a number of nozzle geometries to attempt to increase performance, such as in a study by Trávníček and Tesař [51] which considered an annular jet. These findings indicated that if the

2.4. IMPINGING JET HEAT TRANSFER

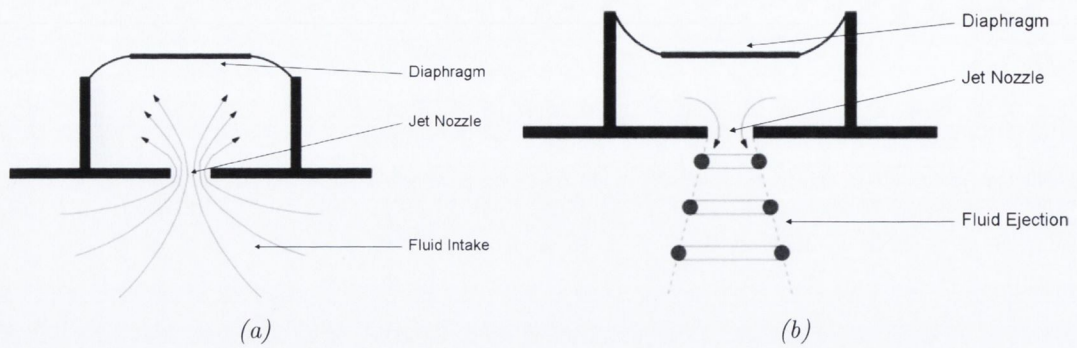


Figure 2.24: Illustration of fluid (a) suction and (b) ejection processes due to a synthetic jet with an orifice nozzle, Krishnan and Mohseni [50]

amplitude of the actuator was to be increased the mass transfer of the jet would also increase. From the results presented, it was also clear that an increase in the frequency caused an increase in the mass transfer, but this is not consistent. The increase in the mass transfer with increasing frequency was reported to be valid up to a point, beyond which the level of mass transfer drops. This was reported to be as a result of the flow undergoing a significant change in structure.

The effect of various synthetic jet operational parameters on convective heat transfer characteristics has been considered thoroughly in many different studies of impinging synthetic jet heat transfer [52–55]. These parameters include the stroke length, L_o , the Reynolds number, Re , the size of the jet nozzle, D in the case of a circular nozzle, and the distance between the jet and the target plate, H , amongst others. Heat transfer results from the synthetic jet were also compared to a standard continuous jet under similar conditions. Major findings established from studies with this impinging jet arrangement included that the maximum heat transfer occurs when the actuator is set at a frequency equivalent to the resonance frequency of the jet cavity and that the stroke length of the synthetic jet plays a large part in the fluid dynamics and the heat transfer from the impingement surface.

2.4.5 Swirling Impinging Jets

The main focus of this study is to characterise the convective heat transfer of a swirling impinging jet relative to the behaviour of a non-swirling jet. Therefore much of the examination of past work has been focused in this area, specifically in the area of guide vane swirl generators.

Swirling impinging jets are quite diverse in terms of their design. Different approaches have been taken over the years to develop a method of generating a swirling flow such as superimposing a tangential flow onto an axial flow, the use of guide vanes or direct rotation via a rotating pipe. The pressure requirements of tangential entry swirl generators are relatively high, hence industries which commonly employ swirl generators, combustion systems for example, are inclined to implement the guide vane approach.

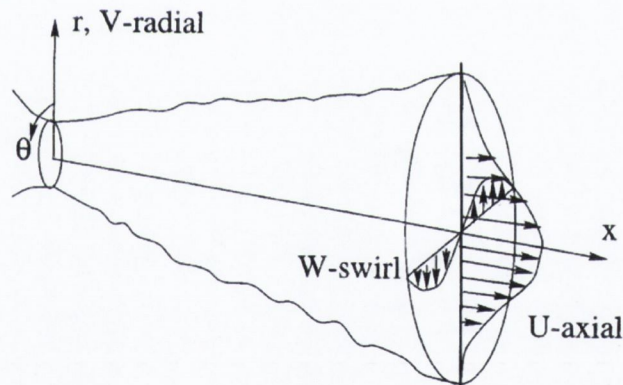


Figure 2.25: Axial and radial velocity gradients of a swirling impinging jet, Shiri et al. [56]

Figure 2.25 illustrates the typical velocity profiles associated with a swirling jet. Unlike a conventional jet which would just have an axial component, a swirling jet has an angular or azimuthal velocity around the central axis of the jet. The magnitude of this azimuthal velocity is governed by the level of swirl in the jet and is dictated by the swirl generation technique used.

Many detailed studies into swirling jets have been completed in the past with regard to their flow structure and development as they impinge upon a heated surface, with the main purpose of discovering a design which will encourage a higher heat

transfer rate compared to a conventional impinging jet under the same conditions. These studies are discussed in the following sections.

Tangential Flow

The superposition of a tangential flow onto an axial flow to generate a swirling flow has been used in much research in the past, since a simple adjustment to the tangential flow can change the degree of swirl of the jet. The level of swirl is commonly described by the swirl number, S , which is calculated by comparing the axial flux of angular momentum, G_Φ , with the axial flux of axial momentum, G_X , as shown in equations 2.4 and 2.5, described by Gupta *et al.* [57] and Alekseenko *et al.* [58]. A swirl number of zero is equivalent to a conventional jet.

$$S = \frac{G_\Phi}{\frac{D}{2}G_X} \quad [-] \quad (2.4)$$

$$G_\Phi = \int_0^{r_{max}} \rho u w r^2 dr \quad G_X = \int_0^{r_{max}} \rho u^2 r dr \quad (2.5)$$

where u and w are the axial and azimuthal velocities respectively of the fluid flow [m/s] and r is the radius of the jet nozzle [m].

To apply a flow tangentially to an axial flow, additional components are commonly included in order to direct the tangential flow towards the enclosure containing the axial flow. One such example by Ward and Mahmood [59,60] is shown in figure 2.27. The tangential flow passes through these extra sections and the combination of the flows creates a swirling motion, whose strength is determined by the impact of the tangential flow.

The development and structure of a swirling jet as it exits a nozzle has been investigated in many studies including those by Shiri [61], Shiri *et al.* [56], Toh *et al.* [62,63], Wicker and Eaton [64] and Lee *et al.* [65]. These studies have observed how a swirling jet grows and decays as both the distance from the nozzle and the swirl number increase. The study by Lee *et al.* [65], which particularly focused on the combination of swirling flows, chose an annular formation for the jet nozzle in

an attempt to control the spread of the jet by way of experimental and numerical methods. Figure 2.26 demonstrates the spread of a swirling jet as the swirl number is increased. This sequence of images recorded by Toh *et al.* [62] compares well with other studies and truly illustrates the importance of swirl number regulation since jets with high swirl numbers, such as in image (f), have little central structure and it will be shown that at these levels of swirl, significantly low heat transfer occurs in the stagnation region.

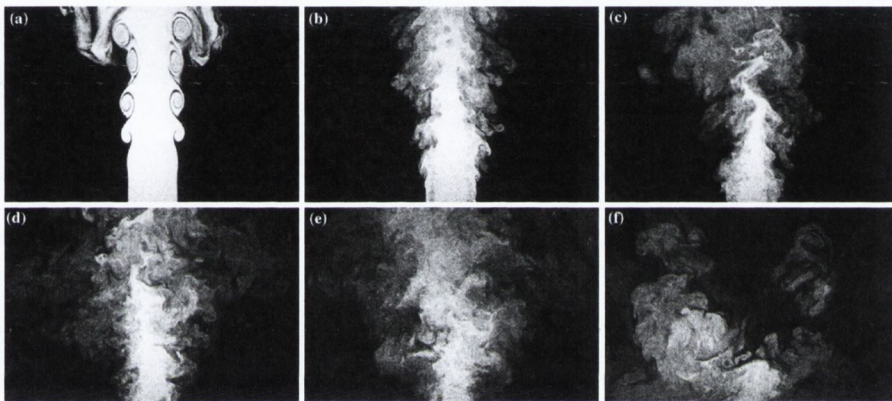


Figure 2.26: Breakdown of flow structure of jet as swirl number, S , increases with (a) $S=0$, (b) $S=0.06$, (c) $S=0.29$, (d) $S=0.65$, (e) $S=0.94$ and (f) $S>0.94$, Toh *et al.* [62]

Ward and Mahmood [59, 60] generated a swirling impinging jet by applying this method and using the system illustrated in figure 2.27. The tangential flow enters into an annular cavity that envelops the tube containing the axial flow. This tube includes four parallel slots, as shown, through which the tangential flow enters and combines with the axial flow. Through experimental testing at different jet to surface distances, Reynolds numbers and swirl numbers it was discovered that as the level of swirl increased, the heat transfer decreased.

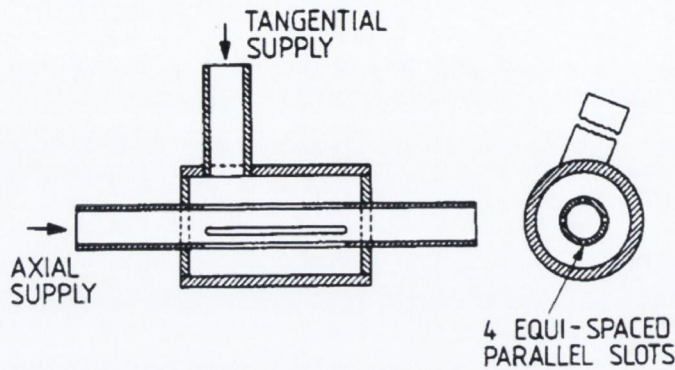


Figure 2.27: Swirling jet generator as used by Ward and Mahmood [59, 60]

The highest swirl number examined, $S=0.48$, showed a very low level of heat transfer at the stagnation point, while the local maximum was located at $r/D=1.5$. However, when this jet arrangement was set up as a square array, the swirling impinging jets caused an enhancement in the heat transfer. The enhancement of heat transfer, compared to an array of non-swirling jets, was found to be up to 20% at the closest nozzle to surface distance examined and for low swirl numbers. As the swirl number increased, this enhancement factor decreased.

Ichimaya and Tsukamoto [66] used a similar approach to Ward and Mahmood [59] but with lower Reynolds numbers and smaller nozzle to surface spacings. The findings illustrated that a swirling impinging jet can both improve and diminish the heat transfer compared to a non-swirling jet, depending on the swirl number chosen. In this investigation it was revealed that a swirl number ranging from $0 < S < 0.8$ leads to an increase in heat transfer, with a maximum effect at $S \approx 0.4$. From these results it can be deduced that a swirling impinging jet, using the superposition of a tangential flow method, can enhance the heat transfer from a system under certain conditions. However, at swirl numbers above $S=0.8$, a reduction in the heat transfer has been noted. For example, Ichimaya and Tsukamoto [66] noticed a 20% decrease in the mean Nusselt number for a swirl number of $S=1$.

Guide Vanes

Guide vane swirl generators can be used, depending on the geometry of the jet nozzle, to alter the angular component of the flow. It was noted by Yajnik and Subbaiah [67] that creating a swirling jet by way of guide vanes has advantages over other swirl developing methods since they do not create secondary flows. The theory outlined previously for calculating the equivalent swirl number, equation 2.4, can also be used for this set up. However, a simpler definition of the swirl number has been created for guide vane swirl generators taking into consideration the inner and outer diameters, d_1 and d_2 respectively, of the generator and the angle at which the vanes are positioned, θ , as demonstrated in figure 2.28. This formula is presented in equation 2.6.

$$S = \frac{2}{3} \frac{\left(1 - \left(\frac{d_1}{d_2}\right)^3\right)}{\left(1 - \left(\frac{d_1}{d_2}\right)^2\right)} \tan\theta \quad [-] \quad (2.6)$$

To highlight the difference between the flow of a non-swirling jet and a guide vane generated swirling jet with varying swirl numbers, Alekseenko *et al.* [69] used flow visualisation techniques to measure the mean and fluctuating velocities of the different jets.

It was discovered that, near the jet exit, the swirling jet examined had a near zero velocity at its centre and a maximum velocity between $0.2 < r/D < 0.4$ for a high degree of swirl, compared to a non-swirling jet which has a consistent velocity for $0 < r/D < 0.5$. The velocity fluctuations for a swirling jet also changed appreciably compared to a normal jet. Fluctuations in velocity near the jet exit for a non-swirling jet were shown to be near zero for the span of its diameter. For a swirling

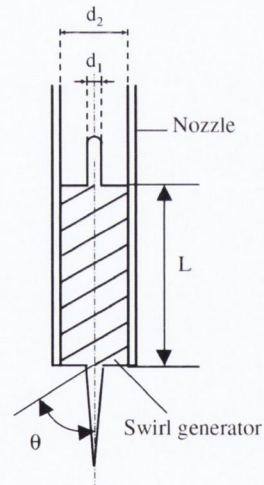


Figure 2.28: Example of guide vane style swirl generator in a straight pipe nozzle, Bakirci and Bilen [68]

jet were shown to be near zero for the span of its diameter. For a swirling

2.4. IMPINGING JET HEAT TRANSFER

jet however there appeared to be a local minimum in fluctuations at the centre followed by a local maximum at $r/D \approx 0.2$. This research was continued by Alekseenko *et al.* [58] who applied an external force on the swirling flow which succeeded in increasing the turbulence levels significantly for low swirl numbers. Examples of the flow visualisation produced by Alekseenko *et al.* [58] next to the swirling jet geometry used are displayed in figure 2.29. The images correspond well to those from Toh *et al.* [62] shown in figure 2.26.

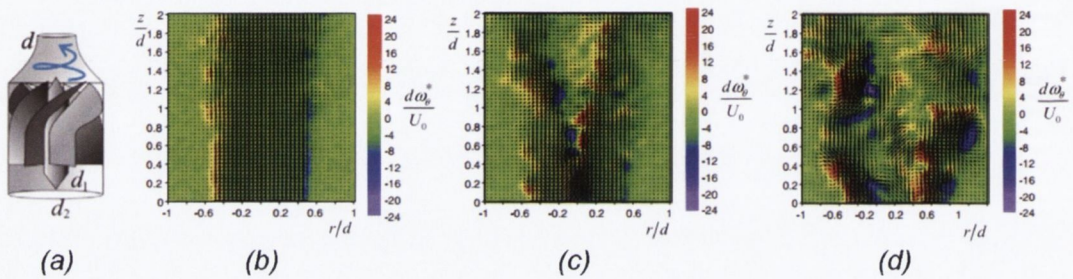


Figure 2.29: Swirling jet geometry (a) and flow visualisation of swirling jets with swirl numbers of (b) $S=0$, (c) $S=0.41$ and (d) $S=1.0$, Alekseenko *et al.* [58]

Another study on the development of free swirling jet flows as they leave a nozzle has been conducted by Majidi and So [70]. This work has provided evidence in support of a number of the points made previously about the development of swirling jet flows. While the generators used to create the swirling motion may be similar in geometry and design between different studies, a change in the angles of the vanes can alter the flow substantially. The level of decay of the jet can generally be related to the swirl number, with an increase in the swirl number corresponding to an increase in the rate of decay of the fluid flow.

Straight Pipe Nozzle Geometry with Axial Vanes

The most common method used to generate a swirling impinging jet is to incorporate axial guide vanes in a straight pipe nozzle, as previously described. The main reason for this comes down to the simplicity of being able to change the guide vane section within the pipe. The guide vanes, or swirl generators as they are more commonly

referred, are generally made from a solid metal cylinder (steel or aluminium) which is then machined to produce channels that create the desired angular flow. Senda *et al.* [71], Lee *et al.* [72], Bakirci and Bilen [68], Huang and El-Genk [73], Wen [74] and Yuan *et al.* [75] all took similar approaches in this respect. A twisted tape method, whereby a strip of metal is twisted along its longitudinal axis, has also been used by Nanan *et al.* [76] and Nuntadusit *et al.* [77, 78] for a range of twist ratios which correspond with certain swirl angles.

Senda *et al.* [71] used three separate swirl generators to create swirling impinging jets with corresponding swirl numbers of $S=0$, 0.22 and 0.45. As with many other studies, the $S=0$ case includes the swirl generator in the nozzle but the channels or vanes are parallel to the flow. This arrangement is commonly referred to as a multi-channel impinging jet (MCIJ). The generators in this study were positioned $1D$ from the nozzle exit as seen in figure 2.30.

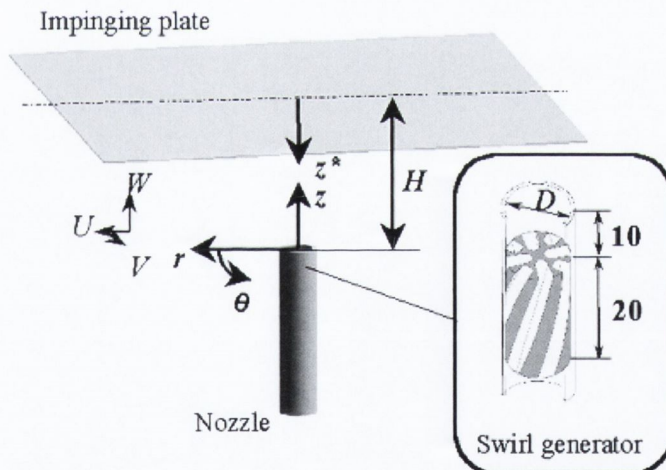


Figure 2.30: Impinging jet arrangement as used by Senda *et al.* [71]

Using thermo-sensitive liquid crystals, the heat transfer from the heated test surface was determined. For each of the three swirl numbers tested at a height of $2D$, a significant decrease in the heat transfer at the stagnation point compared to a conventional impinging jet was noted. This reduction in heat transfer was considered to be caused by a blockage effect from the swirl generator, especially for the $S=0$ case. This local minimum in heat transfer at $r/D=0$ is followed by a point of maximum heat transfer at a location which varies with swirl number, ranging from $0.5 < r/D$

2.4. IMPINGING JET HEAT TRANSFER

<1 , indicating an outward spread in the fluid flow. As the height, H/D , is increased to 4 and 6, the stagnation point heat transfer, while low, remains consistent for each of the swirl numbers, but the local maximum noted at $H/D=2$ decreases considerably.

A similar investigation was conducted by Lee *et al.* [72], examining the same swirl numbers as Senda *et al.* [71] but with the addition of one higher swirl number, $S=0.77$. The swirl generators used in this study are depicted in figure 2.31. Since the Reynolds number for this study was nearly four times higher than that of Senda *et al.* [71], the heat transfer magnitudes vary but the same trends in the Nusselt number distributions appear. For a swirl number of $S=0$ a local minimum in the heat transfer is noted at the stagnation point although in this case it is slightly higher than the stagnation point Nusselt number for the non-swirling jet. As the level of swirl is increased, the stagnation point Nusselt number drops, for all heights examined, and the location of the maximum Nusselt number moves away from the stagnation point indicating the spread of the fluid flow as identified by Senda *et al.* [71]. The drop in heat transfer at the stagnation point can be associated with the outward spread of the fluid as the swirl number increases, as noted by Senda *et al.* [71], however the primary reason can be attributed to the central core of the swirl generators causing a blockage. The generators were positioned at the leading edge of the jet nozzle, which denied the separated flow streams space to recombine and consequently created multiple flow streams instead of one singular swirling flow.

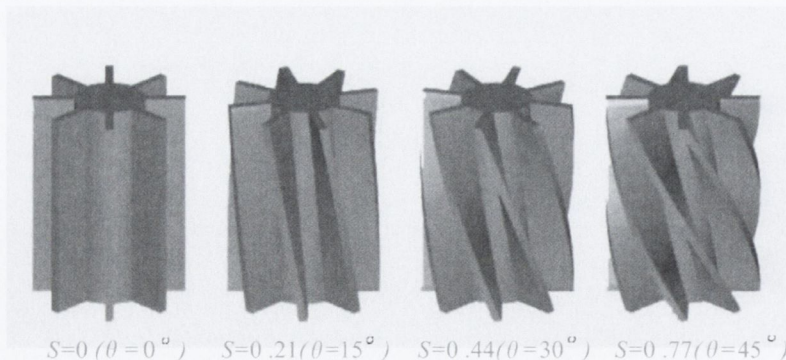


Figure 2.31: Schematic of swirl generators as used by Lee *et al.* [72]

The influence of a blockage from the insertion of swirl generators into a nozzle can only be minimised by either allowing an area for the separated flows to recombine, as

performed by Senda *et al.* [71], or by gradually decreasing the size of the blockage, as done by Bakirci and Bilen [68]. The study by Bakirci and Bilen [68] examined five different jets; a conventional (CIJ), a multi-channel (MCIJ) and three swirling (SIJ) impinging jets, as displayed in figure 2.32.

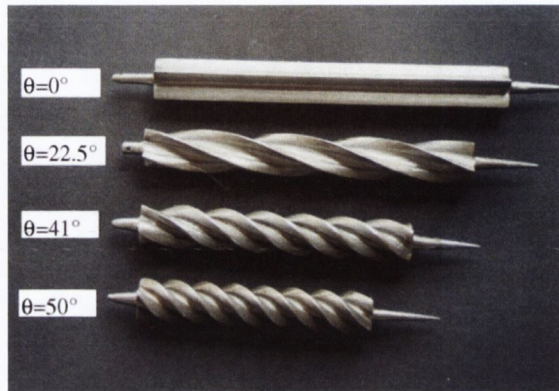


Figure 2.32: Flow inserts for a MCIJ and three SIJs of different angles as used by Bakirci and Bilen [68]

By applying temperature sensitive liquid-crystals on the impingement surface the temperature distribution across the surface was visualised and the information extracted was converted to the corresponding non-dimensional Nusselt number. For the CIJ and the MCIJ, the temperature distribution on the surface was shown to have no radial variation. However, as the swirling impinging jets were examined, the separation of the streams became apparent. For lower angles of swirl, the separation was not very noticeable. For the higher angles of swirl examined, however, four separate flows are distinctly visible. Figure 2.33 shows both the liquid-crystal display and the associated Nusselt number distribution for the two higher swirl angles. It is clear to see from the raw images of the liquid-crystal technique that there are four distinguishable impingement areas instead of a uniform distribution radially outward from the stagnation point.

This leads to a second problem. Since the Nusselt number distributions show a non-uniform cooling effect radially outwards from the center, the heat transfer can vary depending on the direction in which the local Nusselt number is recorded. While radially averaging the Nusselt number would give a result for a given area, it would not adequately describe the true distribution caused by the impinging jet.

2.4. IMPINGING JET HEAT TRANSFER

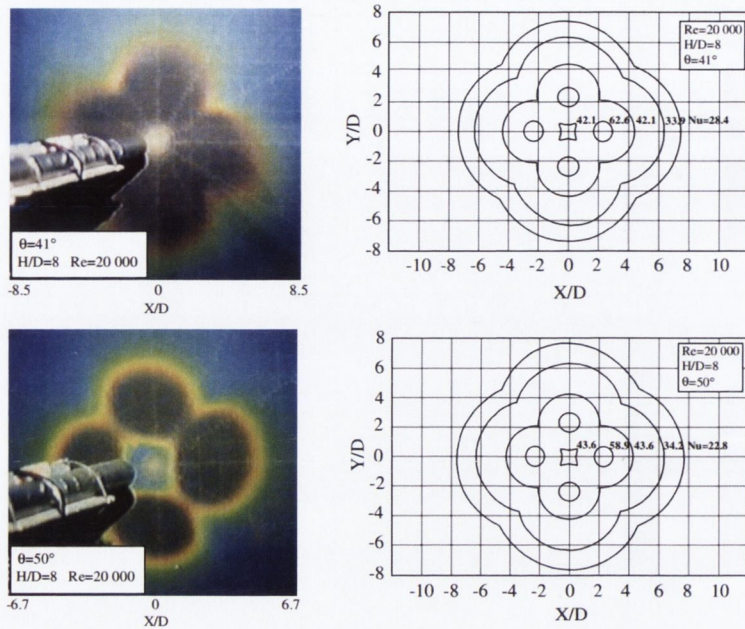


Figure 2.33: Surface temperature visualisation using liquid-crystal techniques and contours of constant Nusselt number for two swirling impinging jets with swirl angles of 41° and 50° at $H/D=8$ and $Re=20,000$ by Bakirci and Bilen [68]

This study concluded that minimising the angle of swirl led to higher levels of heat transfer for nozzle-to-surface heights of $6 < H/D < 14$ and that a MCIJ had the highest heat transfer levels of all five scenarios. With closer proximity to the impingement surface, different results are produced as reported by Huang and El-Genk [73] who looked at multiple swirling impinging jets with different angles of swirl for a height range of $1 < H/D < 6$. The design and set-up of the swirl generators is similar to Lee *et al.* [72] as the generators used are positioned $1D$ from the nozzle exit, figure 2.34.

At a nozzle height of $1D$ above the surface, Huang and El-Genk reported a significantly elevated level of heat transfer for all angles of swirl. As the height is increased up to $6D$, the heat transfer levels drop as the fluid flow spreads outwards giving way to a higher stagnation point heat transfer for the CIJ. However, the SIJs show higher heat transfer levels compared to the CIJ in an area approximately $2D$ outside the stagnation point.

From this review, one can determine that swirling impinging jets, based on straight pipe nozzles, have a higher chance of enhanced heat transfer when they are placed in close proximity to the impingement surface.

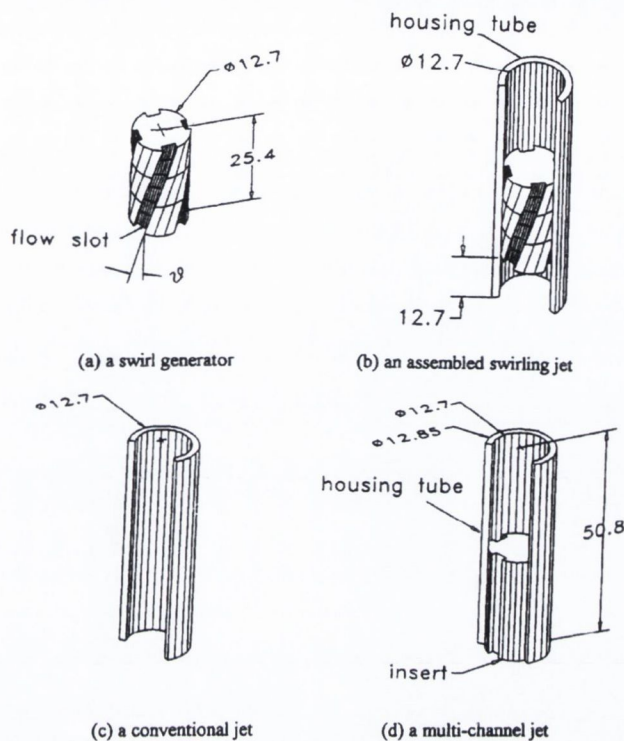


Figure 2.34: Impinging jet arrangement for a CIJ, MCIJ and different SIJs, with swirl angles of 15° , 30° and 45° as used by Huang and El-Genk [73]

Contoured Nozzle Geometry with Axial Vanes

While use of swirl generators is less common in contoured nozzles than in straight pipe nozzles, the results from past investigations correspond well with one another, as evident from the flow visualisations by Toh *et al.* [62] shown in figure 2.26 and Alekseenko *et al.* [58] shown in figure 2.29. Such similarities include the breakdown of the jet structure and increase in the spread of the jet radially outward as the swirl number is increased. The two heat transfer studies discussed in this section, Nozaki *et al.* [79] and Kinsella *et al.* [80], take different approaches to generate a swirling flow in a nozzle which narrows in diameter towards the exit.

Nozaki *et al.* [79] positioned the swirl generator far from the nozzle exit, allowing the streams of the flow to combine as the nozzle narrows towards the exit. Although this reduced the blockage effect noted in earlier studies, a local minimum Nusselt number was found at the stagnation point for both swirl numbers examined. As the swirl number increased, the local minimum became more pronounced and the point of

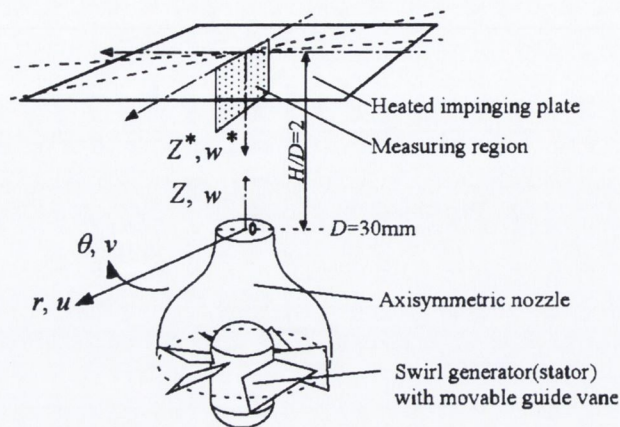


Figure 2.35: Swirling impinging jet set-up as used by Nozaki et al. [79]

maximum heat transfer was displaced further from the stagnation point.

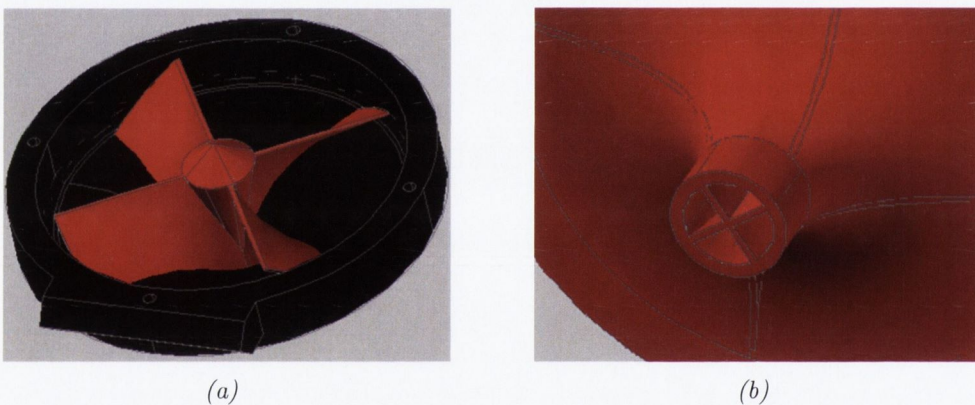


Figure 2.36: Position of swirl generating guide vanes as used by Kinsella et al. [80]

Kinsella *et al.* [80] took a different approach to insert swirl generating vanes by constructing the nozzles with the vanes built in, as demonstrated in figure 2.36. This concept, however, leads to a similar result to that reported by Bakirci and Bilen [68]. Thus, since the vanes continue to the exit of the nozzle, the four distinct flow streams cause varying levels of heat transfer at constant radial distances from the stagnation point. An example of this is shown in figure 2.37, revealing the variation in heat transfer distribution depending on the radial direction examined.

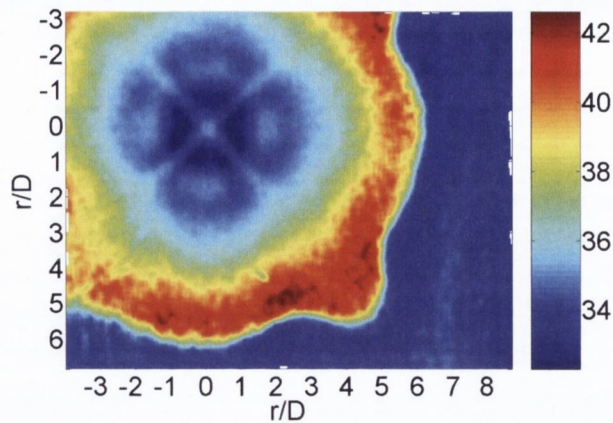


Figure 2.37: Thermal image showing surface temperature distribution on impingement surface under influence of swirling impinging jet by Kinsella *et al.* [80]

Nozzle Geometries with Radial Vanes

Radial vanes are employed before the nozzle exit with nozzle geometries broadly similar to contoured nozzles but not necessarily with a curved transition from a large to a small diameter. Such is the case in studies by Yajnik and Subbaiah [67], Yilmaz *et al.* [81], Ortega-Casanova [82] and Sheen *et al.* [83]. While the studies by Yajnik and Subbaiah [67] and Yilmaz *et al.* [81] did not focus on impinging jets with a swirling component, they used radial vanes in order to create a swirling flow through a straight pipe. To change the direction of the flow by 90° , as is necessary for radial vanes, a cone or ‘deflecting element’ is introduced into the design to channel the flow. One such element is displayed in figure 2.38. Sheen *et al.* [83] also incorporated this element into their set-up for an annular swirling impinging jet as did Kinsella *et al.* [80] with their guide vane system, seen in figure 2.36a.

Sheen *et al.* [83] examined the change in the flow regime when radial guide vanes and the Reynolds number of the flow are changed. In doing so, a new correlation for the swirl number was formed. This correlation, shown in equation 2.7, takes into account the number of vanes in the system, z , the angle at which they are positioned, ϕ and what is known as ‘the blockage factor’, ψ . Equation 2.6 cannot be used for this style of swirl generator since it is designed for an axial generator and the geometric dimensions necessary cannot be determined.

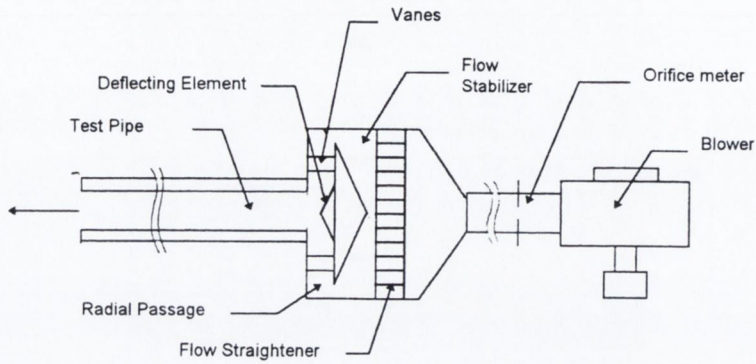


Figure 2.38: Experimental set-up displaying deflecting element in accordance with Yilmaz et al. [81]

$$S = C_1 (Re) \sigma (\phi) \quad [-] \quad (2.7)$$

$$\begin{aligned} \text{where } C_1 (Re) &= 0.28 \times [1 - \text{sech} (0.026Re^{0.67})] \\ \sigma (\phi) &= \frac{1}{1 - \psi} \left(\frac{\tan \phi}{1 + \tan \phi \tan (\pi/z)} \right) \\ \psi &= zs/2\pi R_1 \cos \phi \end{aligned}$$

where s is the thickness of each guide vane and R_1 is the radius from the center of the jet to the trailing edge of the guide vanes. Because the vanes are not placed close to the exit, as seen in many other cases, there is a relatively minimal blockage effect.

Swirling Flow Generated by Rotating Pipe

Besides the methods for generating a swirling flow already discussed, a quite uncommon way of producing it is through an axially rotating pipe. Studies involving such a design were carried out by Billant *et al.* [84], Maciel *et al.* [85] and Matsubara *et al.* [86]. This approach to generate a swirling flow, like that of adding a tangential flow to an axial flow or the use of radial vanes, encounters no blockage effects in the exit flow, but a more complex system is necessary. Each of these studies concern themselves with the development of a swirling flow as it emerges from a jet nozzle through flow measurement techniques such as laser doppler velocimetry (LDV), particle image

velocimetry (PIV) and computational fluid dynamic simulations. These methods are described in further detail in section 2.5. The development of a swirling jet is well illustrated in the work by Billant *et al.* [84] and shows the flow from a swirling jet divide into a conical shape. This is shown in figure 2.39, which explains why the local maximum heat transfer for a swirling jet impinging on a heated surface is located away from the stagnation point. In addition, as the angle of swirl is increased, the conical structure widens, as was also seen in figure 2.26, and the maximum heat transfer moves away from the stagnation point.

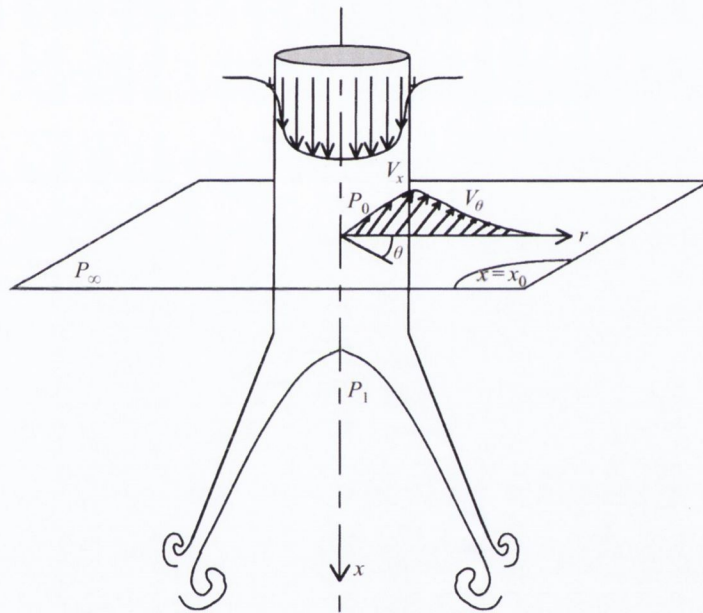


Figure 2.39: Development of swirling jet flow as it emerges from the jet nozzle as reported by Billant *et al.* [84]

The use of large-eddy simulations (LES) allowed Maciel *et al.* [85] to visualise the swirling flow generated from different perspectives including a downstream view which illustrates the central core of the jet's flow. The image shown below, figure 2.40, represents the downstream view of a swirling jet reported by Maciel *et al.* [85]. It can be noted from this that the flow is concentrated at the outer region of the jet, i.e. $0.3 < r/D < 0.5$. This compares well with what Billant *et al.* [84] described and corresponds well with the low heat transfer which is consistently reported at the stagnation point which is followed by a local maximum.

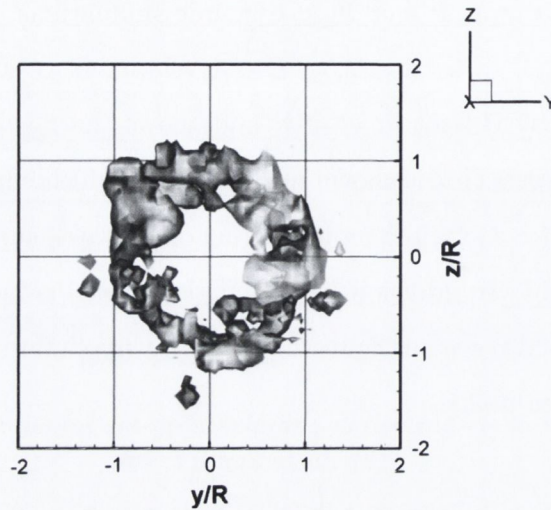


Figure 2.40: Downstream view of swirling jet as reported by Maciel et al. [85]

The past studies regarding the flow structure and heat transfer capabilities of swirling impinging jets have been discussed in this section. Common aspects in both of these fields include the spread of the jet as the angle of swirl, or swirl number, is increased, irrespective of the presence of an impingement surface, and the diminished heat transfer levels compared to a conventional impinging jet for many of the experimental configurations studied. However, it is possible for an enhancement factor to be established under specific conditions such as low nozzle to surface heights. The majority of studies regarding the heat transfer properties of swirling impinging jets is not assisted by flow visualisation to truly understand the flow mechanisms causing the respective heat transfer levels. The change in the method of swirl generation between the different studies may also have an influence on the structure of the flow emerging from the jet nozzles.

2.5 Flow Visualisation and Measurement Techniques

Flow visualisation techniques are implemented in experimental research to determine how the working fluid flow field develops and how it may be affected by surrounding objects or environmental conditions. Different methods of flow visualisation are commonly applied in such examples as the observation of fluid as it passes over an air-foil to illustrate boundary layer separation at certain angles of attack or in the design of sports vehicles to increase performance. Such techniques include those which measure the velocity of fluid flow at specific points and those which can map the entire flow regime. This section will address different techniques used to examine both swirling and non-swirling impinging jets and discuss the findings from such investigations.

Smoke-Wire

A smoke-wire device consists of a fine wire commonly coated in oil. When a current is passed through the wire, the heat generated causes the oil to evaporate and smoke is created. When this wire is placed in the path of a flow, for instance from an impinging jet, the smoke is carried by the fluid flow and produces an image of the flow. Visualisation of the fluid flow which emerges from an impinging jet nozzle with a contoured geometry was explored by Popiel and Trass [87] and Baydar and Ozmen [88].

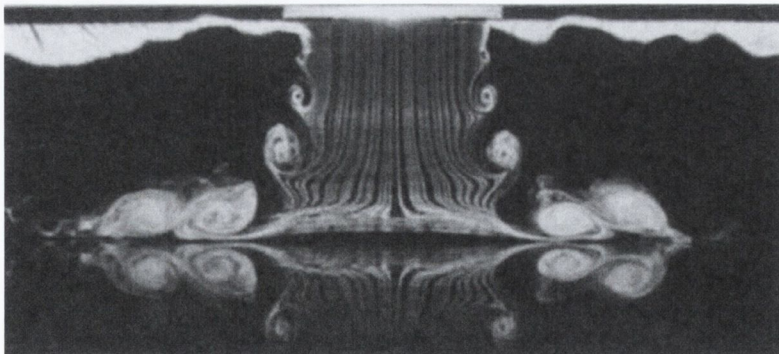


Figure 2.41: Illustration of jet development at $H/D=1.2$ and $Re=5,000$ by Popiel and Trass [87]

2.5. FLOW VISUALISATION AND MEASUREMENT TECHNIQUES

Popiel and Trass [87] used this technique to further understand the interaction of an impinging jet with a flat surface. The resulting images give incredible insight into the development of vortex maturity as the jet fluid mixes with the ambient air surrounding it; an example of such is shown in figure 2.41. As these vortex structures impinge upon the surface they are diverged outwards in a radial direction and form the radial wall jet as indicated in figure 2.3.

Baydar and Ozmen [88] focused on the differences in the flow when the jet nozzle introduces a confinement aspect to the system. This confined area was reported to have a significant effect on the fluid flow for nozzle spacings up to an equivalent of two nozzle diameters, $H/D=2$. Figure 2.42 depicts the difference in the level of recirculation between a confined and an unconfined flow as noted by Baydar and Ozmen [88].

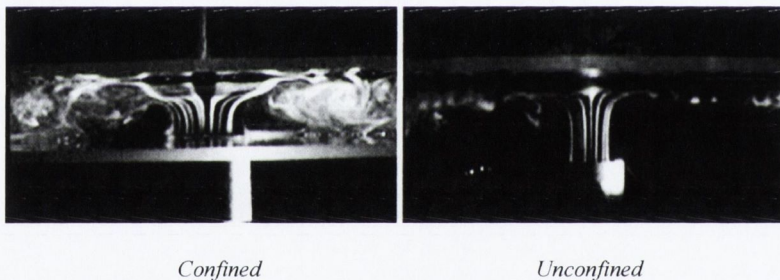


Figure 2.42: Influence of confinement on impinging jet flow at $H/D=1$ and $Re=4,800$ by Baydar and Ozmen [88]

Using the smoke-wire method, Huang and El-Genk [73] were able to visually examine the swirling impinging jets and define the flow characteristics while comparing them to a conventional impinging jet. The flow fields sketched in figure 2.43 demonstrate the variance between the two flows. Figure 2.43a corresponds with the flow structure seen previously in figure 2.3 for a conventional impinging jet.

While figure 2.43b appears similar in terms of the overall structure, the rotational aspect of the flow alters the inner structure considerably. The twisting effect of a swirling flow causes the free jet to rotate axially resulting in the flow area widening compared to that of the conventional impinging jet. The impinged region, zone (2) in figure 2.43b, contains a region of back flow and internal mixing caused by the swirling motion. This viewpoint compares well with the flow configuration developed

by Billant *et al.* [84] with regard to the back flow towards the center line of the jet.

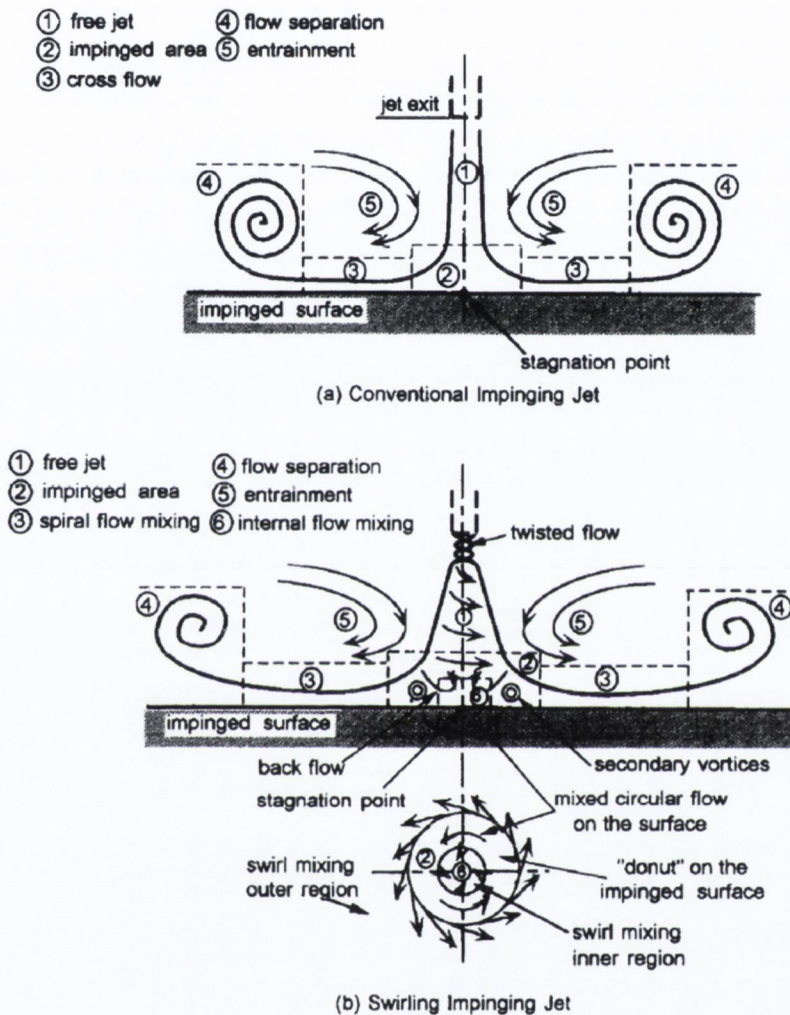


Figure 2.43: Variation in flow dynamics between (a) a convention impinging jet and (b) a swirling impinging jet as reported by Huang and El-Genk [73]

Laser Doppler Velocimetry (LDV)

Also known as laser doppler anemometry (LDA), LDV is a non-invasive approach to fluid velocity measurements. In its simplest form the application involves two intersecting beams of monochromatic laser light, typically split from a single beam. The intersection of the beams is focused on by a set of optics and a photo-detector. When a particle crosses into the path of the laser intersection the reflected light is recorded by the photo-detector and the frequency at which the reflected light fluctuates

2.5. FLOW VISUALISATION AND MEASUREMENT TECHNIQUES

can be related to the velocity of the particle. This method was used by Fitzgerald and Garimella [40] to study the flow field which develops in a confined impinging jet. By examining different heights and Reynolds numbers, the velocity of the fluid flow as it impinged upon a horizontal surface and travelled outwards from the stagnation point was examined and showed that the velocity of the flow near the surface decreased as the distance from the stagnation point increased.

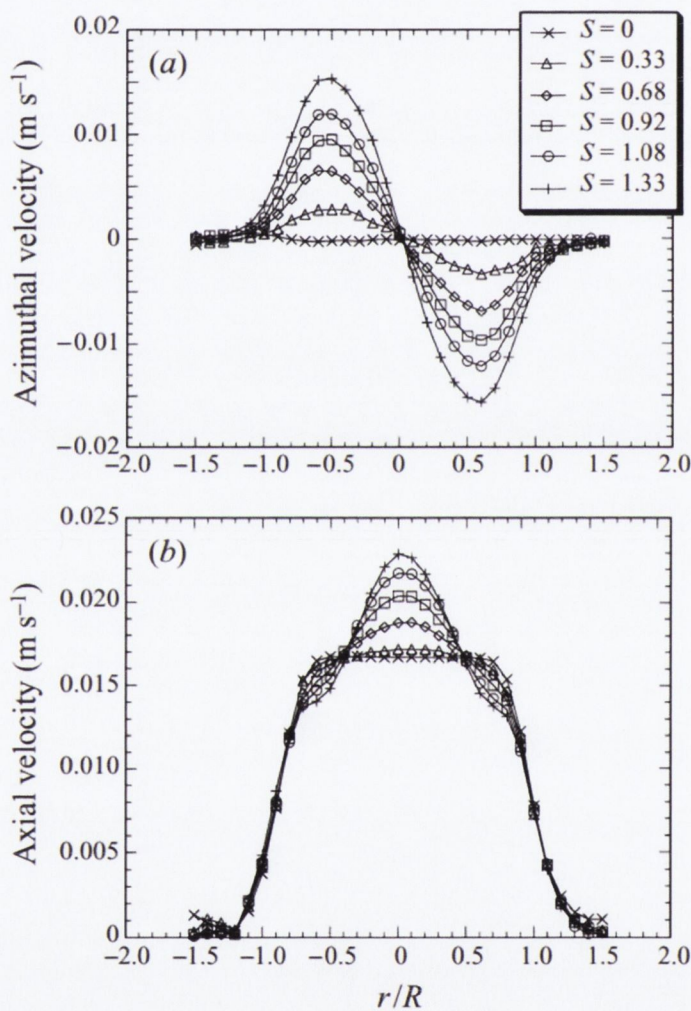


Figure 2.44: Azimuthal and axial velocity distributions for a jet flow with increasing swirl number as reported by Billant *et al.* [84]

Similarly, Billant *et al.* [84] used this technique to determine both the axial and azimuthal velocities of the swirling jets studied. The result of this investigation produced a clear view of what occurs inside a swirling flow as the level of swirl increases.

As portrayed in figure 2.44, the azimuthal velocity of a jet changes dramatically as a swirling motion is induced.

Initially with a swirl number of zero, there is no rotational motion, as would be expected. As the swirl number is increased so does the angular aspect to the flow and it appears to have a maximum velocity at $r/D \approx 0.3$. The axial velocity also changes as the swirl number is increased, from a near uniform velocity gradient for $S=0$ to a steep bell-shaped curve with a maximum velocity at the stagnation point, which increases as the swirl number increases.

Particle Image Velocimetry (PIV)

Like LDV, particle image velocimetry (PIV) is a non-invasive approach to flow field measurement but is designed to encompass a larger viewable region. A typical PIV set-up, as shown in figure 2.45, includes a high resolution camera focused on a desired region which is illuminated by a laser light sheet created using optical lenses. The flow field which is being examined is seeded with small particles, such as smoke for air or glass spheres for water. As each particle passes through the light of the laser sheet it is illuminated and the positions of all of the particles within the area are recorded by the high resolution camera.

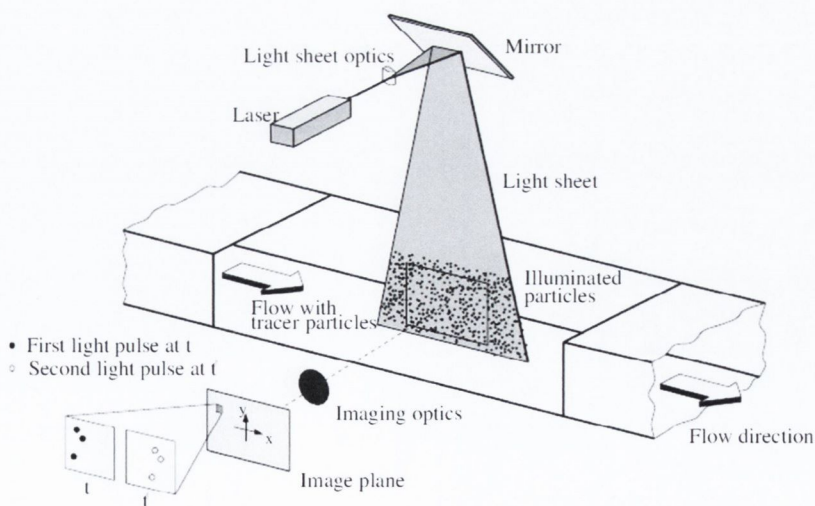


Figure 2.45: Typical set-up for particle image velocimetry, Raffel et al. [89]

2.5. FLOW VISUALISATION AND MEASUREMENT TECHNIQUES

Light scattered by the seeding particles changes as the angle the particles are viewed at changes; this is commonly referred to as Mie scattering. The level of light scattered changes depending on the type of seeding used. A Mie scattering for a $1\ \mu\text{m}$ oil particle, for example, is shown in figure 2.46, and shows that the location of the camera relative to the laser sheet is important in order to get distinct images of the seeding particles.

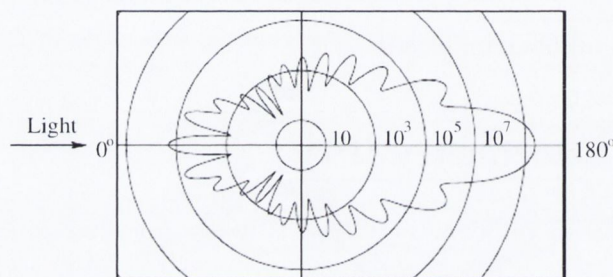


Figure 2.46: Mie scattering for $1\ \mu\text{m}$ particle of oil as described by Raffel et al. [89]

The recording of the flow is done on two separate occasions with the time between the two recordings being determined by the area the camera views and the speed of the fluid flow. The images recorded are divided into subsections known as ‘interrogation areas’. By way of statistical methods, the displacements of the particles between the two images are determined for each of the interrogation areas, given the assumption that the particles in one interrogation area have moved homogeneously between the two images. The displacement calculated is displayed as a vector which describes both the velocity and direction of the fluid flow. Further details regarding particle image velocimetry are contained in section 3.4.

This technique of flow visualisation and flow measurement is commonly used in the investigation of impinging jets due to its unobtrusive measurement method and its ability to capture details of the full flow field in contrast to point measurement techniques such as LDV or invasive methods such as hot-wire probes. The use of PIV to explore swirling jets has been used by Felli *et al.* [90] with water as the working fluid and Burattini *et al.* [91] with air as the working fluid. Both studies display a region around the central axis of the swirling jet with near-zero axial velocity, similar to the results seen by Maciel *et al.* [85] in figure 2.40.

In the case of Felli *et al.* [90], as the fluid impinges against a wall the flow spreads out from the stagnation area creating an area of near-zero velocity, an example of which is shown in figure 2.47. This is consistent with the findings of Huang and El-Genk [73], Nozaki *et al.* [79] and Senda *et al.* [71].

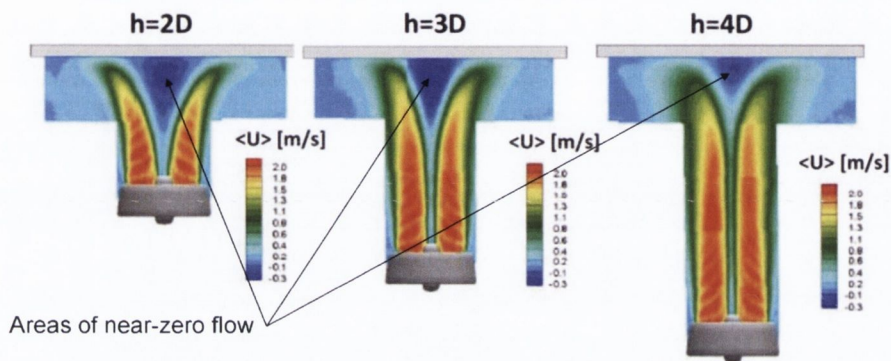


Figure 2.47: Flow field velocity for $H/D = 2, 3$ and 4 as reported by Felli *et al.* [90]

2.6 Concluding Remarks

This section has examined many aspects of impinging jets from both a fluid dynamics and a heat transfer standpoint. The main focus of this chapter has been on the characteristics of swirling impinging jets and on the methods used to generate them. Taking into account former studies on the subject, decisions can be made on the design of swirl generators to be used in this study in order to obtain a level of enhancement in heat transfer caused by a swirling jet in comparison to a conventional jet. One of the important characteristics that will govern the design of the swirl generator for this study will be the reduction of blockages in the nozzle of the jet which has been seen to reduce the heat transfer of a swirling jet significantly at the stagnation point. A guide vane approach to swirl generation will be employed in this study due to the minimal amount of additional components needed in the jet assembly and of extra space required, unlike the tangential flow and rotating pipe methods.

Through both experimental and numerical analysis, past studies have found common trends in heat transfer distributions caused by conventional impinging jets. Such

2.6. CONCLUDING REMARKS

trends include a local minimum in heat transfer at the stagnation point followed by a pair of local maxima at locations of $r/D \approx 0.5$ and 2 for a conventional impinging jet and a tertiary peak at $r/D \approx 2.5$ under specific conditions, but there is some disagreement about what is the cause of this tertiary peak. With regard to the swirling impinging jets, a significant decrease in the stagnation point heat transfer compared to a conventional impinging jet and a high level of flow spreading radially outwards from the center of the jet as the angle of swirl or swirl number increases has been consistently reported. However, the heat transfer results of the swirling impinging jets can vary from case to case depending on swirl generation method. Without simultaneous acquisition of both the flow field of the swirling impinging jet and corresponding heat transfer measurements, the true mechanisms of the swirling impinging jet cannot be connected.

To investigate the local heat transfer from a heated horizontal surface due to both a conventional and a swirling impinging jet, the method of infrared thermography will be employed. Using this technique, the influence of the impinging jets can be seen over a specific area, as opposed to point measurement methods which may miss defining features. In conjunction with this, a hot-film sensor will be employed to evaluate the heat transfer fluctuation levels on the impingement surface to determine the aspects of the local heat transfer distributions discovered. To link these heat transfer results to the flow structure of each of the impinging jets, flow visualisation and particle image velocimetry measurements will be used to identify the flow characteristics which correspond with the heat transfer levels.

Chapter 3

Test Facility and Instrumentation

This chapter describes the different experimental set-ups designed to explore the heat transfer characteristics due to the impinging jets examined, for various flow conditions and test parameters. Two experimental set-ups are used, each having a different thermal boundary condition, uniform wall flux and uniform wall temperature respectively, and a different measurement method. Firstly, a description of the impinging jet used in this study, together with the swirl generating inserts designed, is presented.

3.1 Impinging Jet Geometry

The impinging jet used in this study employs a contoured nozzle, as seen in figure 3.1. This geometry was chosen from the three previously discussed since it requires less space to create a fully developed flow than a straight pipe nozzle, allowing it to be utilised in confined applications, and would not be influenced by confinement issues which are common with orifice plate nozzles. The nozzle has an internal diameter of 5 mm. Before entering the nozzle, the working fluid flow through a chamber with an inner diameter of 80 mm, therefore the ratio between the diameters before and after the contoured contraction is 16. This value is important when comparing to results obtained from other contoured jet nozzles. Clearly, the closer this ratio is to unity, the closer the results are to those from a straight pipe nozzle geometry. The contoured nozzle extrudes from the main jet assembly by 20 mm. This corresponds to a nozzle length to diameter ratio of 4, as compared to an orifice nozzle which would be zero.

3.1. IMPINGING JET GEOMETRY

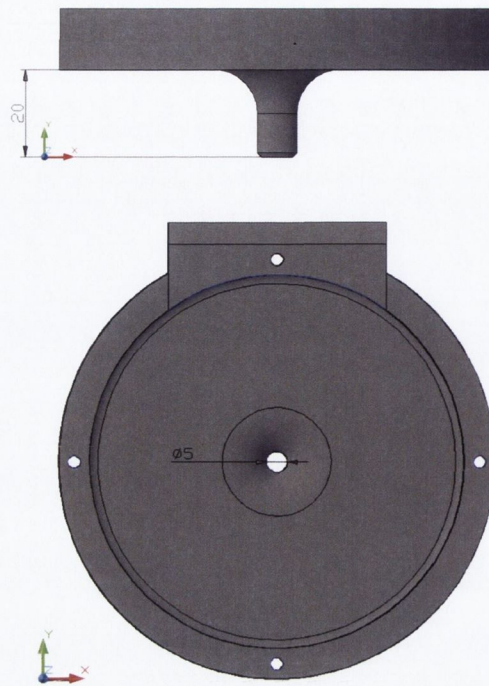


Figure 3.1: Impinging jet nozzle geometry; elevation view (top) and plan view (bottom)

This nozzle geometry is combined with two other components; a top section into which the fluid enters through four channels, indicated in figure 3.2a, and a centre section, figure 3.2b. The four separate flows combine in the completed assembly, then passes through a mesh (not pictured) located in the centre section of the assembly in order to straighten the flow before it reaches the jet nozzle at the bottom of the assembly. The air is supplied via an external compressor which generates a sufficient level of pressure to sustain the flow rates necessary for this study. The flow passes through a settling chamber which removes any vibrations or excitations in the fluid flow before entering the jet assembly. In Case 1, the flow rate of the air is measured using an Omega FMA-1600 flow-meter, which operates by calibrating the pressure difference across the device to a specific flow rate measured in L/min . In Case 2, the flow rate is regulated by an MKS mass flow controller, which allows a specific flow rate desired by the user via the Labview system used. The temperature of the fluid is measured by a T-type thermocouple in the center of the jet assembly.

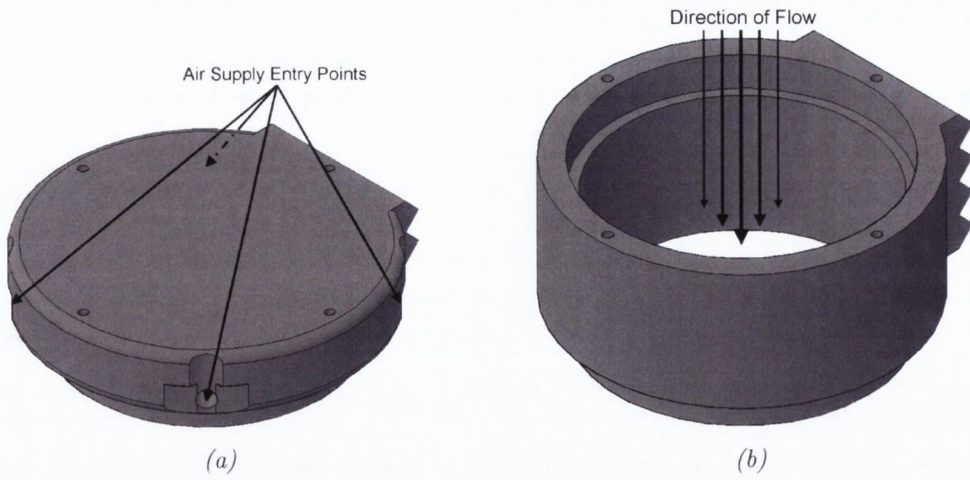


Figure 3.2: Top section (a) and central section (b) of jet assembly

The completed assembly, as shown in figure 3.3, is mounted perpendicular to the impingement surface at a distance governed by the user.

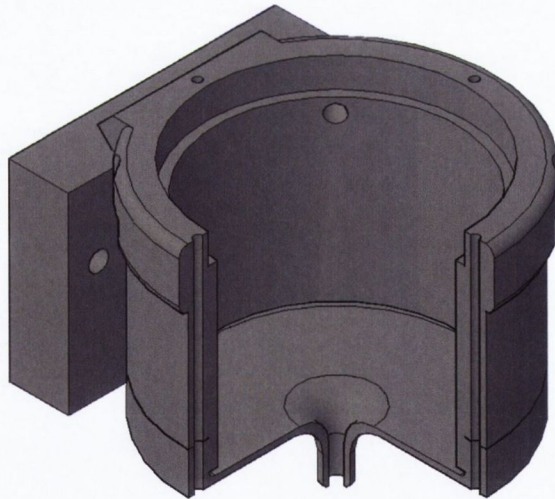


Figure 3.3: Cross-section of full jet assembly

3.1.1 Swirl Generators

The swirl generators used in this study were designed specifically to avoid the blockage issues seen in past studies and to work with the contoured nozzle geometry shown in figure 3.1. Four swirl generators were created through rapid prototyping, each one having a certain characteristic altered in order to identify the effect of this change. The swirl generators illustrated in figure 3.4 were designed to generate a flow in a way that is broadly similar to the techniques of Yilmaz *et al.* [81], Ortega-Casanova [82] and Sheen *et al.* [83].

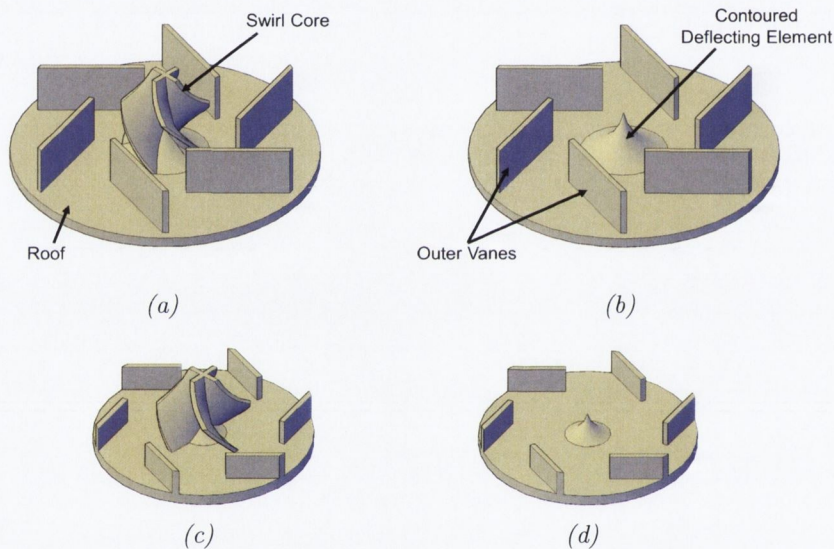


Figure 3.4: Swirl generators (a) Large, with swirl core - “ L_c ”, (b) Large, no swirl core - “ L_{no} ”, (c) Small, with swirl core - “ S_c ” and (d) Small, no swirl core - “ S_{no} ”

The swirl generators effectively have four elements to their design which also determine the title designated for each one.

- Roof: The roof section is a circular disc 2 mm thick upon which the guide vanes are positioned. The purpose of the roof is to ensure that the flow through the jet assembly is contained while travelling radially through the sets of guide vanes towards the nozzle exit. Generators with a roof diameter of 60 mm are designated ‘L’ for large while those with a roof diameter of 40 mm are designated ‘S’ for small.

- Deflecting Cone: Each of the generators has a contoured deflecting element, similar to that in figure 2.38, in the centre of the roof which ensures a smooth transition for the horizontal flow through the guide vanes to a vertical flow downwards.

- Outer Vanes: A set of six vanes are positioned such that they are aligned at an angle of 45° to a line joining their centroid to the center of the generator, displayed in figure 3.5. Since generators L_c and S_c contain a central guide vane section, known as the swirl core (described below), these outer vanes have no influence of the angle of swirl which emerges from the jet nozzle, but direct the flow

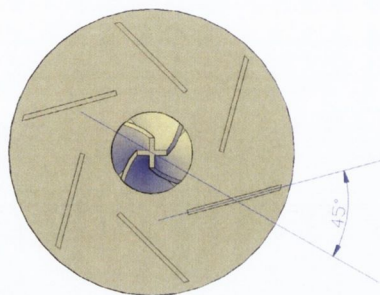


Figure 3.5: Position of outer vanes

inwards towards the swirl core. However, for generators L_{no} and S_{no} , these outer vanes are the primary method of swirl generation.

- Swirl Core: The swirl core is only present in two of the four generators. The inclusion of this element is to replicate the flow generated by axial swirl generators as seen in previous studies. The swirl core was created by axially twisting a column with a ‘ \times ’ cross-sectional shape so that the edges are angled at 45° to the horizontal plane. The swirl core is placed in the center of the generator in conjunction with the deflecting cone and extends from the roof of the generator to the point when the nozzle straightens after the contoured contraction, figure 3.1. A generator including a swirl core in its design is given the subscript ‘c’ while a generator without a swirl core is given the subscript ‘no’. The main dimensions of each of the swirl generators are listed in table 3.1.

3.1. IMPINGING JET GEOMETRY

Table 3.1: Characteristic dimensions of swirl generators

Swirl Name	Roof Diameter [mm]	Height [mm]	Outer Vane Height [mm]	Vane Thickness [mm]	Swirl Core	Swirl Core Length [mm]
" L_c "	60	12	10	1	Yes	18
" L_{no} "	60	12	10	1	No	–
" S_c "	40	7	5	1	Yes	13
" S_{no} "	40	7	5	1	No	–

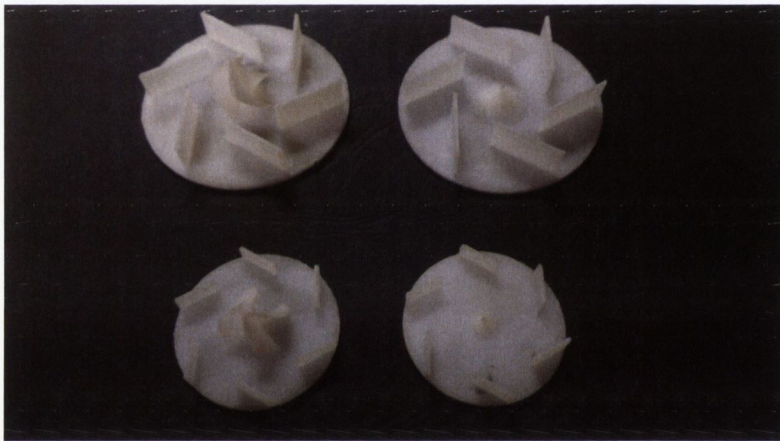


Figure 3.6: Image of each of the four swirl generators to further illustrate the size and aspect differences

When a swirl generator is placed inside the jet assembly displayed in figure 3.3, the flow is forced outwards to manoeuvre around the roof of the generator. The chosen Reynolds number and the generator employed will determine the velocity of the fluid as it passes through the outer vanes. In the cases of swirl generators L_c and S_c , the fluid will pass through the swirl core, governing the swirl number of the flow, before exiting the nozzle. For these two cases, the swirl number is calculated using equation 2.6 as $S \approx 0.67$ for both generators. Thus, the determining factor in assessing these cases will be whether the change in the scale of the generator affects the surface heat transfer distribution.

In the cases of swirl generators L_{no} and S_{no} , there is no swirl core so the fluid is directed downwards, after the outer vanes, towards the nozzle exit. Unlike the previous pair of generators, the swirl numbers for L_{no} and S_{no} cannot be evaluated

using equation 2.6; instead equation 2.7 is used since it is formulated specifically for radially positioned swirl generators. Using equation 2.7 the swirl number for both of these generators is estimated to be $S \approx 0.19$.

The swirl number values indicated are for demonstrative purposes. This study does not investigate the difference in heat transfer results due to swirling impinging jet with different angles of swirl, which has been done in past studies, but explores the change in heat transfer with varying swirl generator design.

An illustration of the position of swirl generator L_c and L_{no} in the jet assembly is shown in figures 3.7 and 3.8.

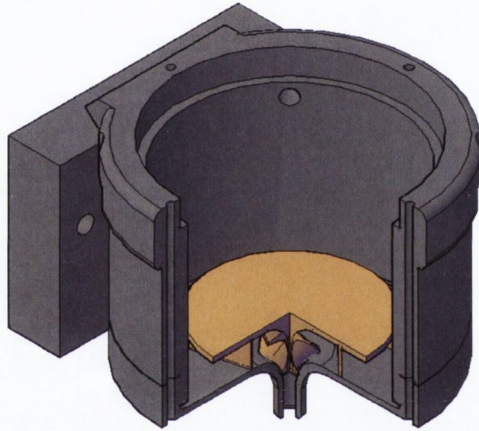


Figure 3.7: Cross-section of full jet assembly including swirl generator “ L_c ”

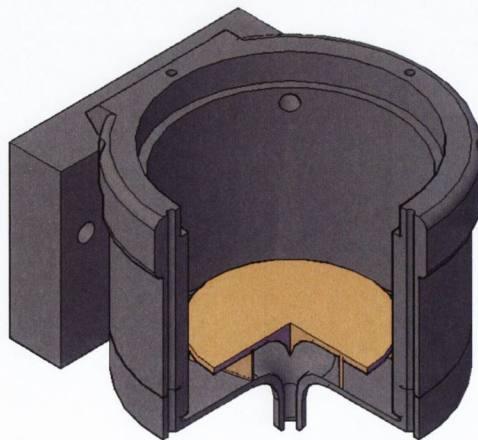


Figure 3.8: Cross-section of full jet assembly including swirl generator “ L_{no} ”

3.2 Case 1: Infrared Thermography

As mentioned at the beginning of this chapter, two different experimental set-ups and associated heat transfer measurement techniques were used in this study. Case 1 estimates the heat transfer from an impinging jet as it acts upon a surface with a uniform wall flux thermal boundary condition using infrared thermography. The technique of infrared thermography involves the employment of an infrared thermal imaging camera. In this study, the camera is aimed at a target heated surface to evaluate the temperature of the surface while under the influence of an impinging jet.

3.2.1 Impingement Surface

This test facility uses a Goodfellow stainless steel AISI-321 foil as the heated impingement surface. The foil, with an area of $0.15 \times 0.19 \text{ m}^2$ and a thickness of $25 \text{ }\mu\text{m}$, is clamped at both ends by a pair of copper bars. To ensure maximum contact between the foil and the copper bars, Loctite 3888TM electrically conductive adhesive is applied. The sets of copper bars are connected to a Lambda GEN6-200 DC power supply, shown in figure 3.9, to complete the circuit.

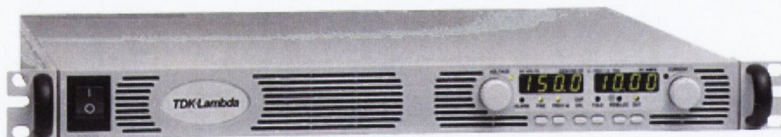


Figure 3.9: Lambda GEN6-200 power supply

This set-up allows the user to apply a constant current through the foil, thereby heating it up to a desired temperature. With no external force being applied, the foil can warp as electricity passes through and heats it, which can interfere with the focus of the thermal imaging camera. To remove this warping effect, the foil is attached to a tensioning device. One end of the foil, which is clamped between one set of copper bars, is fixed to a perspex mount while the opposite end is fixed to a movable perspex section mounted on slider bearings. The movable section tensions the main section by a set of springs and in doing so keeps the foil taut at all times during testing. An illustration of the impingement surface is presented in figure 3.10. The complete

impingement surface is mounted horizontally on an aluminium frame. This aluminium frame is also used to mount other devices such as a flow-meter, a regulatory valve, the jet assembly and the thermal imaging camera.

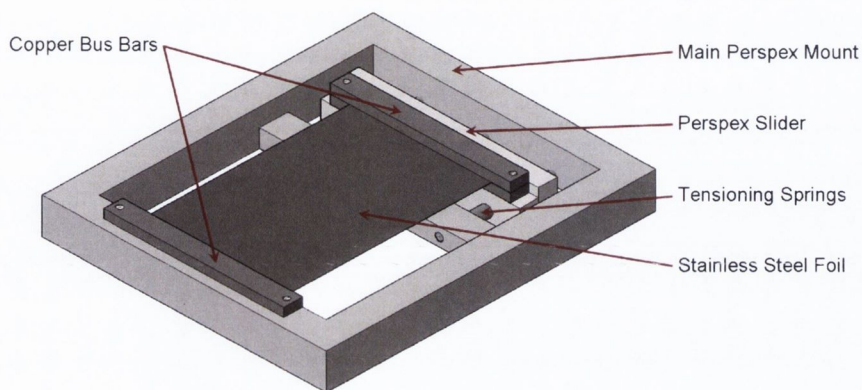


Figure 3.10: Impingement surface for Case 1

3.2.2 Thermal Imaging Camera

The thermal imaging camera, a FLIR Systems A-40, shown in figure 3.11a, is positioned so that it is focused on the bottom face of the stainless steel foil. This side of the foil is coated in a layer of matt black paint to reduce reflection and increase the accuracy of the temperature measurements. The camera is connected to a computer via a fire-wire cable and displays the camera's image using ThermaCAM Researcher Pro 2.8. The resolution of the camera is 240 by 320 pixels, equivalent to approximately $0.11 \times 0.15 \text{ m}^2$, giving the camera a spatial resolution of approximately 0.46 mm per pixel width.

The contoured impinging jet described in section 3.1 is fixed above the foil, directed at the centre of the surface and directly above the thermal imaging camera. The air which emerges from the jet nozzle cools the ohmically heated foil and the temperature of the area which is influenced by the impinging jet is recorded by the thermal imaging camera. The foil is assumed to be thermally thin, such that the temperature on the top of the foil due to the cooling effect of the jet is equal to the temperature on the bottom surface of the foil seen by the thermal imaging camera.

3.2. CASE 1: INFRARED THERMOGRAPHY

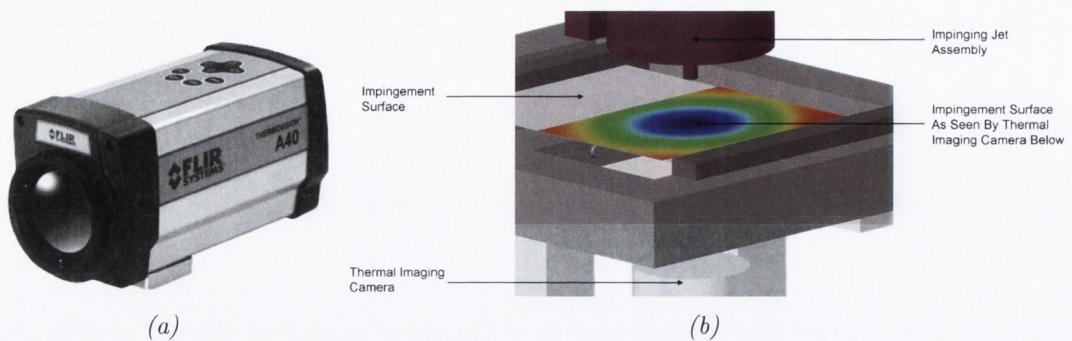


Figure 3.11: FLIR Systems A-40 thermal imaging camera (a) and system arrangement for Case 1 while foil undergoes cooling (b)

The Biot number, Bi , is a measure of the thermal gradient across the thickness of the foil and confirms this to be true. The thermal imaging camera records at a rate of 50 frames per second and is set for a time period of 10 seconds. Each experiment records a set of 500 images.

3.2.3 Time-Averaged Heat Transfer Experimental Procedure

The various impinging jet configurations are tested at different nozzle to surface heights ranging from a H/D of 0.5 to 10 and for Reynolds numbers ranging from 8,000 to 20,000, resulting in 49 sets of results for each impinging jet set-up tested. As previously mentioned, the thermal imaging camera is set to record a set of 500 images of the surface of the foil over a time period of 10 seconds. The camera records two sets of images per test; the first is a set of adiabatic images and the second is a set of heated images. The adiabatic images are recorded as the impinging jet acts upon the unheated foil, while the heated images are recorded as a current passes through the foil under steady state conditions. These two sets of images are averaged, filtered and processed using Matlab. Examples of the surface temperature as seen by the thermal imaging camera for an adiabatic test and for a heated test during cooling are shown in figure 3.12.

The processing method uses the images recorded to analyse the energy balance of the system, as described in section 4.1. This involves subtracting the heat losses from the foil due to natural convection, radiation and lateral conduction from the heat

3.2. CASE 1: INFRARED THERMOGRAPHY

generated in the foil to give the convective heat removal of the impinging jet.

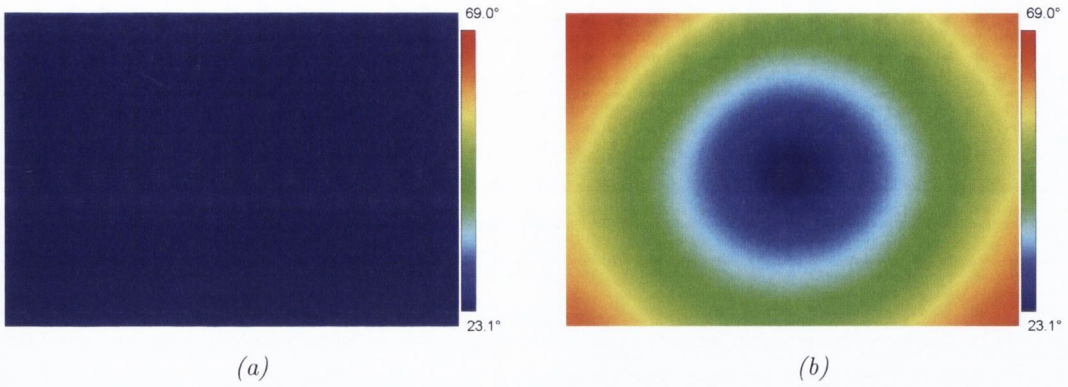


Figure 3.12: Thermal image of foil during jet impingement under (a) an adiabatic and (b) a heated scenario

3.3 Case 2: Hot-Film Sensor Analysis

Case 2 examines the same impinging jet scenarios as in Case 1 but investigates the effect on local heat transfer distributions of a different thermal boundary condition, namely uniform wall temperature.

3.3.1 Impingement Surface

The impingement surface for Case 2 employs a copper plate heated uniformly by a heater mat, supplied by Holroyd Components, to generate a nominally uniform wall temperature thermal boundary condition. Copper is chosen as the material for the impingement plate since it has a high thermal conductivity and is easily workable to accommodate alterations if necessary. The copper plate has a surface area of $425 \times 550 \text{ mm}^2$ and a thickness of 5 mm . The heater mat is placed underneath the plate and consistent contact between it and the copper plate is assured using silicone glue. It is operated using a D.C. power supply which is set to provide a constant voltage of 63.3 volts. The underside of the heater mat not in contact with the copper plate is surrounded by insulation to ensure that the heat generated by the mat transfers to the plate. The copper plate reaches an approximate maximum temperature of 80°C when all heat loss is by natural convection and radiation. The plate is fixed to a traversing table which allows testing to be conducted at specific positions.

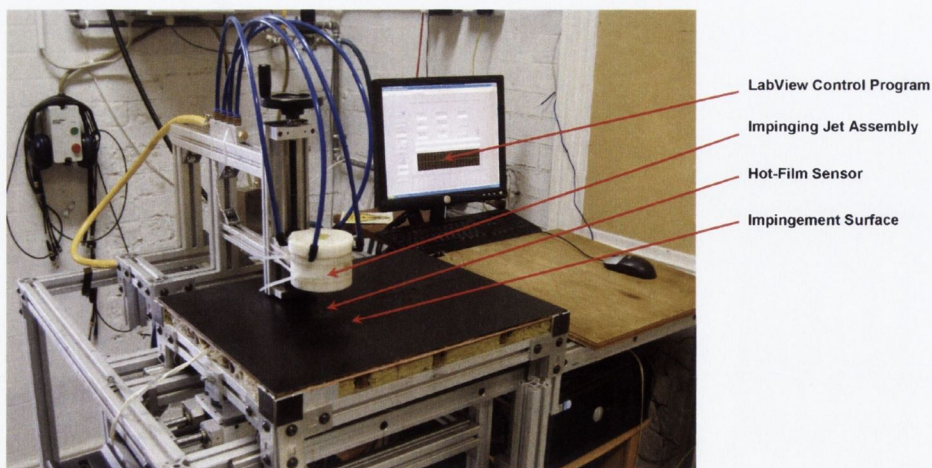


Figure 3.13: System arrangement for Case 2 study

3.3. CASE 2: HOT-FILM SENSOR ANALYSIS

The rate of heat transfer from the surface of the plate is measured using a Senflex hot-film sensor, shown in figures 3.14 and 3.15. The sensor is positioned in a groove in the centre of the plate so that it does not protrude from the surface and thereby disrupt the impinging jet flow. The sensor is comprised of two thin copper leads, with a standard thickness and width of approximately 0.0127 mm and 0.762 mm respectively, joined at one end by a thin nickel film. The nickel film, with dimensions of 0.1016 mm wide by 1.4478 mm long by $20\text{ }\mu\text{m}$ thick, is electro-beam deposited onto a 0.0508 mm thick Upilex S polyimide film substrate¹. The sensor is connected via BNC cable to a constant temperature anemometer which is set to maintain the temperature of the nickel film to a specified temperature above that of the copper plate, which is designated by the term ‘overheat’. The spatial resolution of the hot-film sensor is approximately 0.1 mm , which is different to the spatial resolution of the infrared thermography technique using the FLIR Systems A-40 thermal imaging camera by nearly a factor of five.

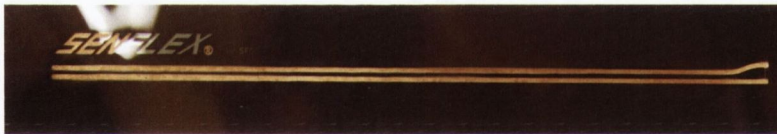


Figure 3.14: Senflex hot-film sensor SF0303

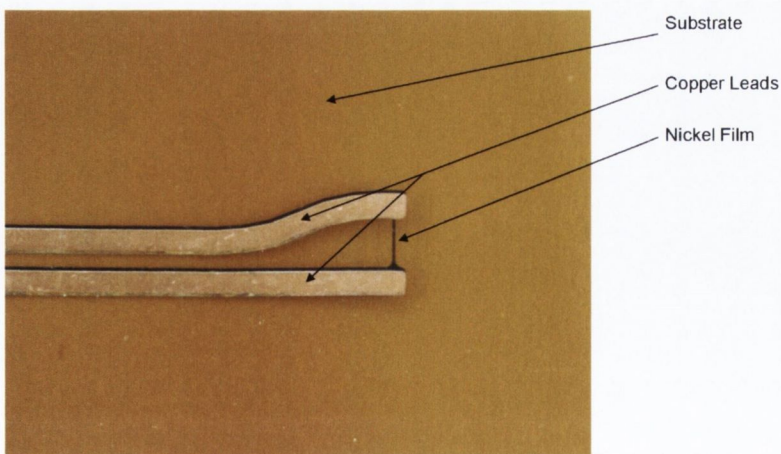


Figure 3.15: Nickel film in Senflex hot-film sensor SF0303

¹<http://www.taosystem.com>

3.3.2 Constant Temperature Anemometry

The hot-film sensor is controlled using a constant temperature anemometer, CTA. The CTA operates on a Wheatstone bridge configuration which has the hot-film sensor as one of the arms of the bridge, as illustrated in figure 3.16. The CTA balances the Wheatstone bridge such that it creates a potential difference across the nickel film, thereby raising its temperature. The CTA is set using user defined values specific to the hot-film sensor employed via a LabView system. The temperature of the impingement surface and the resistance of the probe are recorded at a given time. By calibrating the resistance of the sensor against temperature, for more details see section 4.2, the CTA balances the Wheatstone bridge thereby raising the voltage across the film to generate the desired overheat. The procedure to accomplish this involves the CTA turning off the Wheatstone bridge first and measuring the total resistance of the hot-film sensor, including the nickel film, the copper leads, and the BNC cable along with any other connection materials. This resistance corresponds to a certain operating temperature, since resistance is temperature dependant. The overheat temperature, set by the user, is added to this temperature and converted back to an adjusted resistance governed by the resistance/temperature calibration. The Wheatstone bridge is then activated and by balancing the resistance on either side, this adjusted resistance is achieved and the temperature of the film is set to a desired overheat.

Figure 3.16 displays the layout of the constant temperature anemometer Wheatstone bridge. The arm labelled ' R_{probe} ' represents the resistance of the hot-film sensor, including copper leads and nickel film, together with the resistance of the BNC cables connecting the hot-film sensor to the CTA. The Wheatstone bridge for this study operates with a bridge ratio, $R_2:R_1$, of 20:1. The probe resistance in this circuit changes due to temperature so the decade resistance, R_{decade} , is adjusted in order to balance the bridge. Balancing the Wheatstone bridge encourages the current to pass equally across R_1/R_{probe} and R_2/R_{decade} , such that the potential difference between points (a) and (b), shown in figure 3.16, is zero. Further details concerning the operation of the hot-film sensor and the CTA are contained in section 4.2.

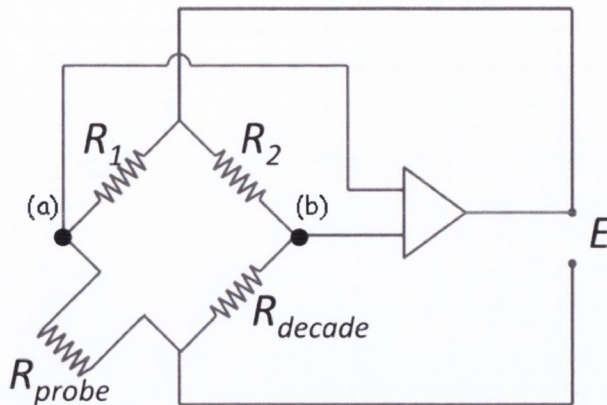


Figure 3.16: Constant temperature anemometer Wheatstone bridge including hot-film sensor probe [16]

3.3.3 Time-Averaged Heat Transfer Experimental Procedure

The same impinging jet configurations are tested with this system as with the infrared thermography approach. A series of Reynolds numbers, ranging from 8,000 to 20,000, and nozzle to surface heights, $0.5 < H/D < 10$, are examined for a non-swirling and four swirling impinging jets. The flush mounted hot-film sensor is positioned directly underneath so that the nickel film is perpendicular to the direction in which the plate will traverse. The heater mat is activated and the plate is allowed to reach a state of thermal equilibrium. Once achieved, a Reynolds number is set using a LabView program connected to the flow controller. The plate is moved horizontally so that the impinging jet is positioned the equivalent of $10D$ away from the stagnation point. When the test program is initialised, the CTA is balanced and key information is recorded about the resistance of the probe, the voltage applied to generate the overheat of the film and the fluctuations in this voltage. Other factors are also recorded, such as the nozzle position and volume flow rate of the air jet along with thermocouple measurements of the temperatures of the plate, the jet flow and the ambient air. These data are recorded over a number of positions along the plate so that a heat transfer distribution from the stagnation point outwards may be evaluated. The fluctuations in the hot-film voltage are recorded in order to estimate the positions of high heat transfer fluctuations on the impingement surface.

Since this is a point measurement method, in the cases of the swirling impinging jets, each of the swirl generators was positioned at different angles inside the jet assembly to prove consistency in the local heat transfer measurements despite the angular position of the generator.

3.4 Flow Visualisation & Particle Image Velocimetry

Flow visualisation and particle image velocimetry testing was performed to provide the flow field information needed to determine the cause of both enhanced and diminished levels of heat transfer occurring in the results obtained from the swirling jet flows. To visualise an air flow, seeding must be introduced to the flow. The scale of the system and the fluid being used determines what type of seeding is permissible since some seeding types may alter the flow. For this study a Concept *Colt 4* smoke machine was used since the particle size produced is around 0.2-0.3 μm in diameter, according to the manufacturer's specifications². To introduce the smoke into the air flow, a chamber containing the smoke generated is connected to a venturi meter placed before the point at which the flow enters the impinging jet assembly. Due to the geometry of a venturi meter, the pressure drop at the narrowing of the device causes the smoke to be sucked in, thereby dispersing the smoke within the air-flow. The density of the smoke within the air-flow can be altered by adjusting the amount of smoke generated by the smoke machine.

The system employed for this study to record images of the impinging jet is a high speed stereoscopic LaVision system with a Quantronix *Darwin – Duo* dual oscillator Nd:YLF laser paired with a LaVision *HighspeedStar6* high speed camera. The system is controlled by the LaVision *Davis* interface, regulating the recording aspects of the camera and the time delay between the two light pulses emitted by the laser. This interface also processes the images recorded, evaluating the velocity vectors amongst other flow variables which can be determined. The instrumentation described

²<http://www.concept-smoke.co.uk>

3.4. FLOW VISUALISATION & PARTICLE IMAGE VELOCIMETRY

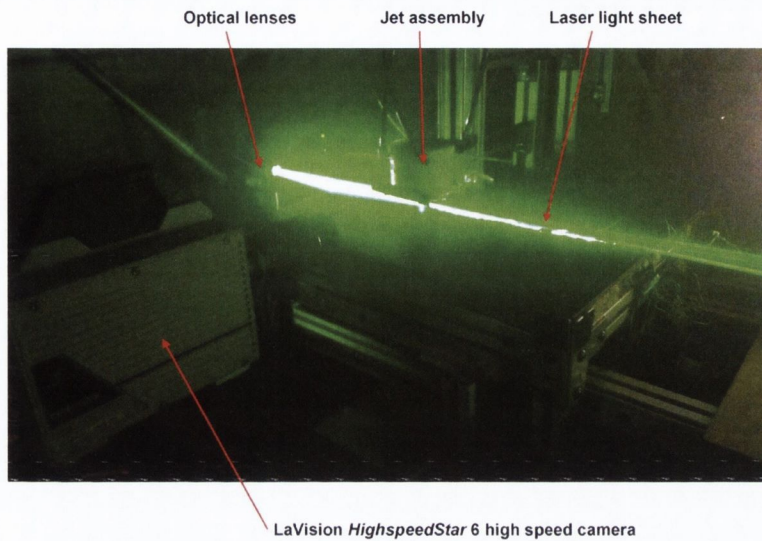


Figure 3.17: Experimental instrumentation used to conduct flow visualisation and particle image velocimetry measurements

is mounted on the experimental set-up for case study 2. The laser is reflected off a series of mirrors in a laser guiding arm and fixed to a set of optical lenses designed to form a laser sheet to span the area being recorded by the high speed camera, as seen in figure 3.17.

3.5 Concluding Remarks

Two experimental set-ups are employed in this study to evaluate the heat transfer of a contoured impinging jet and to compare it with that of four swirling impinging jets incorporated into the same nozzle geometry using specially designed swirl generators. The two case studies employ different heat transfer measuring techniques with respective advantages and disadvantages. For Case 1, using infrared thermography, thermal imaging allows a full temperature field to be evaluated but the spatial resolution is quite poor, approximately 0.5mm per pixel. In Case 2, using a hot-film sensor, the measurement system has a more defined spatial resolution, approximately 0.1mm , and can establish the fluctuations in the signal from a hot-film sensor. However, this method is a point measurement technique and therefore it is possible to miss variations in the heat transfer for non-uniform distributions.

The following chapter will address the data processing and analysis techniques used in this study for both heat transfer measurement systems.

Chapter 4

Experimental Analysis

Both of the measurement techniques described in chapter 3 use specific theoretical approaches to determine the heat transfer to the impinging jet. These different theories are discussed in the following sections. Common factors in both set-ups include the non-dimensionalised height parameter, H/D , where H is the distance from the exit of the nozzle to the impingement surface and D is the diameter of the jet, and the Reynolds number of the flow. The height of the nozzle ranges from $0.5 < H/D < 10$ for this study. The Reynolds number, Re , is a non-dimensional number which compares the inertial forces to the viscous forces of a fluid. The Reynolds number is calculated by combining the rate at which the fluid is moving across/through a structure with a characteristic dimension of the structure along with properties of the fluid.

For this study the Reynolds number is calculated using equation 4.1, where \dot{Q} is the volume flow rate [m^3/s], ν is the kinematic viscosity of the working fluid [m^2/s] and $A_{X,jet}$ is the cross-sectional area of the jet nozzle [m^2]. As mentioned previously, the Reynolds numbers examined in this study range between 8,000 and 20,000.

$$Re_D = \frac{\dot{Q}D}{\nu A_{X,jet}} \quad [-] \quad (4.1)$$

The convective heat transfer results are displayed in terms of the corresponding local Nusselt number for each of the impinging jet scenarios evaluated through equation 4.2, where x is the characteristic length [m], k_f is the thermal conductivity of the fluid [W/mK] and h is the heat transfer coefficient described by Newton's law of

4.1. CASE 1: INFRARED THERMOGRAPHY

cooling [W/m^2K], as shown in equation 4.3, where q'' is the heat flux [W/m^2], T_S is the temperature of the surface being examined [K] and T_∞ is the reference temperature [K]; for example, the ambient fluid temperature in a natural convection system or the temperature of the fluid from an impinging jet in a forced convection system.

$$Nu_x = \frac{hx}{k_f} \quad [-] \quad (4.2)$$

$$q'' = h(T_S - T_\infty) \quad [W/m^2] \quad (4.3)$$

Depending on the situation, the characteristic length used in the calculation of the local Nusselt number can differ. Where necessary, the characteristic length used will be indicated.

4.1 Case 1: Infrared Thermography

Convective heat transfer to the impinging jet using the infrared thermography system described previously is estimated by performing an energy balance on the ohmically heated foil. When the foil is heated and allowed reach a state of thermal equilibrium, the heat generated inside the foil is predominantly lost through natural convection and radiation. However, when the jet impinges upon the surface it causes a temperature gradient across the foil which gives rise to lateral conduction.

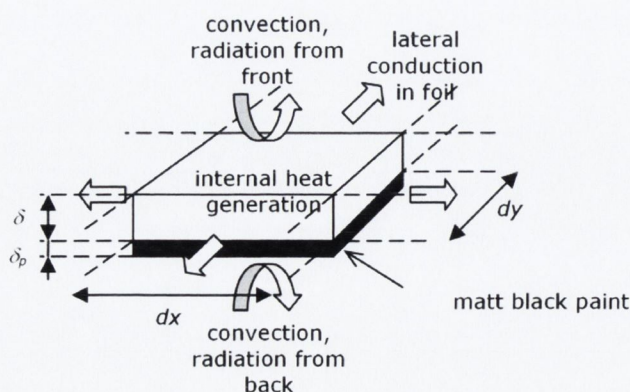


Figure 4.1: Illustration of heat transfer to and from stainless steel foil with one side coated in matt black paint

As the jet is positioned to cool one side of the foil, the heat dissipated on this side is due to forced convection to the jet, while the other side loses heat due to natural convection since there are no external flows acting upon it. In addition to these effects, both sides of the foil lose heat due to radiation. The energy balance of the foil is illustrated in figure 4.1 and represented by equation 4.4, where q'' is the heat flux for each of the heat transfer modes identified.

$$q''_{generated} = q''_{convection,upper,forced} + q''_{convection,lower,natural} + q''_{radiation,upper} + q''_{radiation,lower} + q''_{conduction,lateral} \quad [W/m^2] \quad (4.4)$$

Generated Heat Flux

The heat flux generated ohmically within the foil, represented by $q''_{generated}$, is calculated by dividing the power applied across the foil by the surface area of the foil, equation 4.5, where I is the current passed through the foil [A], R is the resistance of the foil [Ω] and A_S is the surface area of the foil [m^2]. Variations in the thickness, resistivity of the foil may cause the heat flux generated within the foil to be non-uniform. However, these factors are assumed to be negligible, therefore, q''_{gen} is assumed to be uniform for this case study.

$$q''_{generated} = \frac{I^2 R}{A_S} \quad [W/m^2] \quad (4.5)$$

The current passed through the foil is controlled by the power supply mentioned in section 3.2.1. The resistance of the foil is calculated using equation 4.6, where ρ is the resistivity of the material [Ωm], l is the length of the material [m] and A_X is the cross-sectional area of the material [m^2]. The resistance calculated is found to be comparable with the manufacturer's specifications.

$$R = \rho \frac{l}{A_X} \quad [\Omega] \quad (4.6)$$

4.1. CASE 1: INFRARED THERMOGRAPHY

In this study, the parameters governing the heat generated ohmically within the foil, i.e. the power applied and the surface area of the foil, produce a heat flux of approximately $2,000 \text{ W/m}^2$.

Convective Heat Flux

The term designated $q''_{convection,upper,forced}$ signifies the heat flux due to the forced convection effect of the impinging jet on the upper surface of the foil. Mixed convection can occur on a heated surface when the natural convection from the surface is not negligible in comparison with the dissipated heat by the forced convection of the jet. To quantify the level of mixed convection the Grashof number, Gr , which describes the level of buoyancy of a fluid from natural convection, discussed in further detail below, is related to the square of the Reynolds number, Re , of the forced fluid flow. This ratio, known as the Richardson number, Ri , determines which form of convection dominates the system. If $Gr/Re^2 \gg 1$ then forced convection may be neglected; if $Gr/Re^2 \approx 1$ the system must take both natural and forced convection into account; finally, if $Gr/Re^2 \ll 1$ then natural convection may be neglected. For the range of nozzle to surface distances examined, $8,000 \leq Re \leq 20,000$, this factor was noted to be in the range of $0.5 \times 10^{-3} < Gr/Re^2 < 3.5 \times 10^{-3}$ for the lowest Reynolds number investigated, $Re=8,000$, and $0.5 \times 10^{-4} < Gr/Re^2 < 3.5 \times 10^{-4}$ for the highest Reynolds number investigated, $Re=20,000$, therefore, the latter case was found to be the situation for this study. As previously discussed, Koseoglu and Baskaya [38] showed that fluid buoyancy due to natural convection can influence the heat transfer caused by an impinging jet. However, this was noted for Reynolds numbers lower than 3,000, whereas this study looks at the heat transfer due to impinging jets for Reynolds numbers higher than 8,000. Thus, in this case the heat dissipated from the upper surface of the foil is due solely to the forced convection of the impinging jet. The heat flux due to the jet is the unknown factor in equation 4.4, so to determine its magnitude the other factors must be quantified.

The heat flux from the under- or lower-side of the foil is calculated using natural convection theory based on the bottom face of a horizontal heated plate. According to Fujii and Imura [92], the Nusselt number, Nu , of a heated horizontal plate facing

downwards with a uniform wall flux thermal boundary condition, under natural convection, is expressed using the correlation given in equation 4.7. The product of the Grashof number and the Prandtl number is also known as the Rayleigh number, Ra .

$$Nu = 0.58 (Gr.Pr)^{\frac{1}{5}}, \quad 10^6 < Gr.Pr < 10^{11} \quad [-] \quad (4.7)$$

In this correlation, Pr represents the Prandtl number of the system and is the ratio of the kinematic viscosity to the thermal diffusivity of the fluid. The Grashof number, Gr , which was discussed previously, is calculated using equation 4.8, where g is the acceleration due to gravity [9.81 m/s^2], β is the volumetric thermal expansion coefficient [K^{-1}], T_S is the temperature of the surface [K], T_∞ is the ambient temperature [K] and L is the characteristic length parameter [m]. For this set-up, the length parameter is the ratio of the surface area to the perimeter of the foil.

$$Gr_L = \frac{g\beta(T_S - T_\infty)L^3}{\nu^2} \quad [-] \quad (4.8)$$

Since the heated foil is modelled on a uniform wall flux thermal boundary condition, each of the fluid properties are evaluated at a temperature, T_e , except for β which is evaluated at the film temperature, T_f , defined by equations 4.9 and 4.10 respectively, as described by Holman [24] and Thirumaleshwar [93].

$$T_e = T_S - 0.25(T_S - T_\infty) \quad [K] \quad (4.9)$$

$$T_f = (T_S - T_\infty)/2 \quad [K] \quad (4.10)$$

However, equation 4.7 is based on the principle that, while there may be small variations in the temperature due to natural convection, there is no significant temperature gradient across the heated surface. In practice this is not the case since the impinging jet, which acts upon the ohmically heated foil, creates a discernible temperature gradient. Since no correlation was found to determine the Nusselt number for a horizontal surface with an applied thermal gradient of this nature, certain assumptions had to be made. As mentioned in section 3.2, the temperature of the foil is measured

4.1. CASE 1: INFRARED THERMOGRAPHY

using a thermal imaging camera directed at the underside of the foil. The camera has a resolution of 320×240 square pixels. Each of these pixels has a width approximately 0.46mm and records a single temperature. It is assumed that the temperature in the area represented by each pixel is constant. Equation 4.7 is applied to the local temperature of each pixel but using the characteristic length of the full impingement surface, i.e. the ratio of surface area to perimeter, therefore resulting a more accurate Nusselt number distribution across the foil than to use an averaged value of the surface temperature, especially at the stagnation point which has a lower surface temperature than the outer regions of the impingement surface.

When the natural convection Nusselt number is evaluated using equation 4.7, the result is converted into the equivalent heat flux using the definition of the Nusselt number, Nu , and Newton's law of cooling described in equations 4.2 and 4.3 respectively.

An illustration of the natural convection heat flux result obtained for the case of a conventional impinging jet at a nozzle to surface distance of $H/D=1$ and a Reynolds number of 12,000 is shown in figure 4.2. The center of the surface demonstrates a low area of convective heat loss since the temperature difference between the surface and the ambient air is low but increases as the distance from stagnation point of the impinging jet increases.

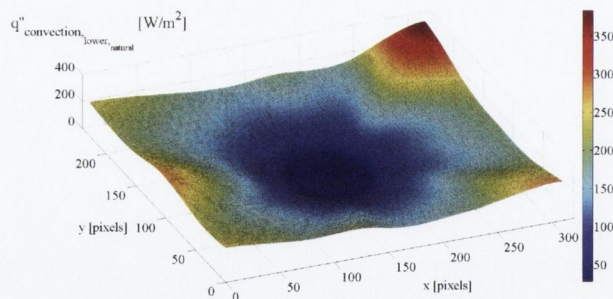


Figure 4.2: Heat flux due to natural convection from the lower side of the foil under the influence of a conventional impinging jet with $Re=12,000$ and $H/D=1$

Radiative Heat Flux

The heat flux due to radiation from each of the sides of the foil is determined from the Stefan-Boltzmann law. This states that the total energy per unit area per unit time radiated from a black-body or the emissive power, E_b , is proportional to the fourth power of the black-body's temperature measured in Kelvin, i.e.

$$E_b \propto T^4 \quad (4.11)$$

The proportionality is balanced by a constant known as the Stefan-Boltzmann constant, σ , which has a value of approximately $5.67 \times 10^{-8} \text{ W/m}^2\text{K}^4$, such that equation 4.11 becomes:

$$E_b = \sigma T^4 \quad [\text{W/m}^2] \quad (4.12)$$

Energy which impacts upon a body by way of radiation is partly reflected, absorbed and transmitted. Since most bodies do not transmit thermal radiation, the radiative energy which strikes the body is partly reflected and partly absorbed [24]. In the case of a body without the characteristics of a black-body placed inside an enclosure with black-body characteristics which emits energy according to the Stefan-Boltzmann law, at the point of temperature equilibrium the energy absorbed by the body must be equal to the energy emitted. When the emissive energy of the body, E , is compared to the emissive energy of a black-body of the same size placed in the same enclosure, E_b , the ratio of the two energies is known as the emissivity, ϵ , as shown in equation 4.13.

$$\frac{E}{E_b} = \epsilon \quad (4.13)$$

The level of radiative energy emitted by real materials is less than that of ideal black-bodies, thus the emissivity factor of common materials is less than one while the emissivity of a black-body is unity. In reality, the emissivity of a material can vary with temperature.

To estimate the thermal radiation heat flux levels for this study, the ohmically heated foil is approximated as a small convex object in a large cavity as outlined by

4.1. CASE 1: INFRARED THERMOGRAPHY

Incropera and DeWitt [9]. Under this approximation the radiative heat flux of each of the sides of the foil can be calculated using equation 4.14.

$$q''_{radiative} = \epsilon \sigma (T_S^4 - T_{Surr}^4) \quad [W/m^2] \quad (4.14)$$

where ϵ is the emissivity of the material and T_{Surr} is the temperature of the surrounding environment [K].

Since both sides of the foil are open to the environment, both dissipate heat through radiation. As pointed out in section 3.2.2, the foil is known to be ‘thermally thin’ since the Biot number is evaluated to be $Bi < 0.1$, therefore the only variable between the top and bottom of the foil in equation 4.14 is the emissivity. While the foil is made of stainless steel, the bottom surface is coated in a layer of matt black paint. It was evaluated through simple temperature tests, using the thermal imaging camera, that the emissivity of the paint was ≈ 0.945 , while the emissivity of the stainless steel is ≈ 0.129 according to the manufacturer’s specifications. This means that nearly 88% of the heat lost due to radiation is dissipated from the lower surface of the foil because of its higher emissivity.

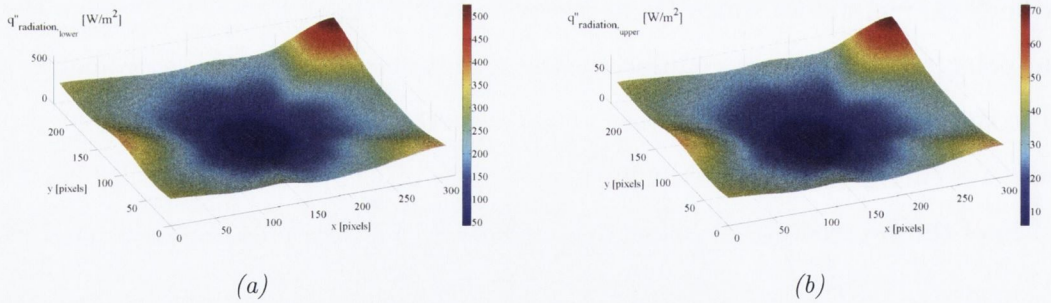


Figure 4.3: Heat flux due to radiation from (a) lower and (b) upper side of the foil under the influence of a conventional impinging jet with $Re=12,000$ and $H/D=1$

The radiative heat flux of the lower and upper sides from the foil under the same conditions as figure 4.2 are shown in figure 4.3a and b respectively. While the two images are very similar in heat flux distribution, the radiative heat flux for the lower side of the foil is approximately seven times higher than the heat flux from the upper surface, since the lower surface is coated with matt black paint which has a higher

emissivity, ϵ . The center of the surface has the lowest temperature due to the impinging jet and therefore has the lowest level of radiative heat loss as seen in both cases.

Conductive Heat Flux

Lateral conduction is also taken into account in this system since there is a temperature gradient laterally across the foil as a result of the impinging jet. To determine the impact that lateral conduction may have on a system such as this, a non-dimensional inequality was established by Hetsroni *et al.* [94] and reported by Patil and Narayanan [95], as shown in equation 4.15, where k_{foil} is the thermal conductivity of the foil [W/mK], t_{foil} is the thickness of the foil [m], d_e is the equivalent diameter of the area of temperature heterogeneity [m] and h_{mean} is the mean heat transfer coefficient over this area [W/m^2K]. If this inequality is true, the lateral conduction can be neglected. While this condition is true for this study, the lateral conduction is nonetheless evaluated and included in the calculation of the convective heat transfer to the impinging jet. The heat flux due to lateral conduction for this two-dimensional scenario is defined by equation 4.16.

$$\frac{4k_{foil}t_{foil}}{h_{mean}d_e^2} \ll 1 \quad (4.15)$$

$$q''_{conduction,lateral} = -k_{foil}t_{foil} \left(\frac{\partial^2 T_S}{\partial x^2} + \frac{\partial^2 T_S}{\partial y^2} \right) \quad [W/m^2] \quad (4.16)$$

This expression can be simplified by modelling the surface using a numerical finite difference method. Equation 4.16 can be translated into a finite-difference formula by way of the three point central difference formula as outlined by Lupton [96]. This is described in equation 4.17, where i and j describe the position of the element currently being evaluated and dz is the length of the side of a single element [m]. Lupton [96] investigated many options into the evaluation of the lateral conduction including radial averaging, curve fitting and the use of specific computer analysis software, but concluded that this numerical method in conjunction with image filtering achieved the best results and accuracy. This approximation becomes more accurate the closer the respective points are to each other and the more points that are included

4.1. CASE 1: INFRARED THERMOGRAPHY

in the approximation. This approach complements the experimental process as each temperature element in equation 4.17 can be associated with each pixel in the images recorded by the thermal imaging camera.

$$q''_{conduction,lateral} = -k_{foil}t_{foil} \frac{(T_{i+1,j} + T_{i-1,j} + T_{i,j+1} + T_{i,j-1} - 4T_{i,j})}{dz^2} \quad [W/m^2] \quad (4.17)$$

While equations 4.16 and 4.17 are described for the stainless steel foil, the paint layer on the underside of the foil is also taken into consideration using the thermal conductivity and thickness of the paint used.

Figure 4.4 illustrates the lateral conduction heat flux under the same experimental conditions as previously illustrated. The high heat flux levels are caused by changes in the temperature gradient on the impingement surface. Two graphs are presented in this figure, representing the lateral conduction heat flux in the foil (a) and the paint (b). The lateral conduction in the foil is approximately six times greater than that in the paint due to their differences in thickness and thermal conductivity.

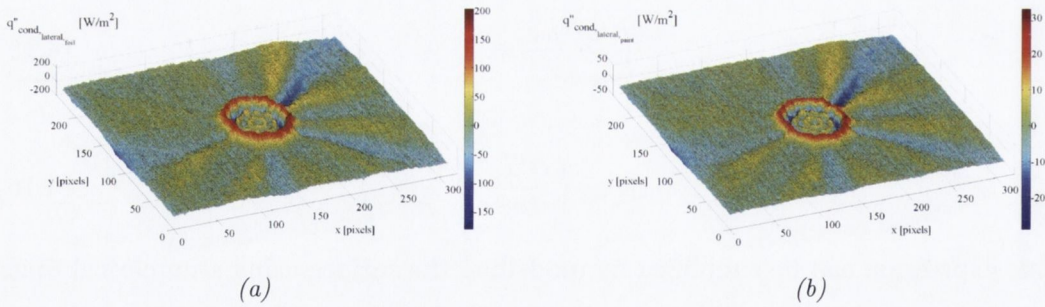


Figure 4.4: Heat flux due to lateral conduction in (a) foil and (b) paint under the influence of a conventional impinging jet with $Re=12,000$ and $H/D=1$

Impinging Jet Heat Flux

Equation 4.4 is rearranged so that the only unknown variable, the heat flux due to the forced convection of the impinging jet, $q''_{convection,upper,forced}$, is localised. This is the parameter of interest for the current study.

$$q''_{convection,upper,forced} = q''_{generated} - q''_{convection,lower,natural} - q''_{radiation,upper} - q''_{radiation,lower} - q''_{conduction,lateral} \quad [W/m^2] \quad (4.18)$$

An illustration of the different heat flux levels due to natural convection, radiation and lateral conduction plotted with the heat flux due to the forced convection of the impinging jet is displayed in figure 4.5. From this figure, it is noted that the heat losses due to natural convection and radiation are small in the stagnation region due to the low temperature difference between the foil and the surrounding environment. The levels of heat lost due to these mechanisms increase as the distance from the stagnation point increases. While the heat flux due to radiation from the top face of the foil (without the paint layer) is consistently low as the radial distance increases, the heat flux levels for natural convection and radiation from the lower face of the foil (with paint layer) increase towards $200 W/m^2$. In the cases of lateral conduction in both the foil and the paint layer, the area of highest influence resides in the stagnation region due to the large temperature gradients. At radial distances greater than $4D$, the heat lost due to lateral conduction is small.

To put these values into perspective, each of the mechanisms is displayed as a percentage of the heat flux generated within the foil in figure 4.6. As mentioned previously, the heat flux generated within the foil has a uniform magnitude of approximately $2,000 W/m^2$. From figure 4.6 it is noted that radiation from the bottom surface of the foil accounts for the highest level of heat loss across the impingement surface ranging from 3% at the stagnation point to 10% at $r/D=10$. Natural convection from the bottom surface is also a major contributor ranging from 2% to 7% from $r/D=0$ to 10. The influence of lateral conduction in the foil varies across the foil due to the different temperature gradients present.

4.1. CASE 1: INFRARED THERMOGRAPHY

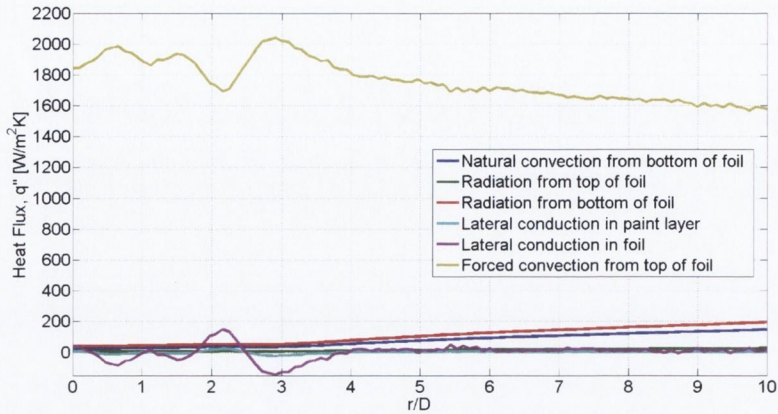


Figure 4.5: Heat flux levels of heat loss mechanisms for a conventional impinging jet at a nozzle to surface height of $H/D=1$ and Reynolds number of 12,000

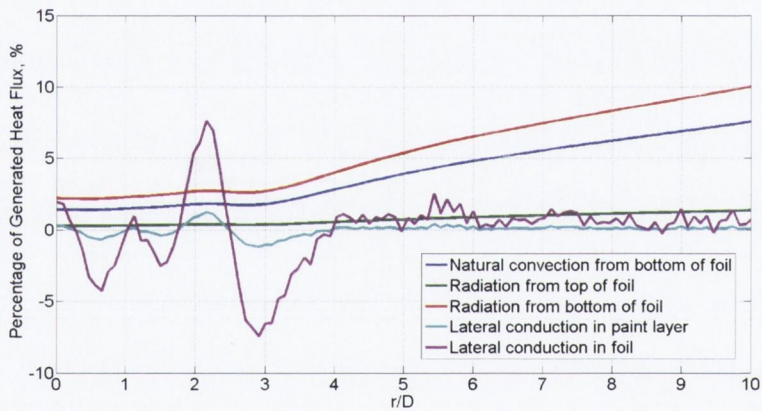


Figure 4.6: Heat flux levels of heat loss mechanisms as a percentage of the heat flux generated within the foil for a conventional impinging jet at a nozzle to surface height of $H/D=1$ and Reynolds number of 12,000

When the heat losses are removed from the heat generated within the foil, according to equation 4.18, the convective heat flux due to the impinging jet is realised. Since each of the heat flux calculations uses information from the temperature maps recorded by the thermal imaging camera, the resultant impinging jet heat flux is a 320×240 array, an example of which is shown in figure 4.7a.

Using Newton's law of cooling, the heat flux is converted into the heat transfer coefficient, h , as illustrated in figure 4.7b, using equation 4.3, and by using equation 4.2 the corresponding Nusselt number, Nu , similar to that of Astarita *et al.* [97], is produced, as shown in figure 4.8.

4.1. CASE 1: INFRARED THERMOGRAPHY

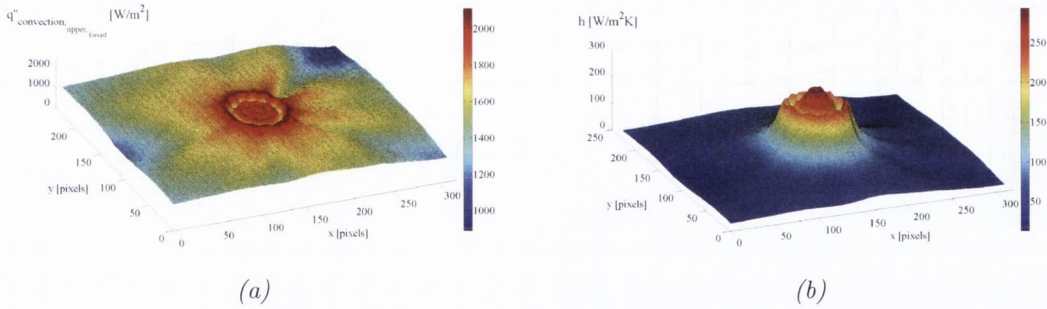


Figure 4.7: Resultant (a) heat flux and (b) heat transfer coefficient due to conventional impinging jet with $Re=12,000$ and $H/D=1$

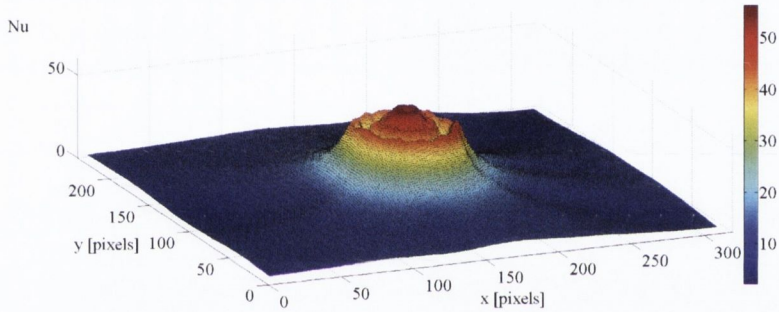


Figure 4.8: Resultant Nusselt number due to conventional impinging jet with $Re=12,000$ and $H/D=1$

To compare the resulting Nusselt numbers for each of the experimental tests performed, separate distributions of the Nusselt number from the stagnation point outwards up to a distance of $r/D=10$ were extracted, as shown by figure 4.9.

The Nusselt number distributions are taken along these lines and averaged to give a simpler illustration of the heat transfer which will also be used to compare with the results from Case 2.

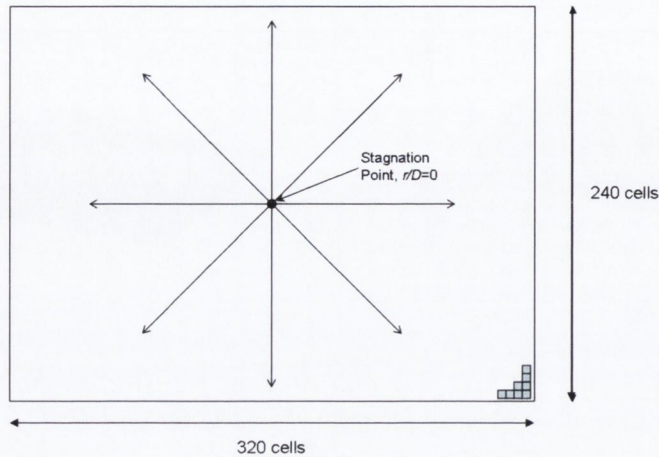


Figure 4.9: Illustration of stagnation point in 320×240 array and directions in which results are extracted

4.2 Case 2: Hot-Film Sensor Analysis

The experimental set-up described in section 3.3 is employed to determine local and fluctuating heat transfer distributions for each of the impinging jet scenarios at the range of jet to surface heights and Reynolds numbers identified. As explained previously, the hot-film sensor is controlled using a constant temperature anemometer, CTA, to keep the temperature of the nickel film at a specific temperature above that of the surface it is attached to, also known as the overheat. To quantify the convective heat transfer measured by the hot-film sensor one must first understand the elements at work.

The sensor overheat is generated through the CTA by adjusting the decade resistance, thereby creating a specific potential difference across the nickel film. A LabView program is designed to operate this balancing sequence. The Wheatstone bridge on which the CTA operates, as illustrated in figure 3.16, is initially deactivated for a period of time until the system is known to be steady. The resistance across the sensor is measured and the bridge is activated to generate the required overheat. This resistance, R_{sensor} , is defined as the resistance of the entire probe arm of the bridge less the resistance of the cables and copper elements of the probe.

$$R_{sensor} = R_{probe} - R_{cables} \quad [\Omega] \quad (4.19)$$

The resistance of the sensor relates to a specific temperature which is evaluated using the following correlation.

$$R_{sensor} = 0.0277 \times T_S + 5.5962 \quad [\Omega] \quad (4.20)$$

This correlation between the resistance and temperature of the sensor was generated by insulating the sensor on the heated plate and measuring the resistance of the complete probe for a range of temperatures between 30 – 95°C. The results of this calibration are shown in figure 4.10. The resistance of the cables, R_{cables} , was then subtracted from the calibration equation generated to give the corresponding resistance of the sensor in accordance with equation 4.20. This calibration allows the temperature coefficient of resistance (TCR), designated the letter α [$1/K$], to be evaluated using the following expression, equation 4.21, where T_{ref} is the reference temperature [commonly 20°C]. The temperature coefficient of resistance for the hot-film sensor employed in this study was calculated to be approximately $0.0045 K^{-1}$.

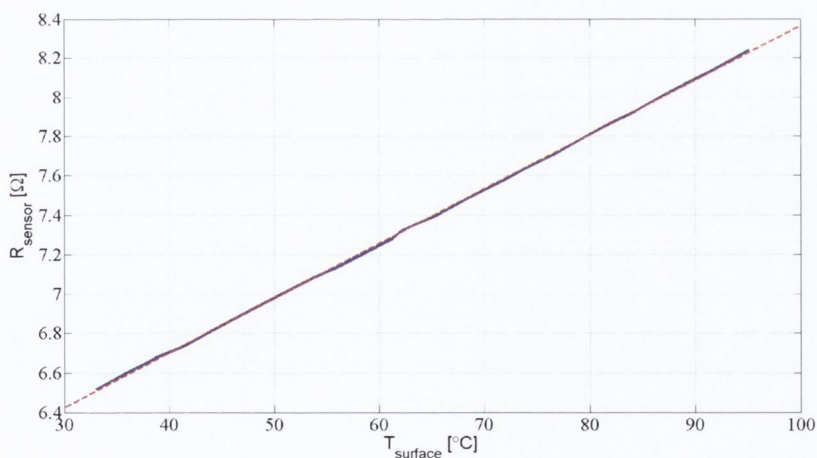


Figure 4.10: Calibration of hot-film sensor resistance versus temperature

$$R|_{T_S} = R|_{T_{ref}} (1 + \alpha (T_S - T_{ref})) \quad [\Omega] \quad (4.21)$$

From equation 4.21, the system converts the measured resistance of the sensor to its corresponding temperature, adds the desired overheat to this temperature and then converts it back to its equivalent resistance. The decade resistance, R_{decade} , is adjusted

4.2. CASE 2: HOT-FILM SENSOR ANALYSIS

by the CTA in order to balance the bridge with this new sensor resistance in mind. When the decade resistance is adjusted, the potential difference across the hot-film bridge heats up the nickel film to the desired overheat. This potential difference is recorded along with the resistance of the sensor.

The heat generated in the hot-film sensor is dissipated by way of forced convection from the impinging jet and conduction into the sensor substrate. Heat lost due to radiation is neglected due to the sensor's low emissivity of $\epsilon \approx 0.08$. Thus, equation 4.22 displays the energy balance of the hot-film sensor.

$$Q_{dissipated} = Q_{convection} + Q_{conduction} \quad [W] \quad (4.22)$$

The heat dissipated in the hot-film is calculated by evaluating the electrical power across the nickel film, as defined by equation 4.23, where V is the voltage across the bridge.

$$Q_{dissipated} = V^2 \cdot \frac{R_{sensor}}{(R_{probe} + R_1)^2} \quad [W] \quad (4.23)$$

The heat lost through conduction from the sensor element to the surrounding substrate is evaluated using the same theory as equation 4.23 but the voltage is measured under "no-flow" conditions such that the voltage recorded is designated V_o and is a function of temperature.

Equation 4.22 is rearranged so that the heat lost due to the forced convection to the impinging jet can be calculated from the heat dissipated and the heat lost due to conduction [19, 98, 99].

$$\begin{aligned} Q_{convection} &= Q_{dissipated} - Q_{conduction} \\ &= (V^2 - V_o^2) \cdot \frac{R_{sensor}}{(R_{probe} + R_1)^2} \quad [W] \end{aligned} \quad (4.24)$$

The convective heat flux of the impinging jet, $q''_{dissipated}$, is evaluated by dividing the convective heat lost due to the jet, $Q_{dissipated}$, by the surface area of the sensor's nickel element. As mentioned in section 3.3.1, the nickel element has geometric di-

mensions of 0.1016mm by 1.4478mm , or an area of $1.471 \times 10^{-7}\text{m}^2$. However, due to the heat conducted from the element to the substrate and the sensor's copper leads, the effective area of the element is much larger than the geometric area. The effective area, A_{eff} , is estimated by combining equations 4.2, 4.3 and 4.24 with a known heat transfer correlation for the stagnation point Nusselt number. The correlation initially used in this study was that of Shadlesky [44], equation 2.2, but due to the geometric and Reynolds number constraints of the correlation it was replaced with one that matched the exact experimental conditions of this study. To that end, a correlation was established using the stagnation point Nusselt number measurements evaluated in Case 1 through infrared thermography. More details about this correlation are included in section 5.1.1. This analysis results in an expression for the effective area of the hot-film sensor, equation 4.25.

$$A_{eff} = \frac{R_{sensor} (V^2 - V_o^2) D}{(R_{probe} + R_1)^2 (T_S - T_{jet}) k_{fluid} Nu_{correlation}} \quad [m^2] \quad (4.25)$$

where R_1 is the top resistance in the Wheatstone bridge with a value of 20Ω for this study, T_{jet} is the temperature of the jet [K] and k_{fluid} is the thermal conductivity of the fluid flow [W/mK]. $Nu_{correlation}$ is the stagnation point Nusselt number correlation generated in section 5.1.1. The effective area of the hot-film was calculated for an overheat of 5°C for a range of surface temperatures, to establish its range for typical test conditions. Figure 4.11 is scaled against the geometric area of the sensor to demonstrate the scale of the change in area as the temperature difference between the impingement surface and the impinging jet, ΔT , changes. It was found, for the sensor used, that the effective area of the sensor was about 3-5 times the size of the geometric area, within the range predicted by Beasley and Figliola [100], and was not independent of ΔT , in fact the effective area was found to decrease as ΔT increased.

4.2. CASE 2: HOT-FILM SENSOR ANALYSIS

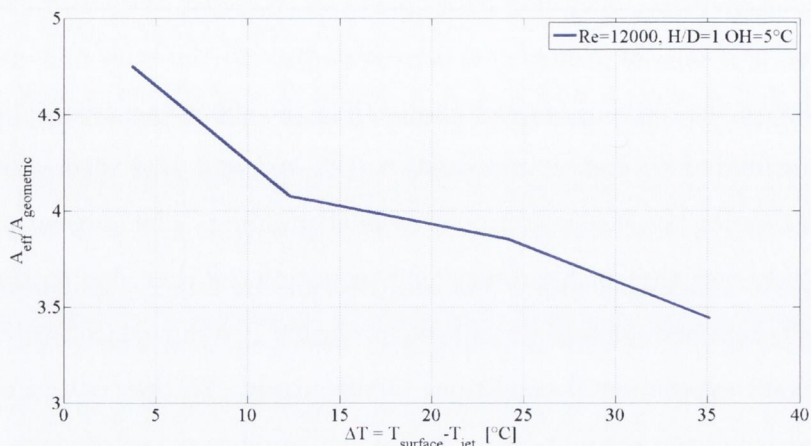


Figure 4.11: Effective area against geometric area of hot-film sensor with respect to the temperature difference between the impingement surface and the impinging jet

Taking the effective surface area into account, the heat flux from the sensor is expressed as:

$$q''_{\text{sensor}} = \frac{(V^2 - V_o^2)}{A_{\text{eff}}} \cdot \frac{R_{\text{sensor}}}{(R_{\text{probe}} + R_1)^2} \quad [\text{W}/\text{m}^2] \quad (4.26)$$

A very detailed study on the use of hot-film sensors for the purpose of measuring convective heat flux from a heated cylinder in cross-flow was completed by Scholten [101]. The same method as described by Scholten [101] is employed in this study. It was reported that when the same experiments were performed for different sensor overheats, the final results differed as the overheat of the sensor was changed. The reason for the difference in measurements was attributed to the shear stress of the flow over the sensor not being taken into account. The shear stress correction, as described by Scholten [101], begins with the representation of the heat flux from the sensor as one-dimensional conduction at the wall:

$$q''_{\text{conduction}} = -k \left. \frac{\partial T}{\partial y} \right|_0 \quad [\text{W}/\text{m}^2] \quad (4.27)$$

where y is the direction normal to the surface. An arbitrary location was then introduced close to the surface, designated y^+ , such that equation 4.27 becomes:

$$\begin{aligned}
 q''_{conduction} &= k \frac{T_{sensor} - T_{y^+}}{y^+} \\
 &= k \frac{T_{surface} + T_{overheat} - T_{y^+}}{y^+} \quad [W/m^2] \\
 &= k \frac{T_{surface} - T_{y^+}}{y^+} + k \frac{(T_{overheat} + T_{y^+,unheated}) - T_{y^+,unheated}}{y^+}
 \end{aligned} \tag{4.28}$$

where $T_{y^+,unheated}$ is the temperature at point y^+ when the surface is unheated. It followed from this that the second term on the right side of equation 4.28 represents the heat flux from the sensor when measuring shear stress, while the first term on the right side is the convective heat flux of the system when the sensor is held at the same temperature as the surface, or:

$$\begin{aligned}
 q''_{sensor} \Big|_{T_{sensor}=T_{surface}+T_{overheat}} &= q''_{convective} \Big|_{T_{sensor}=T_{surface}} \\
 &+ q''_{shear} \Big|_{T_{sensor}=T_{overheat}+T_{ambient}} \quad [W/m^2]
 \end{aligned} \tag{4.29}$$

The expression formulated in equation 4.26 for q''_{sensor} can then be substituted into equation 4.29. Equation 4.26 also represents the heat flux due to shear of the sensor when the impingement surface is unheated, q''_{shear} . This gives rise to equation 4.30 which calculates the true convective heat flux from the heated impingement surface, $q''_{convective}$.

$$\begin{aligned}
 q''_{convective} &= \frac{(V^2 - V_o^2)}{A_{eff}} \cdot \frac{R_{sensor}}{(R_{probe} + R_1)^2} \Big|_{heated} \\
 &- \frac{(V^2 - V_o^2)}{A_{eff}} \cdot \frac{R_{sensor}}{(R_{probe} + R_1)^2} \Big|_{adiabatic} \quad [W/m^2]
 \end{aligned} \tag{4.30}$$

This term, $q''_{convective}$, represents the true convective heat flux from the heated surface when the disrupting effects of film overheat have been removed. This is the parameter that is of interest in this study and it is used, in conjunction with equations 4.2 and 4.3, to determine the Nusselt number distribution.

4.2.1 Fluctuating Heat Transfer Analysis

Measurement of the fluctuating convective heat transfer at a surface is helpful for improving the understanding of the convective heat transfer mechanisms occurring. In the case of impinging jets, increased fluctuating heat transfer at the surface may point to increased local turbulence in the wall jet or to vortex impact on the impingement surface. The theory regarding the fluctuating heat transfer on the impingement surface is derived from the expression describing the heat flux from the hot-film sensor, equation 4.26. Thus, a change in heat flux from the surface is reflected in a change in the voltage recorded from the sensor. Assuming that this change is small, equation 4.31 holds true:

$$\frac{\delta q''_{sensor}}{\delta V} = \frac{q''^*}{V^*} = 2V \cdot \frac{R_{sensor}}{A_{eff} (R_{probe} + R_1)^2} \quad (4.31)$$

By multiplying above and below by $(V^2 - V_o^2)$ on the right-hand side of equation 4.31, the expression becomes:

$$\frac{q''^*}{V^*} = \frac{2V}{(V^2 - V_o^2)} \cdot \frac{(V^2 - V_o^2) R_{sensor}}{A_{eff} (R_{probe} + R_1)^2} \quad (4.32)$$

The second part of the term on the right-hand side of equation 4.32 is the expression for the heat flux from the hot-film sensor, as seen in equation 4.26, therefore:

$$\frac{q''^*}{V^*} = \frac{2V}{(V^2 - V_o^2)} \cdot q''_{sensor} \quad (4.33)$$

An expression for the fluctuating heat flux, q''^* , may then be obtained by localising it on the left side of the equation.

$$q''^* = 2 \cdot q''_{sensor} \frac{V}{(V^2 - V_o^2)} \cdot V^* \quad [W/m^2] \quad (4.34)$$

where V^* is the standard deviation from the mean voltage signal recorded by the hot-film sensor.

By applying Newton's law of cooling, equation 4.3, in conjunction with the definition of the Nusselt number, equation 4.2, the fluctuating Nusselt number, Nu^* , is

calculated. Equation 4.35 demonstrates this calculation.

$$Nu^* = \frac{q''^* D}{k_f (T_S - T_{jet})} \quad (4.35)$$

This value is plotted against the radial distance from the stagnation point, r/D , to compare with the time averaged Nusselt number trends in chapter 5.

4.3 Uncertainty Analysis

An uncertainty analysis was performed on both systems to define the accuracy of each of the measurement methods with a 95% confidence level. The uncertainties of each of the variables in the case studies are estimated using the Taylor Series Method (TSM) as outlined by Coleman and Steele [102].

The standard uncertainty, u , of a system, r , is a combination of systematic error, b , and random error, s , as defined in its simplest form by equation 4.36.

$$u_r^2 = b_r^2 + s_r^2 \quad (4.36)$$

In the case of a system, r , which is a function of different variables, $f(x,y)$, the uncertainty of the system is expanded from equation 4.36 to become:

$$u_r^2 = \left(\frac{\delta r}{\delta x}\right)^2 b_x^2 + \left(\frac{\delta r}{\delta y}\right)^2 b_y^2 + \left(\frac{\delta r}{\delta x}\right)^2 s_x^2 + \left(\frac{\delta r}{\delta y}\right)^2 s_y^2 \quad (4.37)$$

For the case of a system which is a result of several variables a more general solution of equation 4.37 is given by equation 4.38.

$$u_r^2 = \sum_{i=1}^J \left(\frac{\delta r}{\delta X_i}\right)^2 b_{X_i}^2 + \sum_{i=1}^J \left(\frac{\delta r}{\delta X_i}\right)^2 s_{X_i}^2 \quad (4.38)$$

where $r = f(X_1, X_2, X_3, \dots, X_J)$

For a large-sample approximation, the expanded uncertainty of a result at a given confidence level is expressed by equation 4.39, where $t_{\%}$ is the t distribution value based on the confidence level and degree of freedom.

$$U_r = t_{\%} u_r \quad (4.39)$$

Combining equations 4.36 and 4.39, the expanded uncertainty becomes:

$$U_r = t_{\%} (b_r^2 + s_r^2)^{\frac{1}{2}} \quad (4.40)$$

For a 95% confidence level it was concluded that $t=2$ by Coleman and Steele [102]. Therefore, this value can be substituted into equation 4.40 for the expanded uncer-

tainty of the system. The combination of equations 4.36, 4.38 and 4.40 then gives the large-sample expanded uncertainty at a 95% confidence level, shown in equation 4.41.

$$U_{95} = 2 \left[\sum_{i=1}^J \left(\frac{\delta r}{\delta X_i} \right)^2 b_{X_i}^2 + \sum_{i=1}^J \left(\frac{\delta r}{\delta X_i} \right)^2 s_{X_i}^2 \right]^{\frac{1}{2}} \quad (4.41)$$

If it is assumed that all of the systematic and random errors are independent, equation 4.41 can be simplified as:

$$U_{95} = \left[\sum_{i=1}^J \left(\frac{\delta r}{\delta X_i} \right)^2 2^2 u_i^2 \right]^{\frac{1}{2}} \quad (4.42)$$

or

$$U_{95} = \left[\sum_{i=1}^J \left(\frac{\delta r}{\delta X_i} \right)^2 U_i^2 \right]^{\frac{1}{2}} \quad (4.43)$$

where U_i is the 95% uncertainty of each variable X_i in the system. Equation 4.43 is known as the general uncertainty analysis.

Considering the random error of a series of N data pairs (X_i, Y_i) are fitted with a straight line curve, the 95% uncertainty is defined by Montgomery and Peck [103] as:

$$U = t \left\{ s_Y^2 \left[\frac{1}{N} + \frac{(X - \bar{X})^2}{s_{XX}} \right] \right\}^{\frac{1}{2}} \quad (4.44)$$

where \bar{X} is the mean of the N values of X , calculated by equation 4.45, and s_{XX} is defined by equation 4.46.

$$\bar{X} = \frac{1}{N} \sum_{i=1}^N X_i \quad (4.45)$$

$$s_{XX} = \sum_{i=1}^N X_i^2 - \frac{\left(\sum_{i=1}^N X_i \right)^2}{N} \quad (4.46)$$

s_Y , for the set of data (X_i, Y_i) fitted with the straight line curve $y = mx + c$, is evaluated using equation 4.47.

$$s_Y = \left[\frac{\sum_{i=1}^N (Y_i - mX_i - c)^2}{N - 2} \right]^{\frac{1}{2}} \quad (4.47)$$

This analysis provides a detailed estimation of the uncertainties of the parameters described in sections 4.1 and 4.2.

4.3.1 Uncertainty for Case 1

In Case 1, the measurement method of infrared thermography is employed to measure the temperature of an ohmically heated surface cooled by an impinging jet. Due to the temperature gradient across the impingement surface, as previously mentioned, the uncertainty of each of the outlined parameters is not uniform across the surface. To demonstrate this, figure 4.12 displays the percentage uncertainty in the calculations of the natural convection heat flux from the lower face of the foil, the radiation heat flux from both upper and lower faces of the foil, the resulting impinging jet heat flux, the heat transfer coefficient and the Nusselt number for a conventional impinging jet at $H/D=1$ and a Reynolds number of 12,000 from the stagnation point, $r/D=0$, outwards.

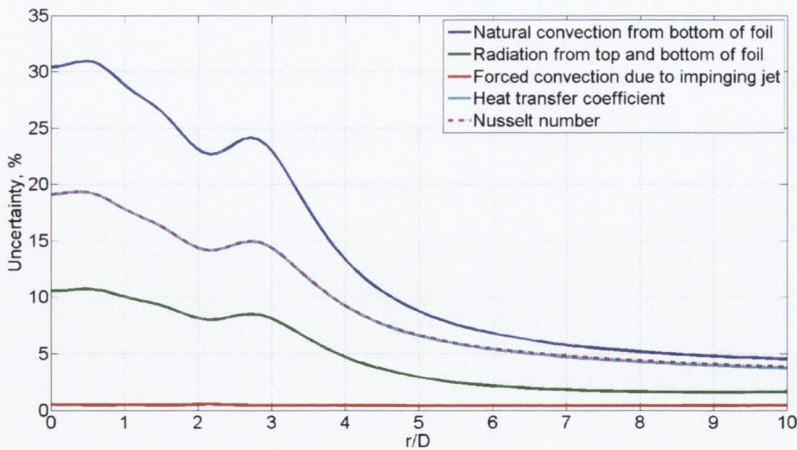


Figure 4.12: Comparison of the uncertainties associated with the calculation of the natural convection heat flux, radiation heat flux, impinging jet heat flux, heat transfer coefficient and Nusselt number for a conventional impinging jet at $H/D=1$ and Reynolds number of 12,000 for $0 < r/D < 10$

Aside from the case of the impinging jet heat flux, it is noted that the highest levels of uncertainty lies in the stagnation region. This is primarily due to the low temperature difference which resides in this area. The less substantial uncertainty for the impinging jet heat flux in the stagnation region is a result of the magnitude difference between each of the parameters, as shown in figure 4.5. Due to the variation in the uncertainty across the surface, the average of each of the parameters evaluated in this case study is displayed in table 4.1.

Table 4.1: Case 1: Uncertainty levels for 95% confidence

<i>Parameter</i>	<i>Uncertainty</i>
Re	2.5%
$q''_{generated}$	1.5%
$q''_{convection,lower,natural}$	7.35%
$q''_{radiation}$	2.69%
$q''_{conduction,lateral}$	0.23%
$q''_{convection,upper,forced}$	0.55%
h	5.2%
Nu	5.3%

4.3.2 Uncertainty for Case 2

A similar analysis was performed for Case 2 with the hot-film sensor technique. The calibration of the resistance of the sensor to the temperature of the surface is used to evaluate the uncertainty of this method using equation 4.44. Thus, since the uncertainty varies with the temperature of the surface, the corresponding heat flux distribution, heat transfer coefficient and Nusselt number uncertainties are not constant across the impingement surface. The uncertainty of the effective area calculation of the hot-film sensor, A_{eff} , is seen to be dependant on the temperature difference between the heated surface and the impinging jet flow, as shown in figure 4.13. As the temperature difference approaches zero, the uncertainty increases.

4.3. UNCERTAINTY ANALYSIS

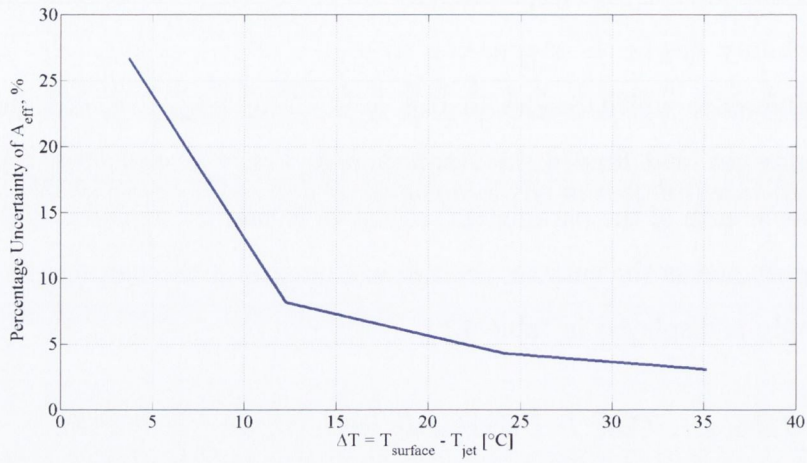


Figure 4.13: Variation of effective area uncertainty as temperature difference between the heated surface and the impinging jet increases

The uncertainty for this method is increased due to the inclusion of the adiabatic correction shown in equation 4.30. The fluctuating Nusselt number, Nu^* , was noted to have the highest level of uncertainty. As with the uncertainty evaluation for Case 1, the average uncertainty of the main characteristics calculated are presented in table 4.2.

Table 4.2: Case 2: Uncertainty levels for 95% confidence

<i>Parameter</i>	<i>Uncertainty</i>
$q''_{convective}$	19.8%
h	20%
Nu	20.1%
Nu^*	46%

Chapter 5

Heat Transfer Results & Discussion

To determine the convective heat transfer characteristics of the conventional impinging jet and the four swirling impinging jets, the corresponding local Nusselt number, Nu , was evaluated for nozzle to surface heights ranging from $0.5 < H/D < 10$ and Reynolds numbers between $8,000 < Re < 20,000$ over a radial distance of $0 < r/D < 10$.

The flow rate, and equivalent Reynolds number, set for the conventional impinging jet is used in the cases of the swirling impinging jets. This determines how the swirling impinging jets perform compared to the scenario with no swirl generator included in the jet assembly. The main findings from Case 1 using the infrared thermography measurement technique are presented and discussed in section 5.1, while section 5.2 looks at the local heat transfer results acquired using the hot-film sensor measurement technique in Case 2. To elucidate these regions of interest and to explain some features in the local heat transfer distributions, fluctuations in heat transfer are described in section 5.3. These provide an insight into the main regions of mixing and turbulence in the flow which may lead to enhanced and/or diminished effects in the time-averaged heat transfer.

Due to the extensive range of test parameters, not all results are presented here. Thus, this chapter focuses on the key characteristics and findings noted through this investigation and additional results are included in appendix A.

5.1 Case 1: Infrared Thermography

When the convective cooling from the conventional impinging jet is examined using infrared thermography, the results are expressed in terms of the local Nusselt number as defined in section 4.1. The experimental approach of infrared thermography provides the advantage of allowing an area of the impingement surface to be viewed, as opposed to point measurement methods. The analysis discussed in section 4.1 converts the temperature maps recorded by the thermal imaging camera, examples of which are shown in figure 3.12, into images which display the heat flux due to each of the heat loss effects, i.e. from natural convection, radiation and lateral conduction, and the resultant heat transfer due to the impinging jet.

A series of examples of the results detailing the heat loss terms and convective heat flux for a conventional impinging jet with $Re=12,000$ and $H/D=1$ are included in section 4.1. For comparative purposes, the Nusselt number distribution shown in figure 4.8 is averaged radially according to the layout shown in figure 4.9 and plotted against the non-dimensional radial distance from the stagnation point, r/D , from $0 < r/D < 10$, to generate figures such as that shown in figure 5.1.

5.1.1 Conventional Impinging Jet - Heat Transfer

Figure 5.1 demonstrates the change in heat transfer which occurs as the Reynolds number is increased from 8,000 to 20,000 when the conventional jet nozzle is positioned at a height of $H/D=1$. The stagnation point, $r/D=0$, is the location of a local minimum which increases in magnitude as the Reynolds number is increased. The increase in the stagnation point Nusselt number, Nu_{stag} , can be related back to the theoretical correlations discussed in section 2.4 which generally report that the stagnation point Nusselt number varies with an exponent of the Reynolds number of the jet flow.

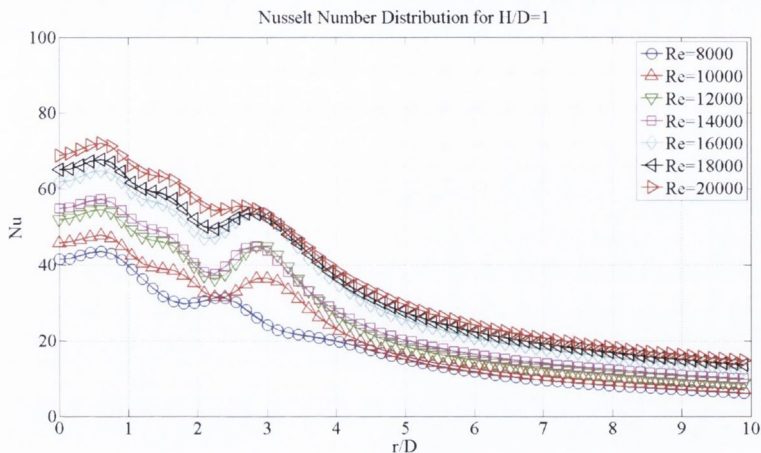


Figure 5.1: Nusselt number distribution for the conventional impinging jet at $H/D = 1$ for all Reynolds numbers using infrared thermography in Case 1

The initial local minimum and the point of maximum heat transfer being located at $r/D \approx 0.6$ are characteristic features for $H/D \leq 4$ [3, 16, 31]. This location of the maximum heat transfer changes as the nozzle to surface spacing increases. When $H/D \geq 6$, the point of maximum heat transfer is located at the stagnation point, $r/D=0$, as demonstrated in figure 5.2, and is consistent with what was described by Incropera and DeWitt [9]. For low nozzle to surface distances, typically $H/D \leq 2$, the Nusselt number distribution generally experiences three peaks in total; a local maximum at $r/D \approx 0.6$, a secondary peak located between $1.6 < r/D < 2.5$ and a tertiary peak located between $2.8 < r/D < 3.2$ depending on the Reynolds number. While the existence of the secondary peak in the Nusselt number distribution is common across the range of Reynolds numbers tested, the tertiary peak is not produced at Reynolds numbers less than 10,000 for $H/D < 2$. The local stagnation point Nusselt numbers for each of the Reynolds numbers examined are comparable to the correlation by Shadlesky [44] for a height of $H/D \leq 2$, despite the Reynolds number range lying outside that of the correlation.

As H/D increases above 6, the Nusselt number becomes bell-curve shaped with no additional peaks beyond the stagnation point. This can be seen in figure 5.2 and compares well with the distribution reported by Incropera and DeWitt [9] in figure 2.4.

The variation in the stagnation point Nusselt number, Nu_{stag} , with H/D is fully illustrated in figure 5.3. This figure shows the change in Nu_{stag} as both the Reynolds

5.1. CASE 1: INFRARED THERMOGRAPHY

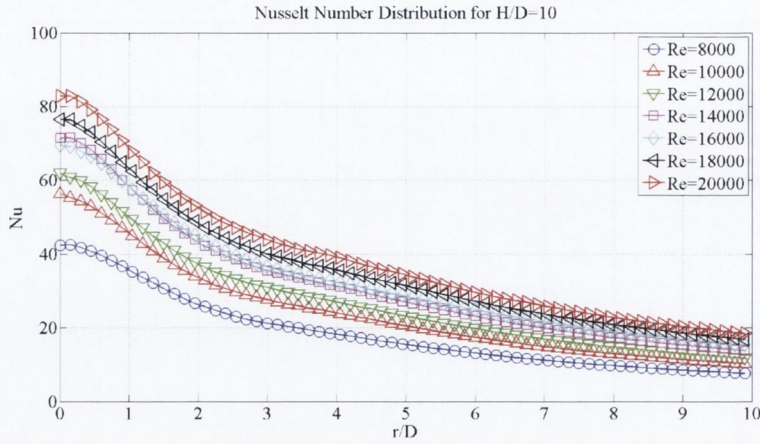


Figure 5.2: Nusselt number distribution for the conventional impinging jet at $H/D = 10$ for all Reynolds numbers using infrared thermography in Case 1

number and the nozzle to surface heights are varied. It is apparent from this figure that the stagnation point Nusselt number, Nu_{stag} , reaches a maximum value when the impinging jet is approximately $6-8D$ from the surface. This value corresponds to the values noted in past studies [6, 14, 15] and has been linked to the end of the potential core of the jet. The area following the potential core is defined by the complete interference of the surrounding vortical structures, described in section 2.2.1. In this region, the Kelvin-Helmholtz induced vortices breakdown and form a turbulent flow. This transition results in the kinetic energy of the jet being dispersed, causing the jet to have a diminished influence at the stagnation point.

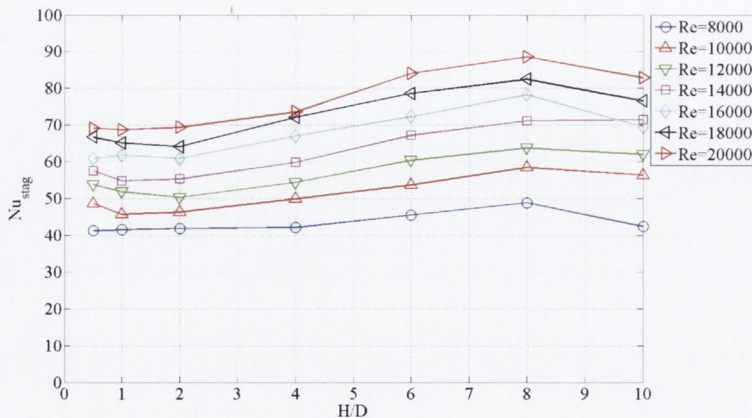


Figure 5.3: Stagnation point Nusselt number for the conventional impinging jet at each H/D and Reynolds number using infrared thermography in Case 1

These results also allow a correlation to be formed for the stagnation point Nusselt number as a function of Reynolds number and nozzle to surface height. Due to the experimental parameters investigated, this correlation has a Reynolds number and nozzle height range more expansive than previously produced for a jet nozzle of this geometry. From figure 5.3 it can be noted that the distributions are not linear, thus the correlation includes a polynomial in H/D . Equation 5.1 describes the best fit for the results presented in figure 5.3 and has a maximum deviation of 8% from the original experimental results.

$$Nu_{stag} = Re^{0.64} \cdot f(H/D) \quad \begin{cases} 0.5 < H/D < 10 \\ 8,000 < Re < 20,000 \end{cases} \quad (5.1)$$

where $f(H/D) = H/D^{0.1} [-0.0003 \cdot H/D^3 + 0.0048 \cdot H/D^2 - 0.0206 \cdot H/D + 0.142]$

In most applications a specific area is to be cooled instead of a single point. To that end, the mean Nusselt number for each of the conditions investigated is evaluated for a radial distance of $0 \leq r/D \leq 5.0$, the result of which is displayed in figure 5.4.

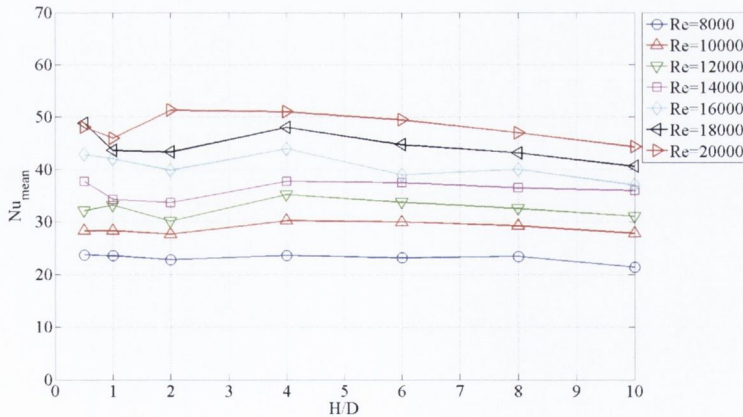


Figure 5.4: Mean Nusselt number for the conventional impinging jet averaged over a distance of $0 < r/D < 5.0$ at each H/D and Reynolds number using infrared thermography in Case 1

From figure 5.4, it is apparent that the changes in the mean Nusselt number, Nu_{mean} , as the height of the nozzle is increased for low Reynolds numbers are very

small. The mean Nusselt number generally reaches a maximum at approximately $H/D=4$ after which it begins to decrease slowly. The small decrease may be associated with the reduction in secondary and tertiary peaks shown in the Nusselt number distributions illustrated in figure 5.1 and contained in appendix A.1.1.

The reduction in these peaks is attributed to the distance between the nozzle and the impingement surface increasing, therefore allowing the jet flow to develop and the intensity of the impinging vortical structures and turbulence levels to be diminished. This change in flow characteristic with nozzle to surface height in the wall jet region will be revisited in chapter 6.

5.1.2 Swirling Impinging Jets - Heat Transfer

An illustration of the temperature field of the ohmically heated foil under the influence of each of the four swirling impinging jets measured using infrared thermography as described in section 3.2, is given in figure 5.5 . These images demonstrate the radial uniformity of each of the swirling impinging jets as they strike the heated surface with a Reynolds number of 14,000 and at a nozzle height of $H/D=2$.

Figure 5.6 shows the heat transfer results produced by each of the swirling impinging jets at a height of $H/D=1$ for each of the Reynolds numbers explored while figure 5.7 illustrates the change in the local heat transfer for each of the swirling impinging jets when the nozzle height is increased to $H/D=8$ for the same range of Reynolds numbers.

Figures 5.6a and c, representing the large and small generators including the swirl core, L_c and S_c , demonstrate local minima in the Nusselt number at $r/D=0$ for each of the Reynolds numbers. This local minimum was found to continue up to a height of $H/D=4$, in some cases extending to $H/D=6$, after which, reflecting that of a conventional impinging jet, a local maximum occurs, as shown in figure 5.7. For the other two cases, figures 5.6b and d representing the large and small generators without the swirl core, L_{no} and S_{no} , the local minimum remains and is significantly sharper for the lower Reynolds number values.

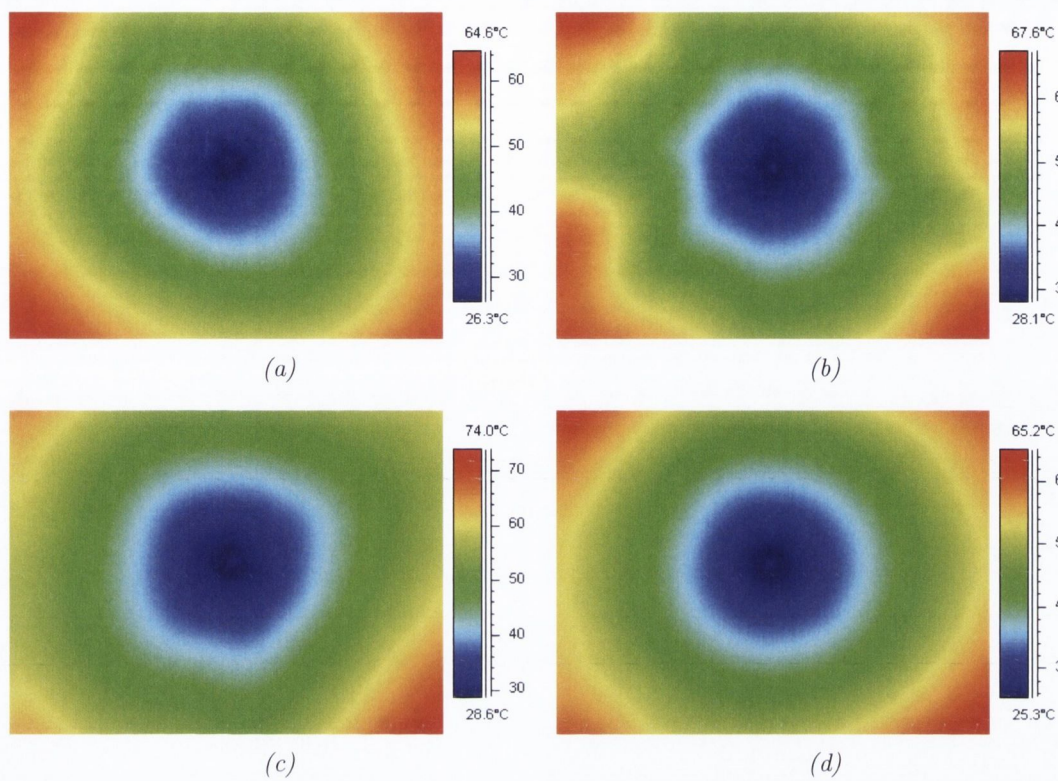


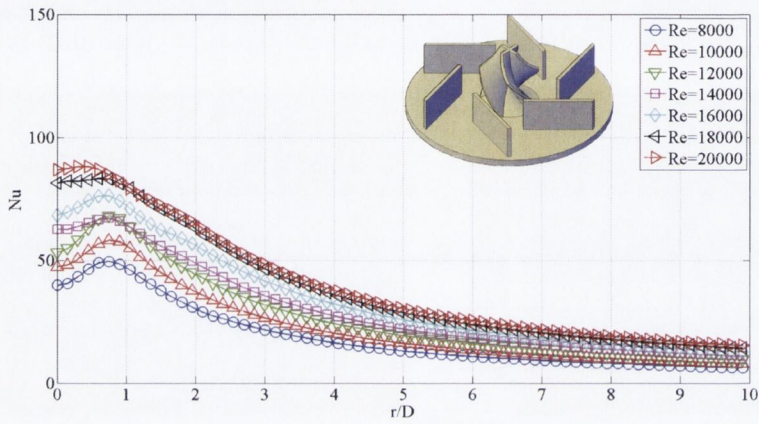
Figure 5.5: Instantaneous temperature distributions for swirling impinging jets employing generators (a) “ L_c ” (Large with swirl core), (b) “ L_{no} ” (Large without swirl core), (c) “ S_c ” (Small with swirl core) and (d) “ S_{no} ” (Small without swirl core) at $H/D = 2$ and a Reynolds number of 14,000

The swirling impinging jets generally exhibit local maxima at $r/D \approx 0.75$ followed by a decrease in heat transfer magnitude with increasing radius. In some cases, slight secondary peaks appear but this is primarily at high Reynolds numbers and when the jet nozzle is in close proximity to the impingement surface, as in figure 5.6b for swirl generator L_{no} at a Reynolds number of 20,000.

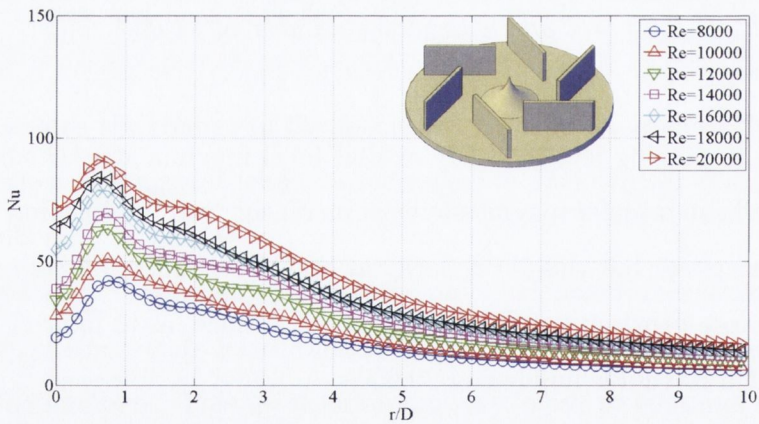
This radial distribution suggests that the swirl generator design causes the motion of the fluid flow to be concentrated principally away from the axis of the jet, similar to what was reported by Maciel *et al.* [85]. Thus, as the flow impinges on the heated surface the maximum heat transfer is located away from $r/D=0$. While a local minimum at $r/D=0$ is also a feature of a conventional impinging jet, as seen in figure 5.1, the relatively stronger reduction in heat transfer magnitude from the swirling impinging jets can be linked to the azimuthal velocity component of the flow. It is also suggested

5.1. CASE 1: INFRARED THERMOGRAPHY

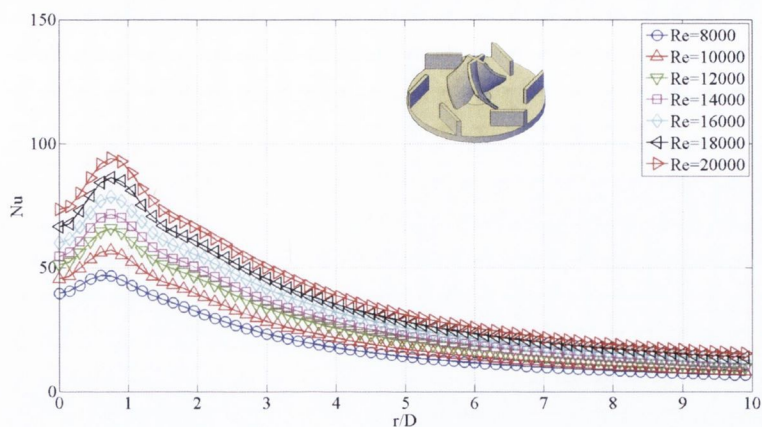
that recirculation of warm fluid towards the stagnation point by the swirl generators without the swirl core, L_{no} and S_{no} , promotes a larger decrease in the local heat transfer at $r/D=0$ than the generators with the swirl core, L_c and S_c . To elaborate on this point further, flow field visualisation of each of the swirling impinging jets is discussed in chapter 6.



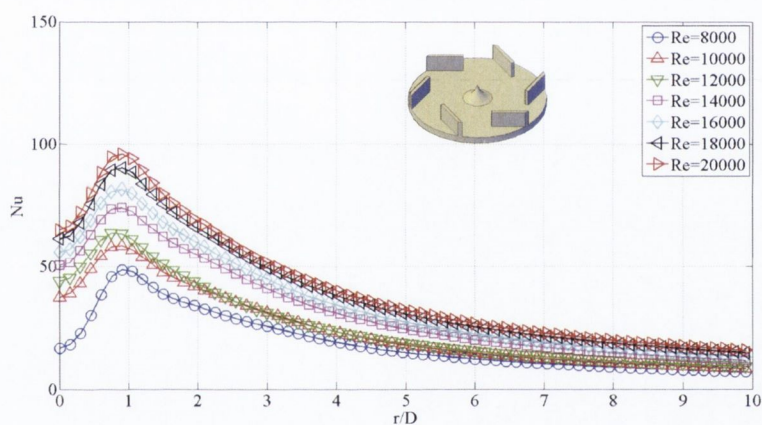
(a)



(b)



(c)



(d)

Figure 5.6: Nusselt number distribution for swirling impinging jets employing generators (a) “ L_c ” (Large with swirl core), (b) “ L_{no} ” (Large without swirl core), (c) “ S_c ” (Small with swirl core) and (d) “ S_{no} ” (Small without swirl core) at $H/D = 1$ for all Reynolds numbers

When the conventional impinging jet was examined, the stagnation point Nusselt number, Nu_{stag} , was shown in figure 5.3 to increase with H/D , for $H/D \leq 8$. As figure 5.8 illustrates, the near opposite occurs for the swirl modified flow. Thus, the generators without the swirl core, L_{no} and S_{no} , shown in figures 5.8b and 5.8d respectively, follow similar trends, having a high magnitude at $H/D=0.5$ followed by a significant decrease; the Nusselt number then increases to a maximum at $H/D \approx 6$ and subsequently decreases as the height increases further.

5.1. CASE 1: INFRARED THERMOGRAPHY

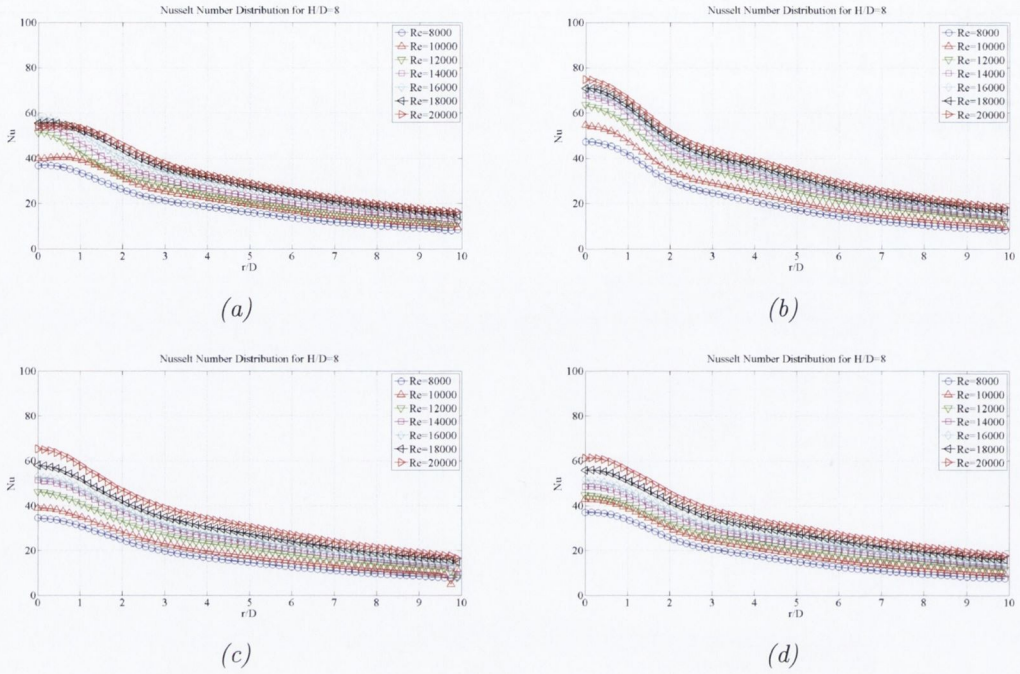


Figure 5.7: Nusselt number distribution for swirling impinging jets employing generators (a) “ L_c ” (Large with swirl core), (b) “ L_{no} ” (Large without swirl core), (c) “ S_c ” (Small with swirl core) and (d) “ S_{no} ” (Small without swirl core) at $H/D = 8$ for all Reynolds numbers

The generators including the swirl core, L_c and S_c , shown in figures 5.8a and 5.8c respectively, also show broadly similar trends, generally having the point of maximum heat transfer at $r/D=0$ when the impinging jet is within close proximity to the surface. As this distance is increased, the Nusselt number at $r/D=0$ tends to decrease, although the trend is less consistent for the large swirl core configuration (figure 5.8a).

5.1. CASE 1: INFRARED THERMOGRAPHY

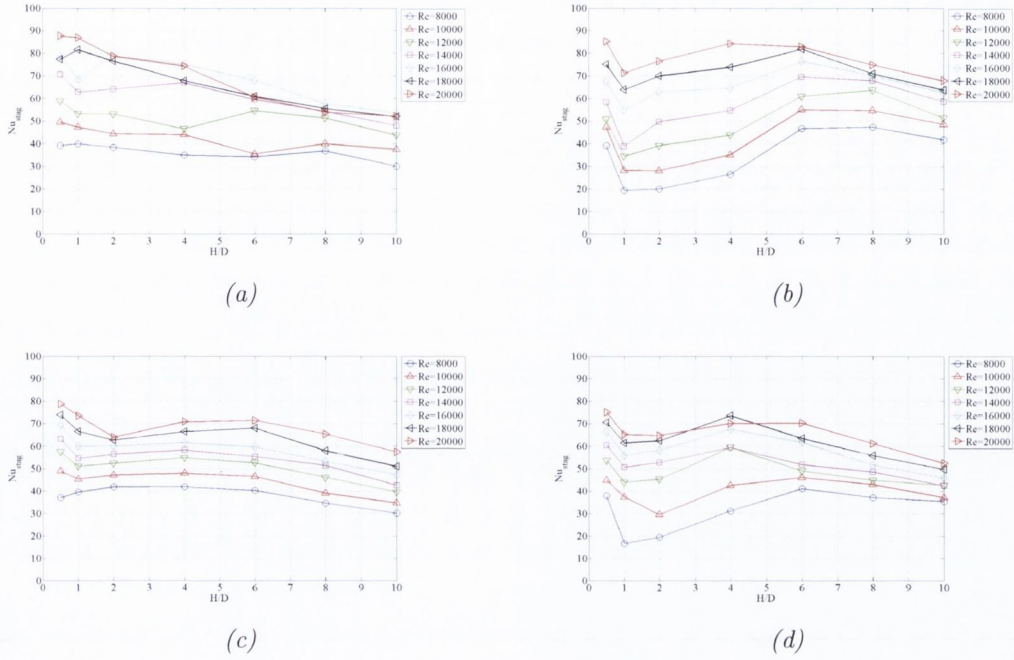


Figure 5.8: Nusselt number at $r/D=0$ for swirling impinging jets employing generators (a) “ L_c ” (Large with swirl core), (b) “ L_{no} ” (Large without swirl core), (c) “ S_c ” (Small with swirl core) and (d) “ S_{no} ” (Small without swirl core) at each H/D and Reynolds number

The mean Nusselt number, Nu_{mean} , for each swirling impinging jet is evaluated in a similar manner to the conventional impinging jet, seen previously. The plots in figure 5.9 display the corresponding mean Nusselt number for each of the swirling impinging jets examined. A common trend is noted for each of the swirling jets: at low nozzle to surface heights, $0.5 \leq H/D \leq 2$, the mean Nusselt number has a maximum value. As the height is increased, Nu_{mean} decreases at a higher rate than for the conventional impinging jet, although the fall off is still quite modest.

This outcome is expected from swirling impinging jets. As reported in section 2.4.5, the spread of a swirling jet increases as the distance from the jet nozzle increases, up to the point when the jet’s cooling impact on a heated surface is small, as seen in figure 5.7 for a nozzle to surface height of $8D$. This trend is clear also from the Nusselt number distributions for each of the swirling impinging jets at higher H/D shown in appendices A.1.2 - A.1.5.

5.1. CASE 1: INFRARED THERMOGRAPHY

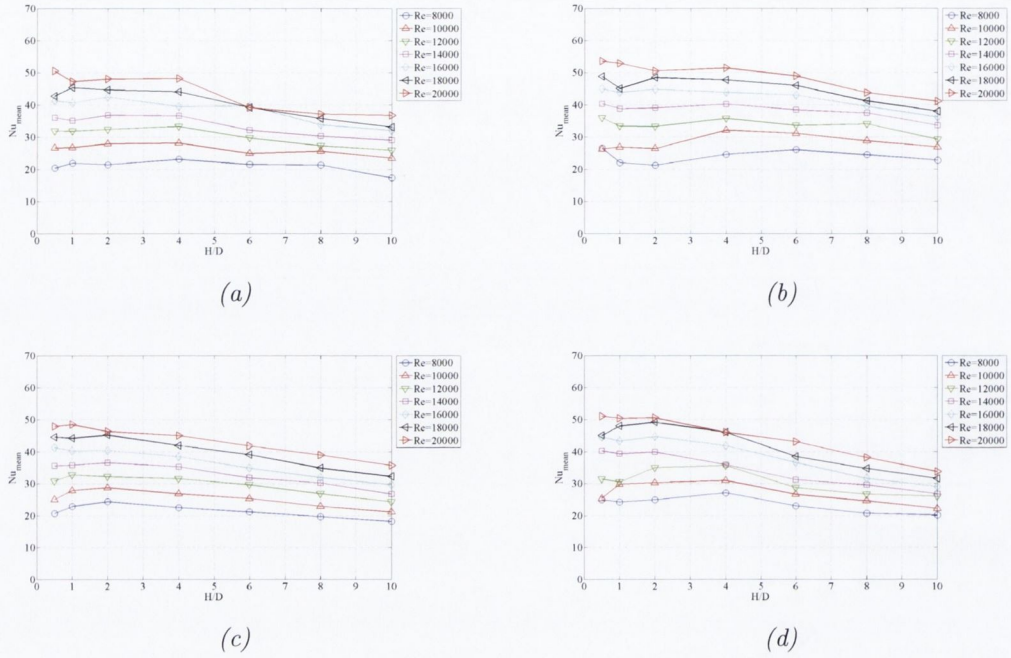


Figure 5.9: Mean Nusselt number for swirling impinging jets employing generators (a) “ L_c ” (Large with swirl core), (b) “ L_{no} ” (Large without swirl core), (c) “ S_c ” (Small with swirl core) and (d) “ S_{no} ” (Small without swirl core) averaged over a distance of $0 < r/D < 5.0$ at each H/D and Reynolds number

5.1.3 Case 1 : Comparison of Conventional and Swirling Impinging Jets

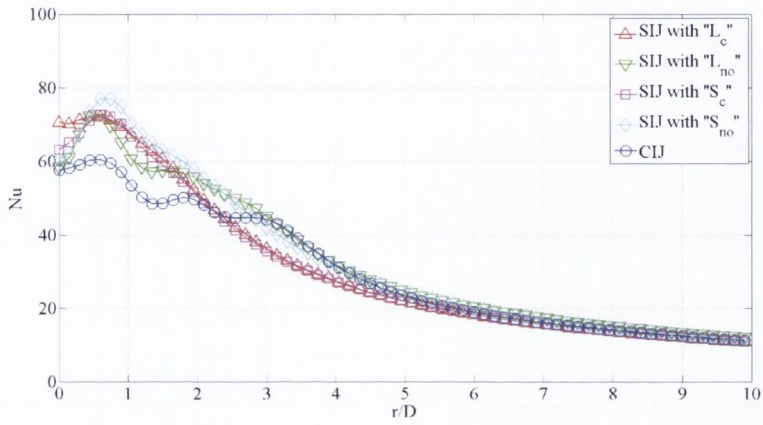
Figure 5.10 compares the performance for each of the five impinging jet configurations investigated, a conventional contoured jet and four swirling impinging jets; the Nusselt number distribution is plotted for a Reynolds number of 14,000 at three different nozzle to surface spacings, $H/D = 0.5, 4$ and 10 . These results are chosen specifically to illustrate the heat transfer enhancement effect of a swirling impinging jet compared to a conventional impinging jet, when operated under the same conditions as the nozzle height is increased.

It is clear from these graphs that each of the swirling impinging jets has a positive enhancement effect on the heat transfer at low nozzle to surface heights; this can be seen in figure 5.10a. As the height is increased to $4D$, figure 5.10b, all of the impinging jets appear to produce rather similar Nusselt numbers, while at $10D$ the swirling impinging jets lead to a significant reduction in heat transfer, as shown in

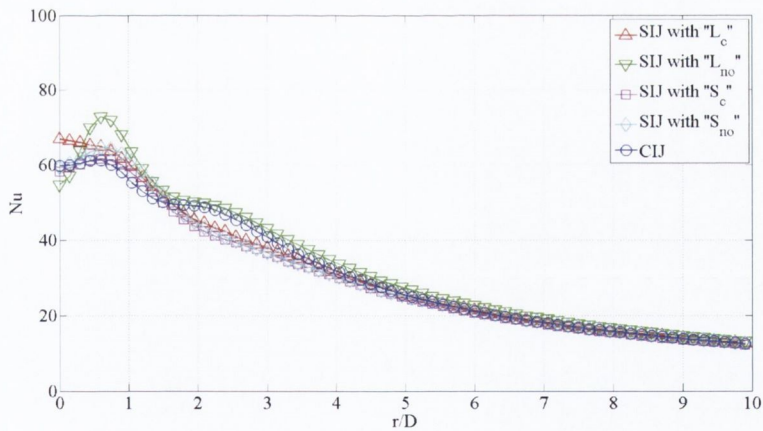
5.1. CASE 1: INFRARED THERMOGRAPHY

figure 5.10c. This result is consistent across the range of test conditions examined.

Although only one Reynolds number is shown here, the heat transfer enhancement due to the induced swirling flow has been noted to increase as the Reynolds number is increased and the height of the jet nozzle above the impingement surface is decreased.

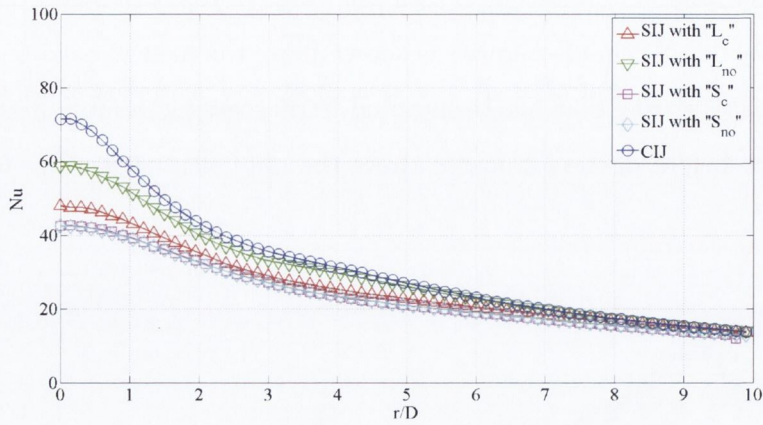


(a)



(b)

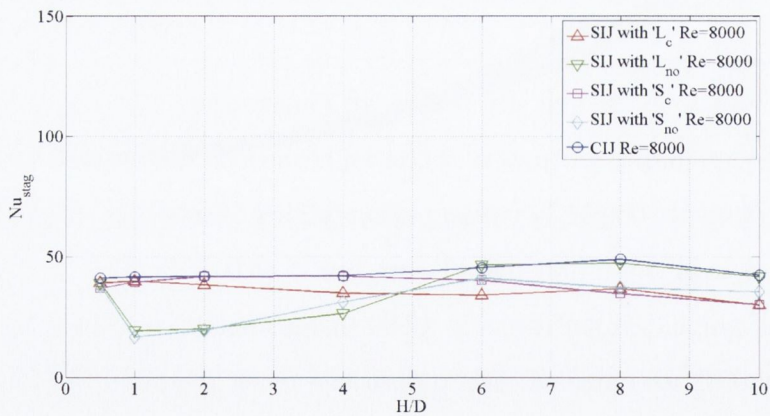
5.1. CASE 1: INFRARED THERMOGRAPHY



(c)

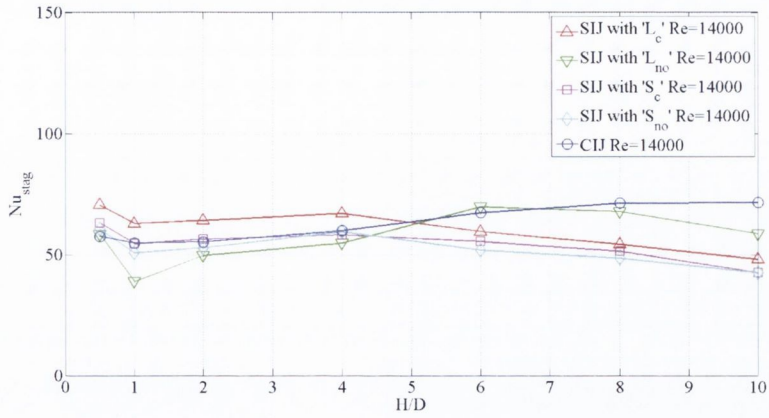
Figure 5.10: Nusselt number distribution for each of the conventional and swirling impinging jets examined with a Reynolds number of 14,000 at H/D of (a) 0.5, (b) 4 and (c) 10

In order to illustrate further the improvement in heat transfer performance with swirl at low heights and high Reynolds numbers, figures 5.11 and 5.12 show Nusselt number at $r/D=0$ and mean Nusselt number respectively at each nozzle height for a selection of the Reynolds numbers tested.

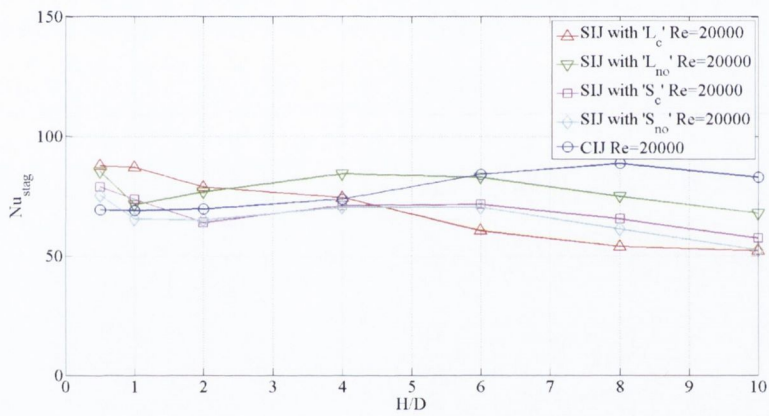


(a)

5.1. CASE 1: INFRARED THERMOGRAPHY



(b)



(c)

Figure 5.11: Stagnation point Nusselt number, Nu_{stag} for each of the conventional and swirling impinging jets examined at each H/D with a Reynolds number of (a) 8,000, (b) 14,000 and (c) 20,000

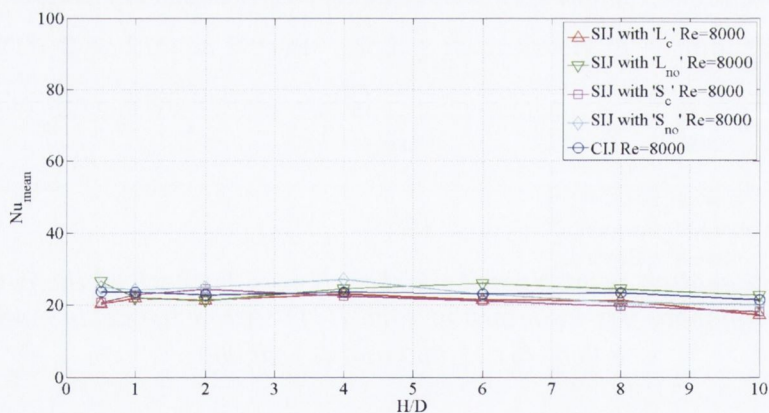
It may be recalled that the Nusselt number distributions for the swirling impinging jets contained a local minimum at $r/D=0$ followed by a local maximum at approximately $r/D \approx 0.75$ for nozzle heights below $4-6D$ (figure 5.6). Figure 5.11a displays Nusselt number at $r/D=0$ for each of the jets for a Reynolds number of 8,000. It is noted that the two swirling jets with the swirl core, L_c and S_c , have similar magnitudes of Nu_{stag} to the conventional jet, while the other two swirling jets have significantly lower values; this holds true for $H/D < 6$. When the mean Nusselt numbers of the five configurations are compared in figure 5.12a for the same Reynolds number of 8,000,

5.1. CASE 1: INFRARED THERMOGRAPHY

it is found that the results are remarkably similar for each nozzle height. Despite the notably lower values of Nu_{stag} for the swirling jets L_{no} and S_{no} , the mean heat transfer stays up at a comparable level to the other scenarios, demonstrating the high levels of heat transfer around $r/D=0$.

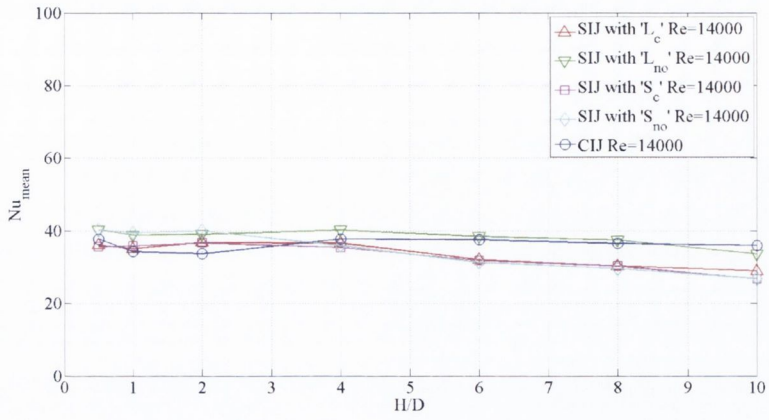
As the Reynolds number is increased for each of the jets, the stagnation point and mean Nusselt numbers increase respectively but only show increased heat transfer compared to the conventional impinging jet for the lower nozzle heights examined.

The drops in both Nu_{stag} and Nu_{mean} at high nozzle to surface distances is indicative of the spread of the swirling impinging jets, as discussed in previous studies [58,69]. This would lead to less effective heat dissipation by the impinging jets at the stagnation point and supports the idea of recirculation of warm fluid towards the axis of the jet. In the next chapter, the flow field for the different jet configurations will be explored, with a view to providing further insight into the convective heat transfer characteristics of the conventional and swirling impinging jets.

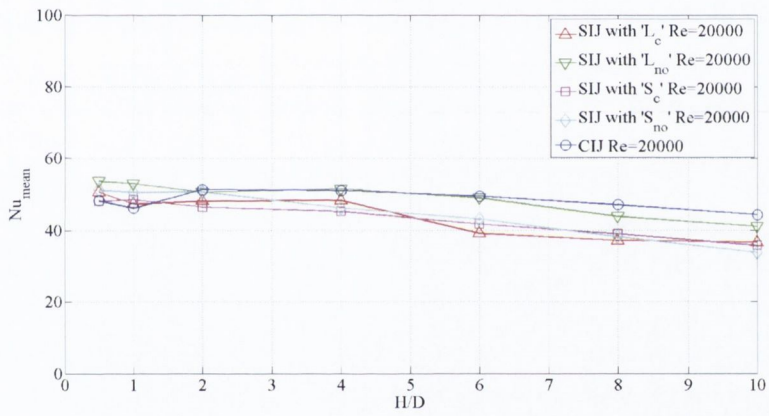


(a)

5.1. CASE 1: INFRARED THERMOGRAPHY



(b)



(c)

Figure 5.12: Mean Nusselt number, Nu_{mean} , for each of the conventional and swirling impinging jets examined at each H/D with a Reynolds number of (a) 8,000, (b) 14,000 and (c) 20,000

5.2 Case 2: Hot-Film Sensor Analysis

Case 2 of this study, on the heat transfer characteristics of conventional and swirling impinging jets, employs a hot-film sensor, as discussed in sections 3.3 and 4.2. As with the results discussed for Case 1 in section 5.1, this section presents the results obtained using this measurement technique that support the main trends reported for Case 1 and discusses the main characteristics discovered from these results. Using the theory outlined in section 4.2, the voltage across the hot-film sensor is converted to the equivalent Nusselt number at each recorded position. The same flow and positioning parameters as in Case 1 are used to evaluate the heat transfer profiles at a range of nozzle to surface heights and Reynolds numbers. A complete set of local heat transfer measurements for each nozzle to surface height and Reynolds number examined are located in appendix A.2.

5.2.1 Conventional Impinging Jet - Heat Transfer

Figures 5.13, 5.14 and 5.15 show the local Nusselt number distributions for the development of the heat transfer for the range of Reynolds numbers tested at nozzle to surface heights of $H/D=1$, 4 and 10 respectively.

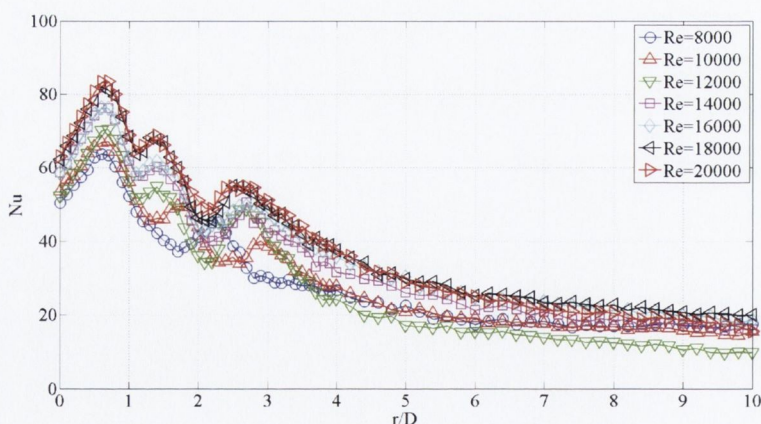


Figure 5.13: Local Nusselt number distribution for a conventional impinging jet at $H/D = 1$ for all Reynolds numbers using a hot-film sensor in Case 2

Comparable to the equivalent results shown in figure 5.1 for Case 1, figure 5.13 demonstrates the Nusselt number dependence on the Reynolds number. Similar aspects to the Nusselt number distribution, with regard to those illustrated for Case 1, include a local minimum at the stagnation point followed by a series of peaks. This can be seen from figure 5.13 for $H/D=1$ but a similar trend was noted for all heights less than $4D$. For low heights, three peaks in total are noted following the local minimum at the stagnation point. However, for a Reynolds number of 8,000 and heights less than $2D$ the Nusselt number distribution reveals only two peaks; the primary peak at $r/D \approx 0.7$ and a secondary peak at $r/D \approx 2.2$, as shown in figure 5.13. As the height is increased to $4D$, the secondary and tertiary peaks appear to be replaced by a single secondary peak while still retaining the local minimum at the stagnation point, as shown in figure 5.14. The secondary peak then reduces in magnitude until indistinguishable and the local minimum at the stagnation point becomes a local maximum as the nozzle height increases to $10D$. An illustration of this change is shown in figure 5.15.

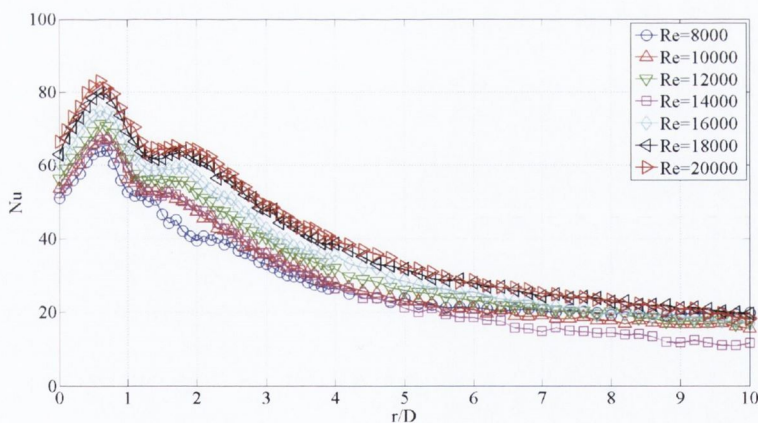


Figure 5.14: Local Nusselt number distribution for a conventional impinging jet at $H/D = 4$ for all Reynolds numbers using a hot-film sensor in Case 2

The three peaks recognised in the local heat transfer distributions for low H/D have been linked to vortical induced turbulence and boundary layer separation on the impingement surface [3,12,13]. Depending on the height of the nozzle and the Reynolds number of the flow, each of these mechanisms can have different levels of influence. For example, the initial peak in the local Nusselt number distribution for low H/D , located

5.2. CASE 2: HOT-FILM SENSOR ANALYSIS

at $r/D \approx 0.7$, is regarded as a consequence of the strong vortical structures, developing at the boundary between the jet flow and the surrounding fluid, impinging upon the heated surface [12]. The second and third peaks together are only noted under specific conditions, primarily when the nozzle is within $4D$ of the impingement surface, as previously mentioned. The number of additional peaks changes as the height of the nozzle is increased, demonstrating that this parameter is key to establishing what the cause of the separate peaks is. This phenomenon is investigated in the following section through fluctuating heat transfer analysis and in chapter 6 via flow visualisation and PIV measurement.

The local minimum at the stagnation point is also seen to change to a local maximum as the height is increased, creating a bell curve Nusselt number distribution, comparable to the distribution shown in figure 5.2 for Case 1. The local Nusselt number distribution characteristics at high H/D is displayed in figure 5.15 for $H/D=10$.

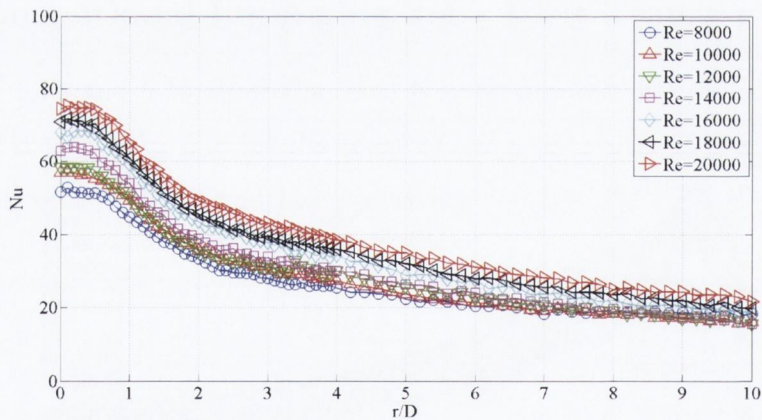
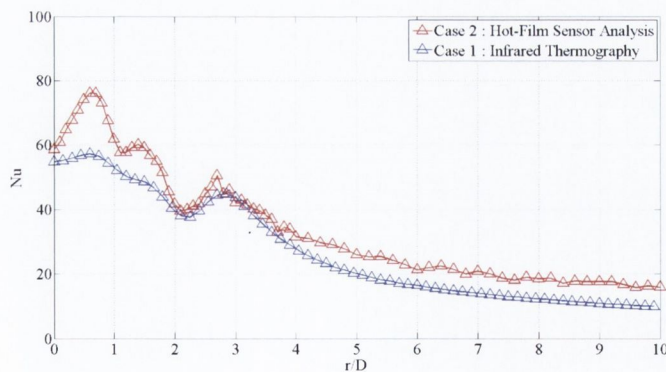


Figure 5.15: Local Nusselt number distribution for a conventional impinging jet at $H/D = 10$ for all Reynolds numbers using a hot-film sensor in Case 2

5.2.2 Comparison of CIJ Heat Transfer: Case 1 vs. Case 2

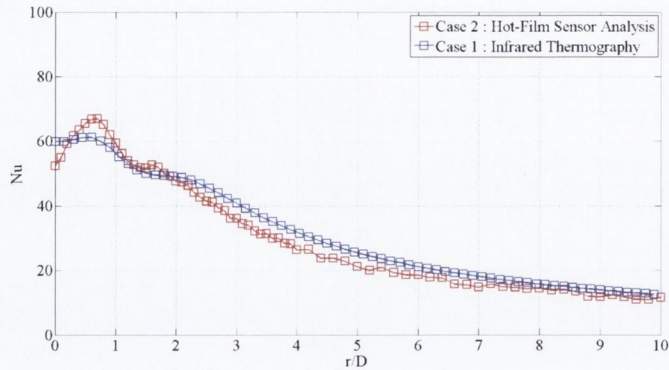
With the heat transfer analysis of a conventional impinging jet complete for two different experimental methods, a comparison between the results can be made. Figure 5.16 shows three examples of the heat transfer distributions evaluated from Cases 1 and 2 at a Reynolds number of $Re=14,000$ and for nozzle to surface distances of $H/D=1, 4$ and 10 respectively. As described previously, the hot-film sensor is calibrated against a correlation generated from the stagnation point Nusselt number results evaluated in Case 1.

The three graphs shown in figure 5.16 demonstrate the close agreement between the two studies at the stagnation point. Figure 5.16a shows the Nusselt number distribution for both case studies at a Reynolds number of $14,000$ and a height of $1D$. As the radial distance increases, while the Nusselt number trends remain broadly similar, the magnitudes vary considerably up to a distance of $r/D=2$. Although the two cases examined relate to different thermal boundary conditions, the difference in the heat transfer within this region can be attributed primarily to the spatial resolution of the experimental method being employed. Both distributions coalesce at a radial distance of $r/D \approx 2$ and continue outwards at similar levels from the stagnation point.

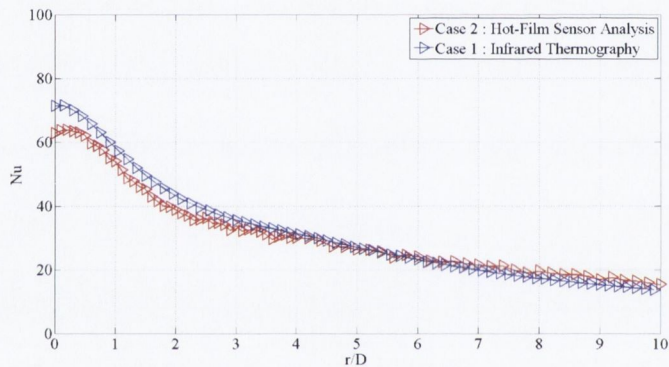


(a)

5.2. CASE 2: HOT-FILM SENSOR ANALYSIS



(b)



(c)

Figure 5.16: Comparison of Nusselt number distributions from Case 1 using infrared thermography and Case 2 using hot-film sensor analysis for a conventional impinging jet at a Reynolds number of 14,000 and H/D of (a) 1, (b) 4 and (c) 10

As mentioned in chapter 3, the resolution of the FLIR systems A-40 infrared thermal imaging camera was measured to be approximately 0.5mm per pixel while the hot-film sensor technique had a resolution of approximately 0.1mm . In order to determine whether this difference in resolution can explain the local variations in the measured heat transfer, a second thermal imaging camera, FLIR systems SC-6000, was set up under the same conditions as before for Case 1. The SC-6000 has a resolution of 512×640 pixels, nearly four times that of the A-40. The spatial resolution of the SC-6000 infrared camera was calculated to be approximately 0.28mm per pixel. Figure 5.17 shows the local Nusselt number distributions for the two different thermal imaging cameras used, along with that of the hot-film sensor analysis.

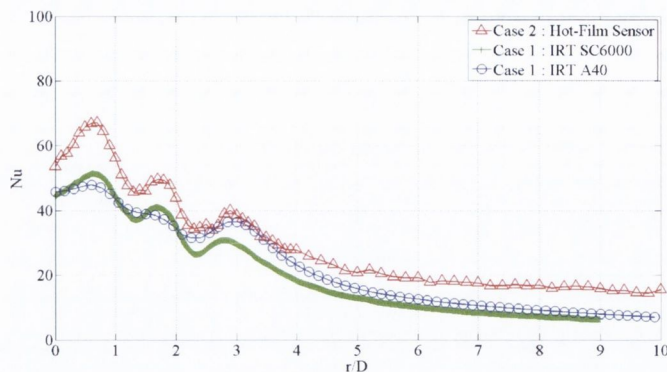


Figure 5.17: Nusselt number distribution from Case 1 using FLIR A-40 and SC-6000 thermal imaging cameras and Case 2 using hot-film sensor analysis for Reynolds number of $Re=10,000$ and $H/D=1$

This comparison shows that the increased spatial resolution of the second thermal imaging camera gives a sharper definition in the three heat transfer peaks, which brings the distribution a little closer to that recorded using the hot-film sensor technique. If it were possible to mimic the resolution of the hot-film sensor with a thermal imaging camera, it is possible that peaks as prominent as those from the hot-film sensor analysis could be obtained. However, this is speculative as there may also be some effect from the difference in thermal boundary condition as shown by Sagot *et al.* [17].

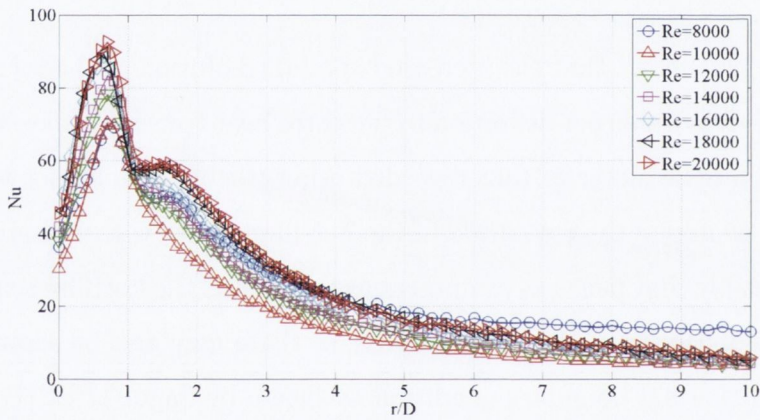
Figures 5.16b and c demonstrate similar comparative characteristics as figure 5.16a, in that the main differences between the two cases appear to be located in the stagnation region, $0 < r/D < 2$, while thereafter the two distributions are almost identical. In the stagnation region, the two distributions have similar characteristics, in terms of the location of maximum and minimum Nusselt numbers. The major difference between the two cases investigated is in the difference in magnitude between the heat transfer peaks.

5.2.3 Swirling Impinging Jets - Heat Transfer

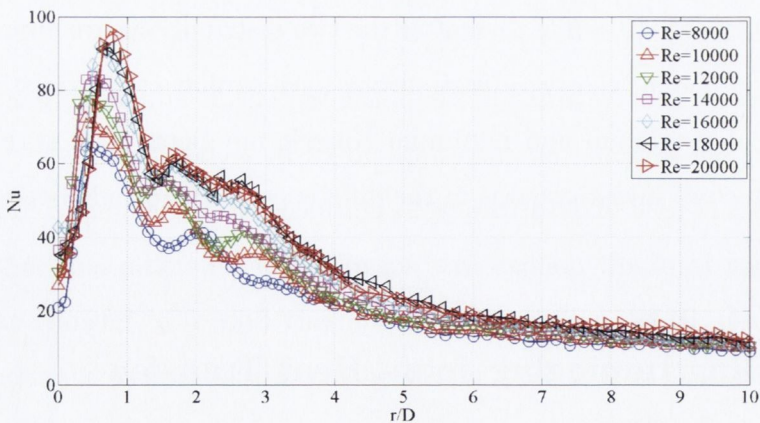
Local Nusselt number distributions are presented in figure 5.18 in order to illustrate the effect of each of the swirl generators on the heat transfer. Similar to Case 1 in section 5.1.2, each of the four graphs below represents one of the swirling impinging jet configurations. One of the key characteristics which each of the swirl geometries

5.2. CASE 2: HOT-FILM SENSOR ANALYSIS

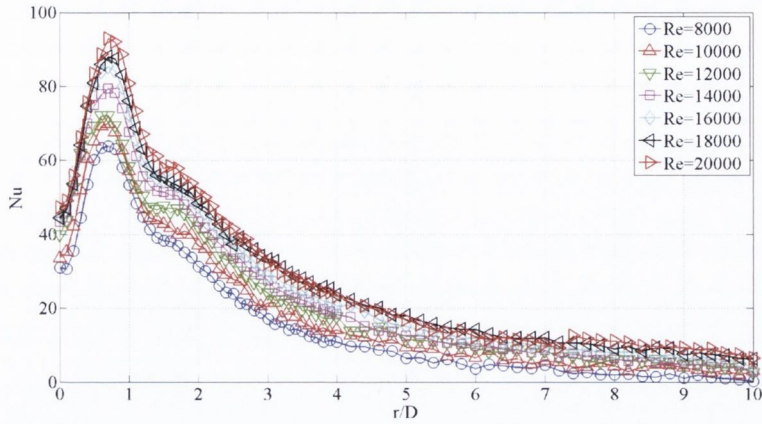
have in common is the prominent local minimum located at the stagnation point. Past swirling impinging jet studies have consistently discovered this significant drop in heat transfer at the stagnation point [68, 71, 72, 80]. This is commonly associated with a blockage in the nozzle geometry or is attributed to the swirling flow primarily being focused at the outer wall of the jet, i.e. $r/D=0.5$, resulting in a lack of fluid flow at the center of the jet. It has also been noted that recirculation of fluid may travel inwards towards the stagnation point as the swirling jet impinges upon a heated surface [73, 84], causing the local heat transfer to be reduced due to the lower local temperature difference.



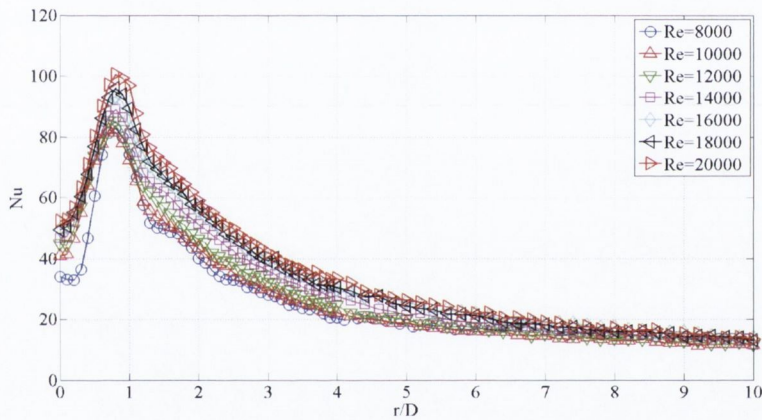
(a)



(b)



(c)



(d)

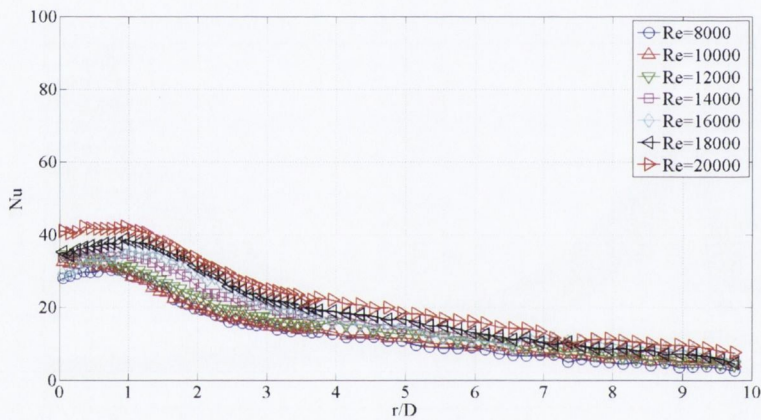
Figure 5.18: Nusselt number distribution for swirling impinging jets employing generators (a) “ L_c ” (Large with swirl core), (b) “ L_{no} ” (Large without swirl core), (c) “ S_c ” (Small with swirl core) and (d) “ S_{no} ” (Small without swirl core) at $H/D = 1$ for all Reynolds numbers

The high local maximum located at $r/D \approx 0.6-0.7$ is a further prominent characteristic of the heat transfer distributions produced, which is common to each of the swirling impinging jets. This maximum is associated with low nozzle to surface heights, $H/D \leq 4$, and can be linked to the concentration of the swirling fluid flow at the outer wall of the jet nozzle. Additional peaks in heat transfer are also noted for some of the swirling jet configurations when in close proximity to the impingement surface. This suggests that these geometries may create additional flow aspects to the

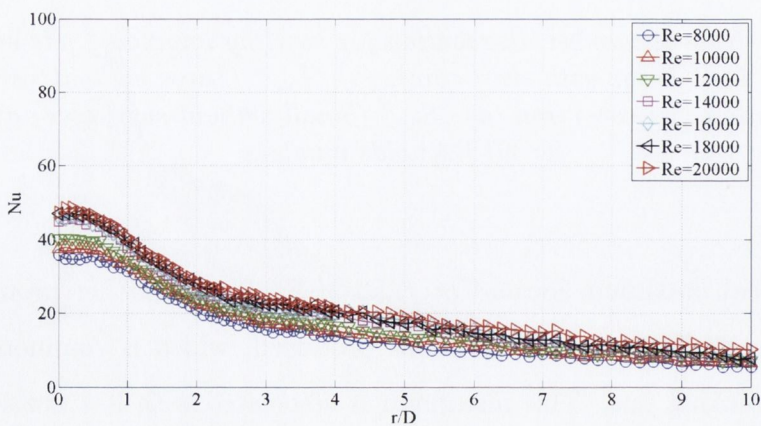
5.2. CASE 2: HOT-FILM SENSOR ANALYSIS

swirling motion which have the ability of enhancing the heat transfer further. This will be investigated further in chapter 6.

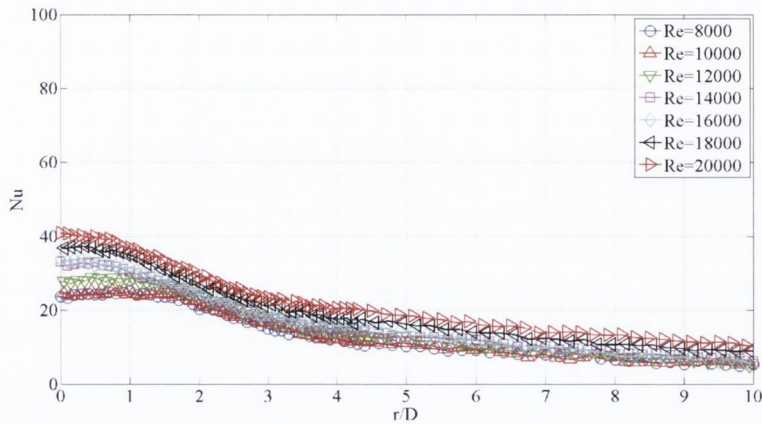
As the nozzle height is increased to $H/D=10$, the influence of each of the swirling impinging jets is reduced substantially. This can be seen from figure 5.19 for each of the swirling impinging jet configurations at $H/D=10$. This was also noted in past studies and explained in section 5.1.2. As the distance between the jet nozzle and the impingement surface is increased, the swirling flow is able to spread further from the central axis of the jet, dissipating much of its kinetic energy away from the target surface.



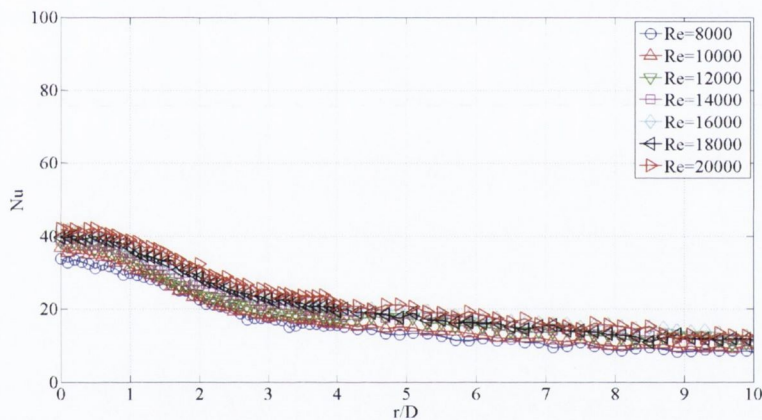
(a)



(b)



(c)



(d)

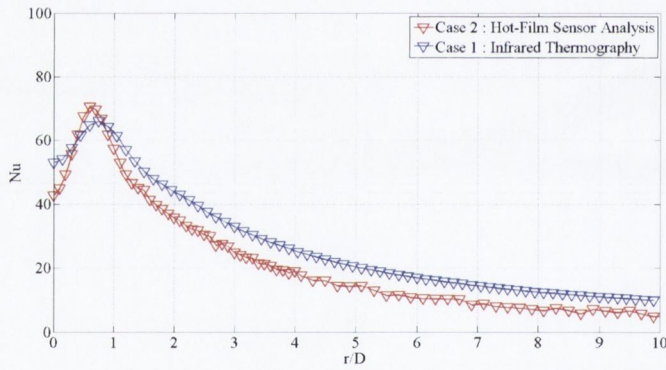
Figure 5.19: Nusselt number distribution for swirling impinging jets employing generators (a) “ L_c ” (Large with swirl core), (b) “ L_{no} ” (Large without swirl core), (c) “ S_c ” (Small with swirl core) and (d) “ S_{no} ” (Small without swirl core) at $H/D = 10$ for all Reynolds numbers

5.2.4 Comparison of SIJ Heat Transfer: Case 1 vs. Case 2

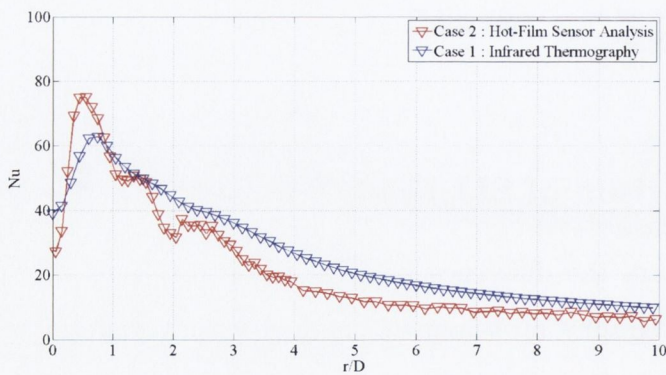
Figure 5.20 illustrates the difference between the two set-ups investigated, namely the infrared thermography measurement method with a uniform wall flux thermal boundary condition in Case 1 and the hot-film sensor technique with a uniform wall temperature thermal boundary condition in Case 2. Comparable to what was discussed previously with regard to figure 5.16, the local Nusselt number distributions

5.2. CASE 2: HOT-FILM SENSOR ANALYSIS

evaluated using the hot-film sensor method were noted to have sharper local features. This is especially noticeable for the local minimum at $r/D=0$ along with the local maximum at $0.5 < r/D < 1$; in each of the distributions from the swirling impinging jets, these features are more prominent for Case 2 than for Case 1. The improved spatial resolution of the hot-film sensor also allows more subtle features in the heat transfer distributions to be identified, such as those produced in figure 5.20b for the swirling impinging jet with swirl generator L_{no} . Thus, in Case 1, the heat transfer results using infrared thermography displayed a steady decrease as the radial location increased from $r/D=0.7$ onwards. However, from the results of Case 2 the appearance of small peaks in the distribution is recognised. This increased level of detail is also observed in figure 5.20c, where a slight secondary peak can just be identified in the results from Case 2 yet is not noticeable from Case 1.

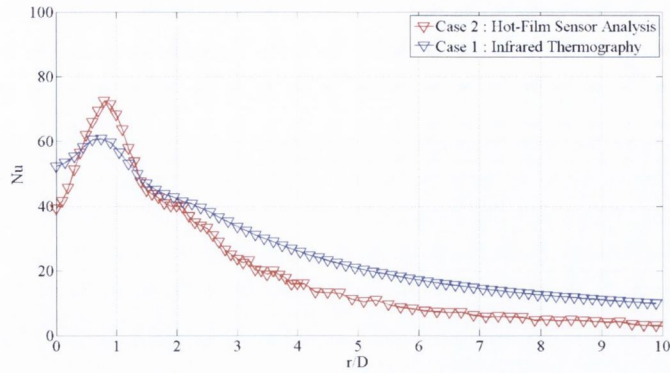


(a)

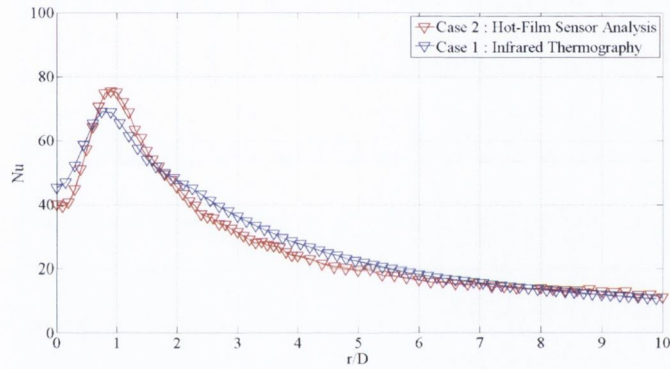


(b)

5.2. CASE 2: HOT-FILM SENSOR ANALYSIS



(c)



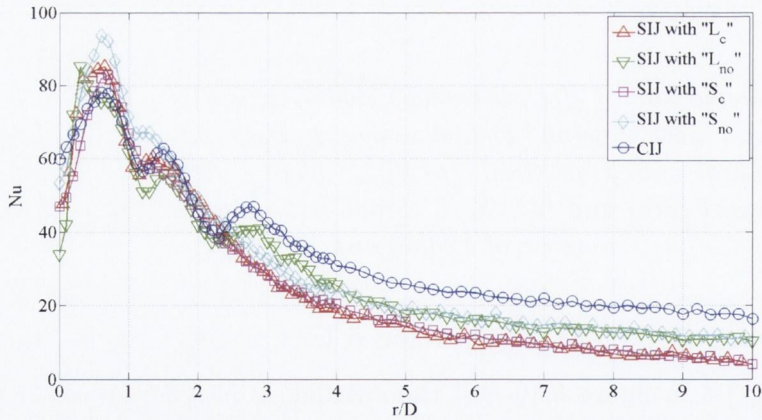
(d)

Figure 5.20: Comparison of Nusselt number distributions from Case 1 using infrared thermography and Case 2 using hot-film sensor analysis for each swirling impinging jet [(a) “ L_c ” (Large with swirl core), (b) “ L_{no} ” (Large without swirl core), (c) “ S_c ” (Small with swirl core) and (d) “ S_{no} ” (Small without swirl core)] at a Reynolds number of 12,000 and H/D of 2

The comparison of the local time-averaged heat transfer results for the conventional impinging jet in figure 5.16 and the swirling impinging jets in figure 5.20 for both experimental case studies have demonstrated that the spatial resolution of the measurement method being used is an important aspect with regard to the difference in the results presented. However, small variations between the two studies may be a result of the thermal boundary conditions differing.

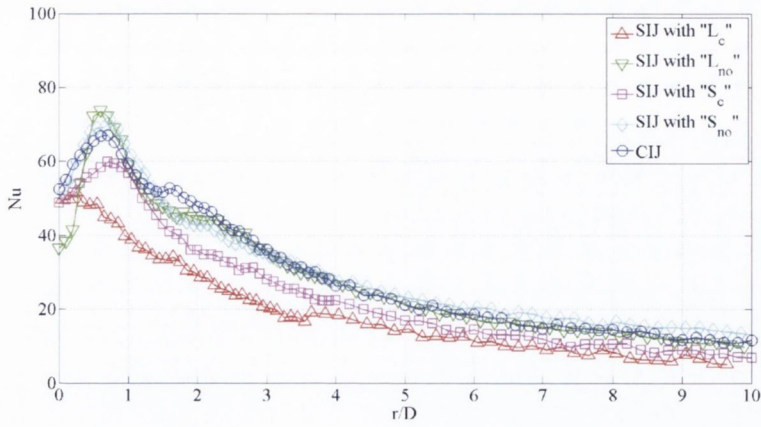
5.2.5 Case 2 : Comparison of Conventional and Swirling Impinging Jets

Just as the heat transfer due to the conventional impinging jet was compared with that of each of the four swirling impinging jets using the results obtained from infrared thermography in section 5.1.3, so too are the results obtained with hot-film sensor analysis compared in figure 5.21. Broadly similar trends due to the introduction of swirl are noted between the two methods but due to the more defined nature of the results from Case 2, the measured enhancement levels are not as significant as was found for Case 1. For example, in Case 1 the Nusselt number distributions for each of the four swirling impinging jet scenarios with a Reynolds number of 14,000 and $H/D=0.5$ showed a consistent level of enhancement in the region $0 < r/D < 2$. The results shown in figure 5.21a for Case 2 display a significant reduction in the local Nusselt number at $r/D=0$. Despite this reduction, the swirling impinging jets show a level of enhancement around $r/D=0.5-0.8$, but this is more localised and less significant than for Case 1.

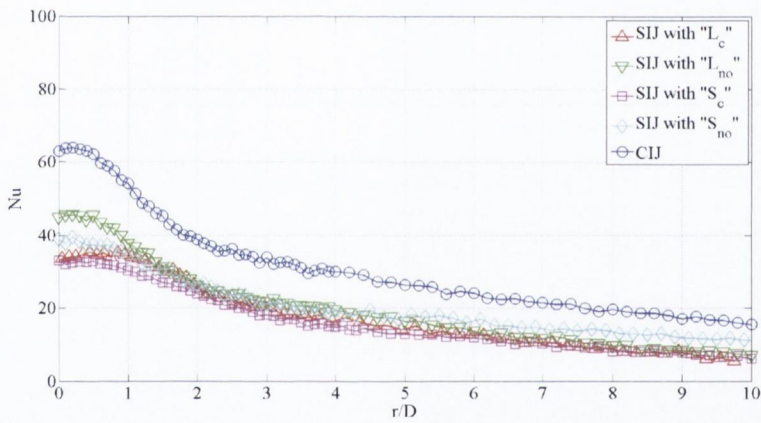


(a)

5.2. CASE 2: HOT-FILM SENSOR ANALYSIS



(b)



(c)

Figure 5.21: Nusselt number distribution for each of the conventional and swirling impinging jets examined with a Reynolds number of 14,000 at H/D of (a) 0.5, (b) 4 and (c) 10

The percentage increase in maximum Nusselt number of the swirling impinging jets relative to the conventional impinging jet, determined from figures 5.10a and 5.21a, are presented in figure 5.22. While the change in experimental method and test set-up has altered the heat transfer distributions, the relative effectiveness of the different swirl generators is almost the same, although the magnitudes evaluated using infrared thermography in Case 1 are higher than those using the hot-film sensor technique in Case 2. In this figure, it is noteworthy that the small swirl generator with no swirl core, “ S_{no} ”, provides a consistent improvement in heat transfer compared to the other

5.2. CASE 2: HOT-FILM SENSOR ANALYSIS

swirling jets as determined from both test methods, figure 5.22.

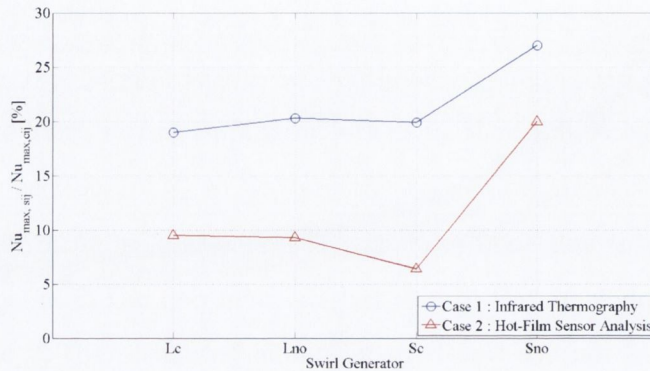


Figure 5.22: Percentage enhancement of maximum Nusselt number for each swirling impinging jet compared to conventional impinging jet at a Reynolds number of 14,000 and $H/D=0.5$ for both experimental measurement methods

The threshold at which the swirling impinging jets become less effective than the conventional impinging jets has been observed to be at a nozzle to surface height of $H/D \approx 4$. This emerged in results from both Case 1 and Case 2. Figures 5.10b and 5.21b illustrate this point by showing the Nusselt number distribution at a nozzle height of $H/D=4$ for each of the five experimental configurations. As this height is increased further to $H/D=10$, a significant reduction in the heat transfer due to the swirling impinging jets is realised; this can be seen from figure 5.21c and corresponds well to the findings for Case 1.

As reported before, the maximum enhancement in heat transfer was observed primarily when the impinging jet was in close proximity to the heated surface and at relatively high Reynolds numbers. Figure 5.23 displays the local Nusselt number distributions for each of the swirling jets, plotted with the corresponding non-swirling jet, at the lowest nozzle to surface height and highest Reynolds number examined in this study. As before, the point of maximum heat transfer occurs at $r/D \approx 0.7$ for each of the configurations.

The swirling impinging jets without the swirl core, “ L_{no} ” and “ S_{no} ”, provide the greatest enhancement of heat transfer at this point. The other two swirling jets, with the swirl core, “ L_c ” and “ S_c ”, provide local enhancement but at a reduced level.

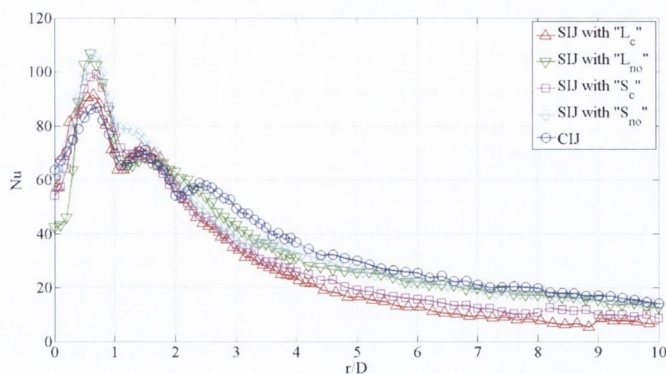


Figure 5.23: Nusselt number distribution for each of the conventional and swirling impinging jets examined with a Reynolds number of 20,000 at $H/D=0.5$

The heat transfer at $r/D=0$ is of particular interest due to the former discussion regarding the recirculation of warm fluid and reduction in heat transfer. From figure 5.23, the swirling impinging jets see a large reduction in the stagnation point Nusselt number relative to the magnitude of the maxima at $r/D \approx 0.7$. The largest reduction is noted for swirl generator “ L_{no} ”, while local Nusselt number at $r/D=0$ for “ S_{no} ” is comparable to that of the conventional impinging jet. Generators “ L_c ” and “ S_c ” are observed to have similar effects at this nozzle to surface distance. This is believed to be due to the inclusion of the swirl core in the design, indicating that the scale of these two generators does not have a large impact on the heat transfer results.

It is suggested that the difference between these two sets of results, acquired using infrared thermography and hot-film sensor analysis, is a consequence of the spatial resolution of the two experimental methods. Other effects caused by the use of two different set-ups with different thermal boundary conditions may also contribute to the difference in results, but further investigation must be conducted. However, from the results obtained in this study, it seems that the infrared thermography method in Case 1 is over-estimating the heat transfer effect caused by induced swirl in an impinging jet, while due to the better resolution of the hot-film sensor in Case 2, the sharp drop at the stagnation point is more defined. This results in the overall heat transfer enhancement of the swirling impinging jets being lower. To understand specific aspects in the local heat transfer further, the fluctuating heat transfer for each of the impinging jet configurations is discussed in the following section.

5.3 Fluctuating Heat Transfer

Evaluation of the fluctuations in heat transfer, using the hot-film sensor as explained in section 4.2.1, provides a link between surface heat transfer and the mixing and turbulence levels on the impingement surface caused by shear and/or vortices from the impinging jet. This section aims to employ the measured local heat transfer fluctuations to help explain aspects of the heat transfer distributions previously discussed. In the next chapter, PIV flow measurements and flow visualisation of the impinging jets will then be used to characterise the fluid flow as it interacts with the heated surface and to explain some aspects of the local and fluctuating heat transfer results.

A full set of fluctuating Nusselt number distributions for all Reynolds numbers, nozzle to surface heights and impinging jet set-ups can be found in appendix A.3.

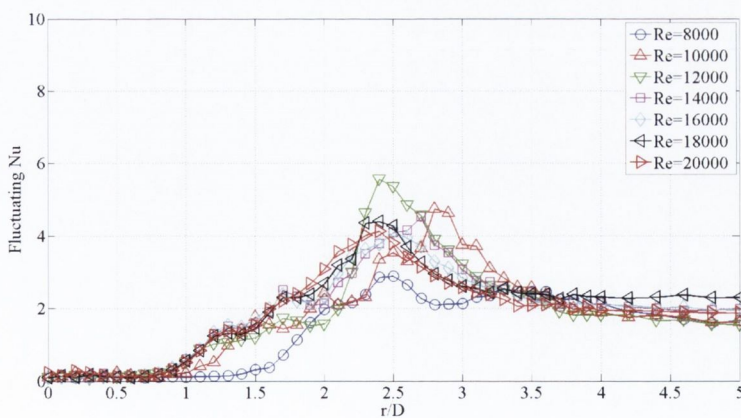
5.3.1 Conventional Impinging Jet - Fluctuating Heat Transfer

The fluctuating heat transfer for the conventional impinging jet examined is presented in figure 5.24. Results are presented for all Reynolds numbers at nozzle to surface heights of $H/D=1, 4$ and 10 , to illustrate the typical change in the fluctuating Nusselt number distribution across the range of nozzle to plate spacings. As the heat transfer fluctuations are determined from the hot-film measurements, the data relate to Case 2, with a uniform wall temperature thermal boundary condition and high spatial resolution measurements.

At $H/D=1$, the fluctuating Nusselt number, Nu^* , peaks at slightly different radial locations for the different Reynolds numbers, before gradually levelling off at $r/D > 4$. Since fluctuations in the heat transfer are likely to be associated primarily with variations in local flow velocity caused by turbulence, the first noticeable region in figure 5.24a is that which lies within $0 < r/D < 0.6$ which has a consistent magnitude near zero, also noted by Alekseenko *et al.* [69]. The explanation for the low fluctuations in heat transfer in this region comes from the uniformity of the flow emerging from the jet nozzle. As discussed previously, the potential core of an impinging jet is the region of the jet flow which remains at the same velocity originally emerging from the nozzle. The width of the potential core narrows as the distance from the nozzle exit

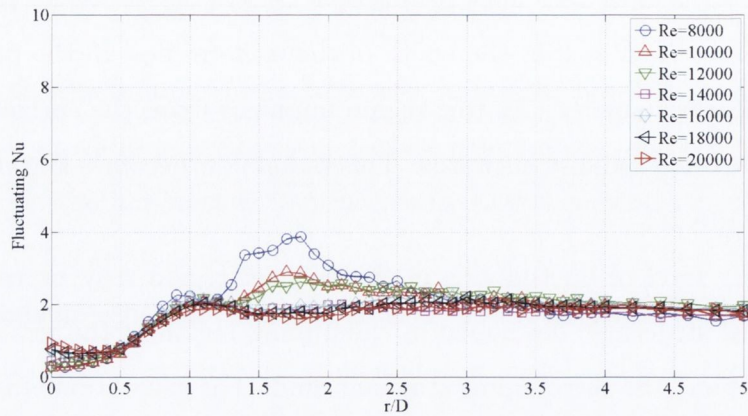
increases. The area of near zero fluctuations seen can be linked to this impinging jet characteristic. Since H/D is low, the width of the uniform flow in the potential core is close to the nozzle diameter. As this region impinges upon the surface below, the uniform flow is directed radially outwards. This radial flow becomes known as the wall jet, as seen in figure 2.3.

The increasing level of fluctuations in the wall jet region may be related to the impact of vortical structures developed in the mixing region of the jet, i.e. between the potential core and the surrounding stagnant fluid. The generation of these vortical structures may explain the increase in heat transfer fluctuations from a level of near zero at $r/D \approx 0.6$. It is apparent from the distributions shown in figure 5.24a that the turbulence level upon the impingement surface increases up to a radial location of $r/D \approx 2.5$ at which point it decreases and then levels off. This rise in fluctuations may be attributed to the evolution of vortices spreading over the impingement surface from the jet, in conjunction with turbulent boundary layer transition on the heated surface. PIV measurement and flow visualisation of the impinging jet presented in the following chapter investigates this further. From this it can also be established that the conventional impinging jet has a large influence on the impingement surface for a limited range in area.

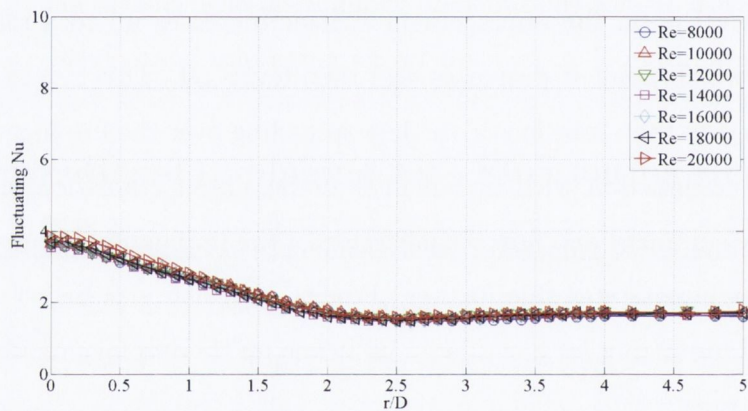


(a)

5.3. FLUCTUATING HEAT TRANSFER



(b)



(c)

Figure 5.24: Fluctuating Nusselt number for a conventional impinging jet at all Reynolds numbers and H/D of (a) 1, (b) 4 and (c) 10

When the nozzle height is increased to $H/D=4$, figure 5.24b, the distribution changes. The stagnation region, having a near zero level of fluctuations at $H/D=1$, now appears to have finite magnitudes of approximately 0.5. This increase in Nu^* may be because the end of the potential core, which is associated with an increase in mixing between the impinging jet and the ambient fluid, is approaching. This is commonly regarded as the point at which maximum heat transfer occurs. Once the end of the potential core has been reached, the turbulent fluid which surrounded the core spans the entire jet flow, resulting in fluctuations in the stagnation region. As the nozzle height is increased to $H/D=10$, figure 5.24c, the impinging flow is fully turbulent,

resulting in high levels of fluctuations on the impingement surface, especially at the stagnation point.

In the wall jet region of the impinging flow for $H/D=4$, the fluctuations in the heat transfer increase as they did at $H/D=1$, however the magnitude of these fluctuations do not reach the same magnitude and do not extend as far. The fluctuations reach a maximum value at $r/D \approx 1.7$, at which point they level off. This indicates that the number of components of the impinging jet flow which can influence the heat transfer reduces as the nozzle height is increased. This is noted further from figure 5.24c for a nozzle height of $10D$, which indicates that the main fluctuations in heat transfer are located at the stagnation point and could be a consequence of turbulent flow at the end of the potential core. This will be explored further in chapter 6, in which local flow structures will be presented for the near wall region.

5.3.2 Conventional Impinging Jet - Local and Fluctuating Heat Transfer

To view the changes in time-averaged local heat transfer as the surface fluctuations increase, the following figures are presented. Figure 5.25 displays the fluctuating Nusselt number distribution, Nu^* , superimposed upon the time-averaged local Nusselt number distribution, Nu , for the conventional impinging jet at a Reynolds number of 14,000 and for heights of $1D$, $4D$ and $10D$. This representation provides a comparative approach which may help in identifying certain features of the local heat transfer distribution.

As shown previously, as the height of the impinging jet is increased, the fluctuating aspect to the heat transfer distribution changes. At a high nozzle to surface spacing, the fluctuation level at the stagnation point is far greater than that at low spacings. When compared with the local Nusselt number distribution, as in figure 5.25c, it is noted that the point of maximum heat transfer occurs at the stagnation point and corresponds with the point of maximum Nu^* . Following the stagnation point is a large decrease in both parameters up to $r/D \approx 2$, and a steady decrease thereafter indicating a decrease in the intensity of the mixing within the wall jet flow as r/D increases.

5.3. FLUCTUATING HEAT TRANSFER

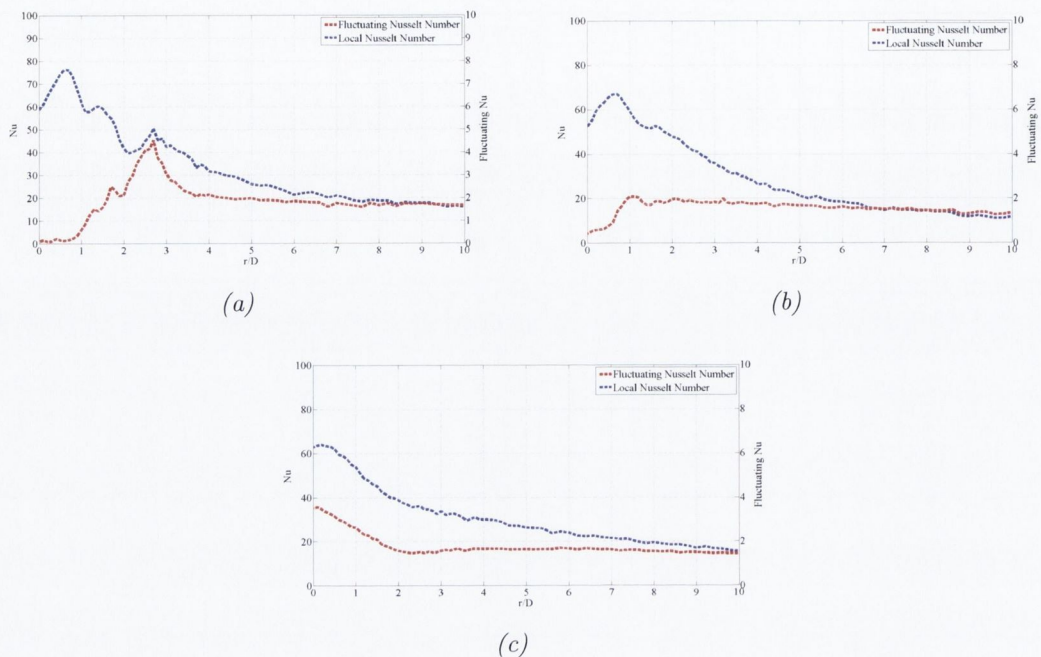


Figure 5.25: Local and fluctuating Nusselt number for a conventional impinging jet at a Reynolds number of 14,000 and H/D of (a) 1, (b) 4 and (c) 10

As the proximity of the nozzle to the surface is increased, the location of Nu^*_{max} is no longer the point of maximum heat transfer. At $H/D=4$, the maximum heat transfer coincides with the transition from a region of low to maximum fluctuations at $r/D \approx 0.65$. Once the maximum fluctuating Nusselt number is reached at this nozzle height, the fluctuation strength gradually decreases as does the local Nusselt number. By comparing only these two heights it appears that different mechanisms in the flow account for the local and fluctuating heat transfer distributions in each case. This is further supported by figure 5.25a for a nozzle to surface spacing of $H/D=1$. The maximum heat transfer at $H/D=1$ is located at $r/D \approx 0.6$ in an area of near zero fluctuations. As Nu^* increases with radial distance, the local Nusselt number drops aside from two peaks at $r/D \approx 1.5$ and 2.7 . These match well with the location of peaks in the fluctuating Nusselt number distribution. While the mechanism causing these local peaks in Nu^* does not increase the local heat transfer above the primary maximum at $r/D \approx 0.6$, these two peaks demonstrate the magnitude of fluctuations necessary to dissipate heat further at these distances from the stagnation point.

At a height of $10D$ it is accepted that the potential core of the impinging jet has

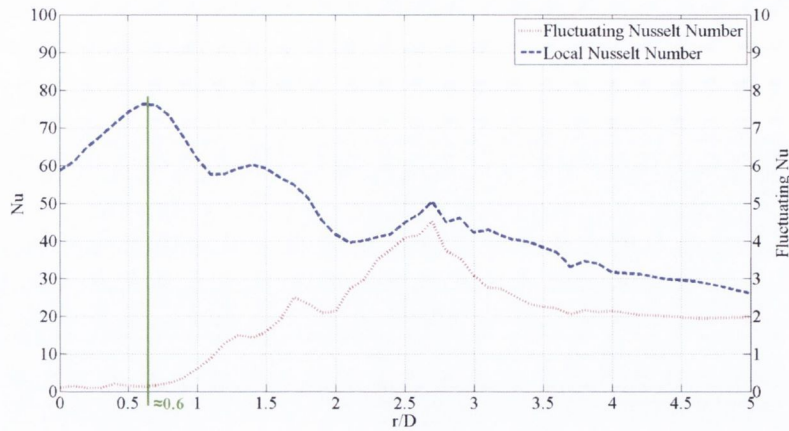


Figure 5.26: Local and fluctuating Nusselt number for a conventional impinging jet at a Reynolds number of 14,000 and $H/D=1$

ended. It is commonly considered that the near end of the potential core is the point of maximum stagnation point heat transfer. It is assumed that this is due to the interaction of the shear layers around the core as they meet at this single point. The radial location of this shear layer moves from $r/D=0$ to 0.5 as the distance from the jet nozzle decreases. The point of maximum heat transfer has been seen to act in the same manner. This points towards the location of the maximum heat transfer being determined by the mixing between the potential core of the impinging jet and the surrounding fluid.

Figure 5.26 displays the local and fluctuating Nusselt number of the conventional impinging jet at $H/D=1$ over a shorter radial range for a clearer view of the distributions. The maximum point in the local Nusselt number, Nu_{max} , is marked by a green line at $r/D \approx 0.6$. At this point on the Nu^* distribution, the fluctuations are beginning to increase. This is an indication of a strong mechanism in the impinging flow which generates such a high level of heat dissipation from the surface. After this point two further regions of interest can be identified at around $r/D=1.5$ and 2.7. In these regions, it appears that some characteristic of the flow field is producing high levels of heat transfer fluctuations, which in turn creates additional peaks in the time-averaged heat transfer distribution.

The next chapter, which focuses on flow measurements and visualisation, will seek to characterise the flow and to identify the flow mechanisms which cause these high

levels of local and fluctuating heat transfer.

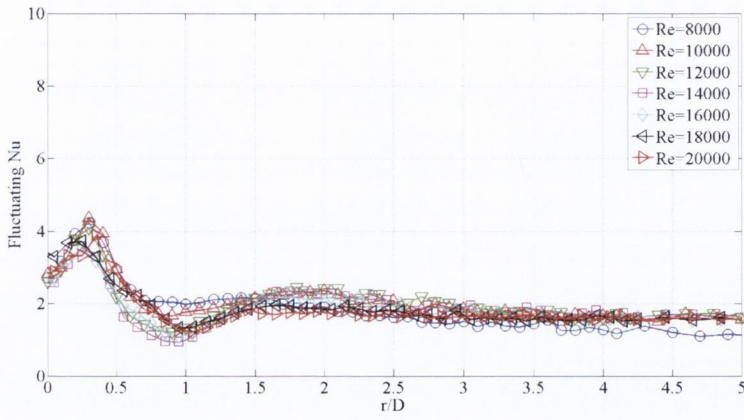
5.3.3 Swirling Impinging Jets - Fluctuating Heat Transfer

The fluctuating heat transfer levels for each of the swirling impinging jets are very different from those of the conventional impinging jet at low nozzle to surface heights. However as the height is increased, the distributions become similar. The fluctuating Nusselt numbers for each of the four swirling impinging jets at heights of $0.5D$ and $6D$ are displayed in figures 5.27 and 5.28 respectively.

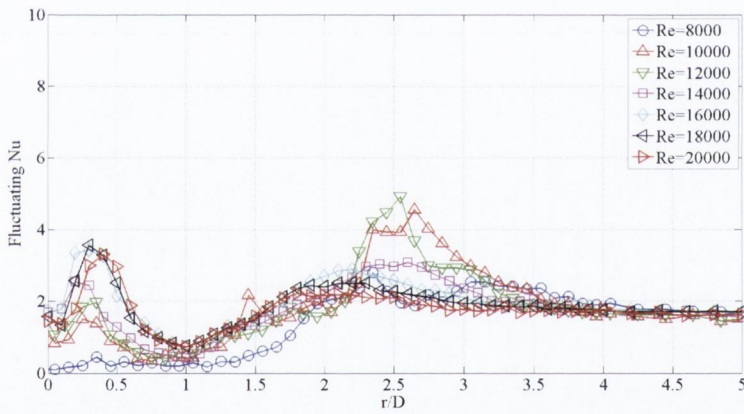
Broadly similar characteristics have been noted for each of the swirling impinging jets for $H/D < 4$, as seen in figure 5.27. Examples at other H/D settings are included in appendix A.3. The Nu^* distributions commonly show a local minimum at $r/D=0$ followed by a local maximum at $r/D \approx 0.3$ for this height range, comparable to the results found by Alekseenko *et al.* [69]. When comparing each of the swirling jet configurations at a height of $0.5D$, the swirling impinging jets with the swirl core exhibit fluctuating Nusselt numbers that are quite similar in magnitude and distribution. This suggests again that the inclusion of the swirl core is the dominant factor in determining the swirl flow pattern, although the difference in scale may be the cause of the small dissimilarity in the two results at $r/D=1$. The larger generator without the swirl core produces a region of increased fluctuations at approximately $r/D=2.5$ whereas the smaller swirl generator without the swirl core produces higher levels of fluctuations in the stagnation region.

In comparison to the fluctuating Nusselt number of the conventional impinging jet, the stagnation region displays high levels of fluctuations for each of the swirling impinging jets; the levels for the CIJ were near zero in the stagnation zone. This change in distribution, which is consistent for each of the swirling impinging jets, points towards a drastic change in the flow field. The change in question can be linked to the azimuthal velocity of the swirling flow. As reported previously, Billant *et al.* [84] determined that the maximum azimuthal velocity of a swirling jet is located at $r/D \approx 0.3$ for all angles of swirl, as seen in figure 2.44. Therefore, Nu_{max}^* in the stagnation region is likely to relate to the maximum azimuthal velocity of the swirling

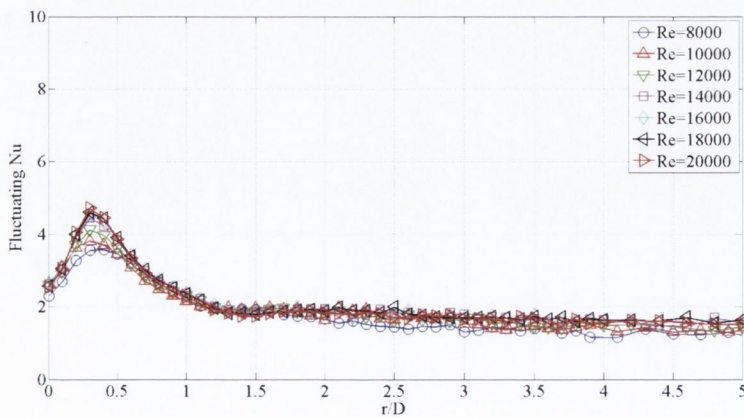
impinging jet, although this will be explored further in chapter 6.



(a)

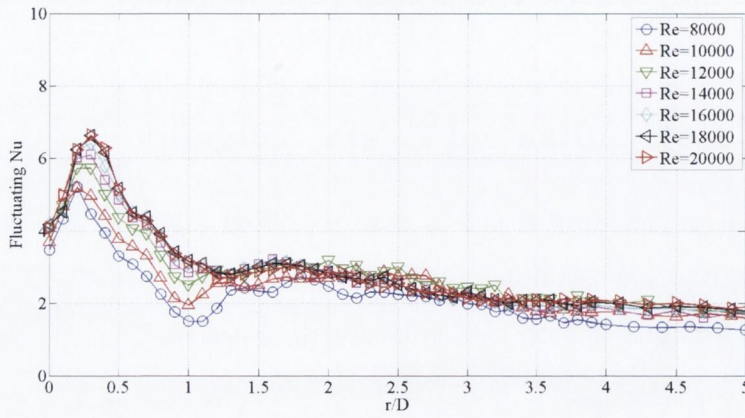


(b)



(c)

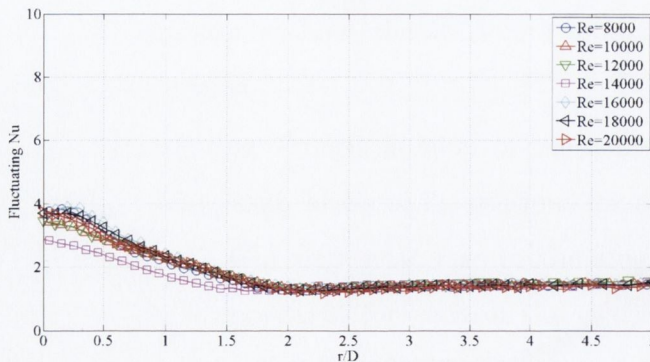
5.3. FLUCTUATING HEAT TRANSFER



(d)

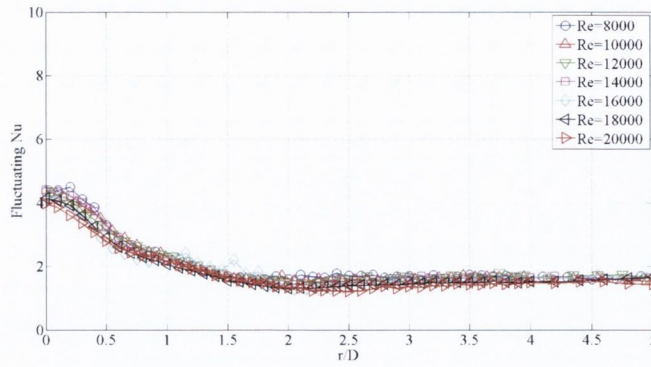
Figure 5.27: Fluctuating Nusselt number for each swirling impinging jet [(a) “ L_c ” (Large with swirl core), (b) “ L_{no} ” (Large without swirl core), (c) “ S_c ” (Small with swirl core) and (d) “ S_{no} ” (Small without swirl core)] at all Reynolds numbers and $H/D=0.5$

When the height is increased to $6D$, as seen in figure 5.28, and the radial distribution is plotted up to $5D$, the fluctuating Nusselt number distribution is seen to be comparable to that of the conventional impinging jet at heights greater than $8D$. The point of maximum fluctuations resides at $r/D=0$ for this range of nozzle to surface distances, $H/D \geq 6$, then decreases up to between $r/D=2$ and 2.5 , at which point it levels off.

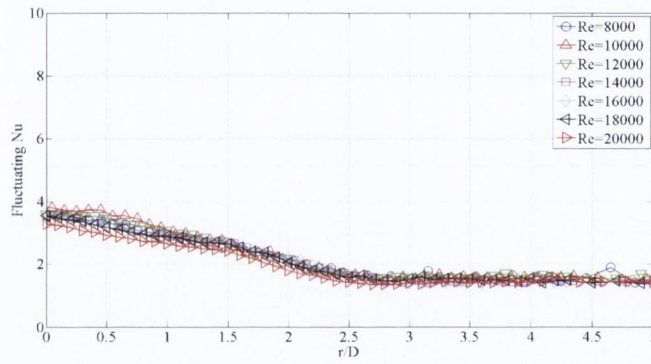


(a)

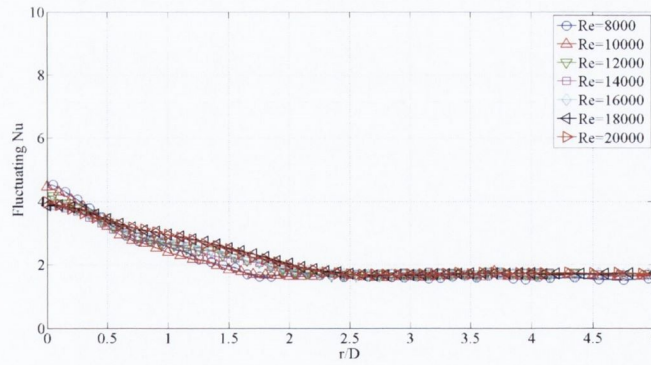
5.3. FLUCTUATING HEAT TRANSFER



(b)



(c)



(d)

Figure 5.28: Fluctuating Nusselt number for each swirling impinging jet [(a) " L_c " (Large with swirl core), (b) " L_{no} " (Large without swirl core), (c) " S_c " (Small with swirl core) and (d) " S_{no} " (Small without swirl core)] at all Reynolds numbers and $H/D=6$

5.3.4 Swirling Impinging Jets - Local and Fluctuating Heat Transfer

Figures 5.29 and 5.30 compare the local time-averaged and fluctuating Nusselt number for each of the swirling impinging jet situations, similar to the comparison for the conventional impinging jet shown in figure 5.25. As discussed before, the maximum in the local fluctuating heat transfer at $r/D \approx 0.3$ is thought to be linked to the point of maximum azimuthal velocity of the swirling impinging jet. Due to the directional nature of this flow, the impinging jet can travel both inwards, towards $r/D=0$, and radially outwards. This motion is best illustrated by Huang and El-Genk [73] and was formerly presented in figure 2.43.

The fluid that moves towards the stagnation point has been warmed by its impingement upon the surface. This warm fluid reduces the local temperature difference between the flow and the impingement surface, thereby reducing the local heat transfer in the stagnation zone as seen in figure 5.29.

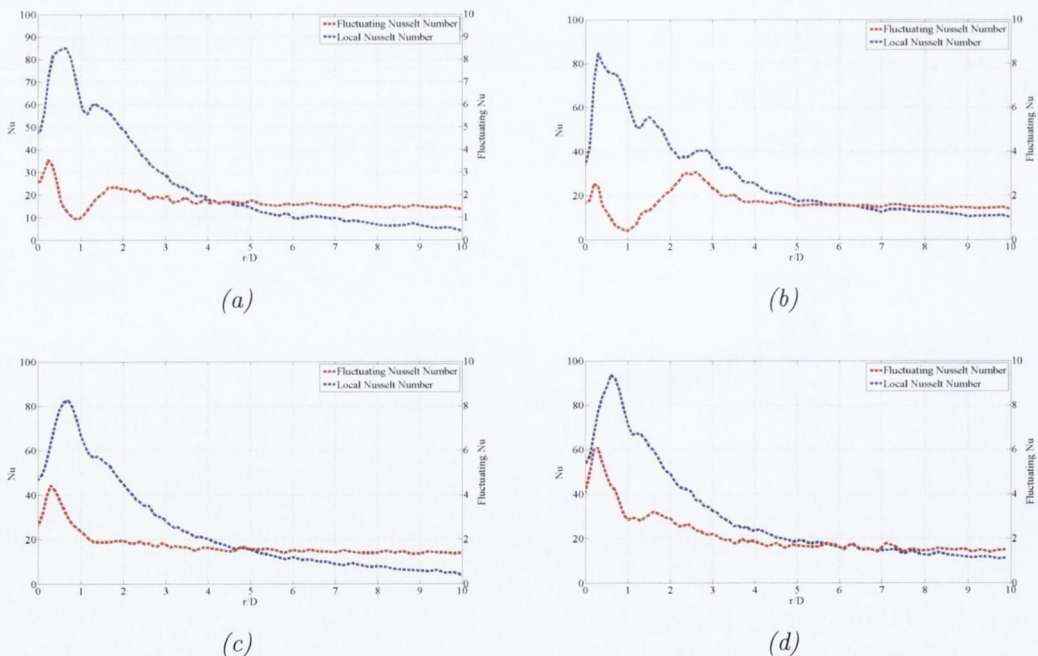


Figure 5.29: Local and fluctuating Nusselt number for each swirling impinging jet [(a) “ L_c ”, (b) “ L_{no} ”, (c) “ S_c ”, (d) “ S_{no} ”] at a Reynolds number of 14,000 and $H/D=0.5$

On the other hand, the fluid flow which travels away from the point of maximum fluctuating heat transfer ($r/D \approx 0.3$) acts similar to a conventional impinging jet, generating a high level of heat transfer and, depending on the swirl generator, additional peaks as r/D increases. These subordinate peaks in heat transfer can be associated with the increasing levels in surface fluctuations, similar to those seen in figure 5.26.

As the height is increased, both the local and fluctuating Nusselt numbers change from the trends seen in figure 5.29 to similar distributions to those seen using the conventional impinging jet. However, the fluctuation levels are lower for the swirling impinging jets in the stagnation region at high nozzle heights, such as $H/D=10$, than for the conventional impinging jets. This explains the decreased level of heat transfer for the swirl jet configurations that was seen in figure 5.21c.

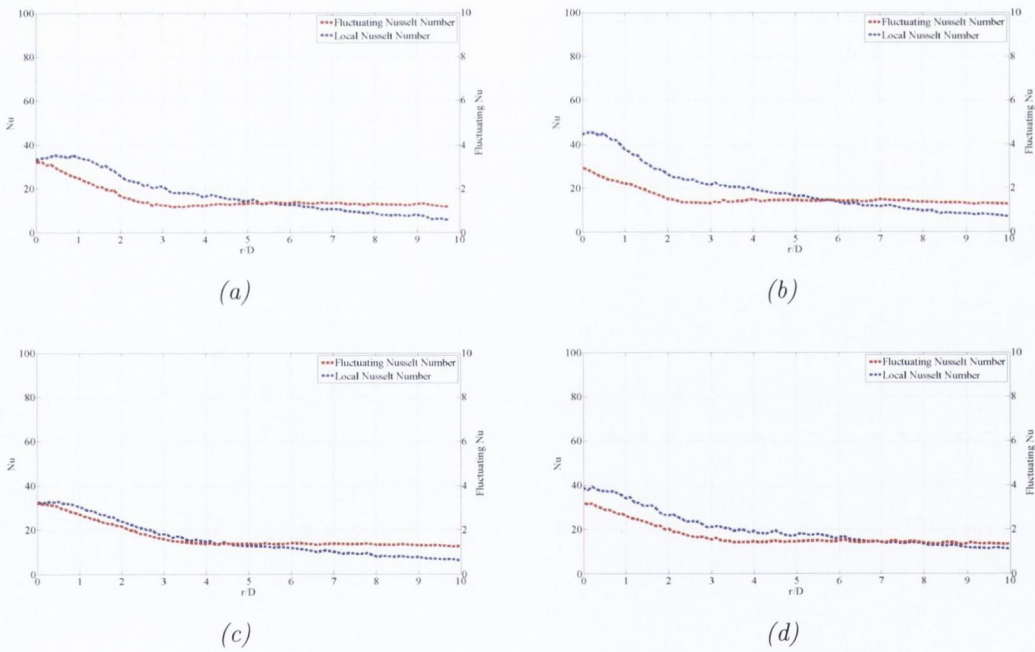


Figure 5.30: Local and fluctuating Nusselt number for each swirling impinging jet [(a) “ L_c ”, (b) “ L_{no} ”, (c) “ S_c ”, (d) “ S_{no} ”] at a Reynolds number of 14,000 and $H/D=10$

To elaborate on this point the resultant distributions for each of the swirling impinging jets at a nozzle height of $10D$ are shown in figure 5.30. Comparable to the trends from the conventional impinging jet at the same height, both the local and fluctuating Nusselt number distributions present a maximum value at $r/D=0$, demonstrating the high level of turbulence of the jets at impingement, following development

over $10D$. However, due to the spreading nature of swirling impinging jets, this value of Nu' is lower than that of the conventional impinging jet, which explains why the local Nusselt number is lower for the jets with swirl.

5.4 Concluding Remarks

This chapter has examined the heat transfer distributions determined from two measurement techniques, infrared thermography for a uniform wall flux thermal boundary condition and hot-film sensor analysis for a uniform wall temperature thermal boundary condition. Definitive aspects of the heat transfer due to each of the five impinging jet configurations have been explored, including the off-center location of maximum heat transfer and the onset of secondary and tertiary peaks at low nozzle to surface heights. With respect to the two testing approaches it was noted that the second case study, using the hot-film sensor analysis technique, showed sharper local features in the heat transfer distributions when compared with the first case study method. The results from Case 2 illustrated the same general trends as the results from Case 1, for both the conventional impinging jet and each of the swirling impinging jets, but some local heat transfer magnitudes were higher for Case 2. It was concluded that, although the differing thermal boundary conditions can have some influence, the cause of the differences reported here is primarily the spatial resolution of the methods being employed. This was reinforced by a comparison of heat transfer profiles determined from two different thermal imaging cameras, with different spatial resolutions. It was shown that the camera with a higher resolution led to a slightly different heat transfer distribution, the change being a higher level of detail at points of local maxima and minima.

With regard to the comparison of local heat transfer characteristics between the conventional impinging jet and the four swirling impinging jet situations, it was discovered that each of the swirling impinging jets delivers enhanced heat transfer within the general stagnation region at low nozzle heights and high Reynolds numbers. The enhancement in heat transfer was greatest at $r/D \approx 0.6$ where the maximum heat transfer occurred. In many cases, a diminished level of heat transfer at the stagnation

point was produced by the swirling impinging jets as compared with the conventional impinging jet. This has been attributed to the rotational aspect of the swirling flows and to recirculation of the fluid flow from the point of impingement towards the center of the jet, although it is expected that the local flow measurements, presented in the next chapter, may elucidate this phenomenon.

The swirling impinging jets were also judged against each other to determine the most effective swirl generator. Of the four investigated, the generators with no swirl core, " L_{no} " and " S_{no} ", proved the most promising in terms of maximum heat transfer. Of these two, the larger generator, " L_{no} ", delivered the better overall result. This was due to additional peaks in the heat transfer profile at low nozzle heights despite a higher reduction in heat transfer at the stagnation point, compared to the other three generators. The generators that included the swirl core, " L_c " and " S_c ", produced similar results in most respects, demonstrating that the swirl core had the dominant influence and that the scale of the outer vanes was not as important in these cases.

In order to characterise the heat transfer distributions from each of the impinging jet configurations further, an investigation into the fluctuating component of the heat transfer was performed using the hot-film sensor and uniform wall temperature test facility of Case 2. The locations of maxima and minima in the heat transfer distributions were compared with the corresponding fluctuating heat transfer trends with a view to understanding the local convective heat transfer mechanisms. For the conventional impinging jet, high levels of fluctuations outside of the stagnation zone appear to be linked to the secondary and tertiary peaks noted in the Nusselt number distributions at low nozzle heights. Fluctuations of a similar scale are noted in some of the swirling impinging jet distributions and also link to additional peaks in the heat transfer profiles away from the stagnation point.

In order to clarify the reasons behind the high heat transfer fluctuations in specific areas, and their link to the time-averaged heat transfer peaks, flow visualisation and particle image velocimetry measurements have been carried out and will be described in the next chapter.

Chapter 6

Flow Visualisation & Particle Image Velocimetry Measurements

This chapter aims to identify the flow field and local flow structures present for the impinging jet configurations investigated in this study, with a view to explaining the local and fluctuating heat transfer distributions described throughout chapter 5. In order to accomplish this, the respective jet flows were examined visually through high speed photography, while densely seeded, and the technique of particle image velocimetry was implemented.

The local and fluctuating heat transfer findings presented in chapter 5 will be compared against the flow fields under the same experimental conditions. In this way, different aspects of the local heat transfer can be related with specific flow structures of the impinging jets. Further illustrations of the conventional and swirling impinging jet flows at each of the nozzle to surface heights examined, $0.5 < H/D < 10$, for a Reynolds number of $Re=14,000$ are included in appendix B.

6.1 Conventional Impinging Jet

In order to determine the flow structure of the conventional impinging jet, each nozzle height has been examined in turn. Due to the small diameter of the jet nozzle, some vortices generated are of the order of $1-2\text{mm}$ in diameter which may be difficult to resolve using PIV. Thus, the high speed images used in the PIV process are presented

6.1. CONVENTIONAL IMPINGING JET

to illustrate the jet's structure in more detail. Figure 6.1 displays the impinging jet flow field for the three nozzle heights with the closest proximity to the impingement surface, $H/D=0.5$, 1 and 2. Since the distance between the nozzle and the surface is quite small in these instances, the shear layer of the impinging flow does not develop visible characteristic vortical structures due to Kelvin-Helmholtz instabilities. However, at a height of $2D$ the beginning of such a structure can just be detected at approximately $1.2D$ from the jet nozzle, as indicated in figure 6.1c.

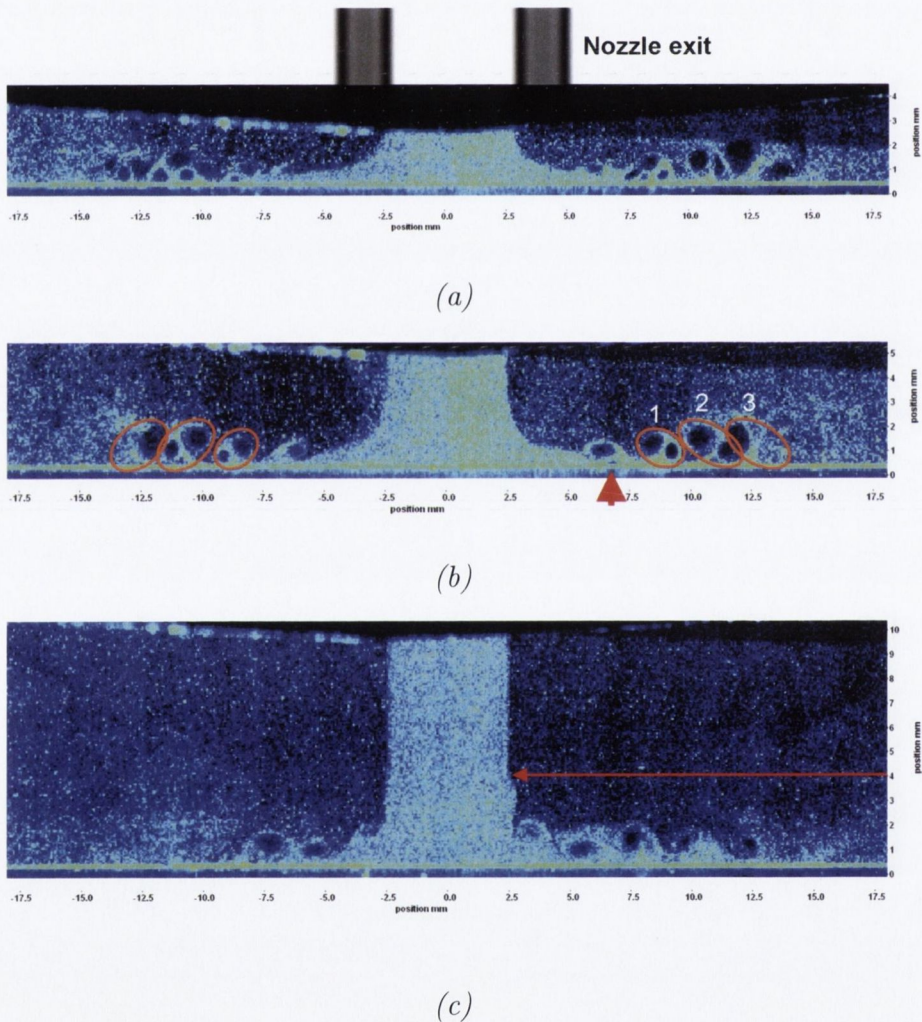


Figure 6.1: Instantaneous flow visualisation of a conventional impinging jet at a Reynolds number of 14,000 and nozzle to surface heights of $H/D =$ (a) 0.5, (b) 1 and (c) 2

At higher nozzle spacings, induced vortices appear and develop, depending on the space given to them. From figure 6.2a, demonstrating the flow field for the conventional

impinging jet for a Reynolds number of 14,000 and $H/D=6$, it is estimated that the vortex structures at the shear layer of the impinging jet break down approximately $4D$ from the nozzle exit, at which point the break down begins to interfere with the internal flow. This reduces the potential core of the jet until a fully turbulent flow is created, as noted for $H/D=10$, as shown in figure 6.2b.

From the images shown in figure 6.1, it is clear that a series of induced vortices spread radially across the impingement surface. However, from visual inspection, not only are there vortices due to the interaction between the jet flow and the stagnant surrounding fluid, but also between the wall jet flow and the impingement surface.

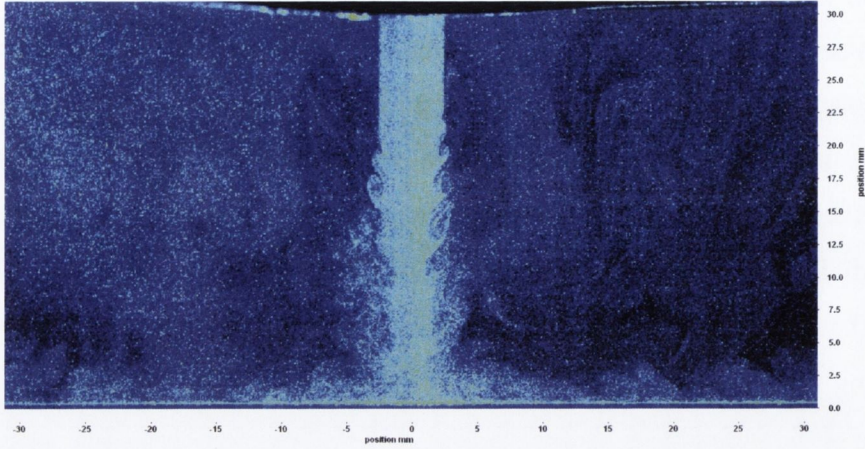
For nozzle heights of this range, the impingement surface restricts the development of shear induced vortices in the outer boundary of the jet flow as previously stated. The vortices are instead produced as the flow alters direction along the surface and are visible from $r/D \approx 1.2$ for $H/D=0.5$ and 1. These vortices mature along the impingement surface, growing in size until they collapse into a random turbulent flow approximately $3D$ from the stagnation point.

However, there is a second mechanism at work on the impingement surface which influences the distribution of vortical structures. From visual inspection, a vortex within the fluid shear layer, at a radial position of $r \approx 6mm$, causes separation of the fluid from the plate, indicated by a red arrow in figure 6.1b. As the fluid continues, this separated layer counteracts the shear layer vortex by rotating in the opposite direction. This newly created vortex is pushed back towards the surface by the shear layer vortex which it paired with, indicated by circle '1', and the vortices in front of it, circle '2'. As the paired vortices move outwards, this new vortex impinges upon the heated surface at $r \approx 12mm$, circle '3', where it breaks down.

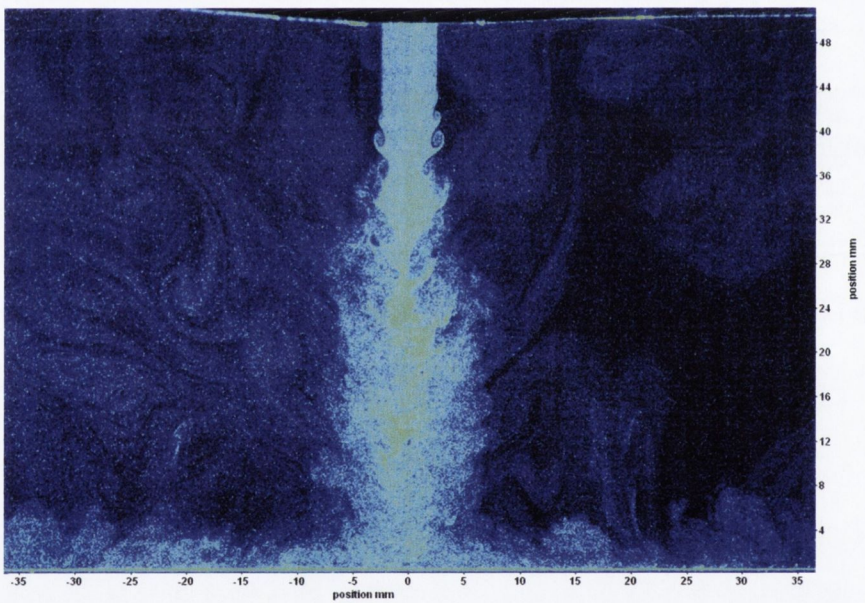
It is postulated that the tertiary peak previously noticed in the local heat transfer distributions from chapter 5 is a result of this additionally generated vortex interacting with the impingement surface, as demonstrated above. The appearance of a tertiary peak was not noted at heights above $2D$, possibly due to large vortices having been produced in the shear layer of the jet before impingement and not having the same impact on the surface. This also suggests that the tertiary peak is a result of vortical interactions on the surface and not a result of the hot-film sensor overheat as was

6.1. CONVENTIONAL IMPINGING JET

suggested by O'Donovan *et al.* [16].



(a)



(b)

Figure 6.2: Instantaneous flow visualisation of a conventional impinging jet at a Reynolds number of 14,000 and nozzle to surface heights of $H/D =$ (a) 6 and (b) 10

The representation of the flow regime at a height of $1D$, figure 6.1b, is superimposed in figure 6.3 against the local and fluctuating heat transfer previously evaluated, in order to further illustrate the importance of these vortical forms and their impact on the heat transfer. In section 5.3, the fluctuating heat transfer from the impingement

surface was compared with the local time-averaged heat transfer and the convective heat transfer mechanisms responsible for specific features in the distributions were examined. Figure 6.3 expands on this discussion and suggests that the increase in heat transfer fluctuations at $r/D=1$ is primarily due to the generation and development of multiple vortical structures in the wall region.

The initial growth in the fluctuating Nusselt number from a level near zero corresponds to the impingement of the shear layer of the jet upon the heated surface. In this region, the velocity is lower than the exit velocity of the jet due to mixing. This can be seen from figure 6.4. Figure 6.4 represents the time-averaged vector distribution of the conventional impinging jet at a Reynolds number of $Re=14,000$ and height of $H/D=1$. The figure is obtained by averaging a series of vector field flow measurements over the time period chosen using LaVision's DaVis program. In this way, anomalies that may occur in the vector prediction process are reduced. Further time-averaged images included in this chapter are produced through a similar method. At the stagnation point, the velocity of the flow is zero and it then increases with radial distance as the flow changes direction to form the wall jet. As the velocity increases, the corresponding Nusselt number also increases, but reaches a maximum in the region where the shear layer of the impinging jet impacts upon the surface. The vortices created above the surface generally slow down the radial flow, but a small region of increased velocity is noticed at $r/D \approx 1.4$, the point at which the new vortex described previously is produced. This local increase in velocity also corresponds with the secondary peak in the local heat transfer seen in figure 6.3. The roll-up of these paired vortices increases the heat transfer fluctuation levels on the impingement surface as they mature with increasing radial distance. This continues until the new vortex breaks down at $r/D \approx 2.7$ in figure 6.3, following which the fluctuation levels decrease and level off as random turbulence from the dispersed wall jet is created.

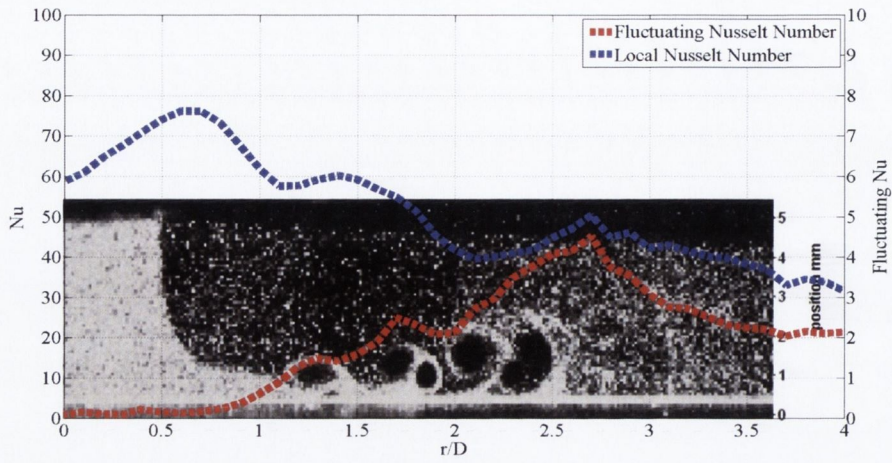


Figure 6.3: Instantaneous flow structure of a conventional impinging jet superimposed against the corresponding local and fluctuating Nusselt number at $Re=14,000$ and $H/D=1$

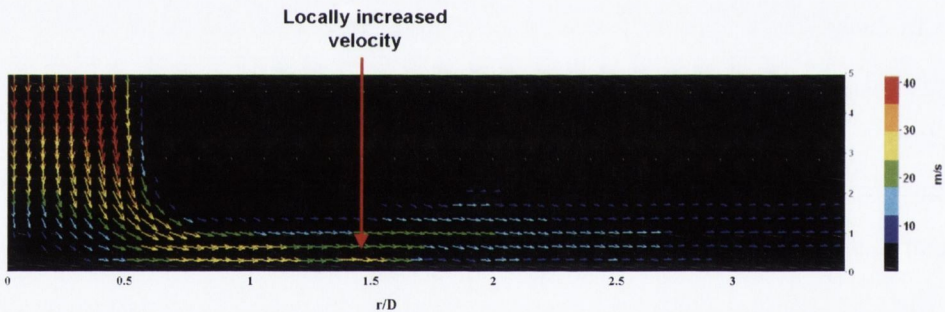


Figure 6.4: Time-averaged velocity vector distribution using particle image velocimetry of flow field from conventional impinging jet with a Reynolds number of $14,000$ and $H/D=1$

As seen in chapter 5, the presence of tertiary peaks in the Nusselt number distributions occurs up to a height of $H/D=2$. At a height of $4 \leq H/D < 6$, only a secondary peak is observed. Beyond $H/D=6$, no additional peaks in the heat transfer are noted and the local minimum at the stagnation point is replaced by a local maximum. Examination of the flow regimes of the impinging jet at these various heights, allows the change in the heat transfer distributions with varying H/D to be explored in more depth.

The appearance of tertiary peaks is a result of the proximity of the jet nozzle to the heated surface. Since Kelvin-Helmholtz vortices do not form in the shear layer of

the jet before it impinges upon the surface, in their place vortices are created in the wall jet region, causing high levels of heat transfer fluctuations and additional vortical structures which influence the local heat transfer. When the height is increased to between $4D$ and $6D$, the tertiary peak in heat transfer does not appear any longer. But the secondary peak, located at $r/D \approx 1.4$ for low H/D , moves to $r/D \approx 2$. The impinging jet develops a ring of vortices around its perimeter before reaching the surface. These vortices generate high levels of mixing in the outer boundary of the jet, thereby reducing the width of the potential core. As the jet strikes the heated surface, the developed vortices are carried along the surface, similar to what is seen at the lower nozzle heights, and due to their entrainment of cool fluid from the ambient air, a peak in the heat transfer is noted. The impact of these vortices is especially significant at lower Reynolds number where it is apparent that they have higher levels of heat transfer fluctuations corresponding to the secondary peak.

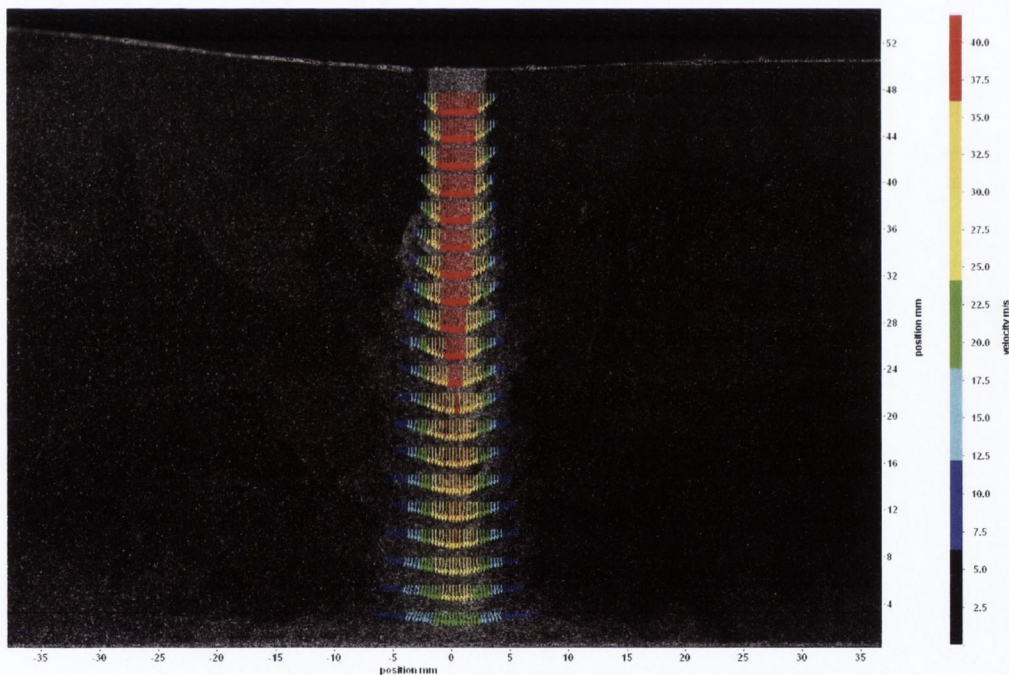
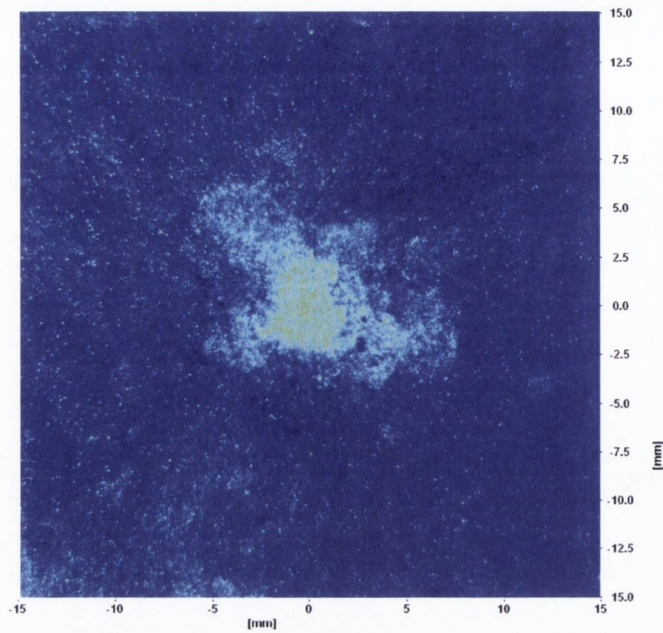


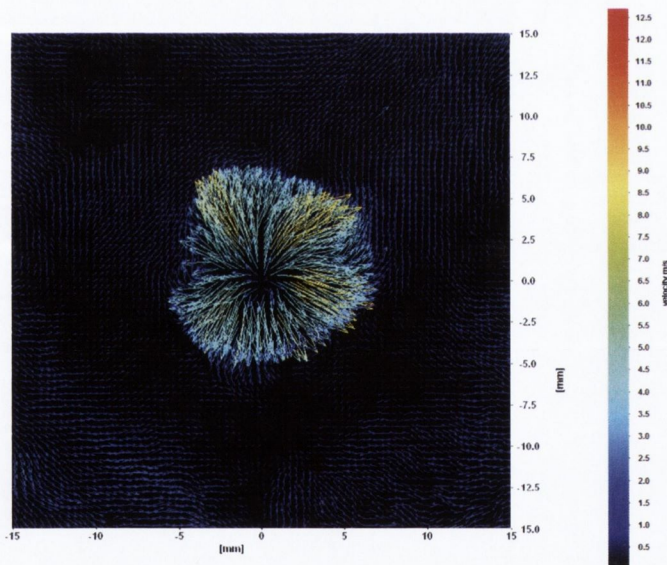
Figure 6.5: Illustration of reduction of internal flow velocity for conventional impinging jet with Reynolds number of 14,000 at $H/D=10$

As the height is increased further, the jet flow develops into a fully turbulent flow due to the end of the potential core and the spreading of the surrounding shear layer. This is shown in figure 6.5 in which the high velocity region in the center of the jet, represented in red, indicates the region referred to as the potential core. With increasing distance from the nozzle exit, one can see the reduction in the width of this region. From this method the potential core was estimated as approximately $6D$ in length, which corresponds with past research and with the maximum stagnation point Nusselt number results previously presented in chapter 5.

A cross-section of the flow from the conventional impinging jet, in a plane parallel to the impingement surface, is presented in figure 6.6. This image was recorded $2mm$ above the impingement surface with the nozzle positioned $5D$ from the surface; the Reynolds number was set to 14,000. The raw image of the impinging flow in figure 6.6a shows the concentration of the seeding particles contained in an area the size of the jet nozzle. Around the outside of this area, additional clusters of particles are created from vortices which developed around the jet, seen clearly in figure 6.2. A PIV analysis of this flow, figure 6.6b, shows the expansion of the flow outwards from the center as the flow approaches the impingement surface. The large vectors directed outwards from the center of figure 6.6b, $r/D=0$, illustrates the radial flow of the impinging jet as the impingement surface is in close proximity, similar to what was seen in figure 6.4.



(a)



(b)

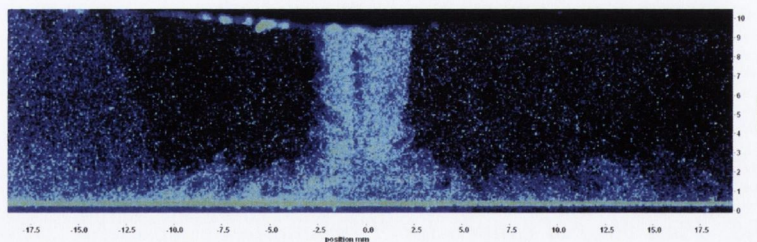
Figure 6.6: Plan view of conventional impinging jet recorded 2mm above impingement surface with Reynolds number of 14,000 at $H/D=5$: (a) Instantaneous raw image showing concentration of the seeding particles, (b) time-averaged velocity vectors demonstrating direction of motion of the jet

6.2 Swirling Impinging Jet

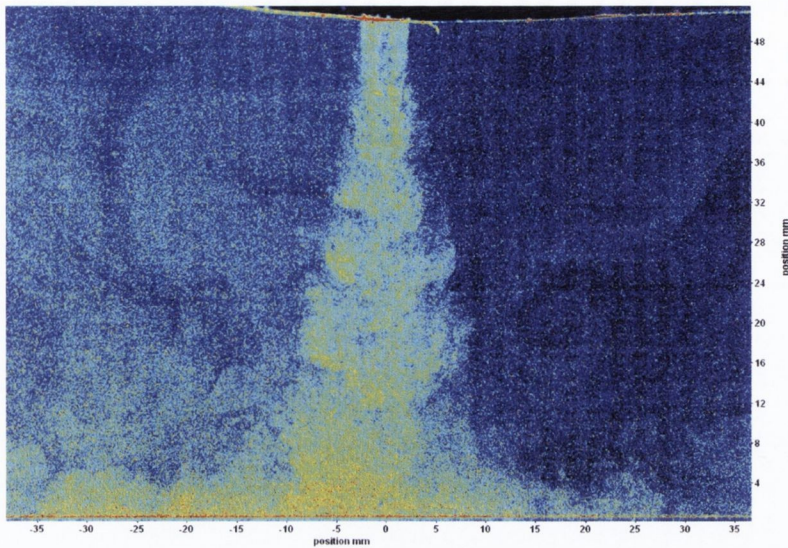
The following section aims to bring to light the flow structures present in each of the swirling impinging jets in order to further explain the local heat transfer results noted in chapter 5. This section will also present plan view visualisations of the swirling flows measured through particle image velocimetry at a height of $2mm$ above the impingement surface when the jet nozzle height is $5D$ and set to a Reynolds number of 14,000. Appendices B.2 to B.5 contain raw images of the flow regimes established under each of the swirling impinging jets with generators L_c , L_{no} , S_c and S_{no} respectively at a Reynolds number of 14,000 for all heights examined.

6.2.1 Large generator with swirl core L_c

The heat transfer due to the swirling impinging jet with generator L_c was reported to have a local minimum Nusselt number at $r/D=0$ for low nozzle to surface heights while maintaining significant levels of fluctuations in the same region. This was shown in figure 5.29. From the image of this swirling flow displayed in figure 6.7a it is noted, for low nozzle to surface heights, that the impinging flow generates high levels of mixing along with small vortical structures which influence the local heat transfer. As the jet height is increased away from the surface, the flow has time to break down, dispersing the flow outwards, as seen in figure 6.7b. This decreases the impact it has on the impingement surface and subsequently the local and fluctuating heat transfer.



(a)

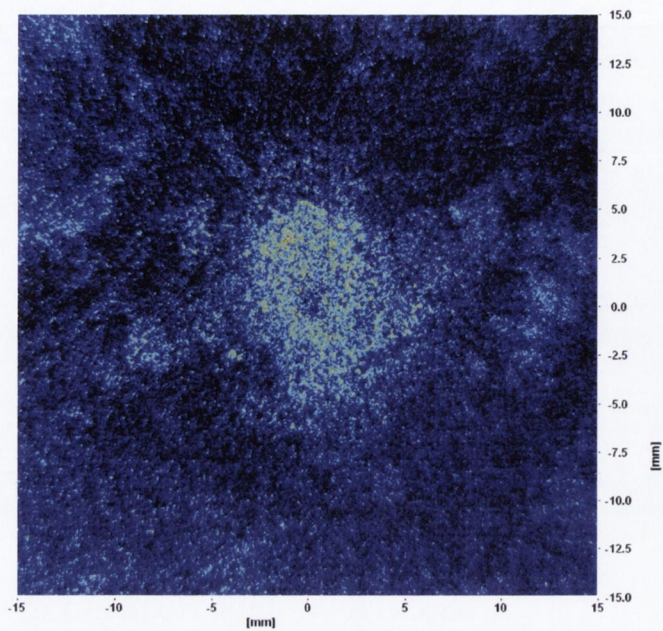


(b)

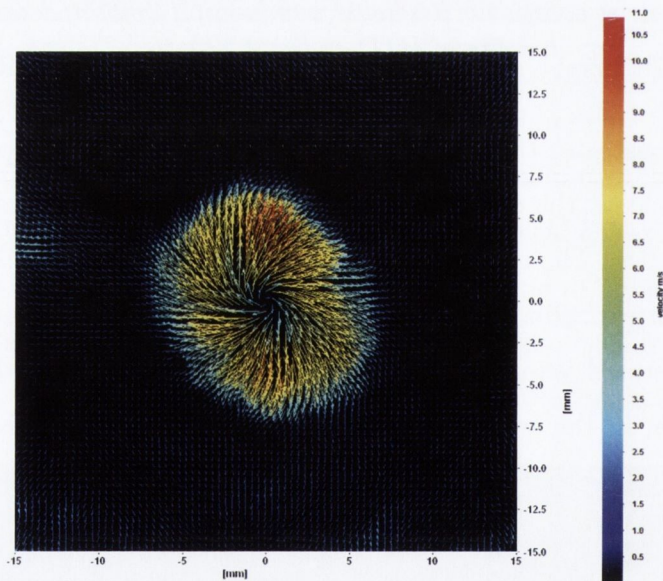
Figure 6.7: Instantaneous flow visualisation of swirling impinging jet with generator “ L_c ” (Large with swirl core) at a Reynolds number of 14,000 and nozzle to surface heights of $H/D = (a) 2, (b) 10$

Figure 6.8 demonstrates the rotational aspect of this swirling impinging jet. The images were recorded at the same parameters as for the conventional impinging jet presented in figure 6.6. The raw image displayed in 6.8(a) exhibits the dispersion of seeding particles corresponding to the expansion of the swirling jet seen in figure 6.7. With the PIV generated velocity vectors in 6.8(b), the swirling motion of the jet is realised. The center of the swirling flow has a velocity near zero which increases to a maximum at approximately $r/D=0.6$ and then decreases as the distance from the center increases. While these images were recorded at a nozzle height of $H/D=5$, this change in velocity with radial distance is a characteristic of the swirling impinging jets over a range of heights and points to the cause of the low heat transfer at $r/D=0$ and high heat transfer at $r/D \approx 0.6$ at low nozzle to surface heights seen in chapter 5.

6.2. SWIRLING IMPINGING JET



(a)



(b)

Figure 6.8: Plan view of swirling impinging jet with generator L_c recorded 2mm above impingement surface with Reynolds number of 14,000 at $H/D=5$: (a) Instantaneous raw image showing concentration of the seeding particles, (b) time-averaged velocity vectors demonstrating direction of motion of the jet

Figure 6.9 illustrates the local and fluctuating heat transfer for this swirling impinging jet set against the instantaneous flow structure of the jet with a Reynolds number of 14,000 and set to a nozzle height of $H/D=1$, similar to figure 6.3 for the conventional impinging jet. It is noted that the maximum Nusselt number occurs at the point at which the impinging flow is directed away from the center of the jet and forms the wall jet at $r/D \approx 0.7$. Small vortical structures in the wall jet, between $1 < r/D < 2$, stop the Nusselt number levels from decreasing as rapidly as they do at $r/D=1$. The fluctuating Nusselt number recognises a local maximum much closer to the stagnation point at $r/D \approx 0.4$, close to the point of maximum azimuthal velocity for a swirling jet, as reported by Billant *et al.* [84]. The increased level in fluctuations at the stagnation point indicates a high level of mixing within the flow structure of the jet.

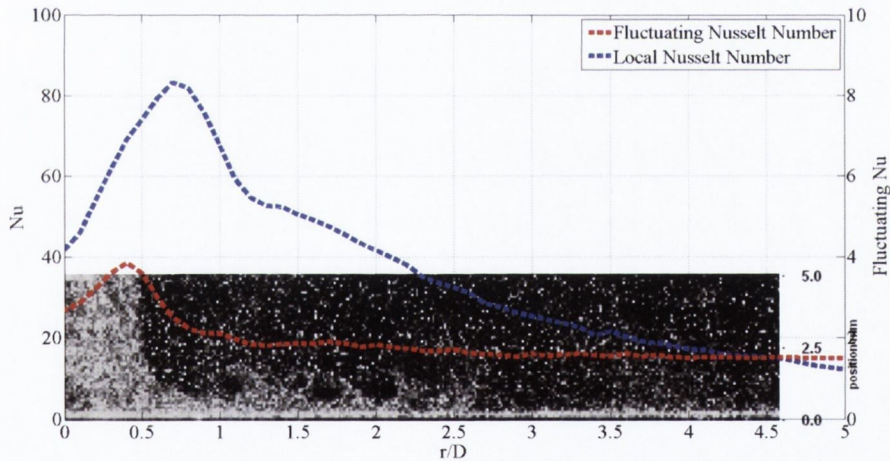


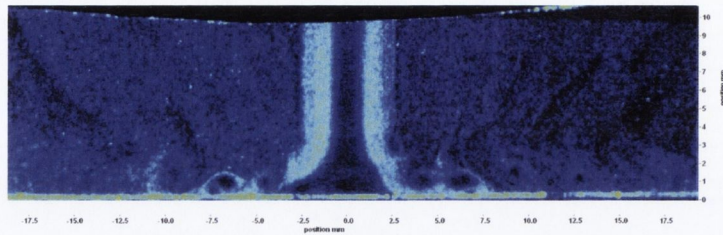
Figure 6.9: Instantaneous flow structure of a swirling impinging jet with generator “ L_c ” superimposed against the corresponding local and fluctuating Nusselt number at $Re=14,000$ and $H/D=1$

6.2.2 Large generator without swirl core L_{no}

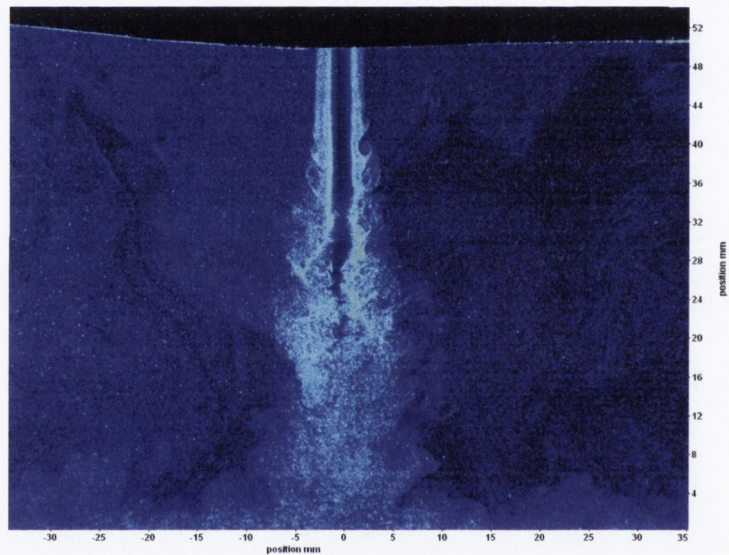
The flow structure developed by the swirling jet employing generator L_{no} is completely different to that of L_c . When a cross-sectional view of the elevation of the swirling jet with L_c was recorded, the seeding was distributed throughout the flow, as shown in

6.2. SWIRLING IMPINGING JET

figure 6.7. However, in this case, the seeding is noted to be concentrated at the outer boundary of the jet flow, as seen in figure 6.10.



(a)



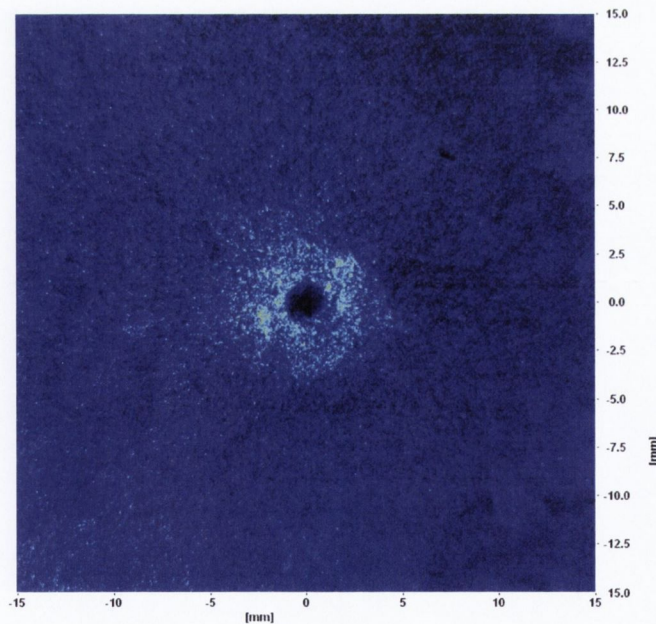
(b)

Figure 6.10: Instantaneous flow visualisation of swirling impinging jet with generator “ L_{no} ” (Large without swirl core) at a Reynolds number of 14,000 and nozzle to surface heights of $H/D =$ (a) 2, (b) 10

This feature is further illustrated by figure 6.11a, which shows a hollow region in the center of the impinging jet where no seeding particles are present. The sudden change in flow characteristics between these two cases, L_c and L_{no} , can be attributed to the inclusion of the swirl core, since it is the only aspect of the two configurations which has changed. Without the swirl core present, the guide vanes of the generator direct the flow towards the wall of the nozzle, causing the seeding in the flow to create this distinctive pattern. Figure 6.11b displays the rotational aspect of this swirling

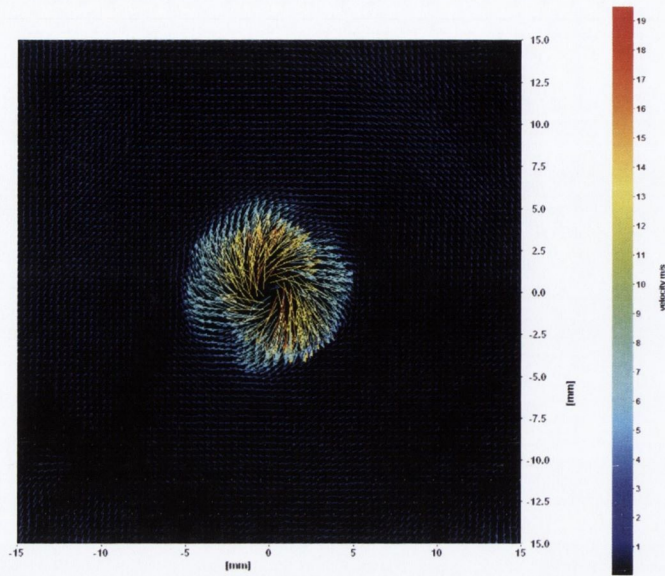
jet. Due to the narrow structure of the jet flow seen in figure 6.10a, the area of swirl is smaller than that seen with generator L_c in figure 6.8b at this height. As the height is increased, this flow structure is seen to break down and the impact area of the jet is wider, as seen in figure 6.10b.

However, the images in figures 6.10 and 6.11 show the flow of the swirling jet at one specific point in time and do not show clearly the recirculation of the flow inwards. An example of the extent of the recirculation is shown in figure 6.12. The internal flow builds up, indicated by the red arrows in figure 6.12, to a point and then is overcome by the downward flow and expelled. When this occurs, the inward flow begins to build up again, leading to a cyclic flow regime in the impinging jet. The recirculation was noticed for nozzle heights up to $\approx 4D$, at which height the flow has developed to the stage where $r/D=0$ is the point of maximum fluctuating heat transfer. Over the course of the impinging flow, the fraction of the flow which travels inwards is caught inside the flow travelling down.



(a)

6.2. SWIRLING IMPINGING JET



(b)

Figure 6.11: Plan view of swirling impinging jet with generator “ L_{no} ” recorded 2mm above impingement surface with Reynolds number of 14,000 at $H/D=5$: (a) Instantaneous raw image showing concentration of the seeding particles, (b) time-averaged velocity vectors demonstrating direction of motion of the jet

The build up of the internal flow is visualised using seeding particles in figure 6.13 for $H/D=2$. The flow towards $r/D=0$ carries heat from the surface with it, therefore lowering the temperature difference in the stagnation region and the corresponding Nusselt number. This effect explains the significant drop in the local Nusselt number at $r/D=0$ while there is a high level of fluctuations, as described previously.

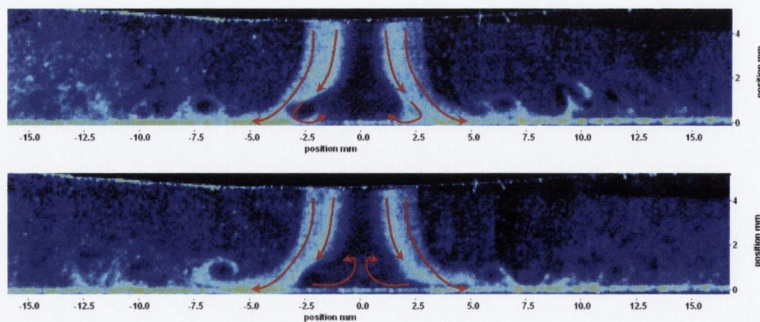


Figure 6.12: Illustration of recirculation intermittency of flow in swirling impinging jet with generator “ L_{no} ” (Large without swirl core) with Reynolds number of 14,000 and $H/D=1$

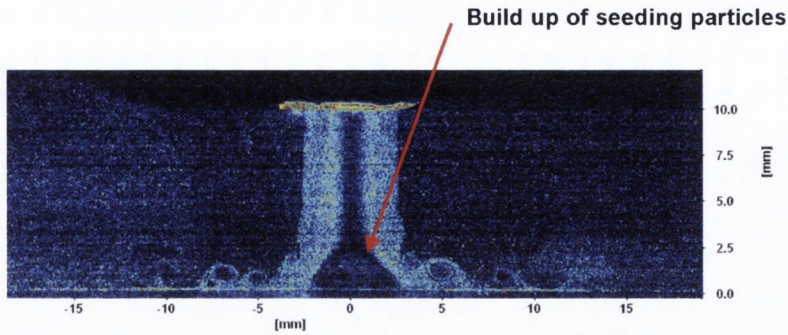


Figure 6.13: Instantaneous flow visualisation of swirling impinging jet with generator “ L_{no} ” (Large without swirl core) at a Reynolds number of 14,000 and nozzle to surface heights of $H/D = 2$

The images shown in figures 6.12 and 6.13 also display the appearance of vortical structures along the impingement surface, in the wall jet, which explain the increased local heat transfer measurements in this region presented in chapter 5.

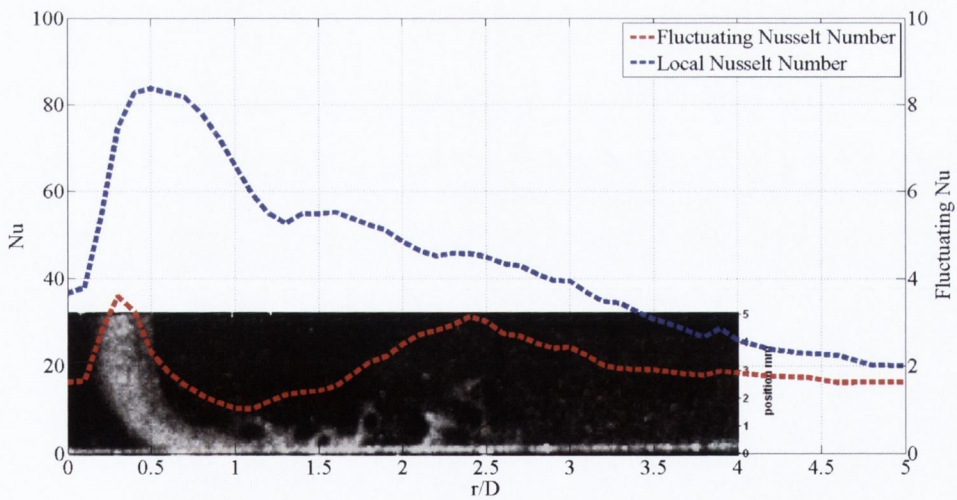


Figure 6.14: Instantaneous flow structure of a swirling impinging jet with generator “ L_{no} ” superimposed against the corresponding local and fluctuating Nusselt number at $Re=14,000$ and $H/D=1$

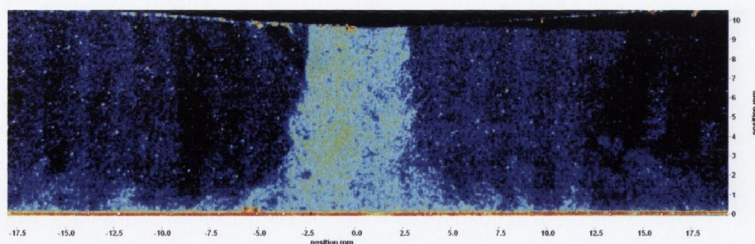
Figure 6.14 is presented to compare the flow regime with the local and fluctuating heat transfer at a Reynolds number of 14,000 and $H/D=1$. This swirling impinging jet is noted to have a different flow structure to that of the swirling jet using generator L_c . The point of maximum heat transfer corresponds to the point at which the inner

edge of the seeded flow strikes the heated surface at $r/D \approx 0.5$. The high level of heat transfer fluctuations at $r/D \approx 0.3$, similar to the case of generator L_c , can be related to the point of maximum azimuthal velocity of the swirling jet. The drop in the local heat transfer is regarded as a result of the inwards recirculating flow previously discussed and illustrated in figures 6.12 and 6.13. As the wall jet flows across the impingement surface, vortical structures are generated, from $1 < r/D < 2.5$, which cause an increase in the heat transfer fluctuations and in the local Nusselt number. After this point the vortices have broken down and the fluctuation levels decrease.

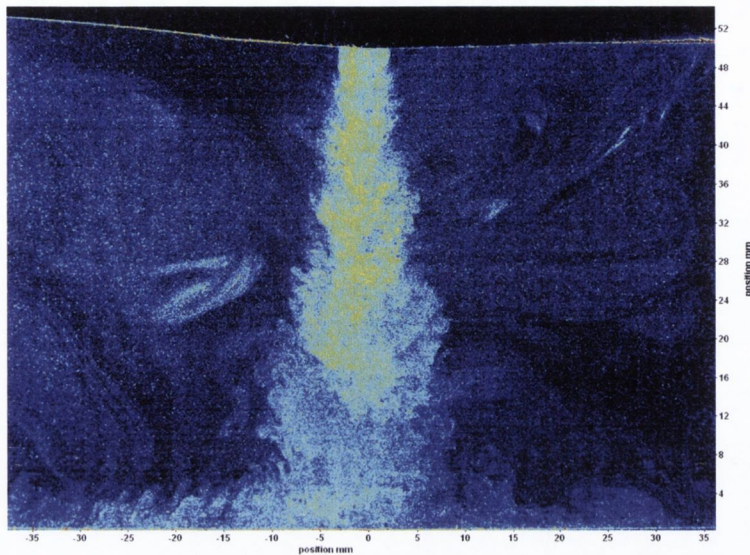
6.2.3 Small generator with swirl core S_c

The third swirling impinging jet examined incorporates the generator S_c . It was noted in chapter 5 that this swirling jet set-up produced similar local and fluctuating heat transfer distributions to the swirling impinging jet using the large generator with the swirl core, L_c . These similarities may be attributed to the flow regimes which are produced in each case. From the images displayed in figure 6.15, the flow emerging from the jet nozzle is comparable to that of the L_c swirling jet that was shown in figure 6.7.

The planar cross-section of the flow, parallel to the impingement surface, presented in figure 6.16 is also similar to that of the L_c swirling jet shown in figure 6.8, demonstrating the dispersed seeding particles and the extent of the flow radially from the center of the jet.



(a)

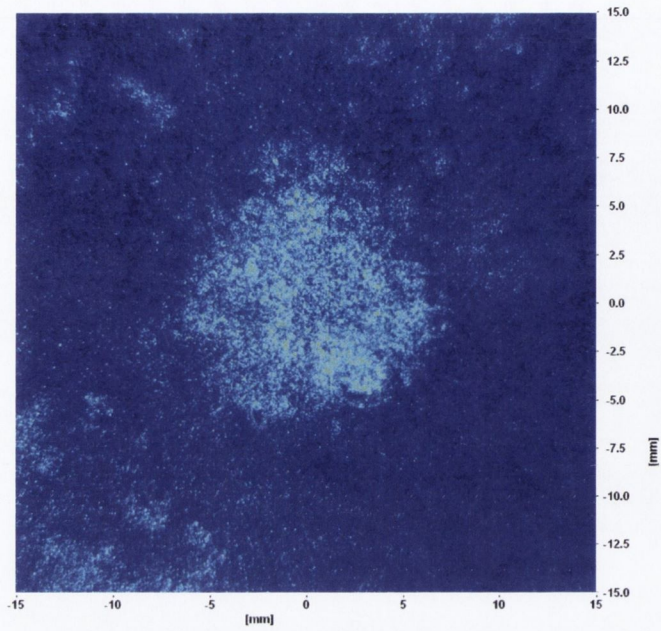


(b)

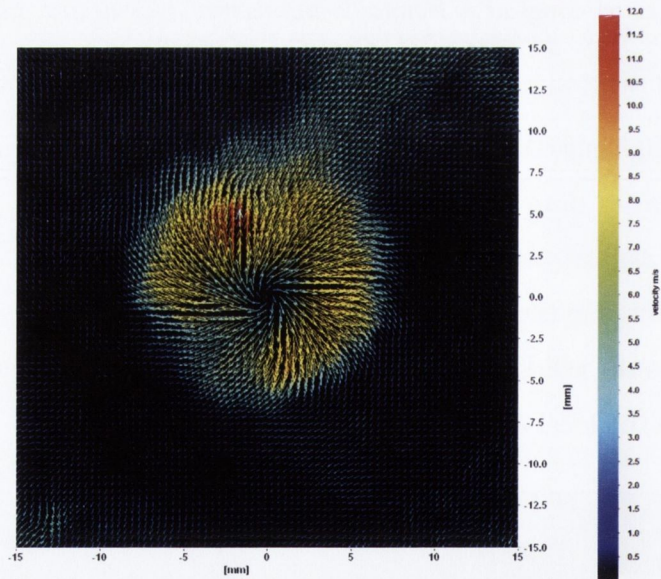
Figure 6.15: Instantaneous flow visualisation of swirling impinging jet with generator “ S_c ” (Small with swirl core) at a Reynolds number of 14,000 and nozzle to surface heights of $H/D = (a) 2, (b) 10$

Despite the change in scale of the generators L_c and S_c , the similarity in both flow fields and heat transfer data points to the idea that the inclusion of the swirl core section is the main aspect governing the flow regime of the swirling impinging jet. For the smaller generator, S_c , the increased velocity of the flow as it passes through the outer vanes towards the swirl core, due to the decrease in size, may account for small differences between the local and fluctuating heat transfer results obtained from these two generators.

6.2. SWIRLING IMPINGING JET



(a)



(b)

Figure 6.16: Plan view of swirling impinging jet with generator “ S_c ” recorded 2mm above impingement surface with Reynolds number of 14,000 at $H/D=5$: (a) Instantaneous raw image showing concentration of the seeding particles, (b) time-averaged velocity vectors demonstrating direction of motion of the jet

The similarities between this swirl generator, S_c , and the large equivalent, L_c , are visible when comparing figure 6.9 to figure 6.17, which illustrates the flow regime of this swirl generator against the local and fluctuating heat transfer distribution for a Reynolds number of 14,000 and $H/D=1$. The dispersed flow in the wall jet of this configuration creates small vortical structures, similar to those seen in figure 6.9, causing a slight increase in the local Nusselt number at $r/D \approx 1.6$. As with the previous two swirl configurations, the fluctuating Nusselt number has a local maximum close to the center of the jet, $r/D \approx 0.3$, which is regarded as the point of maximum azimuthal velocity of the swirling jet.

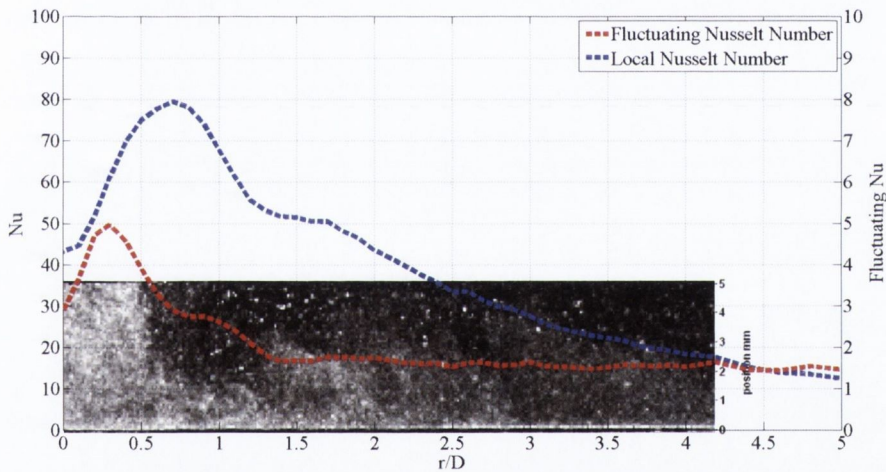


Figure 6.17: Instantaneous flow structure of a swirling impinging jet with generator “ S_c ” superimposed against the corresponding local and fluctuating Nusselt number at $Re=14,000$ and $H/D=1$

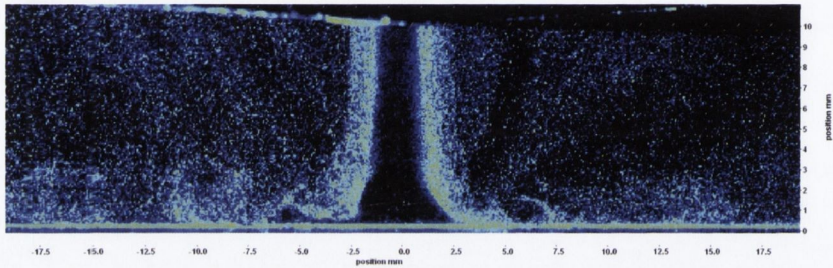
6.2.4 Small generator without swirl core S_{no}

This swirling impinging jet, S_{no} , has the same size and arrangement of guide vanes as S_c but without the swirl core. It is similar in design to generator L_{no} , the only change being the size, and it is expected, therefore, that the flow field should be somewhat similar to the flow field of the L_{no} swirling jet.

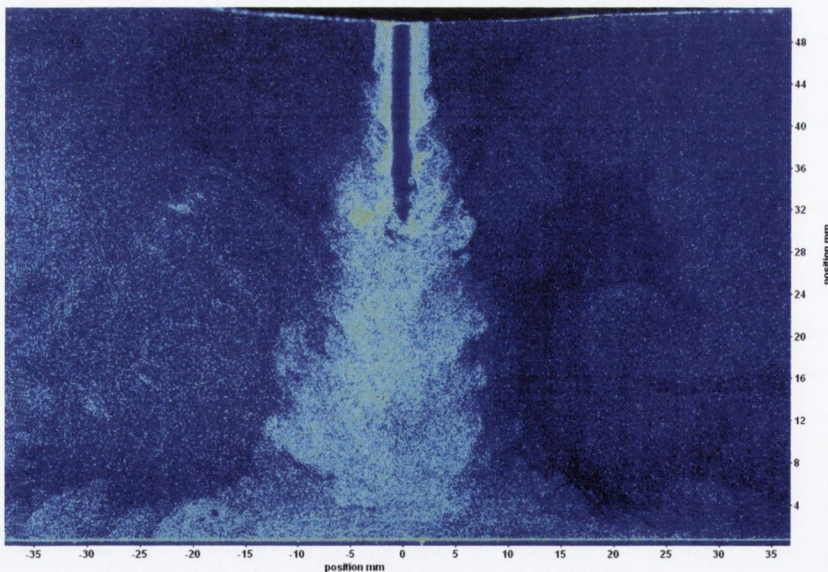
From the images presented in figure 6.18, it is noted that the flow regime is indeed quite similar to the flow regime of generator L_{no} in figure 6.10. The seeding particles

6.2. SWIRLING IMPINGING JET

are concentrated at the wall of the jet nozzle with a region in the center with little or no seeding present. This aspect can also be seen from figure 6.19 which shows the plan of the jet flow before it impinges upon the surface. At the center of the impinging flow, a region of no seeding particles is evident as was the case with generator L_{no} , as seen in figure 6.11a. However, from the PIV analysis shown in figure 6.19b, the flow field shows a wider affected area than the swirling flow from generator L_{no} seen in figure 6.11b. This change in impact region may be associated with the change in scale of the generator.

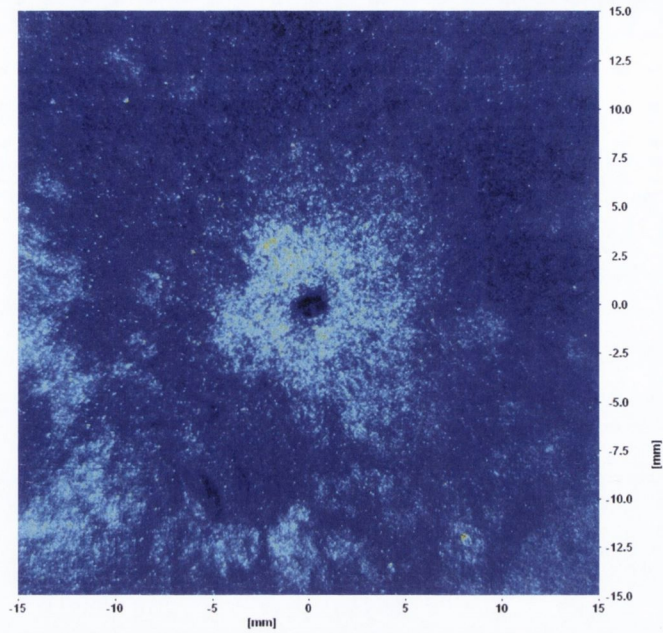


(a)

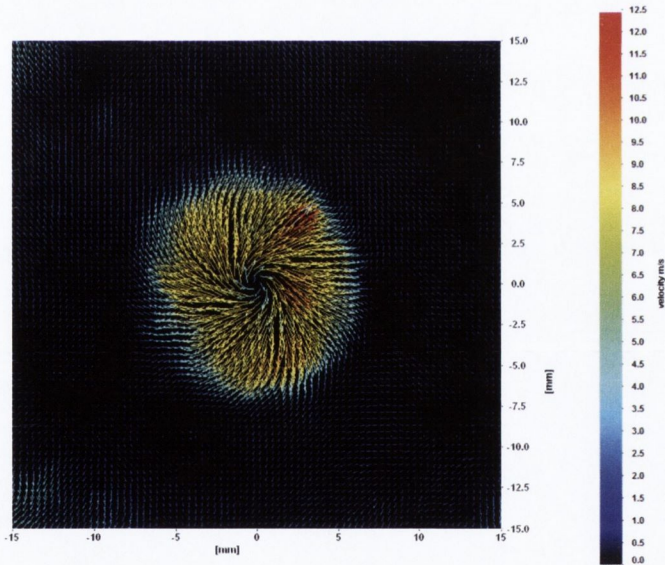


(b)

Figure 6.18: Instantaneous flow visualisation of swirling impinging jet with generator “ S_{no} ” (Small without swirl core) at a Reynolds number of 14,000 and nozzle to surface heights of $H/D = (a) 2, (b) 10$



(a)



(b)

Figure 6.19: Plan view of swirling impinging jet with generator “ S_{no} ” recorded 2mm above impingement surface with Reynolds number of 14,000 at $H/D=5$: (a) Instantaneous raw image showing concentration of the seeding particles, (b) time-averaged velocity vectors demonstrating direction of motion of the jet

6.2. SWIRLING IMPINGING JET

The change in scale of this generator may also explain the differences between the images of the flows in figures 6.10 and 6.18. While both generators show the seeding particles concentrated to the outside of the jet, the length of the inner region with near zero seeding is reduced by $1D$ for the case of the smaller generator, which demonstrated a seeding free zone spanning $4D$, compared to L_{no} , which had an equivalent length of approximately $5D$. Since this inner region is shorter, the break down of the flow occurs earlier which explains the increased radial spread of the jet demonstrated in figure 6.19b in comparison with the larger case, L_{no} .

This small generator without the swirl core also appears to create a similar recirculating flow towards the center of the jet upon impingement, as was reported for generator L_{no} . Thus, figure 6.20 gives an example of the impinging flow from this swirling jet at a nozzle height of $2D$. As the flow emerges from the nozzle the seeding is seen to be concentrated within the outer half of the flow stream. As with generator L_{no} , the flow begins to flow inward towards the axis of the jet, filling the empty space, before reaching a point when the inner flow breaks down and is removed by the downward flow and the cycle is then repeated.

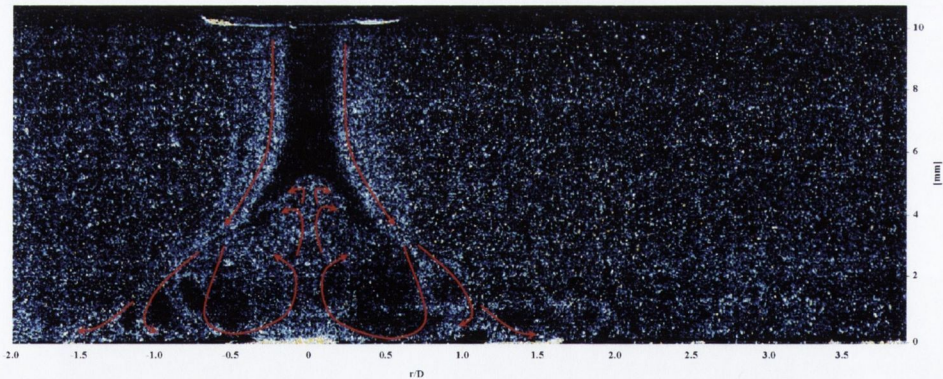


Figure 6.20: Illustration of recirculation of flow in swirling impinging jet with generator S_{no} with Reynolds number of 14,000 at $H/D=2$

The point at which the internal flow begins to travel upwards, seen in figure 6.20 to be at $r/D \approx 0.5$, was seen in figure 5.27 to be the point of maximum fluctuating heat transfer. While this would normally be considered to be a point of increased heat transfer, it is noted that the maximum Nusselt number is located at the outer boundary where the flow impinges upon the surface and flows outwards, $r/D \approx 1.1$.

While the flow inwards provides strong mixing and causes high levels of heat transfer fluctuations, the temperature difference between this recirculating fluid and the surface is less than the temperature difference between the jet exit and the surface. This affects the surface heat transfer in the stagnation region, resulting in the significant drop seen previously in figure 5.18.

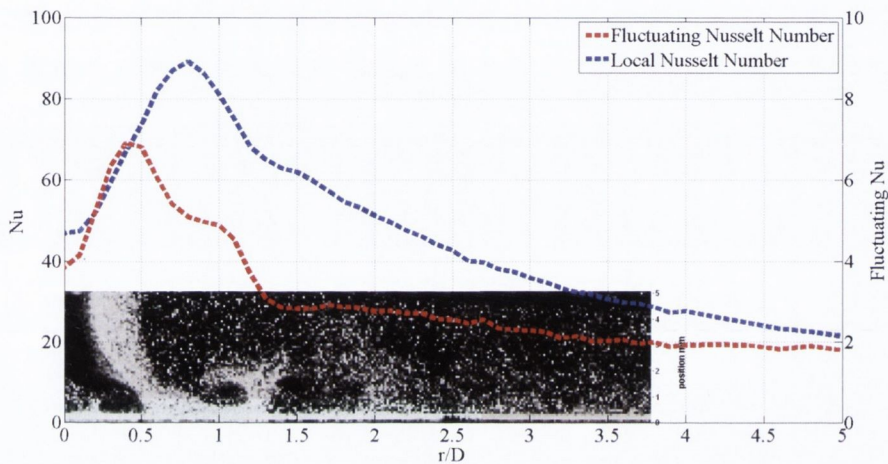


Figure 6.21: Instantaneous flow structure of a swirling impinging jet with generator “ S_{no} ” superimposed against the corresponding local and fluctuating Nusselt number at $Re=14,000$ and $H/D=1$

Figure 6.21 illustrates the local and fluctuating Nusselt numbers superimposed upon an instantaneous visualisation of the flow structure for this swirling impinging jet configuration with a Reynolds number of 14,000 and $H/D=1$, as presented for each of the other impinging jet configurations. This figure shows both the recirculation of fluid towards the center of the jet, causing a reduction in the magnitude of the local heat transfer and the generation of vortical structures at $r/D \approx 1$ generating a secondary peak in the fluctuating heat transfer.

6.3 Concluding Remarks

In the case of the conventional impinging jet, the flow structure was examined at a range of nozzle to surface heights, though most importantly those at the lower end of the scale. The flow development as the jet impinges upon the surface and travels away from $r/D=0$ is of great interest to define the cause of the tertiary peaks noted in the Nusselt number distributions presented in chapter 5. From the images acquired through high speed imagery and particle image velocimetry, it was found that vortex generation within the wall jet across the plate plays a major role in explaining both the appearance of the tertiary peak in the local heat transfer distributions and the significant increase in the local fluctuating heat transfer. The vortex generation at the surface detailed in this section is only apparent for low nozzle to surface heights, thereby explaining why tertiary peaks are only present for low nozzle heights.

With regard to the swirling impinging jets, the flow structures of each of the four designs examined is primarily determined by whether or not a swirl core is present. It was noted that the two sizes of generator with the central swirl core, L_c and S_c , produce similar flow regimes. The flow from each of these jets was seen to have a large radial dispersion as the distance from the jet nozzle increased, corresponding with past research [58, 73, 84]. The other two generators examined, L_{no} and S_{no} , which are the equivalent of the previous two generators without the swirl core in their design, were found to have similar flow characteristics, namely a concentration of the seeding used to visualise the flow at the outside of the jet. At low nozzle heights, recirculation of the flow towards the center of the jet can be inferred from the raw images obtained. While each of the swirling impinging jets demonstrate evidence of low heat transfer at $r/D=0$, the visualisation of recirculation explains the even further reduced heat transfer at this point by the swirling impinging jets employing generators L_{no} and S_{no} as seen in figure 5.11.

From the particle image velocimetry results of the each of the swirling impinging jets, the axial and azimuthal velocity profiles were extracted at a distance of approximately $5D$ from the nozzle exit. Using these profiles an estimation of the swirl number for each of the swirling impinging jets was established according to equation 2.4. The

respective swirl numbers for the swirling impinging jets with generators L_c , L_{no} , S_c and S_{no} were approximated as 0.127, 0.434, 0.157 and 0.289, significantly different from the values evaluated theoretically in section 3.1.1. The difference between these values can be associated with the fact that the swirl numbers estimated from the PIV analysis were done so at a significant distance from the nozzle exit, instead of at the nozzle exit itself. It may also be noted that the theoretical equations used in section 3.1.1 to estimate the swirl numbers of each of the swirling jets examined may not be suitable for the geometry presented in this study.

Chapter 7

Conclusion

7.1 Conclusions

The key aims of this study were to experimentally characterise and elucidate the heat transfer due to a contoured nozzle impinging jet and to evaluate and explain the enhancement which could be achieved by introducing a swirling flow in the same nozzle geometry. The heat transfer characteristics were measured by way of two methods; infrared thermography for a uniform wall flux thermal boundary condition and hot-film sensor analysis for a uniform wall temperature thermal boundary condition. Both systems produced valuable information regarding the local heat transfer due to each of five impinging jet set-ups: a conventional impinging jet and four swirling impinging jets. The hot-film sensor technique also allowed the fluctuations in local heat transfer to be determined. To elucidate the heat transfer results found through these methods, each of the impinging jet flows were visualised via high speed imaging and particle image velocimetry measurements. The following are the key findings in this study.

- The local heat transfer measurements gathered through the methods of infrared thermography and hot-film sensor analysis highlighted how a change in the experimental set-up and instrumentation can affect the measured result. It was observed that the Nusselt numbers obtained through the hot-film sensor analysis tended to be higher, especially in the stagnation region, than the equivalent results evaluated through infrared thermography. This difference in local Nusselt

7.1. CONCLUSIONS

number can be attributed largely to the spatial resolution of the two methods, with the hot-film sensor measuring over $\approx 0.1\text{ mm}$ while the thermal imaging camera employed had a spatial resolution of $\approx 0.5\text{ mm}$. While the heat transfer magnitudes were sensitive to the spatial resolution, the general trends in the Nusselt number distributions were consistent between the two measurement techniques.

- For the hot-film sensor analysis, it is necessary to calibrate the heat transfer due to the impinging jet by relating it to a known correlation under specific conditions. Since the range of nozzle to surface distances and Reynolds numbers examined in this study lies outside the range for the correlations commonly used for this purpose, a correlation for the stagnation point Nusselt number was established from the results obtained from the infrared thermography method. This correlation is a function of the Reynolds number of the impinging jet, Re for $8,000 \leq Re \leq 20,000$, and the height of the jet nozzle above the impingement surface, H/D for $0.5 \leq H/D \leq 10$.
- Relative to the conventional impinging jet, each of the four swirling impinging jets showed a level of heat transfer enhancement in the stagnation region for low nozzle to surface heights and high Reynolds numbers. The enhancement in heat transfer was primarily focused at $r/D \approx 0.6$ with increases of up to 20%. The overall increase in heat transfer was impeded by significant reductions at $r/D=0$ caused by the rotational nature of the swirling flow leading to a low velocity at the center of the jet and to the induced recirculation in the stagnation region for the swirl generators without the swirl core, L_{no} and S_{no} . At a height equivalent to $4D$, the swirling impinging jets were overtaken by the conventional impinging jet with regard to the mean heat transfer.
- Fluctuating Nusselt number distributions were used to assist in identifying local convective heat transfer mechanisms. In the case of the conventional impinging jet, a near zero region in the stagnation zone is followed by large increases in fluctuations caused by mixing in the shear layer of the jet and in the wall jet along the surface of the plate. The near zero region around the stagnation point

can be used to infer the length of the potential core of the jet and, on this basis, the potential core was estimated to be $6-8D$ in length, corresponding well to previous studies and to the height at which the Nusselt number is a maximum. This was also confirmed by particle image velocimetry measurements. For the swirling impinging jets, each show a consistent level of fluctuations at $r/D=0$ and increased levels at $r/D \approx 0.3$ for low H/D . While the majority of tests showed fluctuations to level off at this point, some showed increased fluctuations at extended radial locations, indicating that additional flow structures playing a role in those cases.

- Of the four swirl generators used to create an effective swirling impinging jet, the design of the generators without the swirl core, L_{no} and S_{no} , was shown to perform better than those with the central swirl core, L_c and S_c . While each of the generators led to some enhancement of heat transfer, the two simpler geometries, L_{no} and S_{no} , were shown to have had a greater impact. This allowed the conclusion to be made that the inclusion of the swirl core in the design diminished the positive influence that the generator may have on the heat transfer and that the scale of the swirl generator did not have a significant impact.
- Flow visualisation and particle image velocimetry of the flow structure for the conventional impinging jet at different nozzle heights allowed the mechanisms behind the tertiary peaks in the heat transfer distributions and significant fluctuation levels for low H/D to be determined. The vortical structures generated in the shear layer of the jet are seen to create new structures as they move across the impingement surface. These new vortices explain the increased levels of fluctuating heat transfer and the additional peaks in the Nusselt number distributions that have been identified. This phenomenon only occurs at low H/D since at higher H/D the vortices impinging upon the surface are not strong enough to generate the same effect. It is suggested that the appearance of these vortical structures and equivalent tertiary peaks in the local heat transfer distributions are a result of the contoured nozzle geometry, since this tertiary peak is not noted for straight pipe or orifice plate impinging jet geometries in past

7.1. CONCLUSIONS

studies.

- For the four swirling jets, the flow visualisation identifies two clear flow fields, one for the jets with the central swirl core and one for the jets without this feature. The jets with the swirl core, L_c and S_c , showed large, unstructured flows which spread radially outwards with increasing distance from the jet nozzle. The jets without the swirl core, L_{no} and S_{no} , developed a concentration of seeding particles at the outer edge of the jet flow, illustrated further with planar views of the jet. The latter case also displayed recirculation of the flow inwards as the jet impinges upon the heated surface, which explains the measured decrease in the heat transfer at the center of the jet.

7.2 Further Work

To further this study the following investigations are suggested:

- Increase the size of the nozzle geometry while keeping the aspect ratio consistent to identify the vortex structure of the conventional impinging jet before and after impingement more clearly. The relationship between the tertiary peak in the local heat transfer distributions for the conventional impinging jet at low nozzle heights and the contoured geometry of the nozzle can also be investigated.
- Conduct a study taking a closer look at the influence of the spatial resolution of different heat transfer measurement methods, such as different heat flux sensors on a surface approximating a uniform wall temperature thermal boundary condition. Also, by comparing the results obtained through the use of infrared thermal imaging cameras with different resolutions with an ohmically heated surface to attempt to replicate the findings of the hot-film sensor which has a high spatial resolution.
- Alter the angle of the guide vanes in generator L_{no} or S_{no} . In this study the guide vanes were set at an angle of 45° . By changing this to 0° , 15° and 60° , a full evaluation of the optimal swirl generator can be established.

Publications

Over the course of this study I have had the privilege of presenting my work at the following conferences and symposia:

- K.J. Brown, T. Persoons, T.S. O'Donovan and D.B. Murray. Heat transfer characteristics of swirling impinging jets. In *2009 ASME International Mechanical Engineering Congress & Exposition : IMECE2009* – 11179
- K.J. Brown. Heat transfer characteristics of swirling impinging jets. In *13th Annual Sir Bernard Crossland Symposium* April 28 – 29, 2010, *University College Dublin, Dublin, Ireland.*
- K.J. Brown, T. Persoons, and D.B. Murray. Heat transfer characteristics of swirling impinging jets. In *14th International Heat Transfer Conference : IHTC14* – 22860
- K.J. Brown, T. Persoons, and D.B. Murray. Examination of the local and fluctuating heat transfer due to swirling impinging jets impinging upon a heat surface. In *6th Baltic Heat Transfer Conference*
- K.J. Brown, G. Byrne, T.S. O'Donovan and D.B. Murray. Effect of thermal boundary condition on heat dissipation due to swirling jet impingement on a heated plate. *6th European Thermal Sciences Conference – Eurotherm 2012*

I have also been involved in the following:

- T. Persoons, K. Balgazin, K. Brown and D.B. Murray. Scaling of convective heat transfer enhancement due to flow pulsation in an axisymmetric impinging jet. *Journal of Heat Transfer* - Under review

Bibliography

- [1] G.E. Moore. Cramming more components onto integrated circuits, reprinted from electronics, volume 38, number 8, april 19, 1965, pp. 114 ff. *Solid-State Circuits Newsletter, IEEE*, 11(5):33–35, 2006.
- [2] A. Dewan, R. Dutta, and B. Srinivasan. Recent trends in computation of turbulent jet impingement heat transfer. *Heat Transfer Engineering*, 33(4-5):447–460, 2012.
- [3] R. Gardon and J.C. Akfirat. The role of turbulence in determining the heat-transfer characteristics of impinging jets. *International Journal of Heat and Mass Transfer*, 8(10):1261–1272, 1965.
- [4] R. Örlü and P.H. Alfredsson. The life of a vortex in an axisymmetric jet. *Journal of Visualization*, 14(1):5–6, 2011.
- [5] I.P.D. De Silva, H.J.S. Fernando, F. Eaton, and D. Hebert. Evolution of Kelvin-Helmholtz billows in nature and laboratory. *Earth and Planetary Science Letters*, 143(1):217–231, 1996.
- [6] F. Incropera. *Liquid cooling of electronic devices by single phase convection*. New York: John Wiley & Sons, 1999.
- [7] F. Beaubert and S. Viazzo. Large eddy simulations of plane turbulent impinging jets at moderate Reynolds numbers. *International Journal of Heat and Fluid Flow*, 24(4):512–519, 2003.

BIBLIOGRAPHY

- [8] S. Ashforth-Frost and K. Jambunathan. Effect of nozzle geometry and semi-confinement on the potential core of a turbulent axisymmetric free jet. *International Communications in Heat and Mass Transfer*, 23(2):155–162, 1996.
- [9] F.P. Incropera and D.P. DeWitt. *Fundamentals of Mass and Heat Transfer*. New York: John Wiley & Sons, 6 edition, 2007.
- [10] C.J. Hoogendoorn. The effect of turbulence on heat transfer at a stagnation point. *International Journal of Heat and Mass Transfer*, 20(12):1333–1338, 1977.
- [11] D. Lytle and B.W. Webb. Air jet impingement heat transfer at low nozzle-plate spacings. *International Journal of Heat and Mass Transfer*, 37(12):1687–1697, 1994.
- [12] B.N. Pamadi and I.A. Belov. A note on the heat transfer characteristics of circular impinging jet. *International Journal of Heat and Mass Transfer*, 23(6):783–787, 1980.
- [13] K. Jambunathan, E. Lai, M.A. Moss, and B.L. Button. A review of heat transfer data for single circular jet impingement. *International Journal of Heat and Fluid Flow*, 13(2):106–115, 1992.
- [14] E.U. Schundler and V. Gnielinski. Heat and mass transfer between surfaces and impinging jets. *Chemical Engineering and Technology*, 39:578–584, 1967.
- [15] R. Gardon and J. Cobonpue. Heat transfer between a flat plate and jets of air impinging on it. *Int. Dev. Heat Transfer (ASME)*, pages 454–460, 1962.
- [16] T.S. O’Donovan, T. Persoons, and D.B. Murray. High-resolution hot-film measurement of surface heat flux to an impinging jet. *Measurement Science and Technology*, 22:105402, 2011.
- [17] B. Sagot, G. Antonini, A. Christgen, and F. Buron. Jet impingement heat transfer on a flat plate at a constant wall temperature. *International Journal of Thermal Sciences*, 47(12):1610–1619, 2008.

- [18] R. Neddermeyer. Module 2 - model: Body ambient bondgraph model using heat flux transducer. <http://cnx.org/content/m16249/latest/?collection=col110530/latest>. May, 2008.
- [19] J.W. Scholten and D.B. Murray. Unsteady heat transfer and velocity of a cylinder in cross flow–I. Low freestream turbulence. *International Journal of Heat and Mass Transfer*, 41(10):1139–1148, 1998.
- [20] J.W. Baughn and S. Shimizu. Heat transfer measurements from a surface with uniform heat flux and an impinging jet. *Journal of Heat Transfer (Transactions of the ASME, Series C);(United States)*, 111(4), 1989.
- [21] P. Gulati, V. Katti, and S.V. Prabhu. Influence of the shape of the nozzle on local heat transfer distribution between smooth flat surface and impinging air jet. *International Journal of Thermal Sciences*, 48(3):602–617, 2009.
- [22] D.R.S. Guerra, J. Su, and A.P. Silva Freire. The near wall behavior of an impinging jet. *International Journal of Heat and Mass Transfer*, 48(14):2829–2840, 2005.
- [23] M.D. Limaye, R.P. Vedula, and S.V. Prabhu. Local heat transfer distribution on a flat plate impinged by a compressible round air jet. *International Journal of Thermal Sciences*, 49(11):2157–2168, 2010.
- [24] J.P. Holman. *Heat Transfer*. McGraw-Hill, 9 edition, 2008.
- [25] J. Mi, D.S. Nobes, and G.J. Nathan. Influence of jet exit conditions on the passive scalar field of an axisymmetric free jet. *Journal of Fluid Mechanics*, 432(1):91–125, 2001.
- [26] T.S. O’Donovan. *Fluid Flow and Heat Transfer of an Impinging Air Jet*. PhD thesis, Dept. of Mechanical and Manufacturing Engineering, University of Dublin, Trinity College, 2005.

BIBLIOGRAPHY

- [27] T.S. O'Donovan and D.B. Murray. Jet impingement heat transfer—Part I: Mean and root-mean-square heat transfer and velocity distributions. *International Journal of Heat and Mass Transfer*, 50(17):3291–3301, 2007.
- [28] T.S. O'Donovan and D.B. Murray. Jet impingement heat transfer—Part II: A temporal investigation of heat transfer and local fluid velocities. *International Journal of Heat and Mass Transfer*, 50(17):3302–3314, 2007.
- [29] R.J. Goldstein and A.I. Behbahani. Impingement of a circular jet with and without cross flow. *International Journal of Heat and Mass Transfer*, 25(9):1377–1382, 1982.
- [30] M. Emin Arzutug, S. Yapici, and M. Muhtar Kocakerim. A comparison of mass transfer between a plate and submerged conventional and multichannel impinging jets. *International Communications in Heat and Mass Transfer*, 32(6):842–854, 2005.
- [31] T. Liu and J.P. Sullivan. Heat transfer and flow structures in an excited circular impinging jet. *International Journal of Heat and Mass Transfer*, 39(17):3695–3706, 1996.
- [32] R.J. Goldstein, A.I. Behbahani, and K.K. Heppelmann. Streamwise distribution of the recovery factor and the local heat transfer coefficient to an impinging circular air jet. *International Journal of Heat and Mass Transfer*, 29(8):1227–1235, 1986.
- [33] J. Lee and S.J. Lee. The effect of nozzle configuration on stagnation region heat transfer enhancement of axisymmetric jet impingement. *International Journal of Heat and Mass Transfer*, 43(18):3497–3510, 2000.
- [34] M. Behnia, S. Parneix, Y. Shabany, and P.A. Durbin. Numerical study of turbulent heat transfer in confined and unconfined impinging jets. *International Journal of Heat and Fluid Flow*, 20(1):1–9, 1999.
- [35] M. Fenot, J.J. Vullierme, and E. Dorignac. Local heat transfer due to several configurations of circular air jets impinging on a flat plate with and without

- semi-confinement. *International Journal of Thermal Sciences*, 44(7):665–675, 2005.
- [36] T.L. Lupton, D.B. Murray, and A.J. Robinson. Confinement effects in heat transfer to a miniature compressible impinging air jet. In *ASME–JSME Thermal Engineering Summer Heat Transfer Conference : HT2007–32754*, 2007.
- [37] M.F. Koseoglu and S. Baskaya. The effect of flow field and turbulence on heat transfer characteristics of confined circular and elliptic impinging jets. *International Journal of Thermal Sciences*, 47(10):1332–1346, 2008.
- [38] M.F. Koseoglu and S. Baskaya. Experimental and numerical investigation of natural convection effects on confined impinging jet heat transfer. *International Journal of Heat and Mass Transfer*, 52(5-6):1326–1336, 2009.
- [39] D.W. Colucci and R. Viskanta. Effect of nozzle geometry on local convective heat transfer to a confined impinging air jet. *Experimental Thermal and Fluid Science*, 13(1):71–80, 1996.
- [40] J.A. Fitzgerald and S.V. Garimella. A study of the flow field of a confined and submerged impinging jet. *International Journal of Heat and Mass Transfer*, 41(8):1025–1034, 1998.
- [41] S.V. Garimella and V.P. Schroeder. Local heat transfer distributions in confined multiple air jet impingement. *Journal of Electronic Packaging*, 123:165, 2001.
- [42] L.F.G. Geers, M.J. Tummers, T.J. Bueninck, and K. Hanjalić. Heat transfer correlation for hexagonal and in-line arrays of impinging jets. *International Journal of Heat and Mass Transfer*, 51(21):5389–5399, 2008.
- [43] S.V. Garimella and B. Nenaydykh. Nozzle-geometry effects in liquid jet impingement heat transfer. *International Journal of Heat and Mass Transfer*, 39(14):2915–2923, 1996.
- [44] P.S. Shadlesky. Stagnation point heat transfer for jet impingement to a plane surface. *AIAA Journal*, 21:1214–1215, 1983.

BIBLIOGRAPHY

- [45] T.S. O'Donovan and D.B. Murray. Fluctuating fluid flow and heat transfer of an obliquely impinging air jet. *International Journal of Heat and Mass Transfer*, 51(25-26):6169–6179, 2008.
- [46] O. Vipat, S.S. Feng, T. Kim, A.M. Pradeep, and T.J. Lu. Asymmetric entrainment effect on the local surface temperature of a flat plate heated by an obliquely impinging two-dimensional jet. *International Journal of Heat and Mass Transfer*, 52(21):5250–5257, 2009.
- [47] N. Gao, H. Sun, and D. Ewing. Heat transfer to impinging round jets with triangular tabs. *International Journal of Heat and Mass Transfer*, 46(14):2557–2569, 2003.
- [48] S. Bhattacharya and A. Ahmed. A note on unsteady impinging jet heat transfer. *Experimental Thermal and Fluid Science*, 34(5):633–637, 2010.
- [49] N. Celik and H. Eren. Heat transfer due to impinging co-axial jets and the jets' fluid flow characteristics. *Experimental Thermal and Fluid Science*, 33(4):715–727, 2009.
- [50] G. Krishnan and K. Mohseni. An experimental study of a radial wall jet formed by the normal impingement of a round synthetic jet. *European Journal of Mechanics-B/Fluids*, 29(4):269–277, 2010.
- [51] Z. Trávníček and V. Tesař. Annular synthetic jet used for impinging flow mass-transfer. *International Journal of Heat and Mass Transfer*, 46(17):3291–3297, 2003.
- [52] A. McGuinn, T.S. O'Donovan, and D.B. Murray. Heat transfer measurements of impinging synthetic air jet. In *ASME–JSME Thermal Engineering Summer Heat Transfer Conference : HT2007–32084*, 2007.
- [53] R. Farrelly, A. McGuinn, T. Persoons, and D.B. Murray. Heat transfer behaviour and flow field characterisation of impinging synthetic jets for a wide range of parameters. In *14th International Heat Transfer Conference : IHTC14–22864*, 2010.

- [54] T. Persoons, A. McGuinn, and D.B. Murray. A general correlation for the stagnation point Nusselt number of an axisymmetric impinging synthetic jet. *International Journal of Heat and Mass Transfer*, 54:3900–3908, 2011.
- [55] M. Chaudhari, B. Puranik, and A. Agrawal. Heat transfer characteristics of synthetic jet impingement cooling. *International Journal of Heat and Mass Transfer*, 53(5-6):1057–1069, 2010.
- [56] A. Shiri, W.K. George, and J.W. Naughton. Experimental study of the far field of incompressible swirling jets. *AIAA Journal*, 46(8):2002, 2008.
- [57] A.K. Gupta. *Swirl flows*. Technomic Publishing Co., Lancaster, PA, 1984.
- [58] S.V. Alekseenko, V.M. Dulin, Y.S. Kozorezov, and D.M. Markovich. Effect of axisymmetric forcing on the structure of a swirling turbulent jet. *International Journal of Heat and Fluid Flow*, 29(6):1699–1715, 2008.
- [59] J. Ward and M. Mahmood. Heat transfer from a turbulent, swirling, impinging jet. In *Heat Transfer 1982, Volume 3*, volume 3, pages 401–407, 1982.
- [60] J. Ward. The effect of swirl on mass/heat transfer from arrays of turbulent, impinging jets. In *The 1993 ASME Winter Annual Meeting, New Orleans, LA, USA, 11/28-12/03/93*, pages 57–64, 1993.
- [61] A. Shiri. *Turbulence measurements in a natural convection boundary layer and a swirling jet*. PhD thesis, Department of Applied Mechanics, Chalmers University of Technology, Göteborg, Sweden, 2010.
- [62] I.K. Toh, D. Honnery, and J. Soria. Axial plus tangential entry swirling jet. *Experiments in Fluids*, 48(2):309–325, 2010.
- [63] I.K. Toh, D. Honnery, and J. Soria. Velocity and scalar measurements of a low swirl jet. In *Proc. 4th Australian Conf. Laser Diagnostics Fluid Mech. Comb.*, pages 129–132, 2005.

BIBLIOGRAPHY

- [64] R.B. Wicker and J.K. Eaton. Structure of a swirling, recirculating coaxial free jet and its effect on particle motion. *International Journal of Multiphase Flow*, 27(6):949–970, 2001.
- [65] W. Lee, Y. Park, K. Kwon, and R. Taghavi. Control of shear perturbation in coaxial swirling turbulent jets. *Aerospace Science and Technology*, 14(7):472–486, 2010.
- [66] K. Ichimiya and K. Tsukamoto. Heat transfer characteristics of a swirling laminar impinging jet. *Journal of Heat Transfer*, 132:012201, 2010.
- [67] K.S. Yajnik and M.V. Subbaiah. Experiments on swirling turbulent flows. Part 1. Similarity in swirling flows. *Journal of Fluid Mechanics*, 60:665–687, 1973.
- [68] K. Bakirci and K. Bilen. Visualization of heat transfer for impinging swirl flow. *Experimental Thermal and Fluid Science*, 32(1):182–191, 2007.
- [69] S.V. Alekseenko, A.V. Bilsky, V.M. Dulin, and D.M. Markovich. Experimental study of an impinging jet with different swirl rates. *International Journal of Heat and Fluid Flow*, 28(6):1340–1359, 2007.
- [70] R. Majidi and R. So. Swirl effects on variable-density jet mixing in confined flows. *International Journal of Heat and Fluid Flow*, 9(4):366–372, 1988.
- [71] M. Senda, K. Inaoka, D. Toyoda, and S. Sato. Heat transfer and fluid flow characteristics in a swirling impinging jet. In *National Heat Transfer Symposium of Japan*, volume 3, pages 621–622. Japan Heat Transfer Society; 1999, 2003.
- [72] D.H. Lee, S.Y. Won, Y.T. Kim, and Y.S. Chung. Turbulent heat transfer from a flat surface to a swirling round impinging jet. *International Journal of Heat and Mass Transfer*, 45(1):223–227, 2002.
- [73] L. Huang and M.S. El-Genk. Heat transfer and flow visualization experiments of swirling, multi-channel, and conventional impinging jets. *International Journal of Heat and Mass Transfer*, 41(3):583–600, 1998.

- [74] M.Y. Wen. Flow structures and heat transfer of swirling jet impinging on a flat surface with micro-vibrations. *International Journal of Heat and Mass Transfer*, 48(3):545–560, 2005.
- [75] Z.X. Yuan, Y.Y. Chen, J.G. Jiang, and C.F. Ma. Swirling effect of jet impingement on heat transfer from a flat surface to CO₂ stream. *Experimental Thermal and Fluid Science*, 31(1):55–60, 2006.
- [76] K. Nanan, K. Wongcharee, C. Nuntadusit, and S. Eiamsa-ard. Forced convective heat transfer by swirling impinging jets issuing from nozzles equipped with twisted tapes. *International Communications in Heat and Mass Transfer*, 2012.
- [77] C. Nuntadusit, M. Wae-hayee, A. Bunyajitradulya, and S. Eiamsa-ard. Visualization of flow and heat transfer characteristics for swirling impinging jet. *International Communications in Heat and Mass Transfer*, 2012.
- [78] C. Nuntadusit, M. Wae-hayee, A. Bunyajitradulya, and S. Eiamsa-ard. Heat transfer enhancement by multiple swirling impinging jets with twisted-tape swirl generators. *International Communications in Heat and Mass Transfer*, 2011.
- [79] A. Nozaki, Y. Igarashi, and K. Hishida. Heat transfer mechanism of a swirling impinging jet in a stagnation region. *Heat Transfer–Asian Research*, 32(8):663–673, 2003.
- [80] C. Kinsella, B. Donnelly, T.S. O’Donovan, and D.B. Murray. Heat transfer enhancement from a horizontal surface by impinging jet swirls. In *5th European Thermal Sciences Conference, Eindhoven*, 2008.
- [81] M. Yilmaz, Ö. Çomakli, and S. Yapici. Enhancement of heat transfer by turbulent decaying swirl flow. *Energy Conversion and Management*, 40(13):1365–1376, 1999.
- [82] J. Ortega-Casanova. CFD and correlations of the heat transfer from a wall at constant temperature to an impinging swirling jet. *International Journal of Heat and Mass Transfer*, 55(21–22):5836–5845, 2012.

BIBLIOGRAPHY

- [83] H.J. Sheen, W.J. Chen, S.Y. Jeng, and T.L. Huang. Correlation of swirl number for a radial-type swirl generator. *Experimental Thermal and Fluid Science*, 12(4):444–451, 1996.
- [84] P. Billant, J.M. Chomaz, and P. Huerre. Experimental study of vortex breakdown in swirling jets. *Journal of Fluid Mechanics*, 376:183–219, 1998.
- [85] Y. Maciel, L. Facciolo, C. Duwig, L. Fuchs, and P.H. Alfredsson. Near-field dynamics of a turbulent round jet with moderate swirl. *International Journal of Heat and Fluid Flow*, 29(3):675–686, 2008.
- [86] S. Matsubara, H. Gotoda, A. Adzlan, and T. Ueda. Experiments on dynamic behavior of near-field region in variable property jet with swirling flow. *Experiments in Fluids*, pages 1–11, 2011.
- [87] C.O. Popiel and O. Trass. Visualization of a free and impinging round jet. *Experimental Thermal and Fluid Science*, 4(3):253–264, 1991.
- [88] E. Baydar and Y. Ozmen. An experimental investigation on flow structures of confined and unconfined impinging air jets. *Heat and Mass Transfer*, 42(4):338–346, 2006.
- [89] M. Raffel, C.E. Willert, and J. Kompenhans. *Particle image velocimetry: a practical guide*. Springer Verlag, 1998.
- [90] M. Felli, M. Falchi, and F.J.A. Pereira. Distance effect on the behavior of an impinging swirling jet by PIV and flow visualizations. *Experiments in Fluids*, 48(2):197–209, 2010.
- [91] P. Burattini, G. Buresti, and A. Talamelli. Dynamics of heavy particles in two swirling jets. *Experimental Thermal and Fluid Science*, 33(2):215–221, 2009.
- [92] T. Fujii and H. Imura. Natural-convection heat transfer from a plate with arbitrary inclination. *International Journal of Heat and Mass Transfer*, 15(4):755–767, 1972.

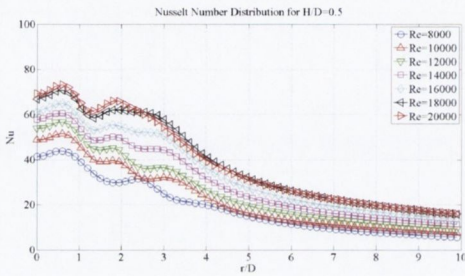
- [93] M. Thirumaleshwar. *Fundamentals of Heat and Mass Transfer*. Pearson, 2006.
- [94] G. Hetsroni, R. Rozenblit, and L.P. Yarin. A hot-foil infrared technique for studying the temperature field of a wall. *Measurement Science and Technology*, 7(10):1418, 1999.
- [95] V.A. Patil and V. Narayanan. Application of heated-thin-foil thermography technique to external convective microscale flows. *Measurement Science and Technology*, 16(2):472, 2005.
- [96] T. Lupton. *Recovery Factor and Conjugate Heat Transfer for Micro Jet Impingement*. PhD thesis, Dept. of Mechanical and Manufacturing Engineering, University of Dublin, Trinity College, 2010.
- [97] T. Astarita, G. Cardone, G.M. Carlomagno, and C. Meola. A survey on infrared thermography for convective heat transfer measurements. *Optics & Laser Technology*, 32(7):593–610, 2000.
- [98] S. Hosder. Unsteady skin-friction measurements on a manoeuvring DARPA2 sub-off model. Master’s thesis, Dept. of Aerospace and Ocean Engineering, Virginia Polytechnic Institute and State University, Virginia, USA, 2001.
- [99] G.J. Kunkel and I. Marusic. An approximate amplitude attenuation correction for hot-film shear stress sensors. *Experiments in Fluids*, 34(2):285–290, 2003.
- [100] D.E. Beasley and R.S. Figliola. A generalised analysis of a local heat flux probe. *Journal of Physics E: Scientific Instruments*, 21:316, 1988.
- [101] J.S. Scholten. *Fluctuating heat transfer of cylinders in cross flow*. PhD thesis, Dept. of Mechanical and Manufacturing Engineering, University of Dublin, Trinity College, 1996.
- [102] H.W. Coleman and W.G. Steele. *Experimentation, Validation, and Uncertainty Analysis for Engineers*. Wiley, 2009.
- [103] D.C. Montgomery and E.A. Peck. *Introduction to Linear Regression Analysis*. Wiley, 1992.

Appendix

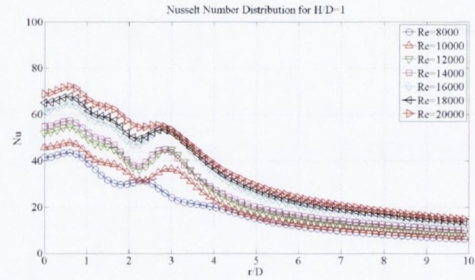
Appendix A - Heat Transfer Results

A.1 Case 1 : Nusselt Number Distribution

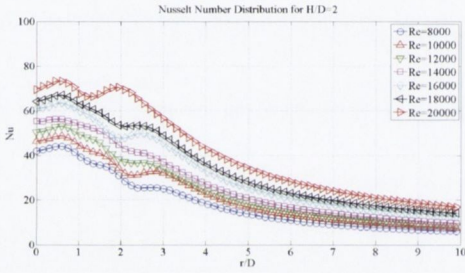
A.1.1 Conventional Impinging Jet



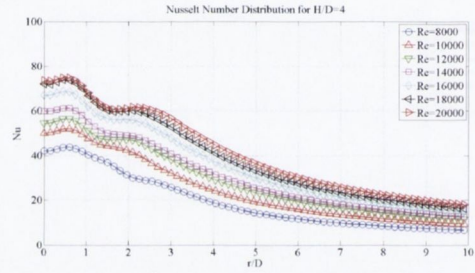
(a)



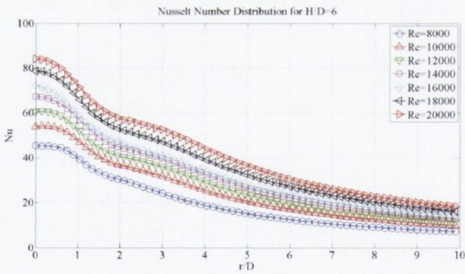
(b)



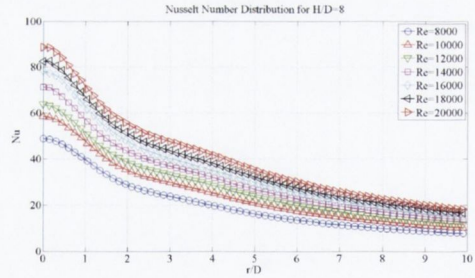
(c)



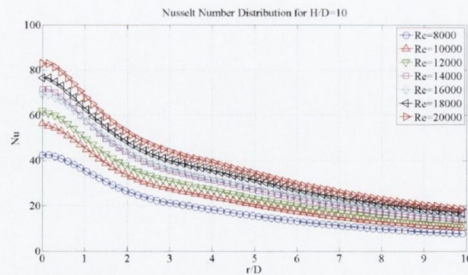
(d)



(e)



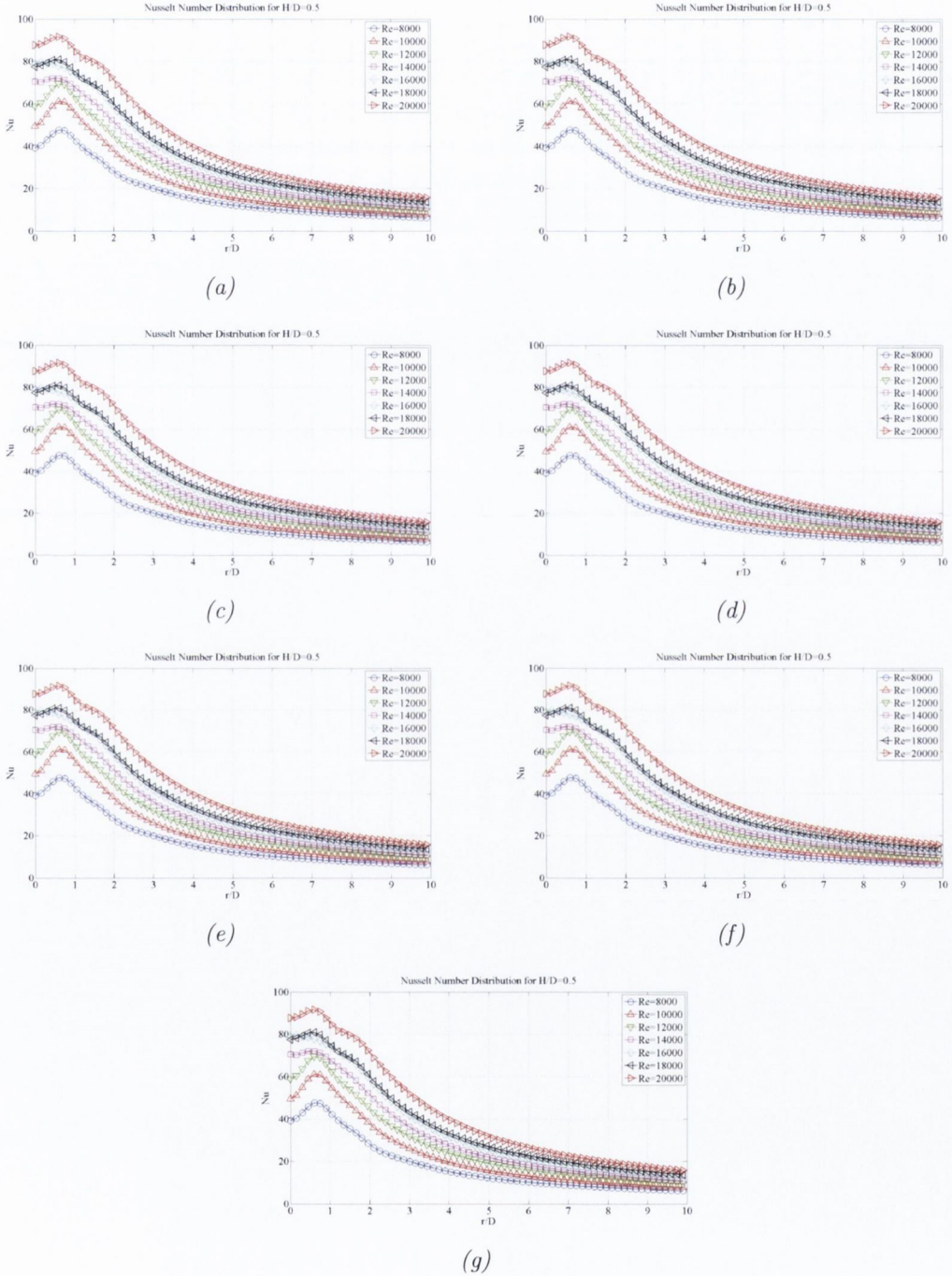
(f)



(g)

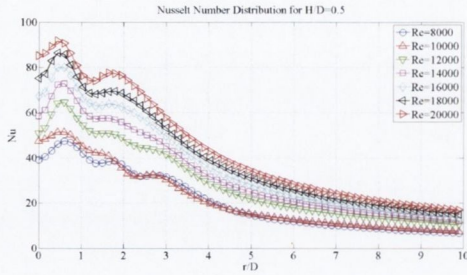
Case 1: Local Nusselt number distribution for conventional impinging jet for all Reynolds numbers at $H/D =$ (a) 0.5, (b) 1, (c) 2, (d) 4, (e) 6, (f) 8, (g) 10

A.1.2 Swirling Impinging Jet with Generator L_c

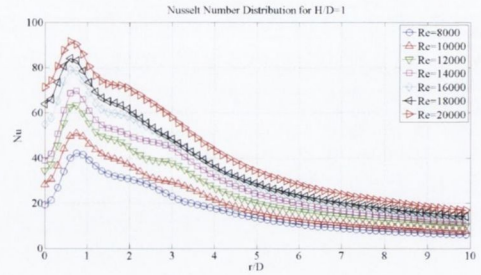


Case 1: Local Nusselt number distribution for swirling impinging jet with generator L_c for all Reynolds numbers at $H/D =$ (a) 0.5, (b) 1, (c) 2, (d) 4, (e) 6, (f) 8, (g) 10

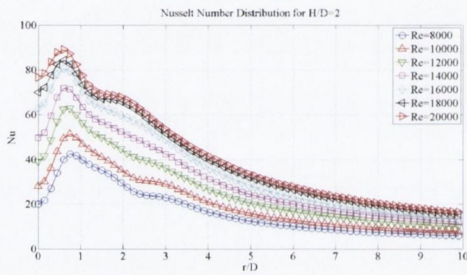
A.1.3 Swirling Impinging Jet with Generator L_{no}



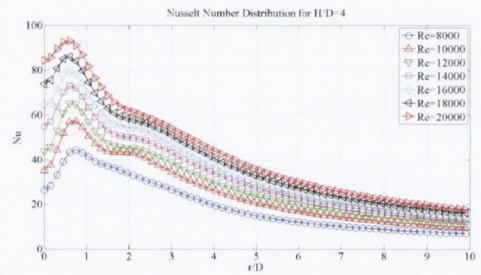
(a)



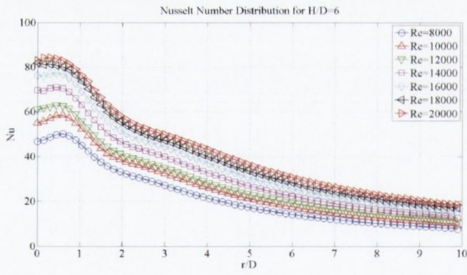
(b)



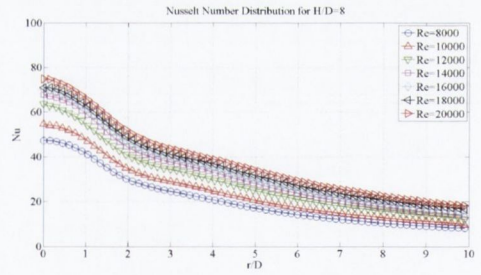
(c)



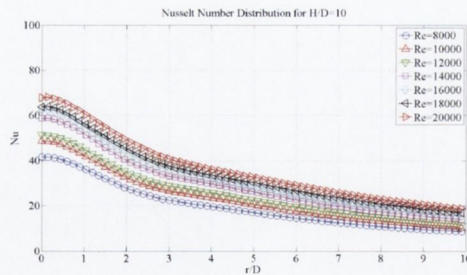
(d)



(e)



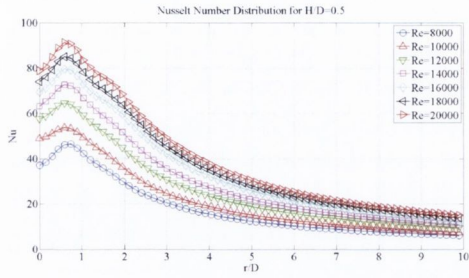
(f)



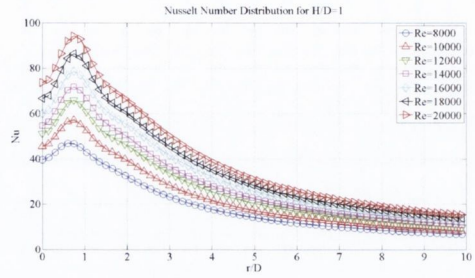
(g)

Case 1: Local Nusselt number distribution for swirling impinging jet with generator L_{no} for all Reynolds numbers at $H/D =$ (a) 0.5, (b) 1, (c) 2, (d) 4, (e) 6, (f) 8, (g) 10

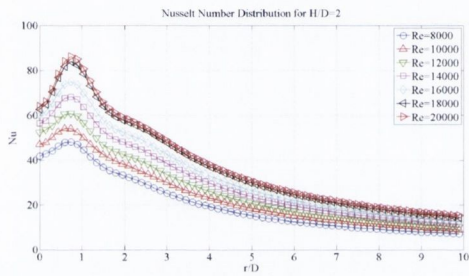
A.1.4 Swirling Impinging Jet with Generator S_c



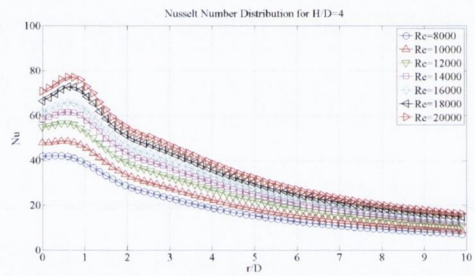
(a)



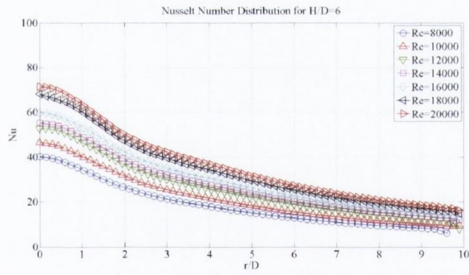
(b)



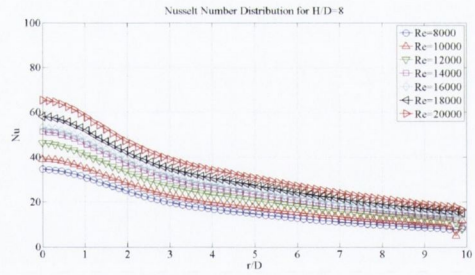
(c)



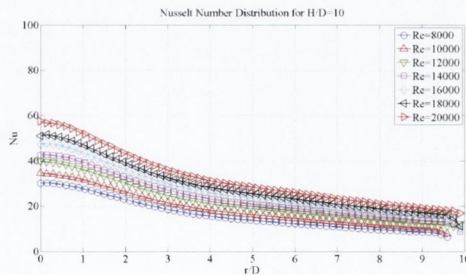
(d)



(e)



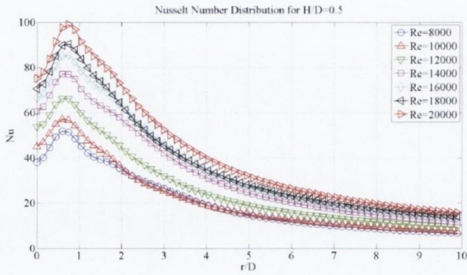
(f)



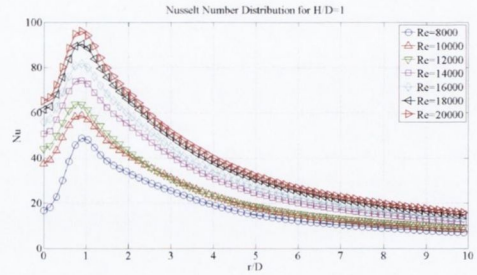
(g)

Case 1: Local Nusselt number distribution for swirling impinging jet with generator S_c for all Reynolds numbers at $H/D =$ (a) 0.5, (b) 1, (c) 2, (d) 4, (e) 6, (f) 8, (g) 10

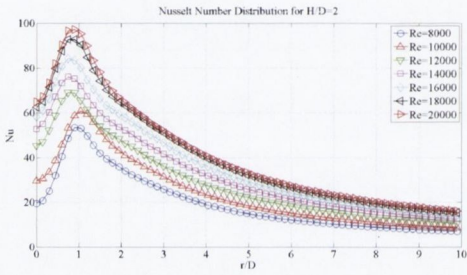
A.1.5 Swirling Impinging Jet with Generator S_{no}



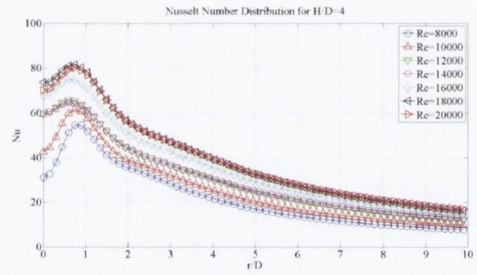
(a)



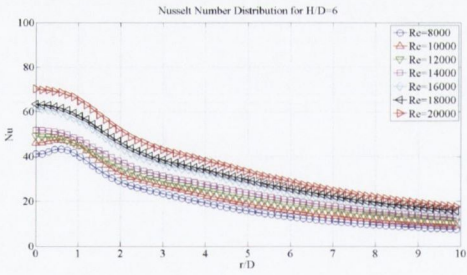
(b)



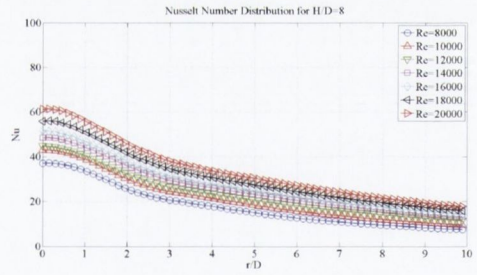
(c)



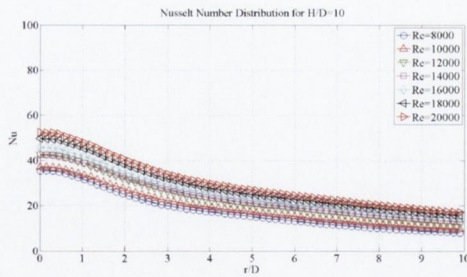
(d)



(e)



(f)

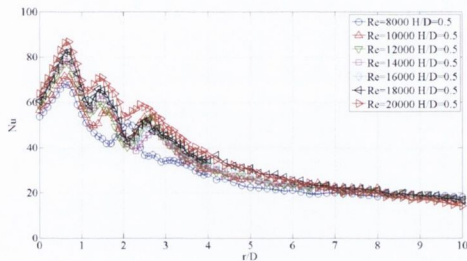


(g)

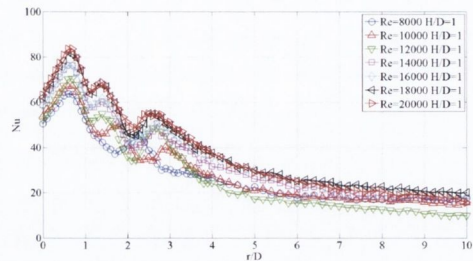
Case 1: Local Nusselt number distribution for swirling impinging jet with generator S_{no} for all Reynolds numbers at $H/D =$ (a) 0.5, (b) 1, (c) 2, (d) 4, (e) 6, (f) 8, (g) 10

A.2 Case 2 : Nusselt Number Distribution

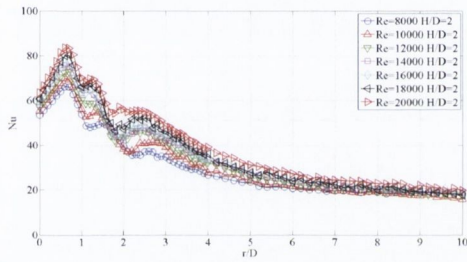
A.2.1 Conventional Impinging Jet



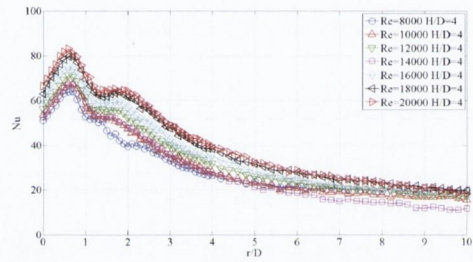
(a)



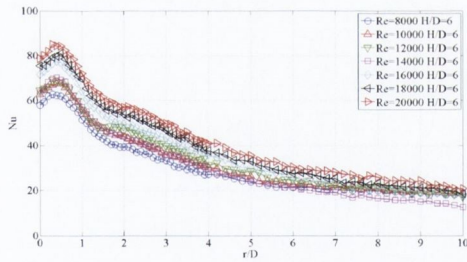
(b)



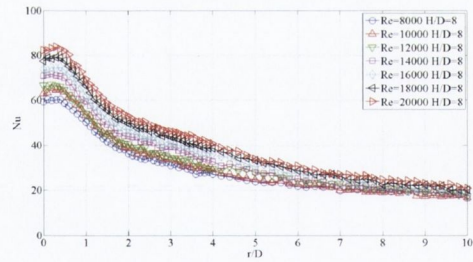
(c)



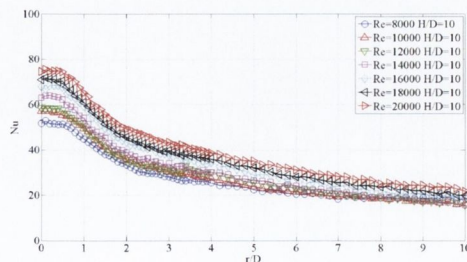
(d)



(e)



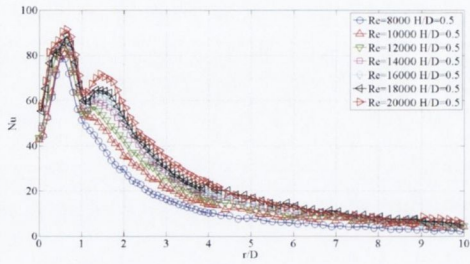
(f)



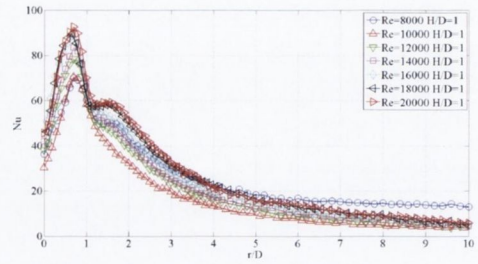
(g)

Case 2: Local Nusselt number distribution for conventional impinging jet for all Reynolds numbers at $H/D =$ (a) 0.5, (b) 1, (c) 2, (d) 4, (e) 6, (f) 8, (g) 10

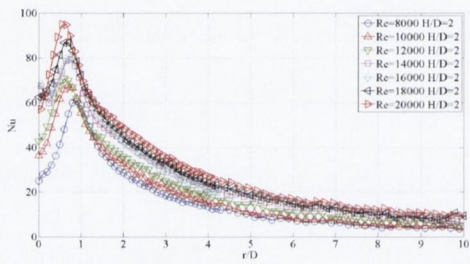
A.2.2 Swirling Impinging Jet with Generator L_c



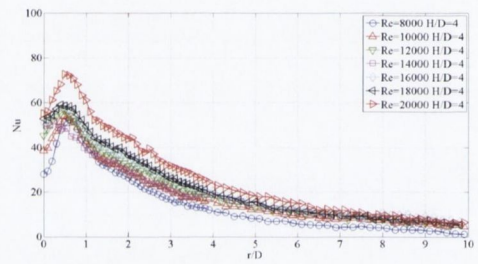
(a)



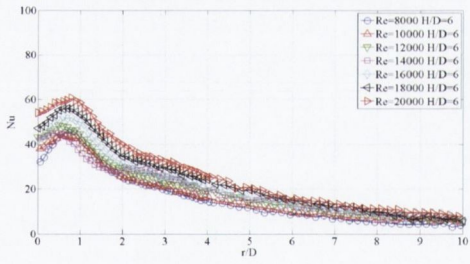
(b)



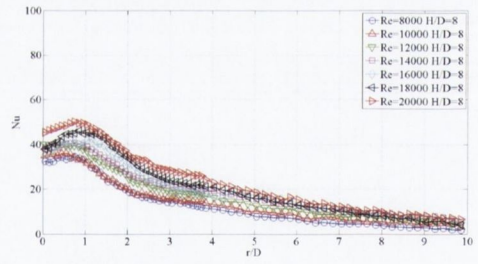
(c)



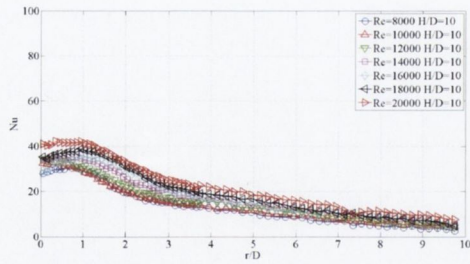
(d)



(e)



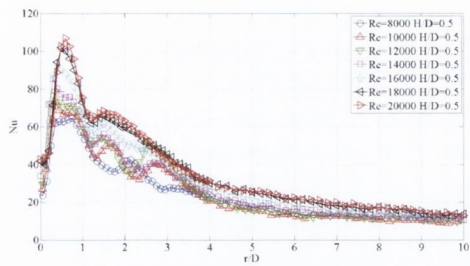
(f)



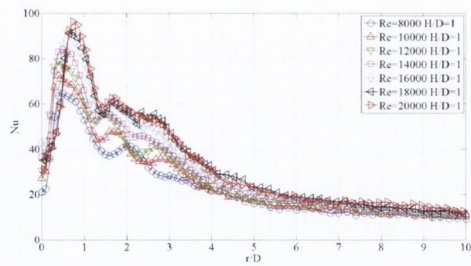
(g)

Case 2: Local Nusselt number distribution for swirling impinging jet with generator L_c for all Reynolds numbers at $H/D =$ (a) 0.5, (b) 1, (c) 2, (d) 4, (e) 6, (f) 8, (g) 10

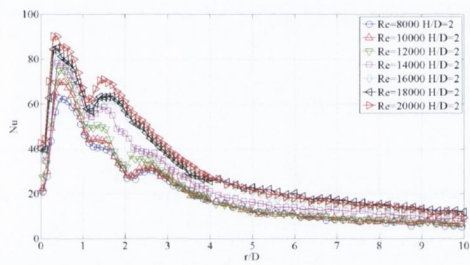
A.2.3 Swirling Impinging Jet with Generator L_{no}



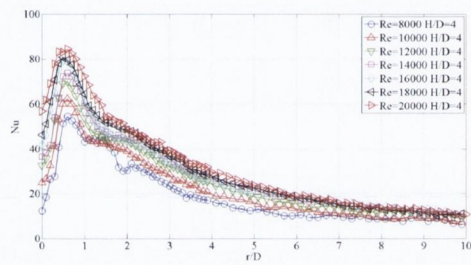
(a)



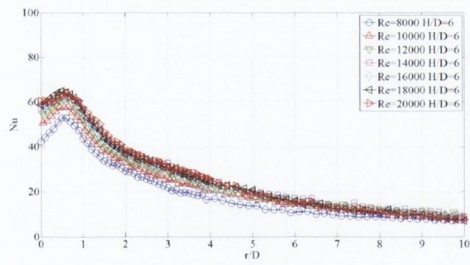
(b)



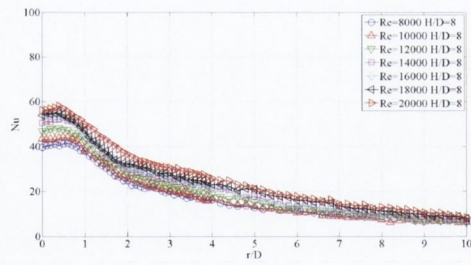
(c)



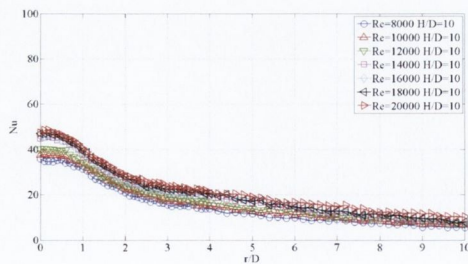
(d)



(e)



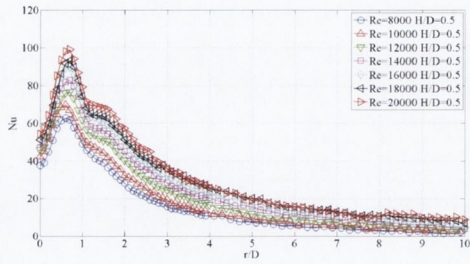
(f)



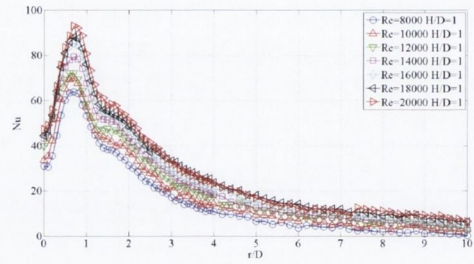
(g)

Case 2: Local Nusselt number distribution for swirling impinging jet with generator L_{no} for all Reynolds numbers at $H/D =$ (a) 0.5, (b) 1, (c) 2, (d) 4, (e) 6, (f) 8, (g) 10

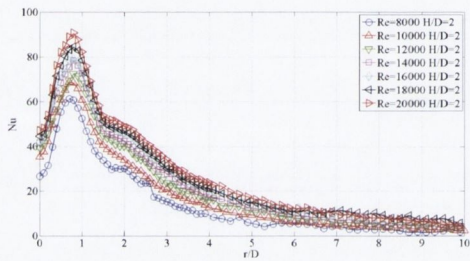
A.2.4 Swirling Impinging Jet with Generator S_c



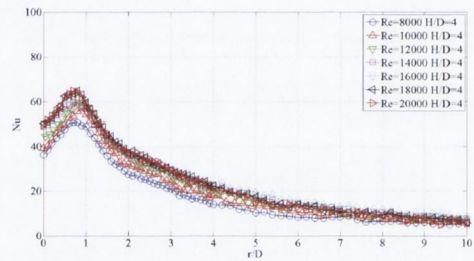
(a)



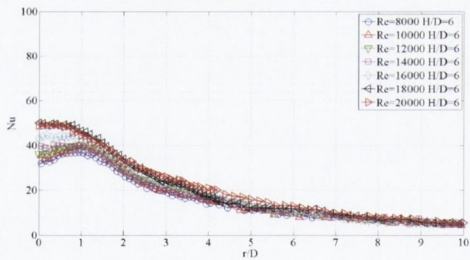
(b)



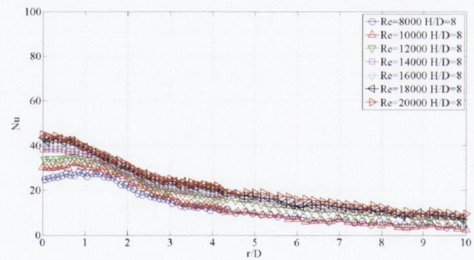
(c)



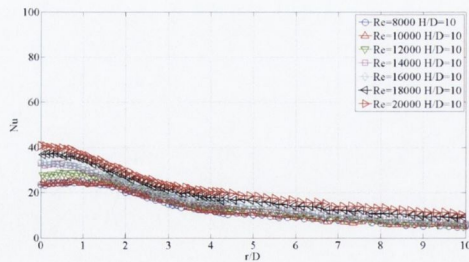
(d)



(e)



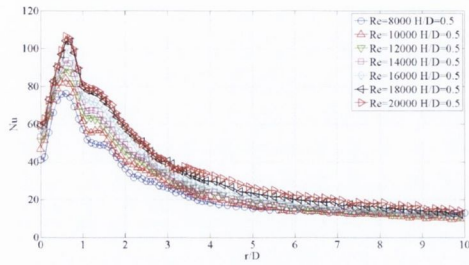
(f)



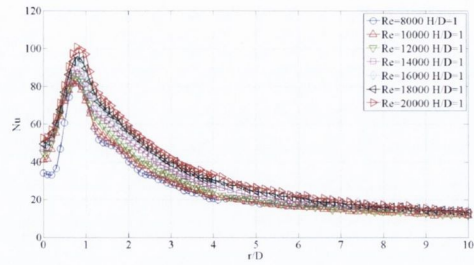
(g)

Case 2: Local Nusselt number distribution for swirling impinging jet with generator S_c for all Reynolds numbers at $H/D =$ (a) 0.5, (b) 1, (c) 2, (d) 4, (e) 6, (f) 8, (g) 10

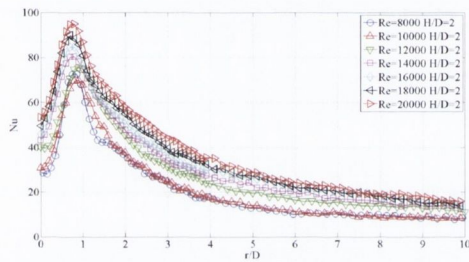
A.2.5 Swirling Impinging Jet with Generator S_{no}



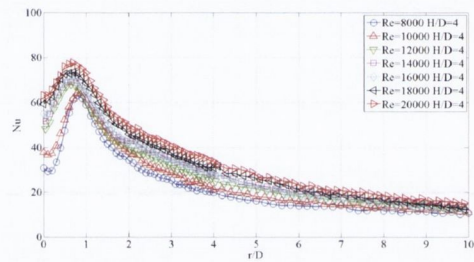
(a)



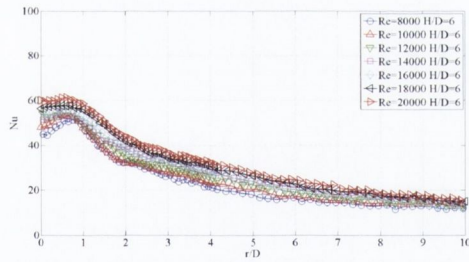
(b)



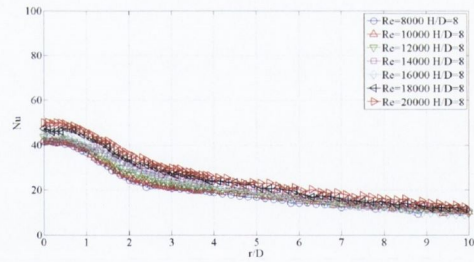
(c)



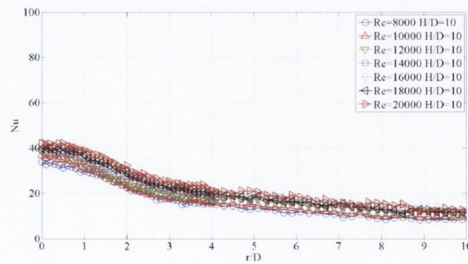
(d)



(e)



(f)

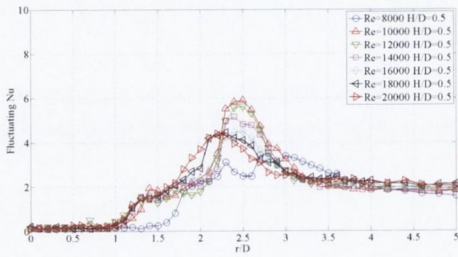


(g)

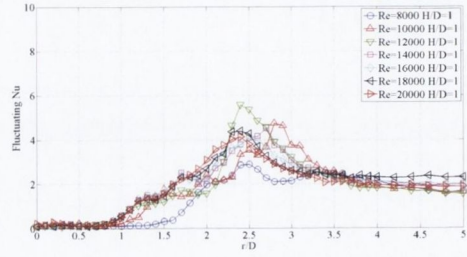
Case 2: Local Nusselt number distribution for swirling impinging jet with generator S_{no} for all Reynolds numbers at $H/D =$ (a) 0.5, (b) 1, (c) 2, (d) 4, (e) 6, (f) 8, (g) 10

A.3 Fluctuating Nusselt Number Distribution

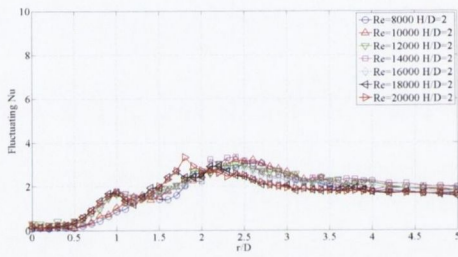
A.3.1 Conventional Impinging Jet



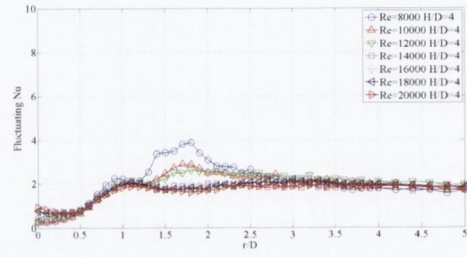
(a)



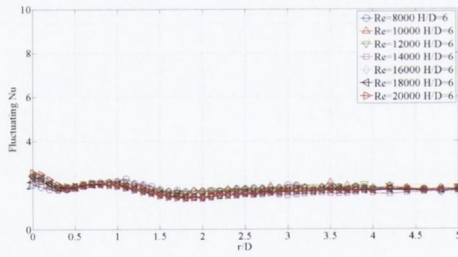
(b)



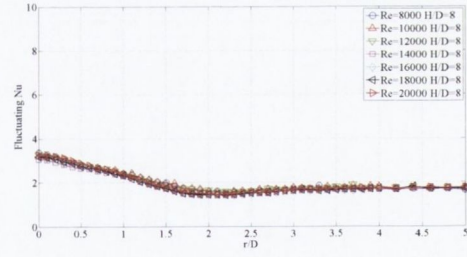
(c)



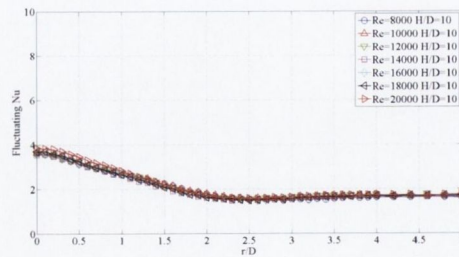
(d)



(e)



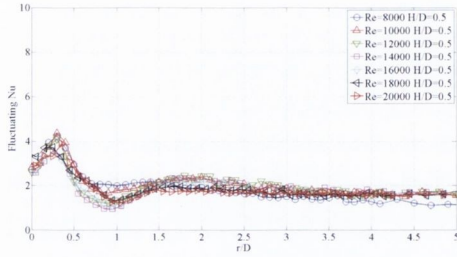
(f)



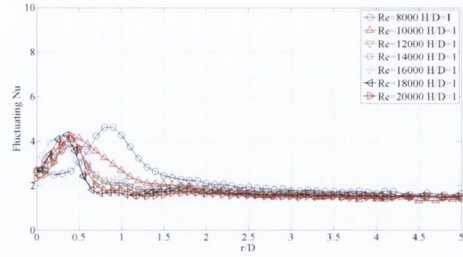
(g)

Fluctuating Nusselt number distribution for conventional impinging jet for all Reynolds numbers at $H/D =$ (a) 0.5, (b) 1, (c) 2, (d) 4, (e) 6, (f) 8, (g) 10

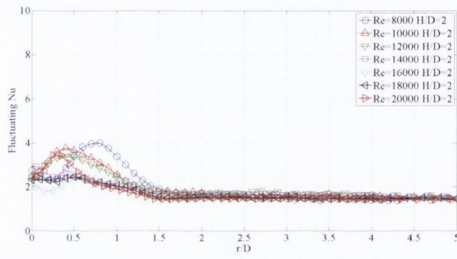
A.3.2 Swirling Impinging Jet with Generator L_c



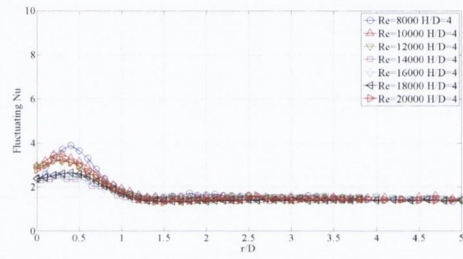
(a)



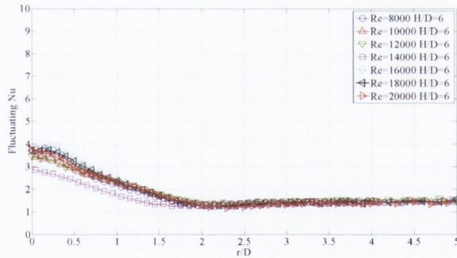
(b)



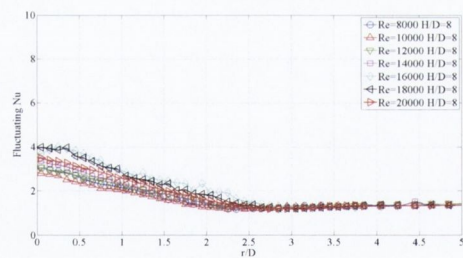
(c)



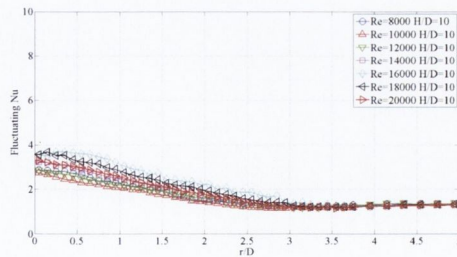
(d)



(e)



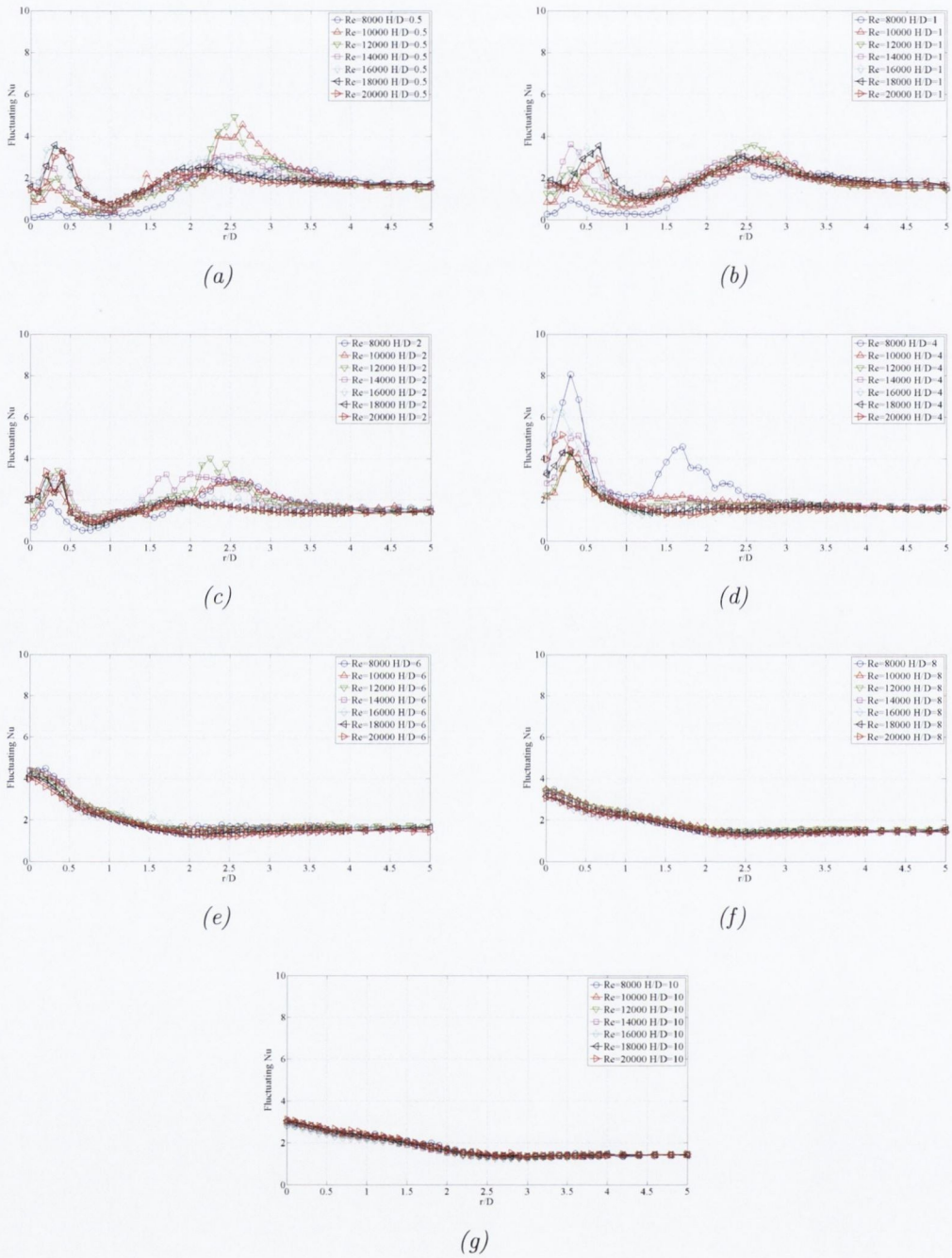
(f)



(g)

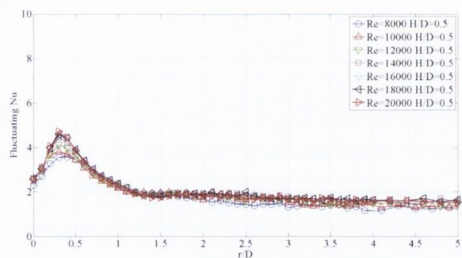
Fluctuating Nusselt number distribution for swirling impinging jet with generator L_c for all Reynolds numbers at $H/D =$ (a) 0.5, (b) 1, (c) 2, (d) 4, (e) 6, (f) 8, (g) 10

A.3.3 Swirling Impinging Jet with Generator L_{no}

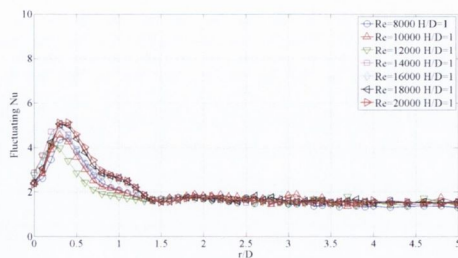


Fluctuating Nusselt number distribution for swirling impinging jet with generator L_{no} for all Reynolds numbers at $H/D =$ (a) 0.5, (b) 1, (c) 2, (d) 4, (e) 6, (f) 8, (g) 10

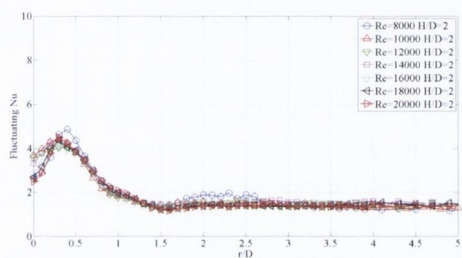
A.3.4 Swirling Impinging Jet with Generator S_c



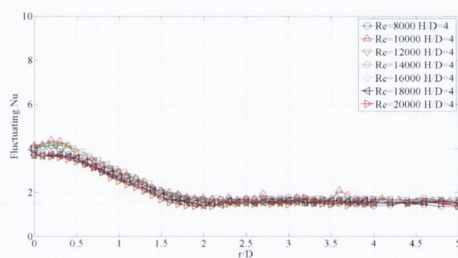
(a)



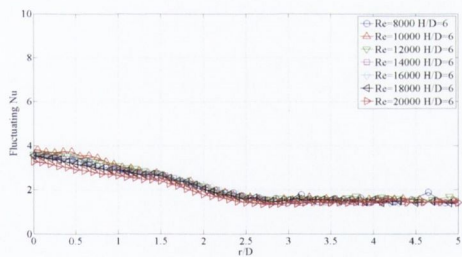
(b)



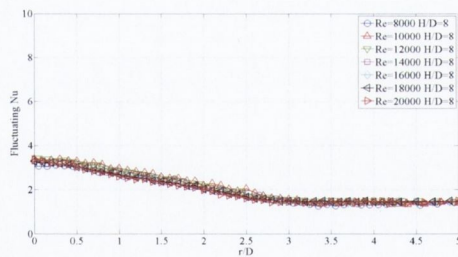
(c)



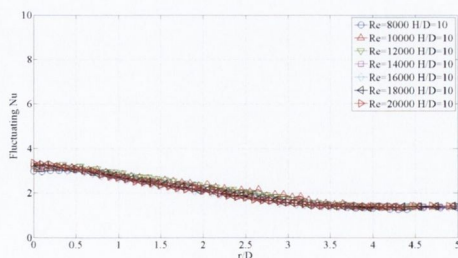
(d)



(e)



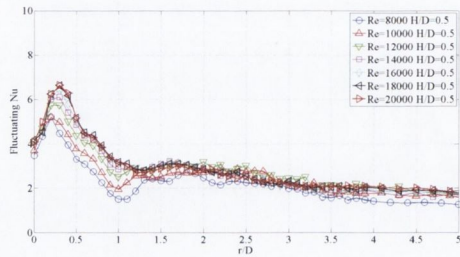
(f)



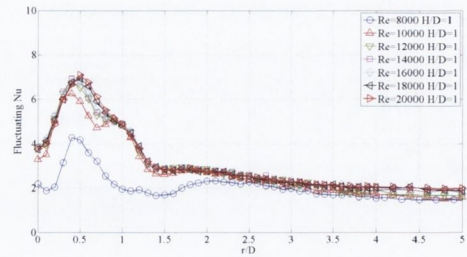
(g)

Fluctuating Nusselt number distribution for swirling impinging jet with generator S_c for all Reynolds numbers at $H/D =$ (a) 0.5, (b) 1, (c) 2, (d) 4, (e) 6, (f) 8, (g) 10

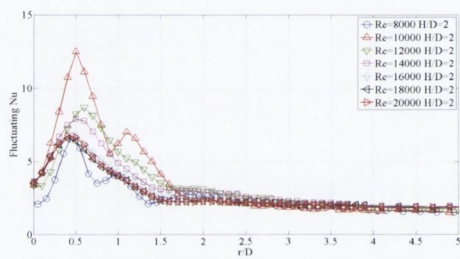
A.3.5 Swirling Impinging Jet with Generator S_{no}



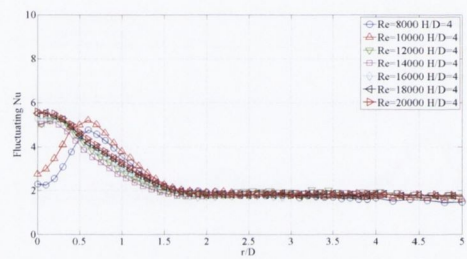
(a)



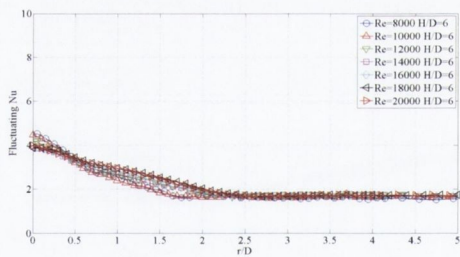
(b)



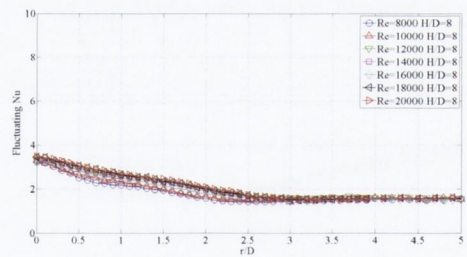
(c)



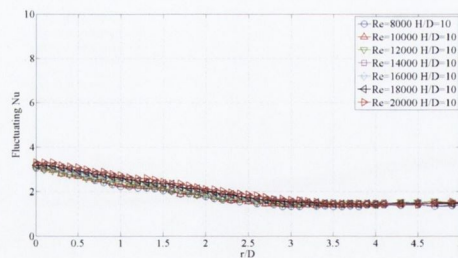
(d)



(e)



(f)

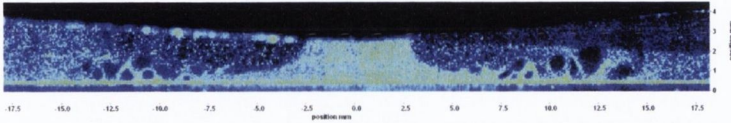


(g)

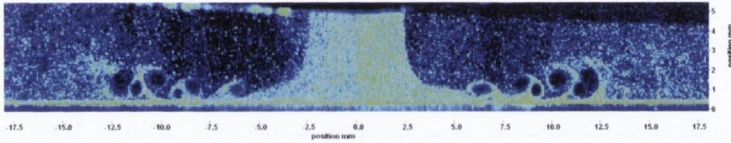
Fluctuating Nusselt number distribution for swirling impinging jet with generator S_{no} for all Reynolds numbers at $H/D =$ (a) 0.5, (b) 1, (c) 2, (d) 4, (e) 6, (f) 8, (g) 10

Appendix B - Flow Visualisation

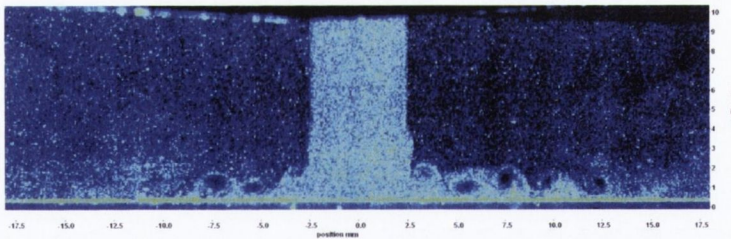
B.1 Conventional Impinging Jet



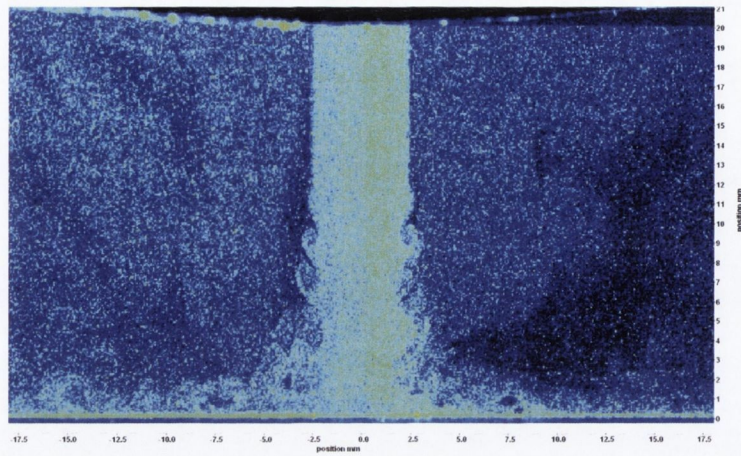
Instantaneous flow visualisation of conventional impinging jet at $H/D=0.5$ and Reynolds number of 14,000



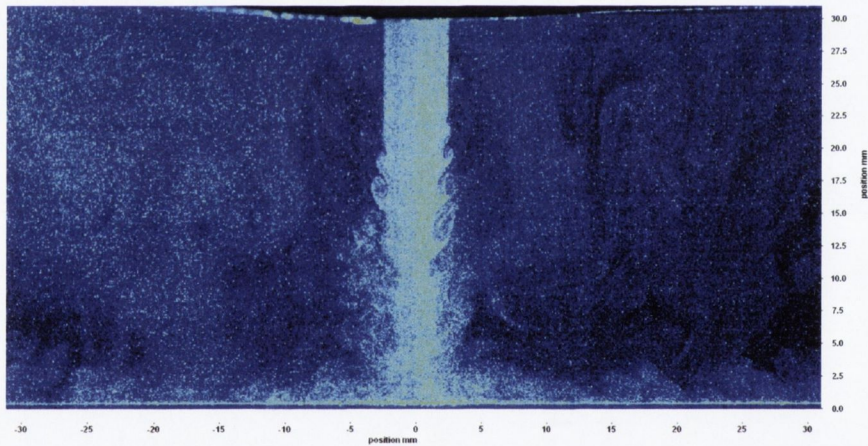
Instantaneous flow visualisation of conventional impinging jet at $H/D=1$ and Reynolds number of 14,000



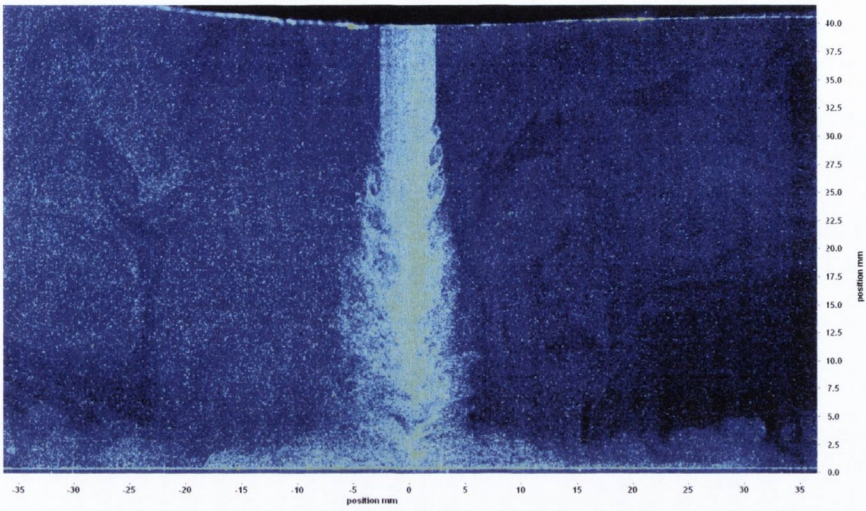
Instantaneous flow visualisation of conventional impinging jet at $H/D=2$ and Reynolds number of 14,000



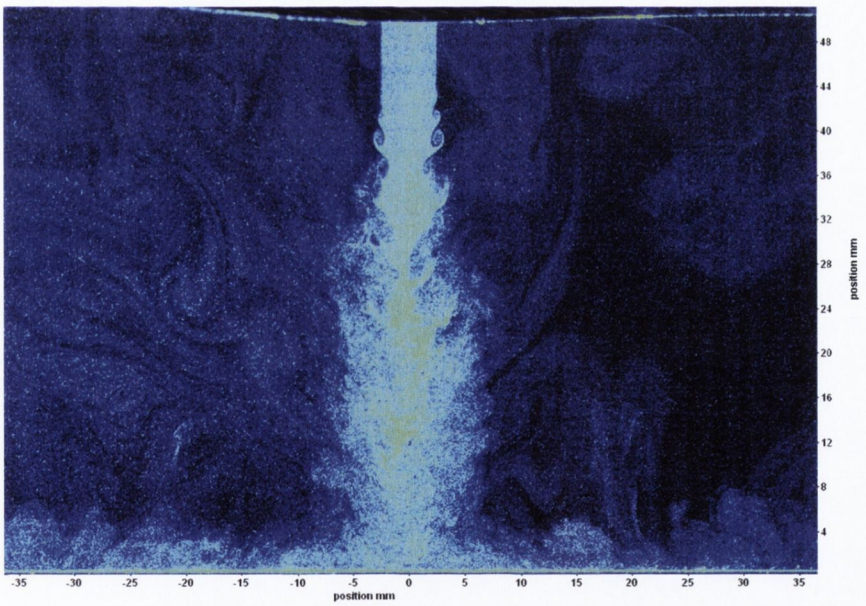
Instantaneous flow visualisation of conventional impinging jet at $H/D=4$ and Reynolds number of 14,000



Instantaneous flow visualisation of conventional impinging jet at $H/D=6$ and Reynolds number of 14,000

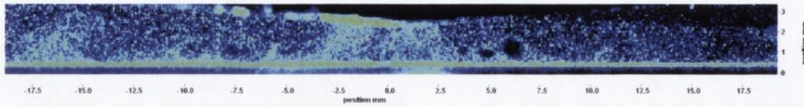


Instantaneous flow visualisation of conventional impinging jet at $H/D=8$ and Reynolds number of 14,000

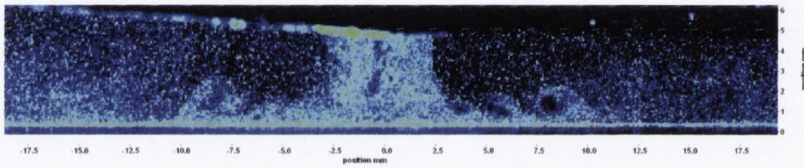


Instantaneous flow visualisation of conventional impinging jet at $H/D=10$ and Reynolds number of 14,000

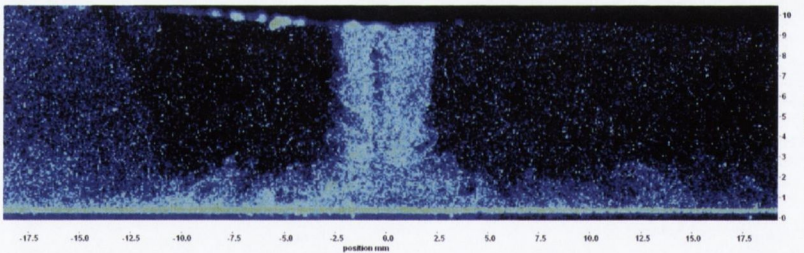
B.2 Swirling Impinging Jet with Generator L_c



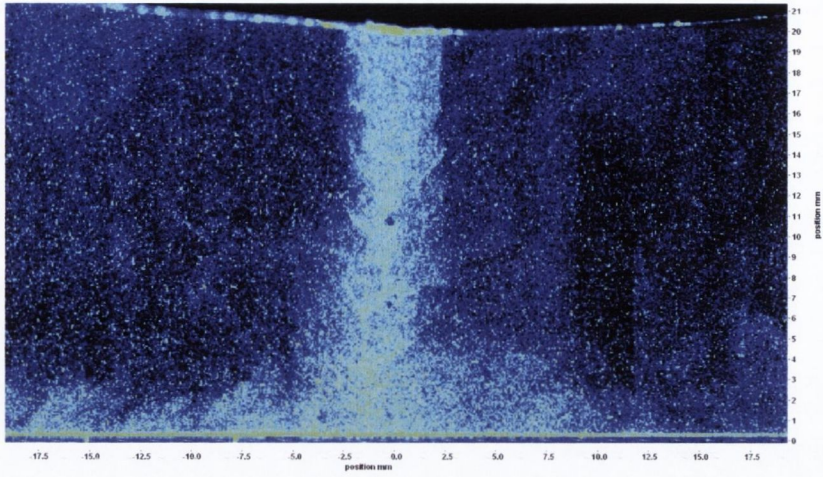
Instantaneous flow visualisation of swirling impinging jet at $H/D=0.5$ and Reynolds number of 14,000



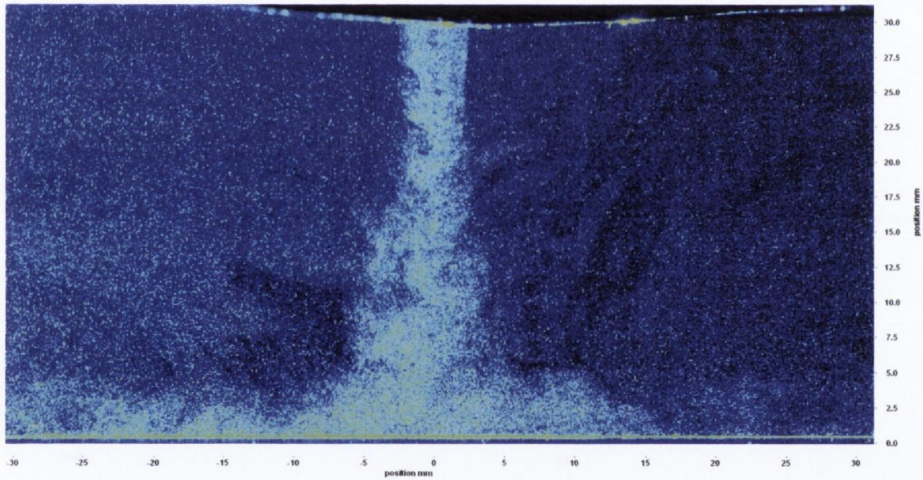
Instantaneous flow visualisation of swirling impinging jet with generator L_c at $H/D=1$ and Reynolds number of 14,000



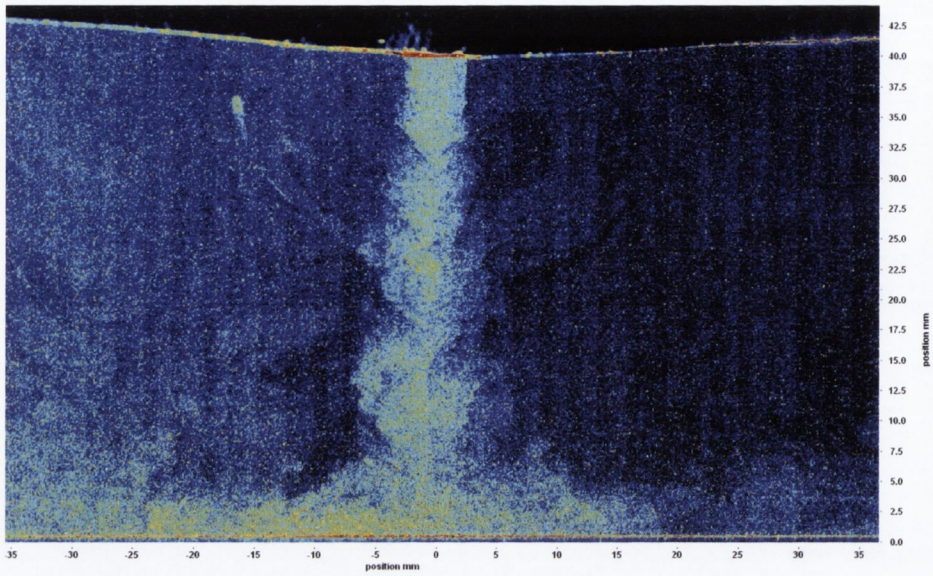
Instantaneous flow visualisation of swirling impinging jet with generator L_c at $H/D=2$ and Reynolds number of 14,000



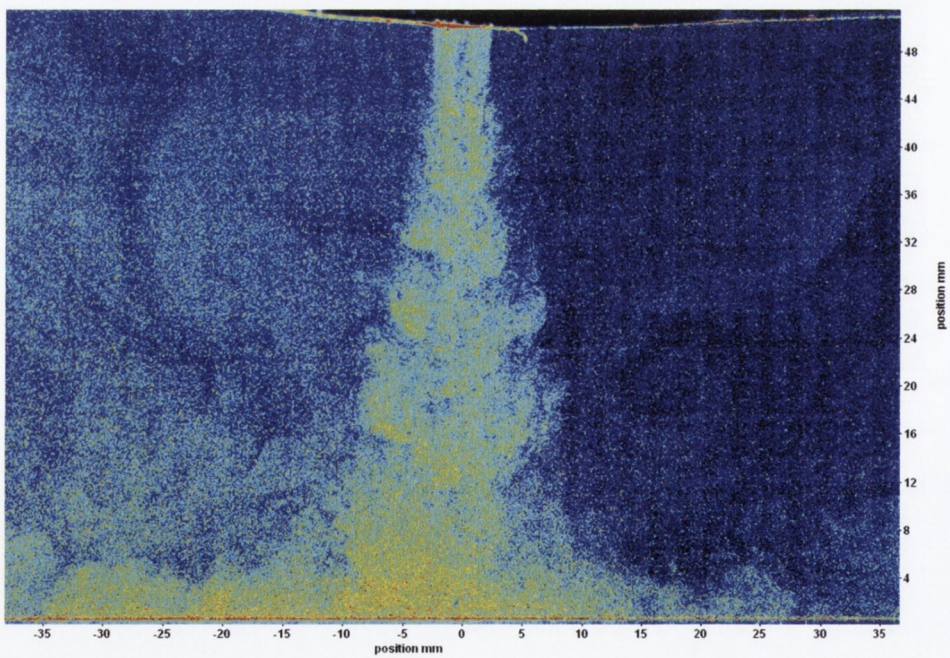
Instantaneous flow visualisation of swirling impinging jet with generator L_c at $H/D=4$ and Reynolds number of 14,000



Instantaneous flow visualisation of swirling impinging jet with generator L_c at $H/D=6$ and Reynolds number of 14,000

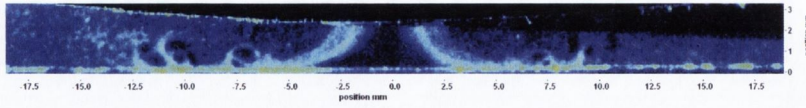


Instantaneous flow visualisation of swirling impinging jet with generator L_c at $H/D=8$ and Reynolds number of 14,000

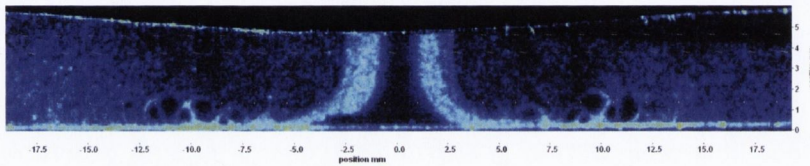


Instantaneous flow visualisation of swirling impinging jet with generator L_c at $H/D=10$ and Reynolds number of 14,000

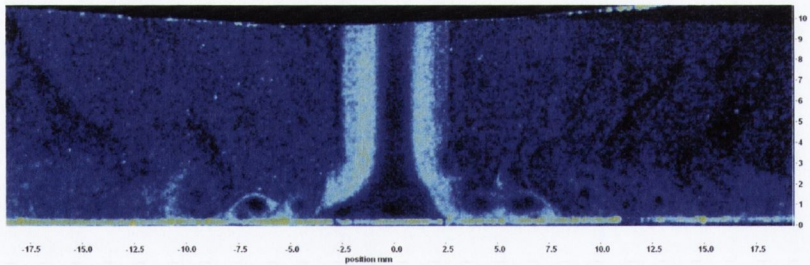
B.3 Swirling Impinging Jet with Generator L_{no}



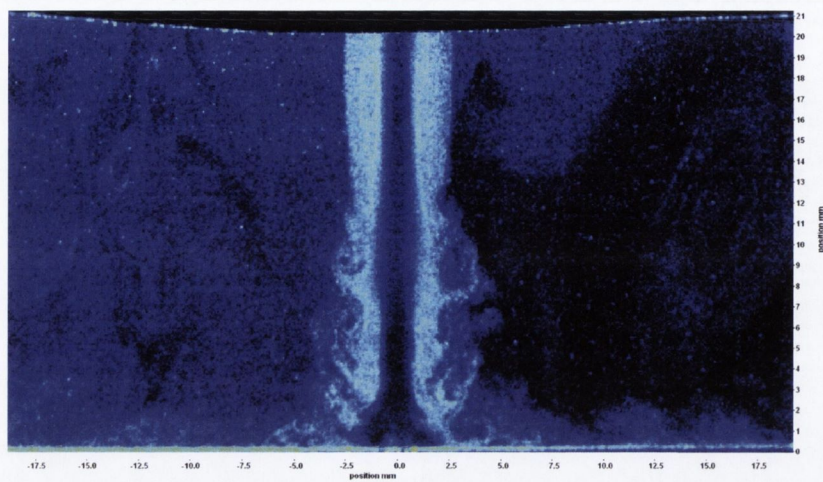
Instantaneous flow visualisation of swirling impinging jet with generator L_{no} at $H/D=0.5$ and Reynolds number of 14,000



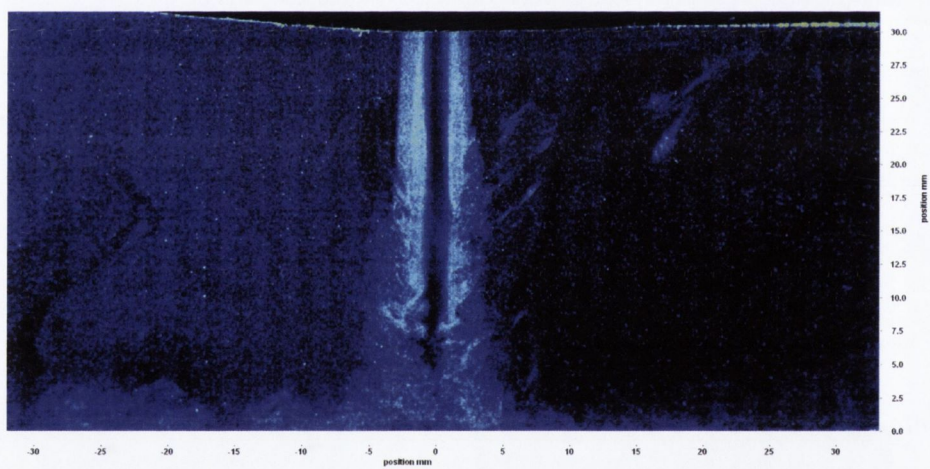
Instantaneous flow visualisation of swirling impinging jet with generator L_{no} at $H/D=1$ and Reynolds number of 14,000



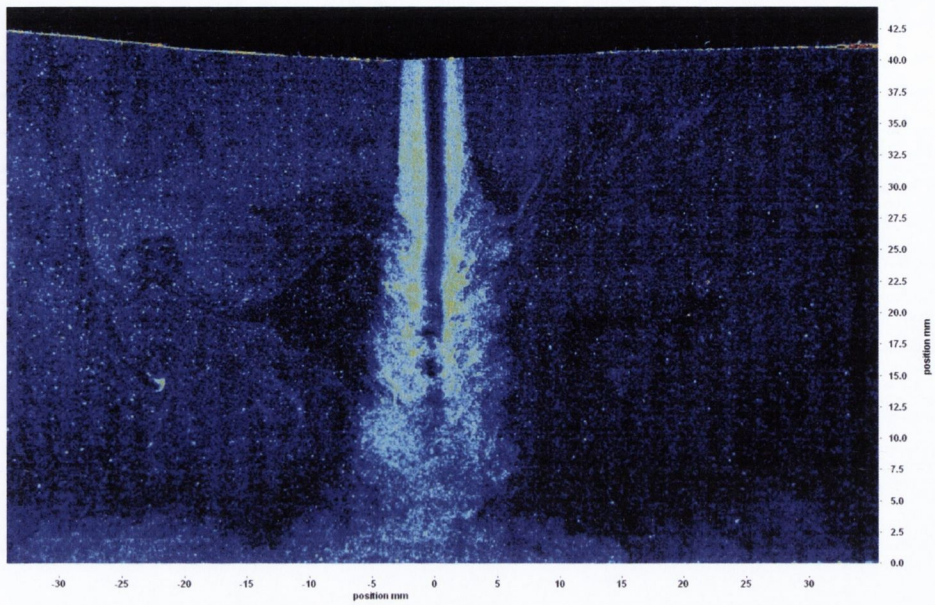
Instantaneous flow visualisation of swirling impinging jet with generator L_{no} at $H/D=2$ and Reynolds number of 14,000



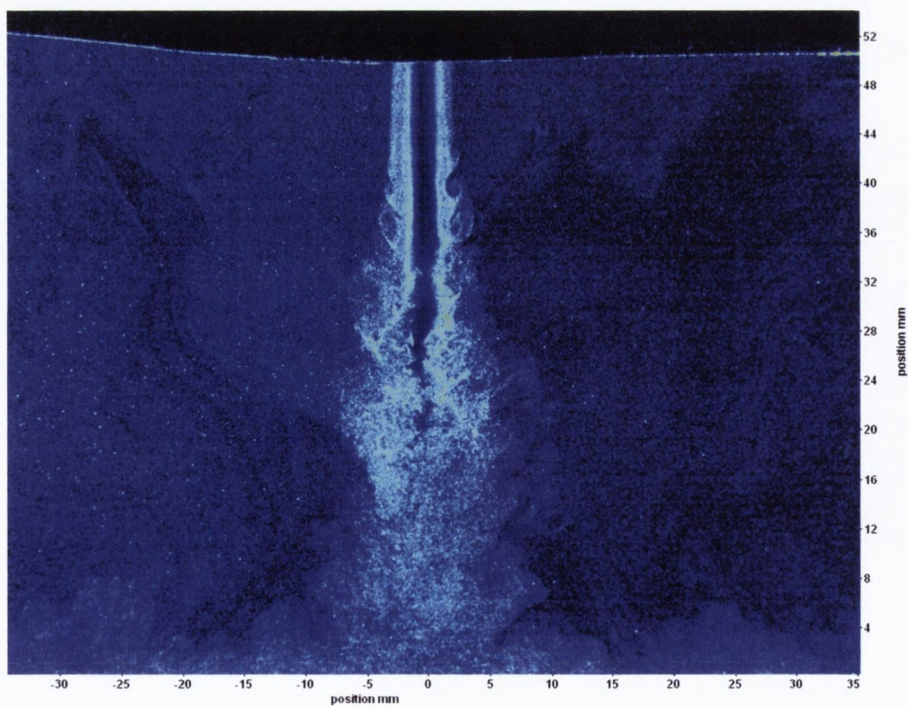
Instantaneous flow visualisation of swirling impinging jet with generator L_{no} at $H/D=4$ and Reynolds number of 14,000



Instantaneous flow visualisation of swirling impinging jet with generator L_{no} at $H/D=6$ and Reynolds number of 14,000

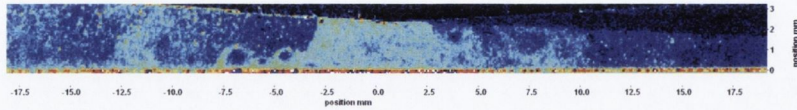


Instantaneous flow visualisation of swirling impinging jet with generator L_{no} at $H/D=8$ and Reynolds number of 14,000

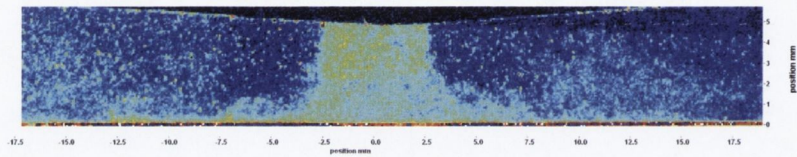


Instantaneous flow visualisation of swirling impinging jet with generator L_{no} at $H/D=10$ and Reynolds number of 14,000

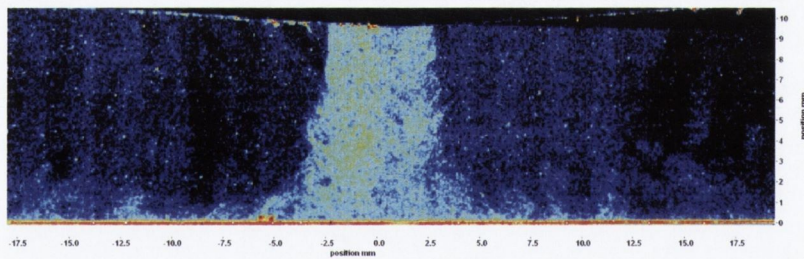
B.4 Swirling Impinging Jet with Generator S_c



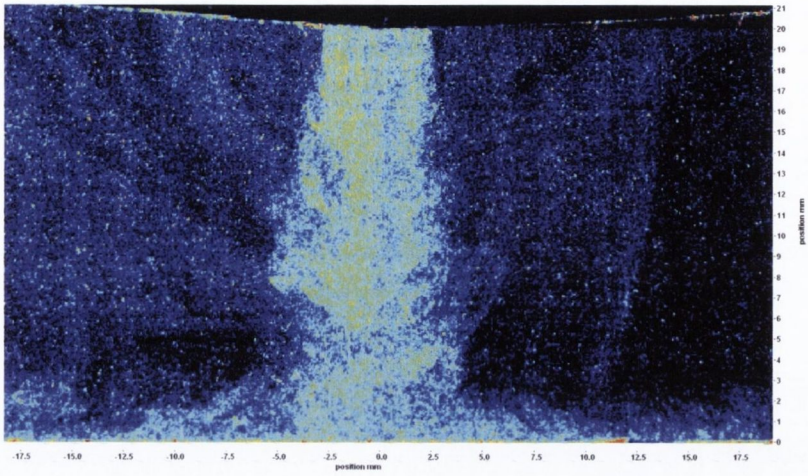
Instantaneous flow visualisation of swirling impinging jet with generator S_c at $H/D=0.5$ and Reynolds number of 14,000



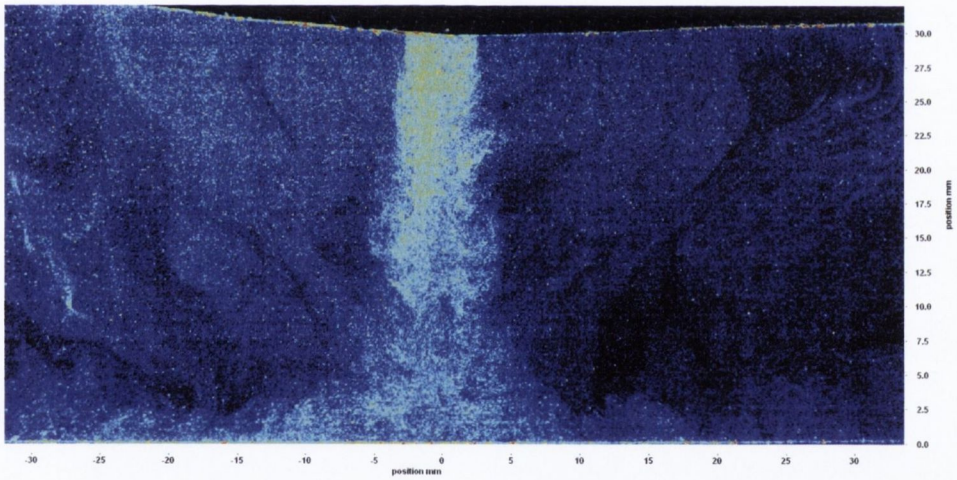
Instantaneous flow visualisation of swirling impinging jet with generator S_c at $H/D=1$ and Reynolds number of 14,000



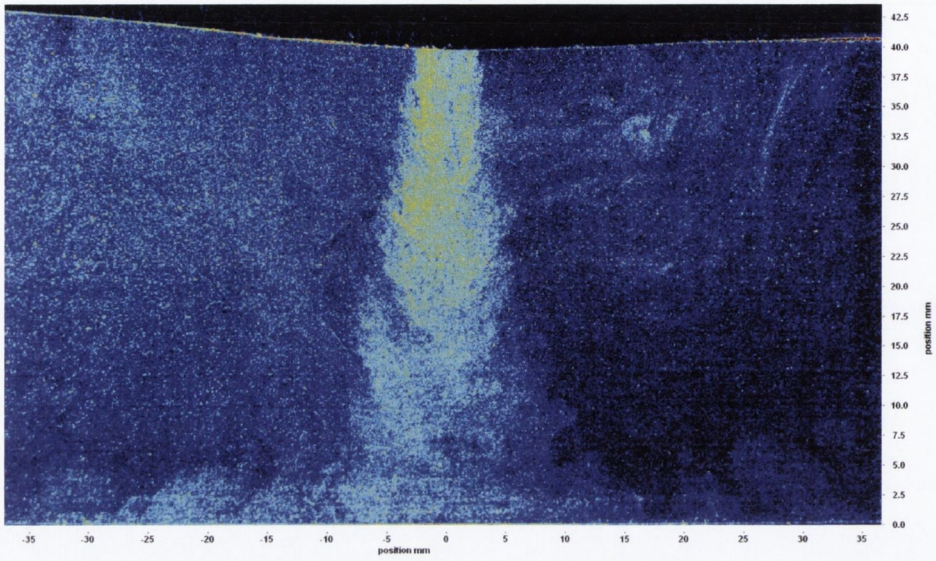
Instantaneous flow visualisation of swirling impinging jet with generator S_c at $H/D=2$ and Reynolds number of 14,000



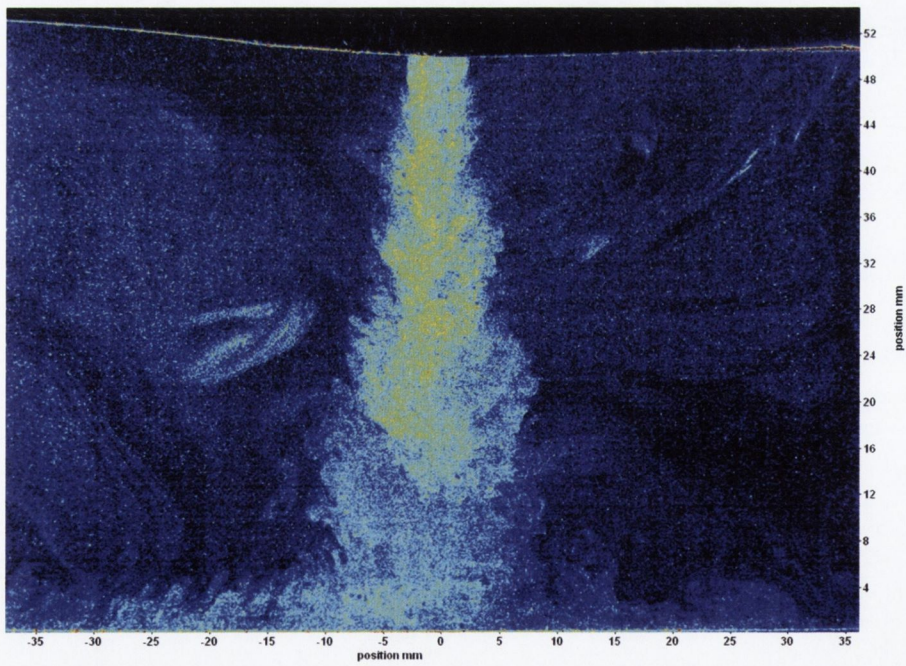
Instantaneous flow visualisation of swirling impinging jet with generator S_c at $H/D=4$ and Reynolds number of 14,000



Instantaneous flow visualisation of swirling impinging jet with generator S_c at $H/D=6$ and Reynolds number of 14,000

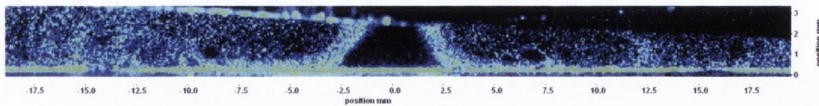


Instantaneous flow visualisation of swirling impinging jet with generator S_c at $H/D=8$ and Reynolds number of 14,000

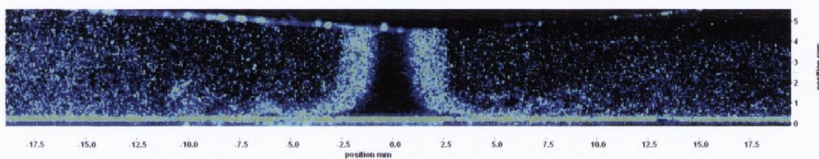


Instantaneous flow visualisation of swirling impinging jet with generator S_c at $H/D=10$ and Reynolds number of 14,000

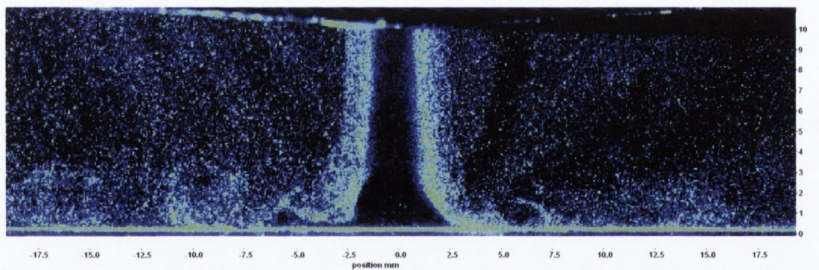
B.5 Swirling Impinging Jet with Generator S_{no}



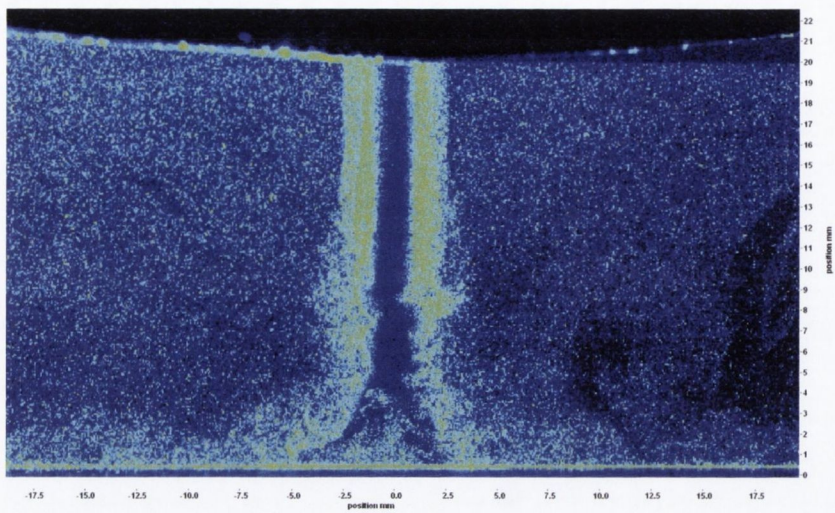
Instantaneous flow visualisation of swirling impinging jet with generator S_{no} at $H/D=0.5$ and Reynolds number of 14,000



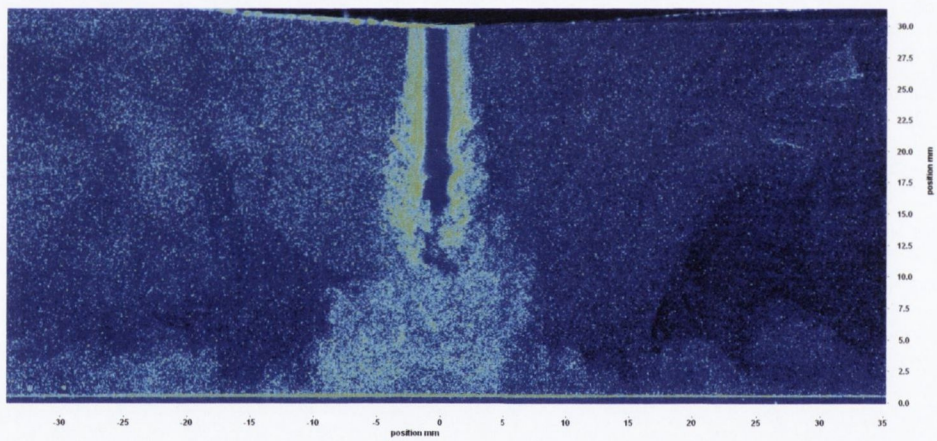
Instantaneous flow visualisation of swirling impinging jet with generator S_{no} at $H/D=1$ and Reynolds number of 14,000



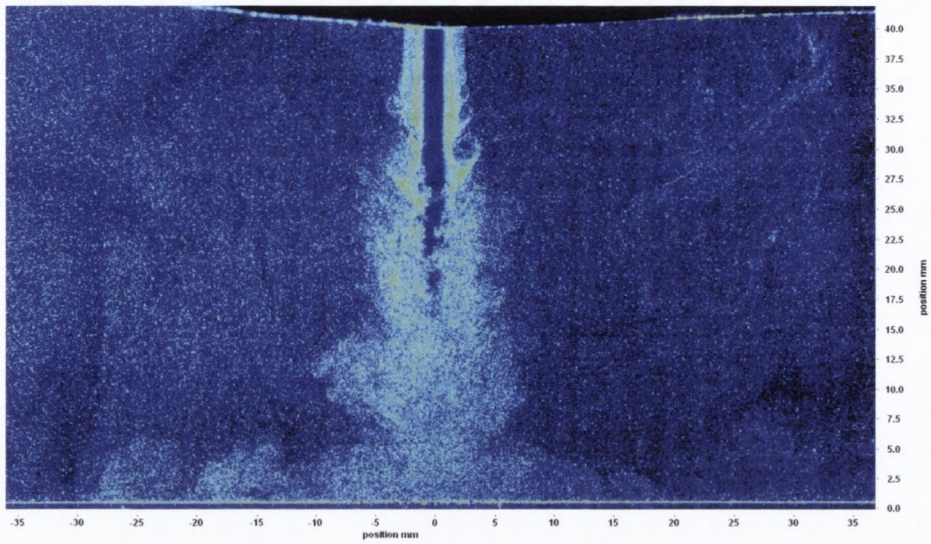
Instantaneous flow visualisation of swirling impinging jet with generator S_{no} at $H/D=2$ and Reynolds number of 14,000



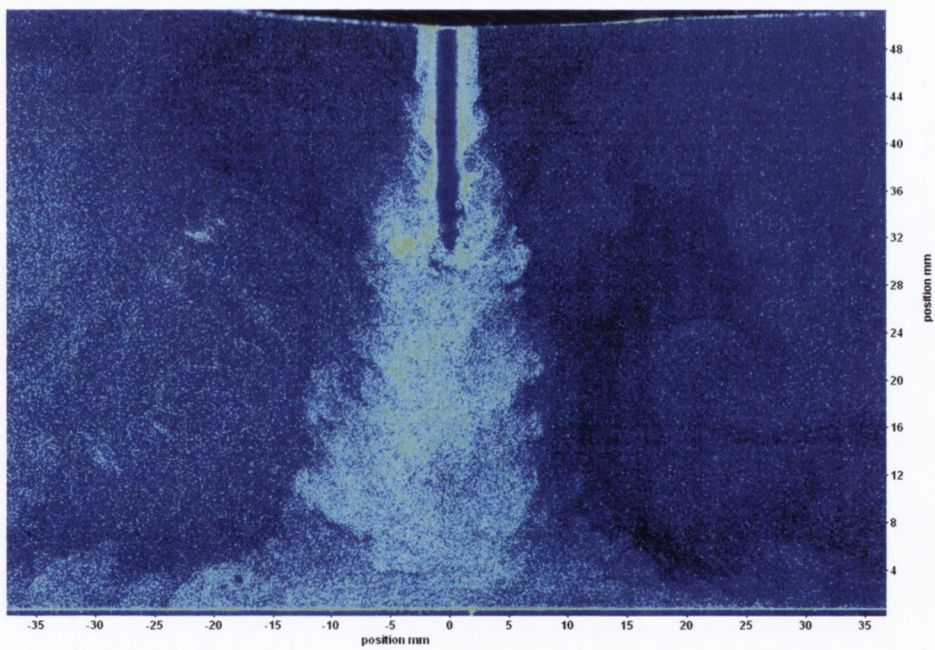
Instantaneous flow visualisation of swirling impinging jet with generator S_{no} at $H/D=4$ and Reynolds number of 14,000



Instantaneous flow visualisation of swirling impinging jet with generator S_{no} at $H/D=6$ and Reynolds number of 14,000



Instantaneous flow visualisation of swirling impinging jet with generator S_{no} at $H/D=8$ and Reynolds number of 14,000



Instantaneous flow visualisation of swirling impinging jet with generator S_{no} at $H/D=10$ and Reynolds number of 14,000

Appendix C - FLIR Systems Calibration Certificate



Certificate No. 02704

Instrument Calibration Certificate

This is to certify that FLIR, THV, ThermoVision, ThermaCAM and SC series of scanners, the FLIR Temperature Reference models BB-150 and BB-400, have been calibrated using radiation sources, the accuracy of which are traceable to National Standards at the Swedish National Testing and Research and Research Institute (Sweden) or at the NIST, National Institute of Standards and Technology (USA).

All readings are within manufacturers specification.

FLIR Systems recommend recalibration every 12 months.

- Service Order No: 097087
- Customer: University of Dublin
- Model: Thermovision A40M F/W
- Serial No: 25000745
- Lenses: 36mm
- Filters: NOF

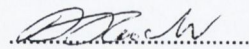
INITIAL CHECK:

Within specification

Out of Specification

... see attached Service Order Report

Calibration performed by: Adrian Goodhand



(sign)

... SERVICE ENGINEER

(Title)

Calibration date: 07/08/2009

All business is conducted according to FLIR Systems Ltd. Standard Terms and Conditions of Sale and Service, a full set, of which, is available on request.

FORM 106 Issue 3

FLIR Systems Instrument Calibration Certificate for Thermovision A-40 thermal imaging camera